Rheology, eruption, and flow of three-phase magma

Jen Truby

A thesis submitted in fulfilment of the requirements
for the degree of Doctor of Philosophy

Department of Earth Sciences, University of Durham

2016

Abstract

A model is developed for the rheology of a three-phase suspension of bubbles and particles in a Newtonian liquid undergoing steady flow. An 'effective-medium' approach is adopted, which treats the bubbly liquid as a continuous medium which suspends the particles. The resulting three-phase model combines separate two-phase models for bubble suspension rheology and particle suspension rheology, which are taken from the literature. The model is validated against new experimental data for three-phase suspensions of bubbles and spherical particles, collected in the low bubble capillary number regime. Good agreement is found across the experimental range of particle volume fraction ($0 \leq \phi_p \lesssim 0.5$) and bubble volume fraction ($0 \leq \phi_b \lesssim 0.3$). Consistent with model predictions, experimental results demonstrate that adding bubbles to a dilute particle suspension at low capillarity increases its viscosity, whilst adding bubbles to a concentrated particle suspension decreases its viscosity. The model accounts for particle anisometry and is easily extended to account for variable capillarity, and bubbles which are larger than the particles, but has not been experimentally validated for these cases. This model is a significant step forward, because it allows the viscosity of many magmas and lavas — which typically contain both crystals and bubbles — to be calculated more accurately.

The model is then used to explain three volcanological problems. Firstly, it is proposed that in a jammed magma mush, the pervasive formation and growth of bubbles of magmatic gas can push the crystals apart, unjamming the mush. Further bubble growth would then lead to a dramatic reduction in viscosity. This concept is tested using analogue suspensions, and it is demonstrated that the growth of bubbles alone is sufficient to mobilize an initially jammed particle suspension. Secondly, lava morphologies found in the crystal-rich 1780 flow field on Volcán Llaima, Chile, are described. Within the 1780 flow field, occur: well-developed 'a'ā, with broad, leveed channels; well-developed pāhoehoe; slabby pāhoehoe with transitions to and from 'a'ā; and a cluster of features that have been termed "'a'ā mounds", which are interpreted to be higher viscosity analogues of rootless shields found on Hawai'i, and comparable to megatumuli and terraces found on Mount Etna. It is proposed that this crystal-rich lava was able to flow as pāhoehoe because bubbles lowered its viscosity. Thirdly, a recent lava flow from Kīlauea is analysed, and the various factors that control viscosity quantified. These include bubble and crystal fractions, crystal shapes, and dissolved volatile contents. These factors are then used to understand down-flow changes in morphology. In each of these volcanological problems, understanding the three-phase rheology is important for understanding the problem, and the related flow behaviour and hazards.

Declaration

I declare that this thesis, which I submit for the degree of Doctor of Philosophy at Durham University, is my own work and not substantially the same as any which has previously been submitted at this or any other university.

Statement of copyright

Acknowledgements

I would like to thank my supervisors — Ed Llewellin and Richard Brown — for their guidance and support throughout my time at Durham.

I would also like to thank:

- Basti Mueller and Heidy Mader, who provided the experimental results used to validate my model in chapter 3 and co-authored the paper on which that chapter is based.
- Jacopo Taddeucci, who supervised my time at INGV, Rome where I carried out the experiments described in chapter 4, and co-authored the paper on which that chapter is based.
- Mike Dungan, who supervised my fieldwork at Volcán Llaima, and co-authored the paper on which chapter 5 is based.
- Tim Orr, who worked with Ed in the field on Kīlauea, and has contributed to the critical reading of chapters 5 and 6.

Last but not least, I'd like to thank my family — in particular mum and Connor — who have encouraged me all the way.

This project was funded by the Natural Environment Research Council (NERC Studentship NE/K500999/1).

Dedication

For my family.

Contents

List of Tables

List of Figures

Chapter 1

Introduction

1.1 Motivation

In the context of volcanology, the rheology of a magma or lava is a primary controlling factor for how it erupts and flows (e.g. Webb and Dingwell, 1990; Mader et al., 2013). Rheology is the study of how a fluid flows in response to an applied stress. It influences the ability of magma to intrude into the crust, and the efficiency with which magmas of different compositions intermingle and mix (e.g. Jellinek et al., 1999; Phillips and Woods, 2002; Petford, 2003). It also influences the way in which stored magma ascends to the surface, and the ease with which volatiles can degas and outgas on the way (e.g. Papale et al., 1998; Llewellin and Manga, 2005; Hale et al., 2007; Edmonds, 2008). Rheology therefore influences whether or not magma will fragment as it depressurizes: and as a result it controls whether or not the magma will erupt explosively or effusively (e.g. Dingwell et al., 1996; Papale, 1999). Once on the surface, rheology influences the way a lava will flow, including its morphology, velocity, and length of flow (e.g. MacDonald, 1953; Peterson and Tilling, 1980). Throughout the magmatic and volcanic system, rheology is an important parameter, and understanding the factors that control it is therefore key for understanding how volcanoes behave. These influences are summarized in figure 1.1.

Decades of research have been dedicated to measuring the rheology of silicate melts. In the field, this may take of the form of estimates based on morphological parameters of lava flows (e.g. Hulme, 1974; Chevrel et al., 2013), or direct measurements with viscometers (e.g. Shaw et al., 1968; Pinkerton and Norton, 1995); in the laboratory, this commonly involves making rheometric measurements on samples of lava at high temperature (e.g. Webb and Dingwell, 1990; Hess and Dingwell, 1996; Caricchi et al., 2008; Avard and Whittington, 2012). In general, these measurements

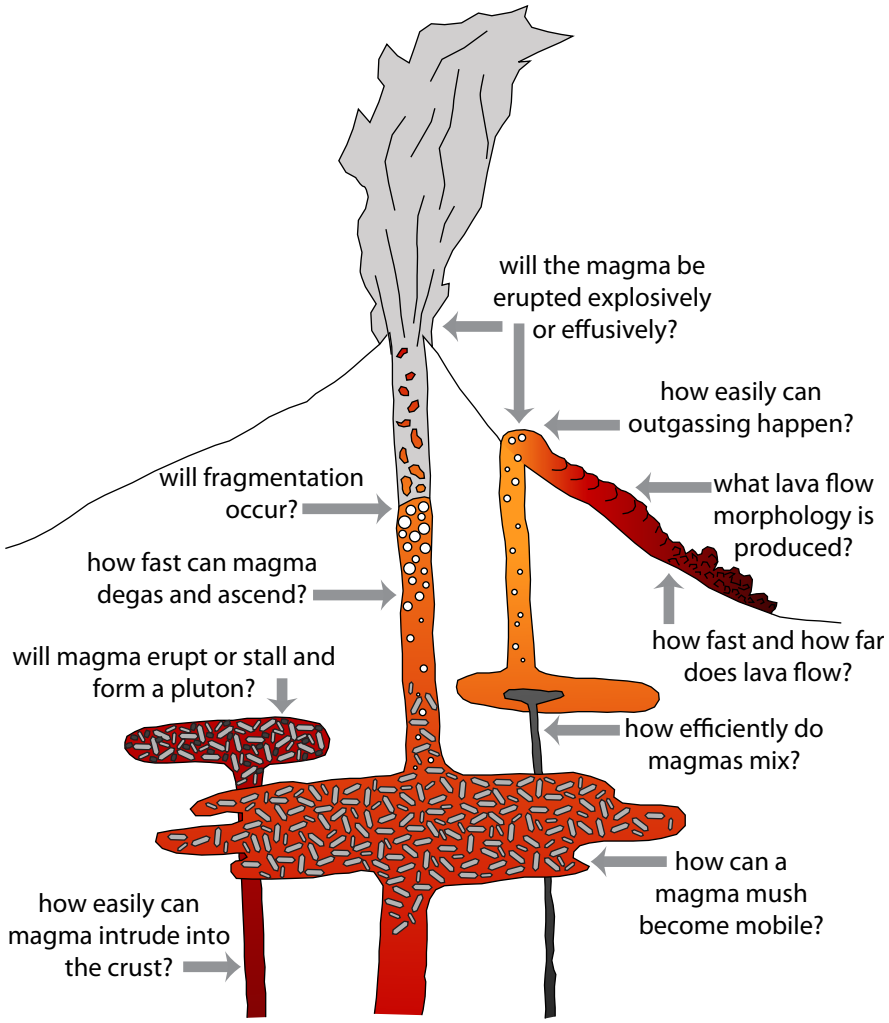

Figure 1.1: Schematic sketch of a volcanic system — not to scale — highlighting locations and processes in which rheology plays a key role.

are complicated by the wide range of compositions found in nature, and the difficulty of preventing additional crystallization and bubble growth during experiments. However, measurements of the rheology of natural lavas are essential for modelling their behaviour.

In addition to measurements of the rheology of pure melts, it is important to understand how the proportion of crystals or bubbles suspended in the melt affects its rheology (Mader et al., 2013). Studies typically approach this problem either from a theoretical point of view, for example by calculating the effect of a single particle or bubble on the flow of a fluid (e.g. Einstein, 1906; Jeffery, 1922), or from an experimental stand-point, measuring the effect of variable particle or bubble fractions on the fluid's rheology (e.g. Rust and Manga, 2002; Llewellin and Manga,

2005; Mueller et al., 2010, 2011). Fewer experiments have used natural magmas or lavas to address the problem of understanding two-phase rheology (e.g. Bagdassarov et al., 1994; Champallier et al., 2008). As a result of this past research, constitutive equations describing most aspects of the rheology of two-phase suspensions have been developed and are routinely applied to predict their rheology (Mader et al., 2013).

However, in volcanological systems, it is quite common to find magmas and lavas that contain both crystals and bubbles. Only a small amount of work has been done on the rheology of three-phase suspensions (Harris and Allen, 2008; Macedonio et al., 2005), and existing two-phase models are often used for magmas, especially when the proportion of one phase is very small. It is unclear how reasonable it is to assume that the smaller volume fraction phase can be neglected in models. This thesis will therefore fill this gap in understanding by describing a constitutive equation and validatory experiments, which provide a rheological tool that can be used to predict the rheology of three-phase suspensions.

1.2 Structure

The thesis will start with a review of the relevant background literature (chapter 2), beginning with existing models for two-phase rheology (section 2.2), and the few studies that have looked at three-phase rheology (section 2.3). Since these models are generally based on idealised analogue systems, the complexities associated with magmatic systems will be discussed next (section 2.4). These include: factors that influence the melt-phase viscosity; the effect of strain rate; the differences between crystals in a natural magma and particles used in an analogue experiment; the controls on bubble nucleation and growth; and the fact that magmatic systems are not static, and may evolve over time. A brief discussion of the relative importance and uses of natural and analogue experiments will follow, explaining why analogue experiments were chosen for the studies presented later (section 2.1). The background chapter will conclude with a more detailed discussion of a number of the ways in which rheology influences volcanic processes (section 2.5).

Chapter 3 is based on a paper published in the Proceedings of the Royal Society (Truby et al., 2015). This chapter introduces the framework from which a three-phase constitutive equation for viscosity is derived (section 3.2), the experiments carried out to validate the equation (sections 3.3, 3.4, and 3.5), and potential (unvalidated) extensions to the equation (section 3.5.3). The three-phase experiments presented in this chapter were carried out by Sebastian Mueller (co-author), and

supervised by Heidy Mader (co-author) at Bristol University. The formulation of the three-phase model, analysis of the data, and proposed extensions to the model were my work. In addition, I wrote the paper with assistance from Ed Llewellin (co-author and supervisor at Durham University), except for the introduction (drafted by me and improved by Heidy Mader), and methods (written by Sebastian Mueller). The paper in its published form is included in Appendix A.

Further experiments are presented in chapter 4, looking at the high crystal-fraction extreme of the experimental range used in chapter 3. The purpose of this chapter is to understand the effects of adding bubbles to a particularly crystal-rich suspension, in order to explain how extremely crystal-rich magma mushes can become mobile enough to erupt (section 4.2). Following the experimental results and discussion (sections 4.3, and 4.4), a generic magma reservoir model is used to demonstrate the effect of bubble growth in a realistic magma reservoir (section 4.5). Conditions under which bubble growth will lead to eruption (section 4.5.3) are compared to circumstances where the magma will fail to become mobile (sections 4.5.4 and 4.5.5). This chapter was submitted as a paper to Nature Communications in August 2015, and was rejected — with the option to resubmit subject to addressing comments by three reviewers. The experiments described in this chapter were carried out by me at the Istituto Nazionale de Geofisica e Vulcanologia (INGV) in Rome, and supervised by Jacopo Taddeucci (co-author, INGV). I carried out the data analysis, applied the results to the generic magma reservoir scenarios, and wrote the paper, with assistance from Ed Llewellin and Jacopo Taddeucci. The submitted version of this paper is included in appendix B.

As the first of two field-based applications of the model developed in chapter 3, chapter 5 uses field observations of lava flows and measurements of crystal and bubble fractions (section 5.3) to understand unusual lava morphologies observed at Volcán Llaima, Chile. By calculating the viscosity of the lavas found at Volcán Llaima, a comparison is made to other volcanoes at which similar lava morphologies are observed, and the differences are explained (section 5.4). The field observations at Volcán Llaima were made by me, Mike Dungan (co-author, University of Oregon) and Ed Llewellin. A paper covering the research described in this chapter, was written by me with assistance from Ed Llewellin, Richard Brown (co-author and supervisor), and Mike Dungan. This paper has been submitted to Journal of Volcanology and Geothermal Research; it is included in appendix B.

Chapter 6 describes the second field-based application of the three-phase model. In this case, the evolution of lava rheology and morphology along a 20 km lava flow at Kīlauea, Hawai‘i was assessed using samples collected from along the active

flow. Measurements of crystal and bubble fractions, and changes in the dissolved volatile content along the flow (section 6.4) were used to calculate its rheology and understand the rheological controls on total flow length (section 6.5). The samples used in this chapter were collected by Ed Llewellin and Tim Orr (U.S. Geological Survey and Hawaiian Volcano Observatory); Hugh Tuffen (Lancaster University) supervised my analysis of dissolved volatiles at Lancaster University, and collected two of the thermogravimetric (TGA) analyses on my behalf. The remainder of the work and analysis was carried out by me.

The concluding chapter brings together the observations and results from chapters 3 to 6 to discuss the rheological evolution of a magma as it travels through the volcanic system, and assess the importance of rheology at numerous locations in the system (section 7.1). The chapter concludes by suggesting some avenues of future work that would supplement and improve the three-phase rheological model (section 7.3).

Chapter 2

Rheological and volcanological background

This chapter will cover the rheological and volcanological background necessary to introduce the subsequent chapters. The majority of this text is based on introductory material from the papers which form the basis for chapters 3 to 5, and therefore provide a theoretical framework for the thesis. A summary of all parameters described in this chapter is given in table 2.1.

2.1 Analogue and natural experiments

Many rheological experiments use analogue materials rather than natural magmas (e.g. Rust and Manga (2002); Llewellin and Manga (2005) for bubble suspensions; and Mueller et al. (2010, 2011); Cimarelli et al. (2011) for particle suspensions). These materials — often syrups or silicone oils — are well-characterized, and their viscosities can be strictly controlled, allowing key parameters of the system — such as particle and bubble volume fractions — to be systematically varied (Mader et al., 2013). This allows experimentalists to understand the effects of changing just a single parameter within the system. The results of such experiments are often expressed in terms of viscosity changes *relative* to the suspending fluid viscosity, as outlined in section 2.2 and equation 2.1.

Experiments on natural magmas are necessary to determine their *absolute* viscosity, but are more difficult both to carry out — requiring magma to be stressed at high temperatures and pressures — and to control — requiring important parameters (such as crystal fraction) to remain constant throughout an experiment. The complex feedbacks that occur in a natural system (section 2.4) mean that it is

Symbol	Description	Units
μ	viscosity	Pa s
η	apparent viscosity	Pa s
η_r	relative viscosity	-
$\eta_{r,0}$	relative viscosity at low Ca	-
$\eta_{r,\infty}$	relative viscosity at high Ca	-
η_*	reference viscosity	Pa s
$\eta_{r,*}$	relative reference viscosity	-
K	consistency	Pa s^n
K_r	relative consistency	s^{n-1}
τ	stress	Pa
τ_0	yield stress	Pa
n	flow index	-
$\dot{\gamma}$	strain-rate	s^{-1}
λ	bubble relaxation time	s
λ_r	melt relaxation time	s
t_c	timescale of shear thinning	s
ϕ	volume fraction	-
ϕ_m	maximum packing fraction	-
ϕ_{m1}	maximum packing fraction for $r_p = 1$	-
r_p	aspect ratio	-
Ca	capillary number	-
a	bubble radius	m
Γ	surface tension	N m^{-1}
G_∞	shear modulus	Pa

Table 2.1: Summary of parameters introduced in this chapter, along with symbols and units. In addition, where subscripts $_b$ or $_p$ appear, this indicates that the parameter relates to the bubble or particle population, respectively.

difficult to isolate the effects of varying fundamental parameters of the system using experiments on natural magmas alone.

Combining the results of analogue and natural experiments allows the true rheology of a magma to be determined, from the absolute viscosity of the natural melt and the relative effect of varying important parameters (Pinkerton and Stevenson, 1992). Both types of experiment are therefore essential for a complete understanding of magma rheology.

It is always important to ensure that the analogue system used to explore a problem is suitable: this is done by performing a non-dimensional analysis of the problem of interest, and scaling the analogue system to match the natural one (e.g. Burgisser et al., 2005). For example, a key non-dimensional parameter for a bubble suspension is the bubble capillary number, which will be introduced in section 2.2.1. If the bubbles in a natural magma are calculated to be in the low capillarity

regime, then it is important to use equations appropriate for low capillarity bubbles. In general this allows experimentalists to design their experiments to match the non-dimensional parameters of a natural system, and therefore be confident that, despite working with spatial length scales, viscosities, and stresses commonly orders of magnitude smaller than the natural system, their results will still be relevant. A summary of these non-dimensional parameters is given in section 2.2.

2.2 Rheology of two-phase suspensions

The rheology of two-phase suspensions (bubbles-in-liquid or particles-in-liquid, where the liquid is Newtonian) has been the subject of extensive experimental and theoretical research for more than a century. In recent years, significant advances have been made and two-phase constitutive equations are now available which have been validated against experimental data for a wide range of conditions (see Mader et al. (2013) for a recent review).

The rheology of a strictly Newtonian fluid is completely described by its viscosity μ. The viscosity is the ratio of the deforming stress and associated strain-rate which, for rheometric flow, is given by $\mu = \tau/\dot{\gamma} = \text{const}$, where τ is the shear stress, and $\dot{\gamma}$ is the shear strain-rate. When bubbles or solid particles are added to a Newtonian liquid, the resulting suspension has a non-Newtonian rheology. In the simplest case, this means that the ratio of stress and strain-rate is a function of strain-rate, and is termed the apparent viscosity $\eta = \tau/\dot{\gamma} = f(\dot{\gamma})$. The viscosity of a suspension is often reported as the relative viscosity η_r, which is the apparent viscosity of the suspension at a specific strain-rate, normalized by the viscosity of the liquid phase:

$$\eta_r = \frac{\eta}{\mu}. \tag{2.1}$$

The following sub-sections will briefly review the constitutive equations for two-phase suspensions. The subscript 'b' refers to bubble suspensions, the subscript 'p' refers to particle suspensions.

2.2.1 Bubble suspension rheology

When a bubble suspension flows, viscous stresses cause the bubbles to deform. If the flow is 'steady' the bubbles reach an equilibrium deformation, which is described by the bubble capillary number:

$$Ca = \lambda\dot{\gamma}, \tag{2.2}$$

where λ is the bubble relaxation time (Taylor, 1934; Llewellin et al., 2002b; Rust and Manga, 2002). The relaxation time describes the characteristic timescale over which the bubble adjusts towards a new equilibrium deformation in response to a change in the strain environment; it is given by:

$$\lambda = \frac{\mu a}{\Gamma}, \tag{2.3}$$

where a is the bubble's equivalent spherical radius and Γ is the liquid–gas surface tension. The flow is steady if the condition $\lambda \ll \dot{\gamma}/\ddot{\gamma}$ has been satisfied for time $t \gg \lambda$ (Llewellin et al., 2002b).

For steady flow, the relative viscosity η_{r_b} of a bubble suspension is given by (Rust and Manga, 2002; Mader et al., 2013):

$$\eta_{r_b} \equiv \frac{\eta_b}{\mu} = \eta_{r,\infty} + \frac{\eta_{r,0} - \eta_{r,\infty}}{1 + \left(\frac{6}{5}Ca\right)^2}, \tag{2.4}$$

where η_b is the apparent viscosity of the bubble suspension, and $\eta_{r,0}$ and $\eta_{r,\infty}$ are, respectively, the relative viscosity of the bubble suspension at low and high Ca. For non-dilute suspensions, $\eta_{r,0}$ and $\eta_{r,\infty}$ are given by: (Llewellin and Manga, 2005; Mader et al., 2013)

$$\eta_{r,0} = (1 - \phi_b)^{-1} \tag{2.5}$$

$$\text{and} \qquad \eta_{r,\infty} = (1 - \phi_b)^{\frac{5}{3}}, \tag{2.6}$$

where ϕ_b is the bubble volume fraction. These expressions, which reduce in the dilute limit (as $\phi_b \to 0$) to the well-known theoretical models of Taylor (1932) ($\eta_{r,0} = 1 + \phi_b$) and Mackenzie (1950) ($\eta_{r,\infty} = 1 - 5\phi_b/3$), show that bubbles increase suspension viscosity at low Ca and decrease suspension viscosity at high Ca. Equation 2.4 is plotted in figure 2.1, which demonstrates that the transition between the asymptotic viscosity regions at low and high capillarity occurs over a fairly narrow range of Ca, centered on $Ca \approx 1$. Consequently, equations 2.5 and 2.6 can be used to calculate bubble suspension viscosity for all Ca, except over the narrow transitional region. As an approximation, the low capillarity limit is up to $Ca \approx 0.1$ and the high capillarity is above $Ca \approx 10$, although specific values depend on the bubble volume fraction.

Equations 2.2 to 2.6 are relevant for monodisperse bubble suspensions (in which only one size of bubble is present) at low and moderate bubble volume fractions ($\phi_b \lesssim 0.5$) (Llewellin et al., 2002b). Most bubble suspensions are polydisperse (they

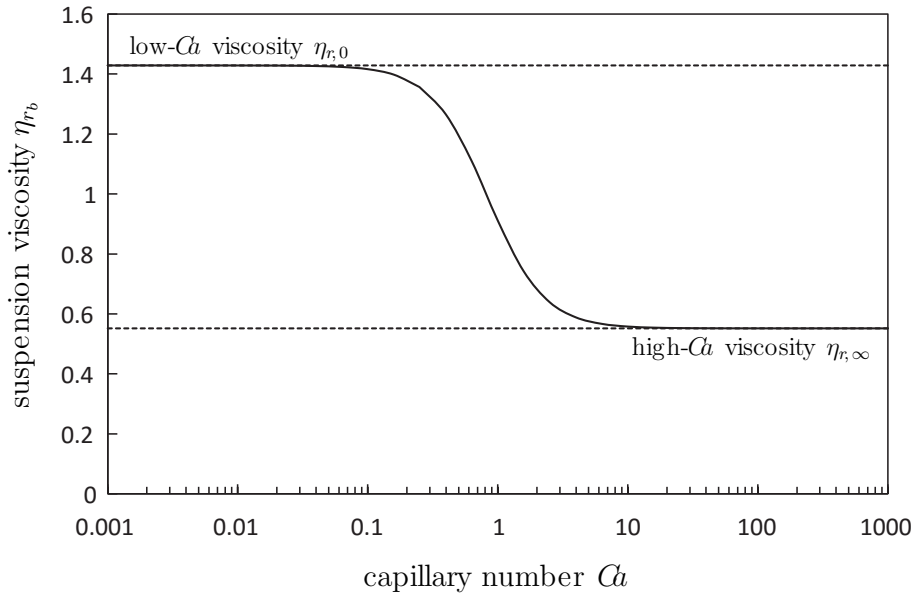

Figure 2.1: Normalized bubble suspension viscosity η_{r_b} as a function of capillary number Ca for $\phi_b = 0.3$ (solid line). Short-dashed lines show the asymptotic values of η_{r_b} at low and high capillary number.

contain a range of bubble sizes) to some extent, resulting in a range of bubble relaxation times; hence also a range of capillarities for a given strain-rate. If all bubbles are in the low capillarity limit, equation 2.5 is sufficient to describe the viscosity of a bubble suspension regardless of its bubble size distribution; similarly, if all bubbles are in the high capillarity limit, equation 2.6 is sufficient. For the more general case of bubbles of intermediate capillarity, or a range of bubbles sizes that span the intermediate capillarity region, a more sophisticated approach is required, in which the contribution of each bubble size fraction to the viscosity of the bulk suspension is linearly superposed; this approach is described in detail in Mader et al. (2013). Bubble suspensions are visco-elastic even when dilute, and elastic behaviour becomes more pronounced as bubble volume fraction increases. However, in steady flow (in which the strain rate is constant), elastic behaviour is not observed (Llewellin et al., 2002b), and so visco-elastic rheology is neglected in this work.

2.2.2 Particle suspension rheology

Particle suspensions commonly show non-Newtonian behaviour when non-dilute, including shear-thinning (e.g. Zarraga et al., 2000), shear-thickening (e.g. Sierou and Brady, 2002; Fernandez et al., 2013), and non-zero normal stress differences (e.g. Singh and Nott, 2000; Tanner et al., 2013). These relationships are demonstrated

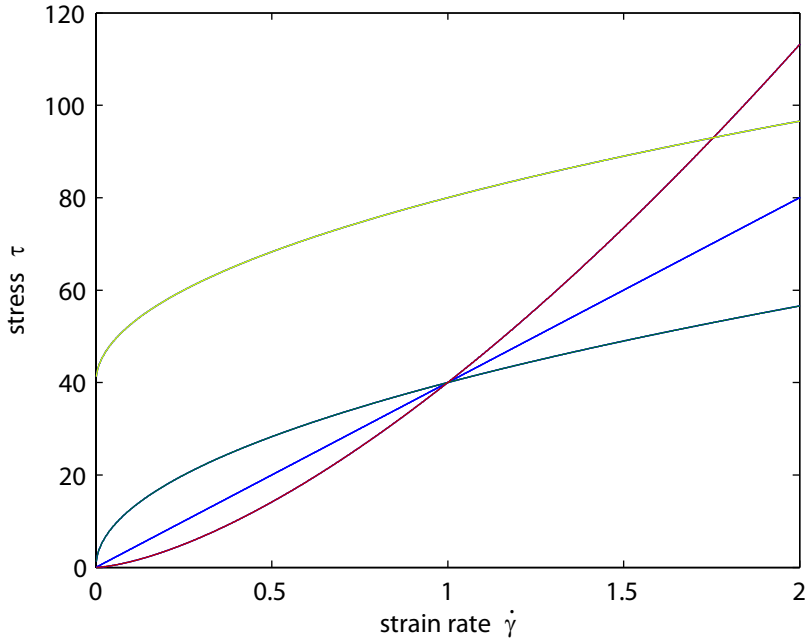

Figure 2.2: Flow curves (plots of stress against strain rate) for various types of rheology. Blue is a Newtonian fluid; red is a shear thickening relationship; dark green is shear thinning; and light green shows both shear thinning and a yield stress, as defined in equation 2.7.

in figure 2.2. When shear-thinning behaviour is observed, the rheology of a particle suspension is often described using the model of Herschel and Bulkley (1926):

$$\tau = \tau_0 + K\dot{\gamma}^n, \tag{2.7}$$

where τ_0 is the yield stress, K is the consistency, and n is the flow index ($n < 1$ when the suspension is shear-thinning). It is worth noting that this definition, common in volcanology, is the opposite of that normally used in geodynamics, where $\dot{\gamma} = A\tau^{n'}$ is typical. In this formulation, $n' = 1/n$. The yield stress is non-zero only for highly-concentrated suspensions, hence it is often neglected, reducing equation 2.7 to a power-law (Ostwald, 1925):

$$\eta_p = K\dot{\gamma}^{n-1}, \tag{2.8}$$

where η_p is the apparent viscosity of the suspension. Although in common usage (e.g. Mueller et al., 2010, 2011; Vona et al., 2013), this approach has the limitation that the consistency has fractional units of $\mathrm{Pa\,s}^n$ and is therefore not amenable to non-dimensionalization when $n \neq 1$; this issue is discussed in detail in Mader et al. (2013) and Mueller et al. (2011). In this work, this limitation is addressed

Parameter	Basalt	Rhyolite	Experiments
Viscosity μ_0	10^2 Pa s	10^8 Pa s	10^2 Pa s
Bubble size a	1 mm	1 mm	100 μm
Temperature T	1500 K	1500 K	300 K
Fluid density ρ_0	3000 kg m$^-$3	3000 kg m$^-$3	1000 kg m$^-$3
Particle density ρ_p	3000 kg m$^-$3	3000 kg m$^-$3	1000 kg m$^-$3

Table 2.2: Parameters required to calculated Peclet number, Reynolds number, and Stokes number for a typical basalt, rhyolite, and analogue experiment.

Number	Equation	Range	Basalt	Rhyolite	Experiment
Reynolds	Re=$\frac{\rho_0 a^2 \dot{\gamma}}{\mu_0}$	Re$< 10^{-3}$	$\dot{\gamma} < 10^2$ s^{-1}	$\dot{\gamma} < 10^8$ s^{-1}	$\dot{\gamma} < 10^4$ s^{-1}
Peclet	Pe=$\frac{6\pi\mu_0 a^3 \dot{\gamma}}{kT}$	Pe$\geq 10^3$	$\dot{\gamma} \geq 10^{-11}$ s^{-1}	$\dot{\gamma} \geq 10^{-17}$ s^{-1}	$\dot{\gamma} \geq 10^{-9}$ s^{-1}
Stokes	St=$\frac{\rho_p a^2 \dot{\gamma}}{\mu_0}$	St$<< 1$	$\dot{\gamma} << 10^5$ s^{-1}	$\dot{\gamma} << 10^{11}$ s^{-1}	$\dot{\gamma} << 10^7$ s^{-1}

Table 2.3: Strain rate range required for the given dimensionless number to be in the appropriate regime.

by introducing a characteristic timescale t_c of a shear-thinning suspension, against which the strain-rate can be non-dimensionalized, giving:

$$\eta_p = \eta_* \left(t_c \dot{\gamma}\right)^{n-1}, \tag{2.9}$$

where η_* is a 'reference viscosity' of the suspension — i.e. the apparent viscosity at strain-rate $\dot{\gamma} = 1/t_c$. No satisfactory microphysical explanation for shear-thinning has yet been proposed for suspensions of the sort considered in this work, in which the particles are not subject to Brownian motion (high Peclet number, Pe$\geq 10^3$), are strongly coupled to the flow (low Stokes number, St$<< 1$) and in which inertial effects can be neglected (low particle Reynolds number, Re$< 10^{-3}$) (Mueller et al., 2010). For clarity, estimates of the strain rates required for a suspension to be in this type of flow regime, based on parameters in table 2.2, are given in table 2.3 for a typical basalt, rhyolite, and the experiments presented later in this thesis. Consequently, there is no physical model from which t_c can be computed *a priori*. However, Mueller et al. (2010) and Mueller et al. (2011) find empirically that the theoretical model of Maron and Pierce (Maron and Pierce, 1956):

$$\eta = \mu \left(1 - \frac{\phi_p}{\phi_m}\right)^{-2} \tag{2.10}$$

accurately captures the rheology of diverse particle suspensions (where ϕ_p is the particle volume fraction, and ϕ_m is the maximum packing fraction) when the consistency is identified with the viscosity; i.e. under the assumption $K \equiv \eta$. This

is equivalent to finding that the characteristic timescale $t_c = 1\,\mathrm{s}$, and making the identity $\eta_* \equiv \eta$ in equations 2.9 and 2.10. This allows these two equations to be linked whilst maintaining strict dimensional consistency, giving:

$$\eta_{r,*} = \left(1 - \frac{\phi_p}{\phi_m}\right)^{-2}, \tag{2.11}$$

where $\eta_{r,*}$ is defined as the relative reference viscosity:

$$\eta_{r,*} \equiv \frac{\eta_*}{\mu}. \tag{2.12}$$

It is proposed that this approach is a useful improvement over that adopted by Mueller et al. (2010, 2011), Vona et al. (2013) and Mader et al. (2013), which included the pragmatic, but inexact, non-dimensionalization $K_r = K/\mu$. Numerically, the values of K_r and $\eta_{r,*}$ are identical when $t_c = 1\,\mathrm{s}$ (as is indicated empirically) so the results of those earlier studies can be transferred directly into this new framework.

The maximum packing fraction in equations 2.10 and 2.11 is a function of particle shape and roughness; Mader et al. (2013) give the following equation for ϕ_m:

$$\phi_m = \phi_{m_1} \exp\left[-\frac{(\log_{10} r_p)^2}{2b^2}\right], \tag{2.13}$$

where r_p is the particle aspect ratio, which is defined as the length of the particle's axis of rotational symmetry divided by its maximum diameter perpendicular to that axis. For smooth particles $\phi_{m_1} = 0.66$ and $b = 1.08$, and for rough particles $\phi_{m_1} = 0.55$ and $b = 1.00$; these values are empirically determined (Mader et al., 2013). Examples of maximally packed suspensions are shown in figure 2.3.

Mueller et al. (2010) report that the flow index n for a particle suspension is a function of the particle volume fraction ϕ_p and the particle aspect ratio. They present a purely empirical relationship:

$$n = 1 - 0.2 r_p \left(\frac{\phi_p}{\phi_m}\right)^4, \tag{2.14}$$

which is valid for $\phi_p/\phi_m \leq 0.8$. This relationship is plotted in figure 2.4.

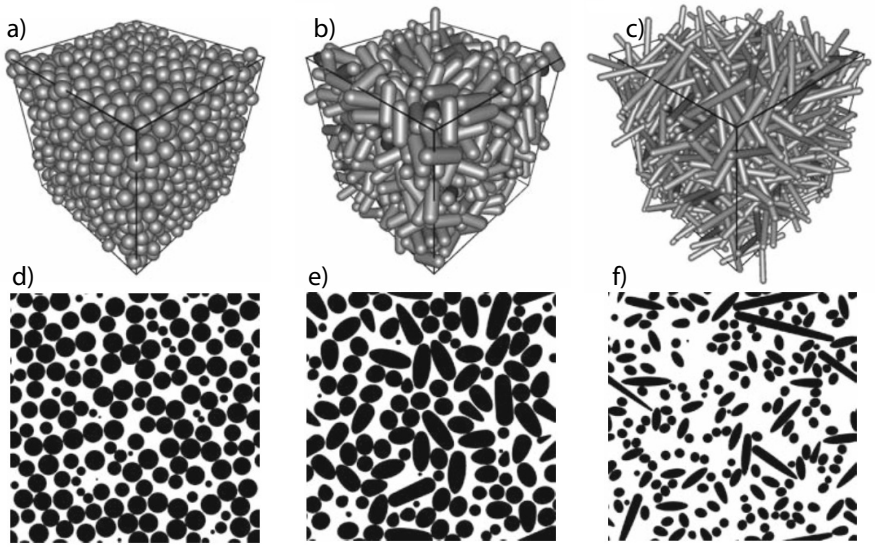

Figure 2.3: Three dimensional (a-c) images of maximally packed suspensions of particles of various aspect ratios, along with two dimensional cross-section through the pack (d-f). a) and d) show a packing of spheres ($r_p = 1$); b) and e) are slightly elongate particles ($r_p = 2$); and c) and f) are highly elongate rod-like particles ($r_p = 10$). Images are from Rudge et al. (2008).

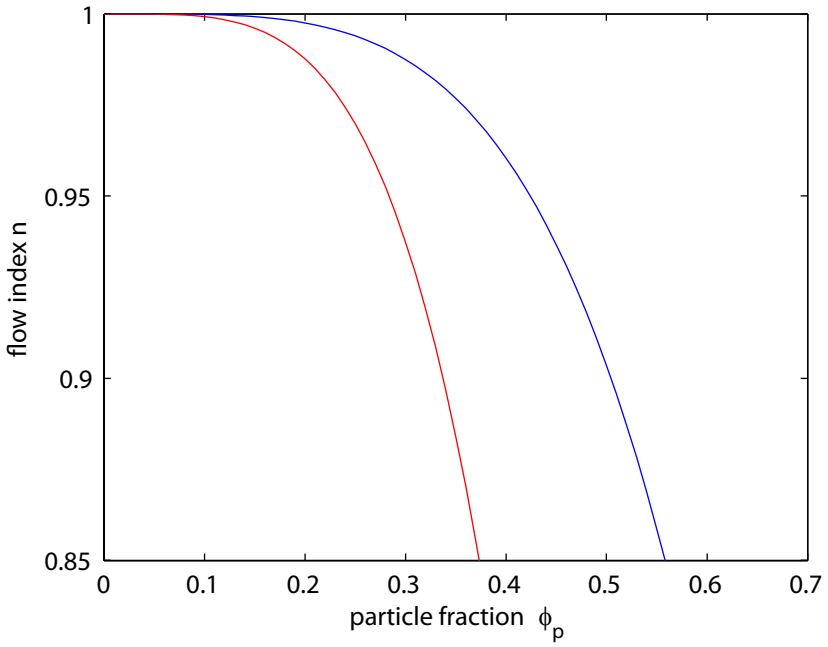

Figure 2.4: Flow index plotted against particle fraction, according to equation 2.14. The blue curve indicates the relationship for equant particles ($r_p = 1$); the red curve indicates the relationship for elongated particles ($r_p = 5$).

2.3 Rheology of three-phase suspensions

Far less work has been done looking at the rheology of three-phase suspensions than for two-phase suspensions. Phan-Thien and Pham (1997) used an effective medium approach (Farris, 1968) to derive an equation for the viscosity of three-phase suspensions, but their theoretical formulation was not experimentally validated. In addition, although they do consider a maximum packing fraction in some variants of their model, their equations become exact only under specific conditions, e.g. $\phi_p \sim \phi_m$, or $\phi_m = 1$.

In the volcanological context, Harris and Allen (2008) applied Phan-Thien and Pham (1997)'s more broadly applicable equations — equivalent to assuming $\phi_m = 1$ — directly to three-phase lavas, and found general agreement between the predicted viscosities and the wide range of viscosities plausible based on observations of the lava flows. Macedonio et al. (2005) also adopted a three-phase equation for magma viscosity, the derivation of which they did not explain in detail, in numerical simulations of conduit flow.

A systematic series of experiments, in which the effects of the particles and bubbles are isolated from the complexities inherent in natural magmatic systems (section 2.4), is the focus of chapter 3. This work fills an important gap in the rheology of suspensions, and allows the resulting three-phase viscosity equation to be used with confidence in its range of validity.

2.4 Complexities associated with volcanic systems

The analogue experiments that are predominantly used to understand the rheology of suspensions are generally simpler than natural magmatic systems. Such suspensions are useful for understanding the fundamental physics and processes that are likely to occur in magmatic systems, but are not sufficient on their own. A number of complexities, relating to the melt viscosity and the populations of crystals and bubbles, need to be considered in order to determine the rheology of a natural magma. In addition, it is important to consider the scaling between the volcanic system and analogue experiments, which are typically carried out on smaller length-scales and shorter time-scales. By considering dimensionless numbers such as the Reynolds, Stokes, Peclet and capillary numbers (defined in table 2.3 and equation 2.2), it is possible to ensure that experiments and nature fall into the same type of flow regime, making the results of experiments applicable to natural scenarios.

2.4.1 Melt viscosity

In a volcanic system, the rheology of the suspending phase — the melt — is commonly not spatially or temporally constant. This section will discuss various controls on silicate melt rheology: composition, water content, temperature, pressure, and strain rate (a summary is provided by Lesher and Spera, 2015). This will provide key background information for chapters 4 to 6. Understanding the controls on melt viscosity requires experiments on natural or synthetic magmas rather than analogues.

Experiments using natural and synthetic magmas of various compositions have demonstrated that melt composition is a strong control on viscosity (e.g. Bottinga and Weill, 1972; Webb and Dingwell, 1990; Giordano et al., 2004; Whittington et al., 2009; Pinkerton and Stevenson, 1992; Hess and Dingwell, 1996). With all other factors the same, high silica magmas (e.g. rhyolites) consistently have a higher viscosity than low silica magmas (e.g. basalts). This is because high silica melts have a high degree of polymerization, which increases their internal resistance to shear, increasing their viscosities (Pinkerton and Stevenson, 1992). The range in viscosity may be as much as ten orders of magnitude under certain conditions: composition is one of the most significant controls on melt viscosity. A set of flow curves for a number of compositions is shon in

The dissolved water content has also been shown to be a significant control on melt viscosity (e.g. Hess and Dingwell, 1996; Robert et al., 2013; Whittington et al., 2009; Dingwell et al., 1996; Giordano et al., 2008). Hydrous melts have lower viscosity than anhydrous melts, and the viscosity increases almost exponentially as water content approaches zero, as shown in figure 2.6. The effects of other volatile species are unknown.

The viscosity of a melt is also very sensitive to temperature (e.g. Webb and Dingwell, 1990; Giordano et al., 2004; Lejeune and Richet, 1995; Giordano et al., 2008), varying as much as ten orders of magnitude from the glass transition to liquidus temperatures (also shown in figures 2.5 and 2.6). The dependence of viscosity on temperature is complicated by the fact that the relationship is non-Arrhenian. The Vogel-Fulcher-Tammann (VFT) equation (Vogel, 1921; Fulcher, 1925)

$$\log \mu = A + \frac{B}{T(\mathrm{K}) - C} \tag{2.15}$$

is commonly used to describe this relationship, in which μ is the melt viscosity in Pa s, T is the temperature in Kelvin, and A, B, and C are adjustable parameters

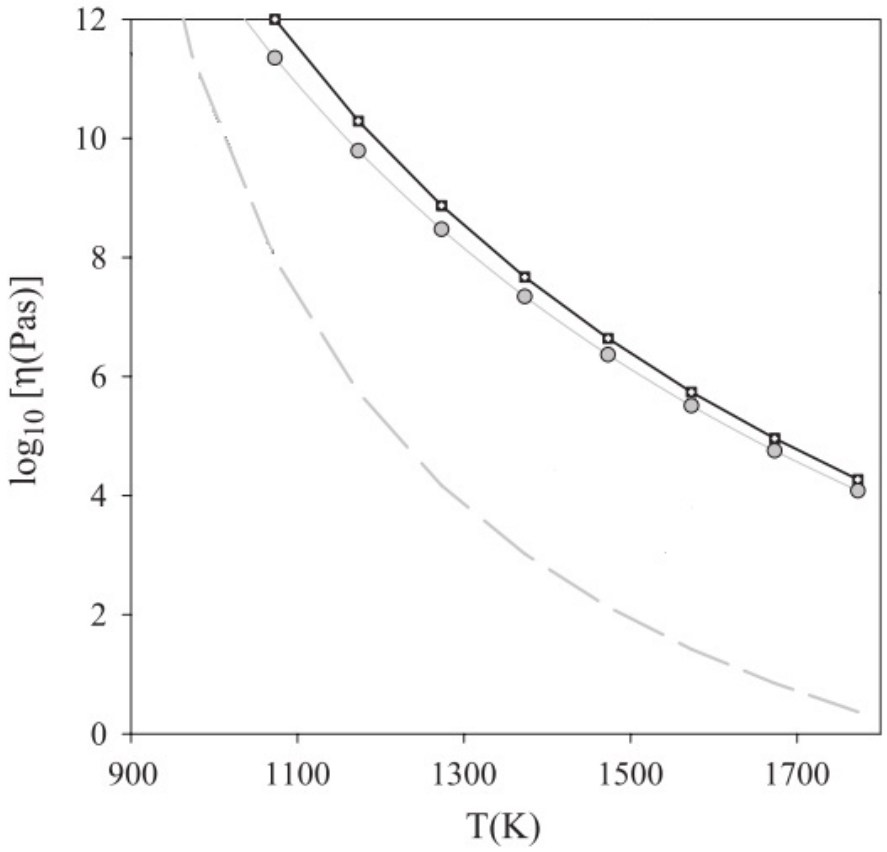

Figure 2.5: Viscosity plotted against temperature for rhyolitic melts (curves with square and circle symbols) and a basaltic melt (dashed curve with no symbols). Figure is adapted from Giordano et al. (2004).

(e.g. Hess and Dingwell, 1996; Giordano et al., 2008). It is therefore possible to account for temperature and composition dependences simultaneously, by assuming that composition — including water content — controls the adjustable parameters.

The natural cases examined in chapters 4 to 6 cover a range of magma compositions and water contents. In all cases, the model of Giordano et al. (2008) was chosen to calculate their viscosity. The model was created by fitting data from > 1770 experiments on natural magmas — with a wide range of compositions and water contents — to equation 2.15, and incorporating the compositional dependence in the adjustable parameters A, B, and C. As a result, the model is appropriate for a wide range of compositions, and is commonly used in the literature; there are alternatives, however these are typically calibrated for a specific magma, and have been less well-received. With its broad applicability and common usage, this model seems to be the most suitable option here.

Pressure has not been investigated as extensively as temperature — indeed the recent summary by Lesher and Spera (2015) does not mention the effect of pressure

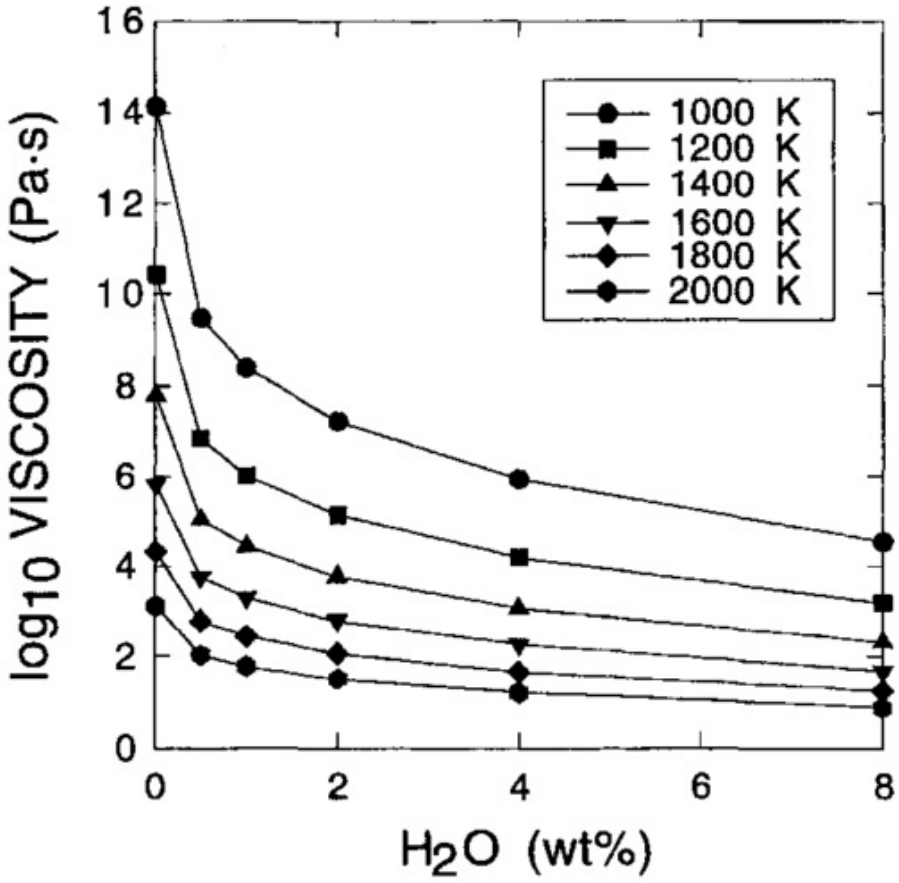

Figure 2.6: Viscosity plotted against water content for a number of isothermal experiments. Figure is from Hess and Dingwell (1996).

on viscosity. Earlier research has found that pressure exerts a much smaller control than temperature on the viscosity of a melt (Kushiro et al., 1976), with less than an order of magnitude decrease in viscosity, from atmospheric pressure (0.1 MPa) to around 3000 MPa. In Al-rich melts, the decrease may be as much as an order of magnitude, due to the coordination of Al in the melt changing with increasing pressure (Kushiro, 1976). The maximum pressure relevant for the applications described in chapters 4 to 6 is 400 MPa: the variability in viscosity due to pressure change below this value is likely to be negligible.

2.4.2 Strain rate

Experiments by Webb and Dingwell (1990) showed that while most melts are Newtonian at low strain-rates, they become shear-thinning at higher strain-rates. The transition between Newtonian and non-Newtonian behaviour depends on the structural relaxation timescale λ_r of the magma. This is essentially the timescale over

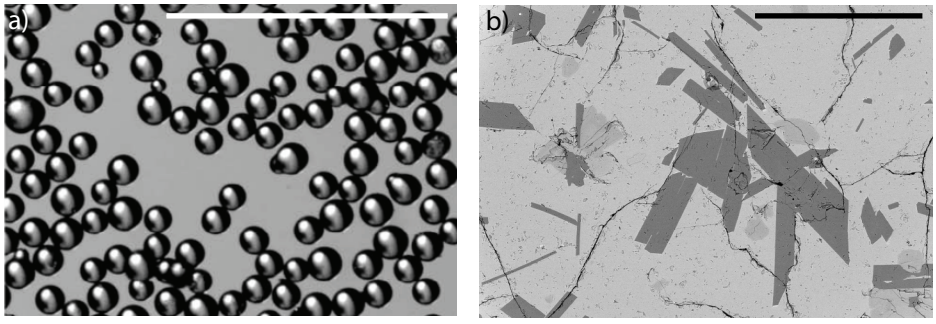

Figure 2.7: Comparison between a) smooth approximately monodisperse spheres used in most analogue experiments (scale bar is 1mm) and b) rough polydisperse crystals found in natural magmas (scale bar is 400μm).

which the internal microstructure of the magma can reorganise in response to strain: if the magma is strained too rapidly, it cannot accommodate the strain, and will fracture in a brittle manner instead of flowing. The relaxation timescale is given by:

$$\lambda_r = \mu_0 / G_\infty, \tag{2.16}$$

where μ_0 is the shear viscosity at zero frequency, and G_∞ is the shear modulus at infinite frequency. Non-Newtonian behaviour occurs in a melt when:

$$\dot{\gamma}_r \geq \frac{10^{-3} G_\infty}{\mu_0} \tag{2.17}$$

(Webb and Dingwell, 1990).

Since analogue experiments tend to use Newtonian suspending fluids, their results will only be applicable to magmas at strain-rates below the limit given in equation 2.17. This covers the majority of natural volcanic systems, but may not cover some extremes: for example, Webb and Dingwell (1990) predict that rhyolitic magma forming ash flow eruptions will become non-Newtonian prior to fragmenting, and Dingwell (1996) suggests that brittle failure occurs during dome collapse and landslide-induced eruptions.

2.4.3 Crystal populations

Unlike the majority of analogue experiments, in most magmas and lavas in nature the suspended particles are often rough, highly non-spherical, and may consist of multiple populations, with a range of shapes and sizes (figure 2.7). Mueller et al. (2011) performed analogue experiments using various aspect ratio particles, and

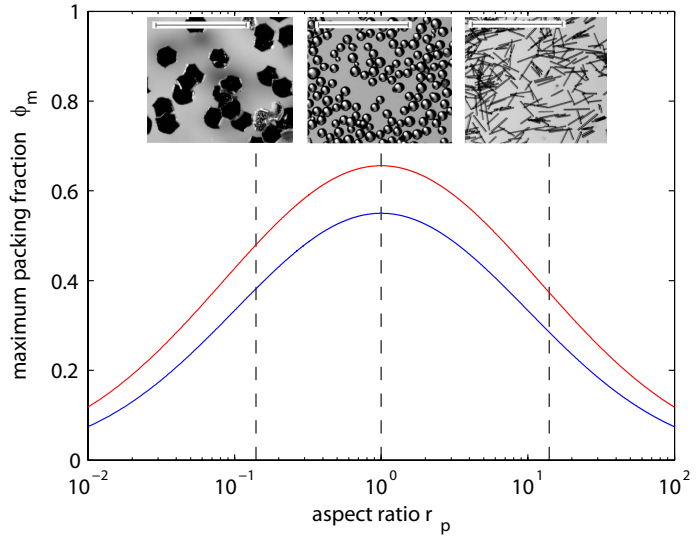

Figure 2.8: Maximum packing fraction against aspect ratio for smooth particles (red curve) and rough particles (blue curve). Insets show particles from Mueller et al. (2011), with 1mm scale bars, and aspect ratios shown by vertical dashed black lines.

demonstrated that the control of particle aspect ratio on viscosity may be dealt with in a straightforward manner. They found that particle aspect ratio controlled the maximum packing fraction ϕ_m, in equation 2.11, such that high aspect ratio particles have a lower maximum packing fraction, and therefore a higher viscosity for a given particle fraction. Mader et al. (2013) present an adaptation of their equation for the relationship between maximum packing fraction and aspect ratio, in order to account for rough particles. These are shown in figure 2.8, and allow viscosity models to be easily adapted to account for aspect ratio and roughness, as defined in section 2.2.2.

In analogue experiments, the particles are commonly approximately monodisperse: they tend to show a narrow normal distribution of diameters around a single mean. It is rare to find a perfectly monodisperse suspension, due to the difficulty in forming a large population of identically sized objects, inexpensively. As such, the results of analogue experiments always implicitly include a small amount of size variation. A number of studies (e.g. Farris, 1968; Chang and Powell, 1994; Castruccio et al., 2010; Cimarelli et al., 2011) have considered polydisperse suspensions that are formed from mixtures of two (or more) monodisperse populations of particles. The common finding is that polydisperse suspensions have lower viscosity at a given total particle fraction than monodisperse suspensions. This is because a polydisperse suspension has a higher maximum packing fraction than a monodis-

perse suspension with the same aspect ratio — small particles can fill in the gaps between large particles. In this thesis, only monodisperse suspensions are used in the analogue experiments, for simplicity. The limitations of this approach, particularly when applying rheological models to natural populations of crystals, will be addressed when appropriate.

In order to account theoretically for multiple populations of particles, some studies have used an effective medium approach (e.g. Farris, 1968; Mader et al., 2013). In this approach, the smallest crystals are considered first, and their effect on the viscosity of the melt is accounted for. The next largest crystals are then considered to be suspended in an already crystal-bearing suspension, with viscosity as calculated from the smaller crystals. The effect of the second population of crystals on the bulk viscosity is then calculated. Adding in further crystal phases allows the full suspension to be built up. This theoretical model has some limitations, however. It assumes that each additional crystal population does not interact with the previous ones - new crystals do not "see" existing crystals, only a contiuous medium. While this is plausible for low concentrations of crystals with a large size difference, it becomes a less defensible scenario as the crystal volume fraction increases, or the crystal populations become closer in size.

2.4.4 Bubble populations

Analogue experiments involving bubbles tend to use gases that are insoluble in the suspending fluids, under experimental conditions. Bubbles in a magma may either be exsolved from the melt, or sourced from another magma—in the case of gas sparging, for example (Bachmann and Bergantz, 2006; Huber et al., 2010). In either case, the solubility of the volatiles and ability of bubbles to nucleate and grow will control the resulting bubble population. As such, the bubble populations in a natural magma are likely to be less well controlled and constrained than in the analogue system, and are likely to vary both spatially and temporally. The factors controlling the bubble population in a natural magma need further consideration when it is necessary to calculate the viscosity of a bubble-bearing magma.

In order for the bubbles to nucleate in a magma, the melt phase must become saturated in volatile species; the most important in a typical magmatic system are H_2O and CO_2. Surface tension provides an energy barrier to bubble nucleation and so a supersaturation of 1-5 MPa to 10-70 MPa (Hurwitz and Navon, 1994) is typically required for, respectively, heterogeneous nucleation (i.e. where nuclei—often crystals—are present) and homogeneous nucleation (in the absence of nuclei).

The solubility of common volatiles in silicate melt decreases with decreasing pressure and increasing temperature. Baker and Alletti (2012) provide a comprehensive review of the solubility and partitioning of numerous volatiles in magmatic systems. When calculating the bubble fraction expected in a natural magma in chapter 4, the model of Newman and Lowenstern (2002) will be used. Progressive crystallization tends to increase the residual volatile content in the melt phase since volatiles are incompatible in anhydrous crystal phases. Consequently, nucleation of bubbles is promoted by decompression, heating, or crystallization of the magma reservoir.

Once bubbles have nucleated, they will grow as volatiles exsolve into them until the melt returns to its saturation limit. They will also change volume in response to pressure changes in the system, or changes in their position within the system — for example, as they rise ambient pressure will be decreasing and the bubbles will expand. This is subject to the caveat that unlimited growth may not be possible in a volume-constrained magma reservoir. In addition, bubble growth is limited by the viscosity of the melt. If bubble growth occurs faster than the structural relaxation timescale of the melt (section 2.4.2), the melt will fragment. This commonly occurs in the conduit during explosive eruptions.

Each of these processes contributes to a bubble population that may contain a wide range of sizes, and therefore a range of capillary numbers. As discussed for polydisperse crystal populations in section 2.4.3, the effect of bubble size distrubtion may be accounted for by using an effective medium method to calculate viscosity. In the case of bubbles, the need to deal with variable capillarity complicates this calculation, particularly in the transitional regime between low and high capillarity. This can be accounted for by decreasing the exponent in equation 2.4 from its initial value of 2, as described in section 7.3 of Mader et al. (2013). Once these factors are accounted for, the viscosity of a bubble-bearing magma can be theoretically determined.

2.4.5 Evolution of the system

Natural magmatic systems change and evolve over time, and these changes may have a complex effect on viscosity. For example, a reduction in temperature will:

- directly increase melt viscosity;
- cause crystallization if the melt moves past the liquidus, thereby increasing the suspended particle fraction and increasing bulk viscosity, and releasing latent heat of crystallization, decreasing melt viscosity;

- lead to concentration of dissolved volatiles in the melt if anhydrous phases crystallize, leading to a decrease in melt viscosity;
- reduce the solubility of water in the melt, potentially leading to exsolution (reducing melt viscosity) and bubble growth (increasing or decreasing magma viscosity, depending on capillary number).

An apparently simple change in the storage conditions of the magma can lead to an overall result that may be quite difficult to calculate — the system contains both positive and negative feedbacks, and many parameters are coupled. The concept of evolving rheology will be explored throughout this thesis, for example, in the context of a crystallizing mush (chapter 4) and a recent effusive eruption on Hawai'i (chapter 6).

2.5 Influence of rheology on volcanic processes

2.5.1 Eruption style

Eruptions of basaltic volcanoes are commonly effusive, producing lava flows, or mildly explosive Hawaiian or Strombolian activity (e.g. Mangan et al., 2014; Giordano and Dingwell, 2003). On the other hand, silicic volcanoes are more commonly violently explosive (e.g. Bachmann and Bergantz, 2008; De Silva and Gregg, 2014). There are, of course, exceptions to each (Mangan et al., 2014; Giordano and Dingwell, 2003; Justet and Spell, 2001; Koleszar et al., 2012) and a spectrum of behaviours at intermediate compositions, but the pattern holds for the majority (e.g. Cashman and Sparks, 2013). This difference in behaviour is predominantly controlled by the viscosity of the melt - mafic melt tends to be significantly less viscous than felsic melt (section 2.4.1 and Giordano et al. (e.g. 2004); Webb and Dingwell (e.g. 1990)). The difference in viscosity affects the ability of the magma to flow, its tendency to fragment (Dingwell et al., 1996; Papale, 1999), and the ability of exsolved bubbles to move through the melt and outgas (Edmonds, 2008).

2.5.2 Eruptability

Many of the largest known explosive volcanic eruptions produce extremely crystal-rich deposits, which are in turn inferred to have come from extremely crystal-rich magma (table 2.4). In order to produce such large eruptions, significant volumes of magma must accumulate in the crust; however, seismic studies do not show evidence

Deposit (reference)	Volume	Crystallinity
Indian Peak Volcanic Field (Best et al., 1989)	3000 km^3	40%[a]
Fish Canyon Tuff, San Juan Volcanic Field (Bachmann and Bergantz, 2003)	>5000 km^3	45%[a]
Lund Tuff, Great Basin (Maughan et al., 2002)	>3000 km^3	>40%[a]
Cerro Galan, NW Argentina (Folkes et al., 2011)	>1200 km^3	40-55%[b]

Table 2.4: Volumes and crystallinities for a number of large explosive eruptions. [a] Crystallinity on a whole rock basis; [b] crystallinity on a vesicle-free basis.

for large volumes of high melt-fraction magma beneath historically active volcanic systems (Hansen et al., 2003), despite being extremely sensitive to variations in melt fraction (Hammond and Humphreys, 2000). This implies that such systems spend a large proportion of their lifetimes with a high crystal fraction, or with only isolated pockets of melt (Cashman and Giordano, 2014). This interpretation is supported by geochemical studies (e.g. Wotzlaw et al., 2013; Cooper and Kent, 2014; Coleman et al., 2004; Frazer et al., 2014), which show that, whilst it can take hundreds of thousands or millions of years to accumulate a large volume magma reservoir, the magma is melt-rich for only a small fraction of that time. The implication is that mush-like magma chambers must be capable of producing voluminous eruptions. This is difficult to reconcile with rheological models for crystal-rich magmas, which indicate that such mushes should be rheologically jammed.

As discussed in section 2.2.2, the viscosity of magma increases with increasing crystal fraction. The increase is approximately linear for low crystal volume fractions (Einstein, 1906), but becomes non-linear as crystal–crystal interactions become increasingly important (Maron and Pierce, 1956; Champallier et al., 2008), following equation 2.11. As the random close maximum packing fraction ϕ_m (which depends on the crystal size distribution and aspect ratios — section 2.4.3) is approached the crystals begin to jam against one another, giving rise to a yield stress (Mueller et al., 2010). If the yield stress is greater than the stress driving deformation, the magma is immobile; this state may be referred to as 'jammed', with the critical crystal fraction for jamming ϕ_{crit}. It should be noted also that the critical fraction for jamming depends on the applied shear stress (Bi et al., 2011). When the maximum packing fraction ϕ_m is reached, viscous deformation can only be accommodated by crystal–melt segregation and crystal fracturing (Caricchi et al., 2007; Pistone et al., 2012); this state may be termed 'locked'. Crystal fractions above ϕ_m require some

degree of crystal intergrowth, which may cause the magma to develop a substantial mechanical strength.

As a magma crystallizes, therefore, it is expected to evolve rheologically, from a low viscosity mobile suspension, to an immobile crystal mush (Marsh, 1981). The conundrum posed by the deposits of the largest eruptions, such as the Fish Canyon Tuff (see table 2.4), is that they often have phenocryst fractions close to, or above ϕ_m. Such magma reservoirs would be expected to remain immobile in the crust, eventually forming plutons. Indeed in many areas, both plutons and massive ignimbrites are present and, in some cases, a genetic link between pluton and ignimbrite has been proposed (Lipman, 2007).

Explaining the mobilization of crystal-rich magma is therefore a significant and general problem in volcanology, and a number of models have been proposed. Some invoke external triggers, including tectonic controls (Gottsmann et al., 2009; Allan et al., 2013; Begue et al., 2014) and seismic shaking (Linde and Sacks, 1998; Namiki et al., 2016), although in some cases these models are not specifically based on a magma mush. Others focus on evidence for intrusion and mixing of a hot, mafic, volatile-rich magma into the pre-existing, more-evolved reservoir (e.g. Kent et al., 2010; Longpre et al., 2014), and invoke 'unzipping' of the mush caused by intrusion of a vesiculating recharge magma (Burgisser and Bergantz, 2011), or 'sparging' of gas through the mush, carrying heat from a recharge magma (Bachmann and Bergantz, 2006; Huber et al., 2010). Some implicitly include some degree of partial melting of the mush, however none explicitly addresses the fundamental issue that the crystal fraction must be below ϕ_{crit} before the magma can mobilize. This topic will be addressed in more detail in chapter 4.

2.5.3 Flow morphology

Basaltic lava flows are conventionally divided into two categories according to their surface morphology: pāhoehoe, which has a smooth, often ropey surface; and 'a'ā, which has a broken, clinkery surface (MacDonald, 1953). The lava flows produced by a single eruption — particularly a long-lived eruption — may switch repeatedly between the two morphologies in both time and space, producing a flow field with complex and heterogeneous morphology (e.g. Jurado-Chichay and Rowland, 1995; Hon et al., 2003). Understanding the development of a flow field is important because it influences the nature of the transport of lava from vent to flow front. Pāhoehoe flows typically develop insulated internal lava tubes that may deliver lava over long distances to a flow front that is usually broad and advances slowly; consequently

such flows may persist for months or years (e.g. MacDonald, 1953; Swanson, 1973; Peterson et al., 1994; Cashman et al., 1999). By contrast, ‘a‘ā flows tend to be fast-moving, spatially-focussed, and channelized, moving with a considerably higher volumetric flow rate (e.g. MacDonald, 1953; Pinkerton and Sparks, 1976; Rowland and Walker, 1990; Cashman et al., 1999).

The morphology of the surface produced by a flow is controlled by the rheology of the lava and by the strain-rate that it experiences at the time the surface is formed (MacDonald, 1953; Peterson and Tilling, 1980). At low viscosities and low strain-rates, the lava surface remains coherent, favouring the development of pāhoehoe. At higher viscosities and higher strain-rates, the lava surface breaks under shear, forming clinkery ‘a‘ā morphology. The surface morphology of a flow is therefore not uniquely linked to the physical properties of the lava that formed it, and it is possible for the still-fluid lava in the interior of a flow to go on to produce either surface type, regardless of its up-stream morphology (Jurado-Chichay and Rowland, 1995; Guest and Stofan, 2005). In particular, it is common for a pāhoehoe flow to transition into an ‘a‘ā flow if either strain-rate or viscosity increases (MacDonald, 1953; Peterson and Tilling, 1980; Polacci et al., 1999; Sehlke et al., 2014). Strain-rate is controlled by flow rate and by the angle of the surface on which the lava flows, hence, for a constant flow rate and viscosity, the transition from pāhoehoe to ‘a‘ā is often associated with a break in slope, to steeper slope angles; the reverse transition sometimes occurs when an ‘a‘ā lava flow reaches a shallower slope (Hon et al., 2003).

An increase in lava viscosity resulting from cooling or crystallization may promote the transition from pāhoehoe to ‘a‘ā (Cashman et al., 1999). More generally, the rheology of a lava dictates its propensity to form pāhoehoe or ‘a‘ā for a given slope angle and flow rate (Peterson and Tilling, 1980). The viscosity of a silicate melt (i.e. the liquid component of a lava) depends on its composition, temperature, and dissolved volatile content (section 2.4.1); in addition, most lavas contain both bubbles and crystals, which may dramatically affect the rheology depending on their volume fractions (sections 2.4.3 and 2.4.4). The crystal fraction of lavas is highly variable, although few have more than 45% crystals, and most lie in the ranges <10% and 25-45% (Ewart, 1976). The bubble fraction of lavas is even more variable, ranging from 0 - 80% (e.g. Cashman and Giordano, 2014). The fraction of each of these components may vary with both time and distance from the vent, in a single lava flow.

As crystal content approaches the maximum packing fraction (given by equation 2.13) the viscosity of the lava increases dramatically and it develops a yield

strength. This favours the formation of ‘a‘ā and it has been observed that, for crystallinity >35%, lava flows almost exclusively as an ‘a‘ā flow (Hoover et al., 2001; Cashman et al., 1999). However, in some cases extremely crystal-rich lava is capable of producing pāhoehoe flows; examples include the “cicirara” lavas at Mount Etna (Lanzafame et al., 2013).

Understanding the complex rheology of three-phase lavas is an important factor in assessing the type of lava flow an eruption is likely to produce, and the hazards related to it. Particularly crystal-rich lavas are uncommon, and could potentially produce different morphologies to those observed regularly at many volcanoes. The topic of crystal-rich three-phase lavas will be discussed in detail in chapter 5, in the context of Volcán Llaima, a volcano in Chile.

Chapter 3

Experimental study of the rheology of multiphase suspensions

3.1 Introduction

Multiphase suspensions of particles and/or bubbles in a continuous liquid phase are common in nature and industry; examples include magma, oil, concrete, foodstuffs, cosmetics, pharmaceuticals, biological fluids and nanofluids. Characterizing, modelling, and controlling the flow of these suspensions requires a constitutive rheological model, encapsulating the viscosity of the suspension as a function of the properties of the suspending liquid, the volume fraction and properties of the suspended phase(s), and the flow conditions.

The rheology of two-phase suspensions has now been well investigated (see chapter 2 and Mader et al. (2013) for a recent review). By contrast, considerably less research has been directed at understanding the rheology of three-phase suspensions (where bubbles *and* particles are suspended in a liquid) primarily owing to the complexity of the problem. Phan-Thien and Pham (1997) present a theoretical treatment — discussed later in section 3.2 — which has been applied in studies of multiphase magma (e.g. Harris and Allen, 2008; Vona et al., 2013), but has not been experimentally validated. Experimental investigation of the rheology of three-phase suspensions appears to be confined to studies of bubble- and crystal-bearing magmas (e.g. Pistone et al., 2012; Vona et al., 2013); these experiments and materials are complex and the resulting data are not well-suited to the validation of three-phase rheological models (section 2.1). Constraining three-phase rheology therefore remains an important, yet outstanding, problem in multiphase fluids research.

In this chapter, published two-phase constitutive equations are combined to gen-

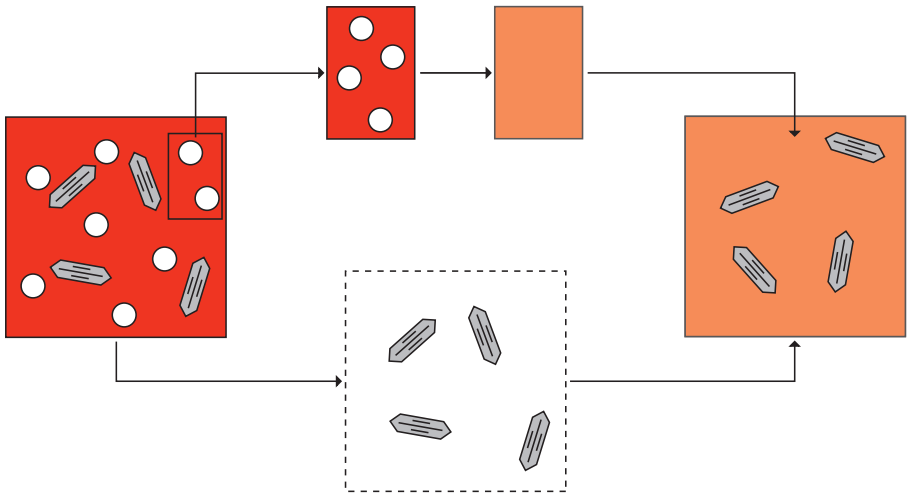

Figure 3.1: Demonstration of the effective medium concept. The three-phase fluid contains melt (red), crystals (grey) and bubbles (white). The interstitial bubble-bearing fluid can be considered separately to the crystals. The viscosity of this two-phase suspension of bubbles relative to the melt (orange) can be calculated according to equation 2.5. The viscosity of the two-phase suspension of crystals relative to the bubbly-melt can then be calculated according to equation 2.11.

erate a three-phase model, by using an 'effective-medium' method in which the bubble suspension is treated as a continuous medium which suspends the particles. The model is validated against new experimental data for three-phase suspensions of bubbles and spherical particles in the low capillarity regime (in which flow is steady and bubble deformation is small). This validation of data containing a wide range of bubble and particle volume fractions is an improvement on the studies of natural samples mentioned previously (Pistone et al., 2012; Vona et al., 2013), in which a very limited range of bubble fractions (0.09-0.12 vol.%) was used.

A number of potential extensions to the model are introduced, although they are not validated by experimental data at this stage. The implications of the model are then discussed for natural magmatic processes. Later thesis chapters 4, 5, and 6 investigate a number of these in more detail.

3.2 A model for the rheology of three-phase suspensions

Equation 2.11 gives the relative viscosity $\eta_{r,*}$ of a suspension of particles in a liquid with viscosity μ. If it is supposed that the particles are instead suspended in a bubble suspension with viscosity η_b (i.e. the bubble suspension is treated as an 'effective medium' - see figure 3.1) the relative viscosity becomes:

$$\frac{\eta_*}{\eta_b} = \left(1 - \frac{\phi_p}{\phi_m}\right)^{-2}. \tag{3.1}$$

Treating the bubble suspension as the continuous phase carries the implicit assumption that the bubbles should be small compared with the particles. At low bubble capillarity, from equation 2.5, $\eta_b = \mu\,(1-\phi_b)^{-1}$; hence

$$\eta_{r,*} = (1-\phi_b)^{-1}\left(1 - \frac{\phi_p}{\phi_m}\right)^{-2}. \tag{3.2}$$

At high bubble capillarity, equation 2.6 would take the place of equation 2.5; whilst for intermediate capillarity, equation 2.4 would take its place, and polydispersity would have to be explicitly accounted for (see section 2.2.1).

This effective medium method has been used elsewhere in rheological models. Of most relevance, Phan-Thien and Pham (1997) use the approach to derive an equation for the viscosity of three-phase suspensions of bubbles and particles that is similar to the model derived above, but contains a different expression for the particle suspension contribution: $(1-\phi_p)^{-5/2}$, which they derive using a differential method. Although they do consider a maximum packing fraction in some variants of their model, their implicit solutions reduce to exact equations only under restrictive conditions, e.g. $\phi_p \sim \phi_m$, or $\phi_m = 1$. Consequently, the treatment of the contribution of the particles to the suspension rheology in the formulation presented here is a significant improvement over that of Phan-Thien and Pham (1997).

3.2.1 Defining volume fractions in three-phase suspensions

Particle volume fraction and gas volume fraction are unambiguously defined for two-phase suspensions; however, care must be taken to define them appropriately for three-phase suspensions. In the model formulation above, the bubble suspension is treated as the effective medium, hence, the appropriate definitions are:

$$\phi_b = \frac{V_b}{V_l + V_b} \tag{3.3}$$

$$\phi_p = \frac{V_p}{V_l + V_b + V_p} \tag{3.4}$$

where V_l, V_b and V_p are the respective volumes of the liquid, bubble and particle phases.

For volcanological applications the goal is often to characterize how the rheology of a suspension of crystals changes as bubbles are added to it (or, equivalently, as

bubbles grow within it). For example, a magma that contains solid crystals may be bubble-free at depth, but become increasingly bubble-rich during ascent. In this case, it is more intuitive to define a particle volume fraction and bubble volume fraction as follows:

$$\phi_b^* = \frac{V_b}{V_l + V_b + V_p} \tag{3.5}$$

$$\phi_p^* = \frac{V_p}{V_l + V_p}. \tag{3.6}$$

In this formulation, the particle volume fraction does not change from its initial value as bubbles grow, and the bubble volume fraction reflects the value that would be measured by applying Archimedes' principle on the bulk sample. The different formulations for volume fractions are simply related:

$$\phi_b = \frac{\phi_b^*}{1 - \phi_p^* \left(1 - \phi_b^*\right)}, \tag{3.7}$$

$$\phi_p = \phi_p^* \left(1 - \phi_b^*\right), \tag{3.8}$$

$$\phi_b^* = \phi_b \left(1 - \phi_p\right), \tag{3.9}$$

$$\phi_p^* = \frac{\phi_p}{1 - \phi_b \left(1 - \phi_p\right)}, \tag{3.10}$$

allowing the three-phase model (equation 3.2) to be applied when it is ϕ_b^* and ϕ_p^* that are known.

In the following sections both of these definitions are used, since equations 3.3 and 3.4 underpin the model formulation, whilst equations 3.5 and 3.6 are more natural for volcanological applications of the model, and aid physical insight. A further volume fraction of interest is the fraction of the total volume that is made up of suspended bubbles *and* particles — the total suspended fraction:

$$\phi_s = \frac{V_b + V_p}{V_l + V_b + V_p}. \tag{3.11}$$

3.3 Experiments

3.3.1 Samples

The three-phase samples were prepared by adding spherical glass beads (Potters Ballotini; density $2448\,\mathrm{kg\,m^{-3}}$, size fraction 63 to 125 μm) to a sugar syrup (Tate & Lyle Golden Syrup; density $1438\,\mathrm{kg\,m^{-3}}$ and surface tension $0.08\,\mathrm{N\,m^{-1}}$ (Llewellin

et al., 2002b)) and aerating with a domestic electric whisk. The rheology of the pure syrup was determined individually for each sample batch and found to be strictly Newtonian; measured viscosities were in the range $55.68 \leq \mu \leq 61.69\,\mathrm{Pa\,s}$ at 20°C (presented later in data table 3.1). Particle volume fraction was controlled by adding a known mass of beads to a known mass of syrup (typically equating to 100-150 ml) to prepare sample suites of similar initial (bubble-free) particle volume fraction $\phi_p = 0.05$, 0.1, 0.2, 0.3, 0.4, and 0.5.

Bubble volume fraction was then varied by adjusting the duration and speed of whisking, and suspension temperature. Errors in particle volume fraction and bubble volume fraction are ±3% and ±5% respectively. Of the resulting three-phase suspension, about 60 ml was used for rheometric analysis, and a small amount was imaged with a Zeiss SteREO V.8 stereomicroscope. With the remaining sample material, the bubble volume fraction ϕ_b^* was determined by measuring its weight and its volume in a 100ml measuring cylinder.

For each sample, therefore, a measurement of ϕ_p and ϕ_b^* was obtained. Equations 3.7 to 3.10 were then used to calculate ϕ_p^* and ϕ_b from these measurements, for each sample.

The bubble size distribution of each sample was determined using the image analysis software JMicroVision. A photomicrograph of a typical sample is presented in figure 3.2, along with its bubble size distribution.

3.3.2 Rheometry

Rheometric data were collected using a ThermoScientific Haake MARS II rheometer with Z40DIN concentric cylinder sensor geometry (rotor diameter 40.0 mm, cup diameter 43.4 mm, gap width 1.7 mm). A standard flow-curve determination consisted of a 20-step 'up ramp' of incrementally increasing shear stress τ up to a maximum value of 500 Pa ('controlled-stress mode'), followed by a 20-step 'down ramp'. At each stress step, the rheometer recorded the corresponding strain-rate $\dot{\gamma}$ once it had reached equilibrium flow conditions. To ensure equilibrium starting conditions for each test, flow-curve determinations were preceded by a 4 minute, continuous 0–150–0 Pa stress ramp as pre-shear treatment (following Mueller et al., 2010). All experiments were performed at 20°C; the error of the stress and strain-rate measurements is estimated at ±2%.

The densities of the particles and the suspending liquid are not well-matched in the experiments (2448 kg m^{-3} and 1438 kg m^{-3} respectively) so settling must be considered; similarly, the bubbles are prone to buoyant rise ('creaming'). The

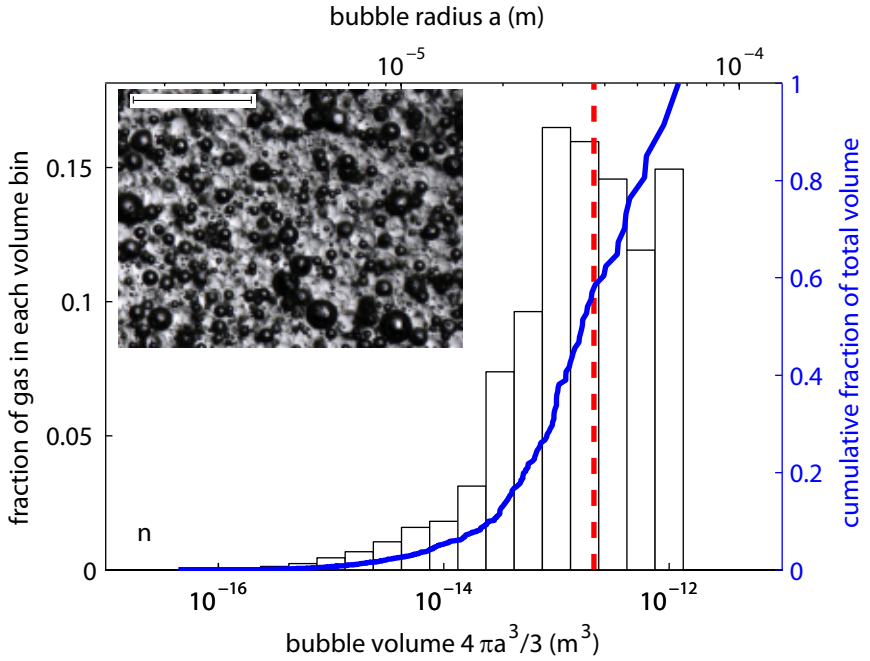

Figure 3.2: Bubble size distribution for sample 3P-42 ($\phi_p = 0.42$ and $\phi_b = 0.29$). Histogram shows the fraction of the total bubble volume in the sample represented in each volume bin. Solid line shows the cumulative fraction of the total bubble volume. Dashed line is the volume-mean-radius $\langle a \rangle \sim 37\mu$m (see section 3.3.3). Inset shows photomicrograph of sample, in which dark-rimmed spheres are bubbles, and glass beads are light and translucent. Scale bar is 500 μm.

concentric cylinder sensor geometry was chosen because it is relatively insensitive to effects of settling and creaming compared with, say, a parallel plate geometry, because particles and bubbles move vertically past the sensor, rather than accumulating in a layer against it. From Stokes' law, the time required for an isolated particle or bubble in a dilute syrup suspension to fall or rise the full length of the sensor is more than 120 hours for the largest particle and around 1.5 hours for the largest bubble; for a concentrated suspension it is much longer because settling and creaming are hindered. Since total runtimes for the rheometric experiments are much shorter for each sample (the mean experiment duration was 5 minutes, maximum 12 minutes), the development of spatial gradients in the particle and bubble volume fractions is considered negligible.

3.3.3 Data analysis

The rheometric experiments yield flow curves of applied shear stress τ against resultant shear strain-rate $\dot{\gamma}$; an example is shown in figure 3.3. For some samples, the highest experimental strain-rates are sufficient that the bubbles cannot be assumed

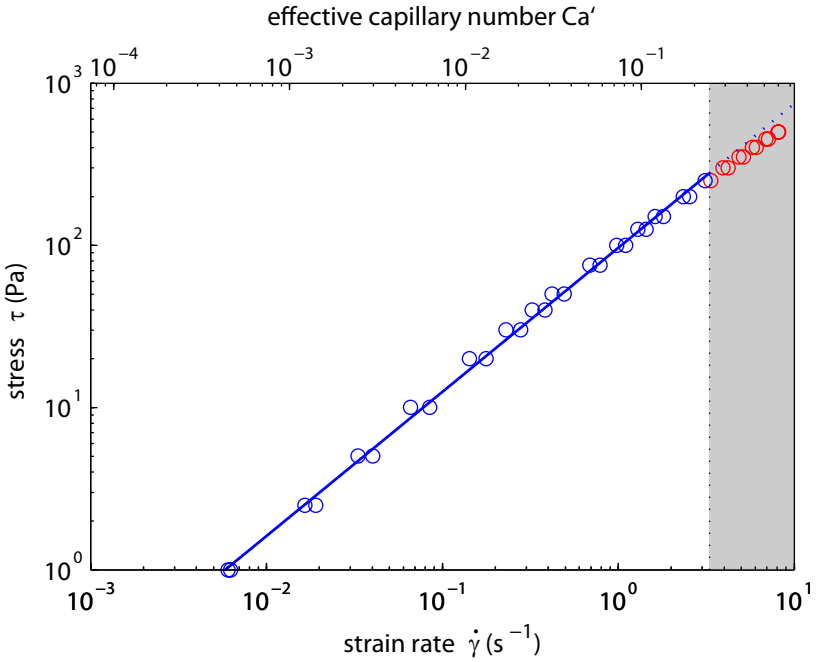

Figure 3.3: Flow curve of shear stress τ against shear strain-rate $\dot{\gamma}$ for sample 3P-30 with $\phi_b = 0.30$ and $\phi_p = 0.04$. Datapoints are collected during both the up-ramp and down-ramp (section 3.3.2). Datapoints are discarded (shaded region) for Ca' (defined in section 3.3.3) greater than the upper bound of the low-capillarity region, defined according to equation 3.13; for $\phi_b = 0.30$, this is $Ca' \geq 0.248$. Solid line is the best fit of equation 3.14 to the remaining datapoints, giving $\eta_{r,*} = 1.74$ and $n = 0.89$; dashed line is the fit extended into the discarded region.

to be in the low-capillarity regime. The data are filtered to remove these datapoints by calculating an upper bound on the low-capillarity region for each sample as follows. For three-phase suspensions, the effective strain-rate in the bubbly effective medium $\dot{\gamma}'$ is higher than the bulk strain-rate $\dot{\gamma}$ because the solid particles cannot accommodate strain through internal shearing. The effective strain-rate is approximately given by $\dot{\gamma}' = \dot{\gamma}/\left(1 - \phi_p/\phi_m\right)$; this is a conservative estimate because it does not account for the accommodation of shear strain through solid-body rotation of the particles. A typical bubble radius for each sample may be calculated as the volume-mean-radius $\langle a \rangle = \sum a^4 / \sum a^3$ where summation is over all measured bubbles in that sample (following Mader et al., 2013). A more conservative criterion is adopted by calculating the capillary number using the radius of the largest bubble measured $a_{\max}$. Putting these values into equations 2.2 and 2.3, an equation for the effective capillary number is: $Ca' = \mu a_{\max} \dot{\gamma}' / \Gamma$. The low-capillarity region is then defined on the basis of the mismatch between the viscosity calculated from equation 2.5 (the low-capillarity asymptotic viscosity), and from equation 2.4 (which is valid for all capillary numbers). The upper bound of the low-capillarity region is set as

the value of Ca' for which the mismatch reaches 5%; i.e., for low-capillarity:

$$\frac{\eta_{r,0} - \eta_{r_b}}{\eta_{r,0}} < 5\% \tag{3.12}$$

or equivalently, from equation 2.4:

$$Ca' < \sqrt{\frac{5}{144\left(0.95 - (1-\phi_b)^{\frac{8}{3}}\right)}}. \tag{3.13}$$

The 5 % threshold is chosen to be in line with experimental error. After filtering, all flow curves comprise at least 15 datapoints. Based on this conservative criterion, the discrepancy (equation 3.12) for a bubble with volume-mean-radius is never greater than 1 %.

The yield stress τ_0, consistency K and flow index n are determined for each sample by fitting the Herschel-Bulkley model (equation 2.7) to each filtered flow curve (figure 3.3), and errors are determined using the bootstrapping method presented in section 3.4.1. For all samples, the yield stress is found to be either small and negative (which is unphysical) or positive, but within 2σ error of zero; hence, yield stress can be neglected and equation 2.7 can be expressed as the simple power law relationship given in equation 2.9. This is consistent with the experimental results of Mueller et al. (2010), who found that yield stress is negligible for $\phi_p/\phi_m \lesssim 0.8$. This allows the data to be fitted for η_* and n in log-space using the relationship:

$$\log \tau = \log \eta_* + n \log t_c \dot{\gamma}, \tag{3.14}$$

which avoids biasing the fit to large values of τ and $\dot{\gamma}$. As discussed in section 2.2.2, it can be assumed $t_c = 1\,\mathrm{s}$, based on previous experimental work (Mueller et al., 2010, 2011). The reference viscosity η_* can be normalized by the viscosity of the syrup μ to give the relative reference viscosity $\eta_{r,*}$ (equation 2.12), hereafter referred to as the relative viscosity.

3.4 Results

Experimental data are presented in table 3.1. Results for relative viscosity are presented in figure 3.4, which plots $\eta_{r,*}(\phi_p)$, with datapoints coloured according to ϕ_b. Similarly, experimental results for the flow index are presented in figure 3.5, which plots $n(\phi_p)$, with datapoints coloured according to ϕ_b.

Sample	ϕ_p	ϕ_p^*	ϕ_b	ϕ_b^*	μ (Pa s)	$a_{\max}$ (μm)	η_* (Pa s)	n	$\dot{\gamma}_{\max}$ (s^{-1})	N_{data}
-	±3%	±5.83%	±5.83%	±5%	-	-	±(error)	±(error)	±2%	-
3P-3	0.102	0.120	0.168	0.151	61.7	455	117 (1)	0.944 (0.004)	0.646	18
3P-5	0.088	0.113	0.237	0.216	61.7	245	118 (1)	0.916 (0.005)	1.15	15
3P-6	0.113	0.120	0.058	0.051	61.7	177	106 (1)	0.979 (0.003)	3.43	32
3P-7	0.102	0.105	0.033	0.030	61.7	122	89.2 (0.4)	0.991 (0.003)	5.73	38
3P-8	0.192	0.207	0.085	0.068	61.7	129	153 (1)	0.965 (0.003)	3.14	36
3P-9	0.165	0.207	0.244	0.204	61.7	*160	159 (1)	0.914 (0.003)	1.44	26
3P-10	0.164	0.207	0.247	0.206	61.7	234	175 (2)	0.935 (0.003)	0.903	24
3P-11	0.177	0.216	0.220	0.181	61.7	144	176 (1)	0.938 (0.003)	1.57	28
3P-12	0.190	0.212	0.127	0.103	61.7	116	143 (1)	0.965 (0.003)	2.60	32
3P-13	0.169	0.212	0.245	0.204	61.7	*160	163 (2)	0.930 (0.003)	1.36	26
3P-14	0.272	0.302	0.135	0.098	61.7	103	235 (1)	0.959 (0.003)	2.28	38
3P-15	0.244	0.303	0.256	0.194	61.7	123	245 (2)	0.908 (0.003)	1.62	32
3P-17	0.274	0.302	0.130	0.094	58.1	*160	234 (2)	0.956 (0.003)	1.59	32
3P-18	0.289	0.306	0.075	0.053	58.1	*160	224 (2)	0.972 (0.003)	2.10	36
3P-19	0.331	0.409	0.287	0.192	58.1	*160	512 (4)	0.845 (0.002)	0.834	34
3P-20	0.338	0.405	0.249	0.165	58.1	150	500 (4)	0.838 (0.002)	0.963	36
3P-21	0.368	0.406	0.147	0.093	58.1	142	498 (3)	0.917 (0.002)	1.07	38
3P-22	0.385	0.405	0.078	0.048	58.1	120	491 (3)	0.937 (0.002)	1.06	38
3P-23	0.000	0.000	0.213	0.213	58.1	229	76.6 (0.7)	0.926 (0.004)	1.72	21
3P-24	0.000	0.000	0.054	0.054	58.1	*160	60.5 (0.4)	0.974 (0.003)	5.30	30
3P-25	0.000	0.000	0.075	0.075	58.1	173	65.4 (0.4)	0.970 (0.004)	3.27	26
3P-26	0.000	0.000	0.095	0.095	58.1	129	63.6 (0.4)	0.959 (0.003)	4.29	28
3P-27	0.000	0.000	0.123	0.123	55.7	136	60.7 (0.4)	0.953 (0.003)	3.58	26
3P-28	0.000	0.000	0.275	0.275	55.7	239	74.4 (0.7)	0.920 (0.004)	1.49	20
3P-29	0.463	0.505	0.157	0.085	55.7	147	1490 (20)	0.771 (0.004)	0.124	38
3P-30	0.042	0.059	0.302	0.290	55.7	99.9	96.5 (0.6)	0.888 (0.003)	3.11	27
3P-31	0.048	0.062	0.240	0.228	55.7	110	97.0 (0.7)	0.919 (0.003)	3.09	28
3P-32	0.057	0.065	0.130	0.123	55.7	150	90.6 (0.6)	0.928 (0.009)	2.84	18
3P-33	0.060	0.065	0.090	0.085	55.7	*160	77.6 (0.6)	0.963 (0.010)	3.57	20
3P-35	0.050	0.050	0.000	0.000	55.9	-	67.4 (0.5)	0.994 (0.006)	7.53	38
3P-36	0.100	0.100	0.000	0.000	55.9	-	81.1 (0.6)	0.994 (0.006)	6.25	38
3P-37	0.200	0.200	0.000	0.000	55.9	-	125 (1)	0.993 (0.006)	4.05	38
3P-38	0.300	0.300	0.000	0.000	55.9	-	222 (1)	0.988 (0.006)	1.36	38
3P-39	0.400	0.400	0.000	0.000	55.9	-	540 (4)	0.955 (0.006)	0.924	38
3P-40	0.500	0.500	0.000	0.000	55.9	-	2260 (40)	0.818 (0.004)	0.083	38
3P-41	0.431	0.508	0.266	0.151	57.0	149	1330 (20)	0.676 (0.002)	0.111	27
3P-42	0.412	0.499	0.295	0.174	57.0	132	1020 (10)	0.689 (0.002)	0.164	27
3P-43	0.449	0.496	0.173	0.095	57.0	133	1280 (10)	0.809 (0.002)	0.177	30
3P-44	0.460	0.497	0.141	0.076	57.0	96.5	1370 (10)	0.803 (0.002)	0.302	38

Table 3.1: Experimental data for each sample, to three significant figures, and one standard deviation errors where appropriate. ϕ_p and ϕ_b^* were measuremed when creating the samples; ϕ_p and ϕ_p^* were calculated subsequently from these values. Column $a_{\max}$ gives the largest bubble measured for each sample, where * indicates that no bubble size distribution was measured, and an average value was used instead. Column $\dot{\gamma}_{\max}$ gives the maximum strain-rate that satisfies equation 3.13, and N_{data} are the number of stress–strain-rate data points that remain after filtering.

It is useful at this stage to confirm that the data for the two-phase end-members (bubble-free particle suspension and particle-free bubble suspension) adhere to the relevant two-phase constitutive equations. The solid curve in figure 3.4 represents the best fit (as described in section 3.4.1) of equation 2.11, in which the only free parameter is ϕ_m, to data for bubble-free particle suspensions ($\phi_b = 0$). An excellent fit is found for $\phi_m = 0.593$, with $R^2 = 1.00$ (to 2 d.p.); this value of the maximum packing fraction is slightly lower than the value of $\phi_m = 0.633$ quoted by Mueller et al. (2010, 2011) for suspensions of monodisperse spheres, but it is noted that the 2σ errors of the two estimates overlap. Both of these values are lower than the value of $\phi_m = 0.66$ calculated from equation 2.13 with $r_p = 1$. It is proposed therefore

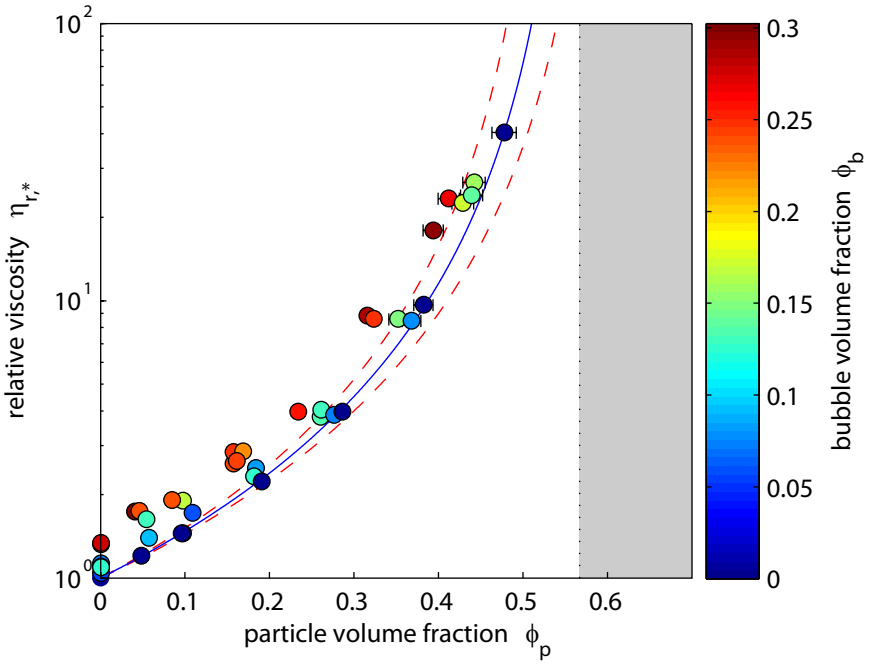

Figure 3.4: Relative viscosity $\eta_{r,*}$ against particle volume fraction ϕ_p for three-phase suspensions; symbols are shaded according to bubble volume fraction ϕ_b. Solid curve is the best fit of the Maron-Pierce equation (2.11) to data from bubble-free suspensions ($\phi_b = 0$, dark symbols). Shaded area shows the region where $\phi > \phi_m$. Dashed curves show the 95% confidence limits for ϕ_m based on the potential error in the data fitting technique, as presented in section 3.4.1. Error bars (1σ) are shown when larger than the data points.

that equation 2.13 overestimates ϕ_m for nearly-spherical particles because it is based on a fit to data that assumes a gaussian relationship between ϕ_m and r_p. Studies of non-sheared particle packs have reported that the maximum packing fraction is actually highest for slightly non-spherical aspect ratios (Delaney and Cleary, 2010; Donev et al., 2004); consequently, the $\phi_m(r_p)$ curve dips around $r_p = 1$ leading to the overestimate given by equation 2.13.

Figure 3.6 plots two-phase data for the relative viscosity of particle-free bubble suspensions; i.e. $\eta_{r,*}(\phi_b)$ with $\phi_p = 0$. The solid curve is equation 2.5, which gives a good fit to the data, with $R^2 = 0.87$. Figures 3.4 and 3.6 therefore demonstrate the validity of the two-phase constitutive models (equations 2.5 and 2.11) on which the three-phase model is built.

3.4.1 Estimation of errors on fitted parameters

A number of important parameters for this study (η_*, n, ϕ_m, τ_0) are found by fitting equations to a set of experimental data. Although a confidence limit can simply be calculated for the fit to the data, this does not account for errors on the experimental

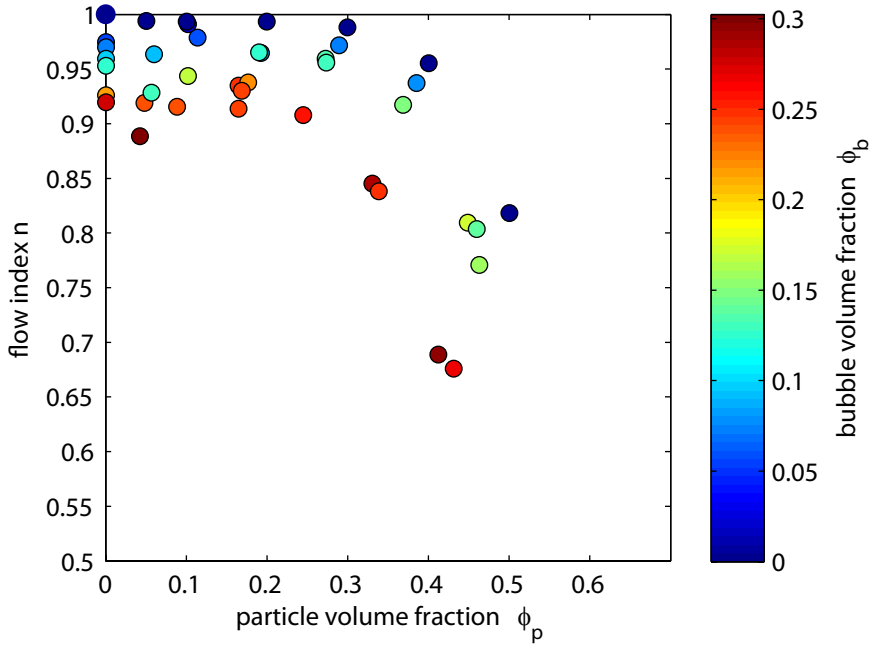

Figure 3.5: Flow index n against particle volume fraction ϕ_p for three-phase suspensions; symbols are shaded according to bubble volume fraction ϕ_b. Error bars (1σ) are shown when larger than the data points.

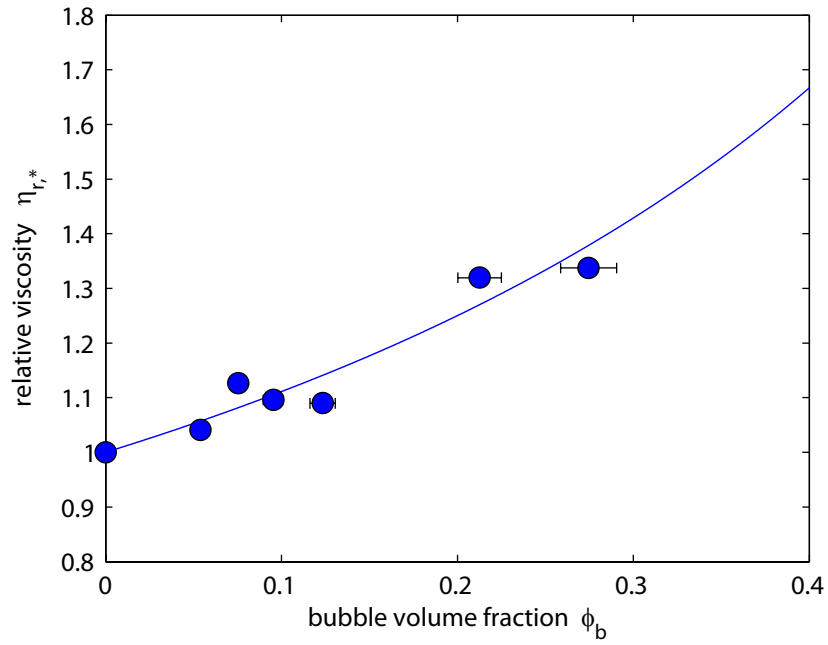

Figure 3.6: Relative viscosity $\eta_{r,*}$ against bubble volume fraction ϕ_b for particle-free (two-phase) bubble suspensions. The solid curve is equation 2.5. Error bars (1σ) are shown when larger than the data points.

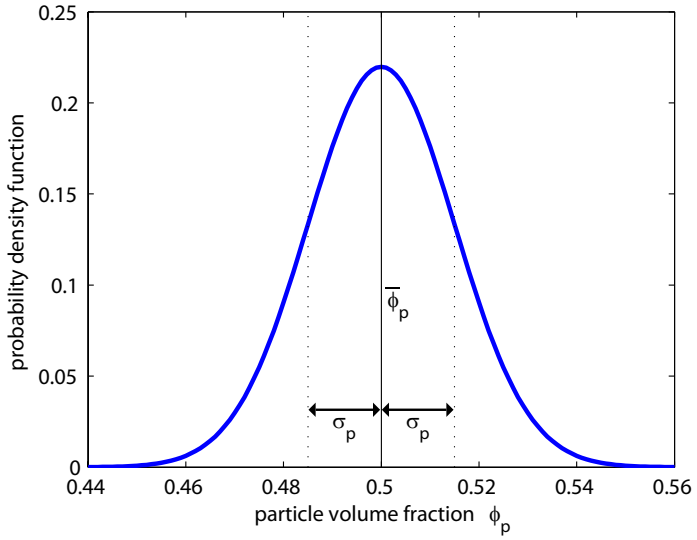

Figure 3.7: Probability density function for $\phi_p = 0.5$, given $\sigma_p = 0.015$.

data. An adaptation of the bootstrapping technique for regression problems is used to estimate errors on the fit, which is described here in the context of fitting a value of ϕ_m to the Maron-Pierce relationship (equation 2.10), given a set of $\eta_{r,*}(\phi_p)$ data and errors (table 3.2).

ϕ_p	σ_p	$\eta_{r,*}$	$\sigma_{\eta r,*}$
0.050	0.0015	1.2045	0.0096
0.100	0.003	1.4496	0.0103
0.200	0.006	2.2263	0.0122
0.300	0.009	3.9697	0.0226
0.400	0.012	9.6470	0.0685
0.500	0.015	40.3865	0.6462

Table 3.2: Experimental data and one standard deviation errors, for bubble-free data. These are the dark blue data points in figure 3.4.

If it is assumed that the errors on $\eta_{r,*}$ and ϕ_p are normally distributed, each measured or calculated value can be used as the mean, together with the known standard deviation error, and a probability distribution for each value can be calculated (e.g. figure 3.7). The entire dataset can then be resampled, drawing values at random from each probability distribution, and these values can be used to calculate a best-fit ϕ_m. Repeating this process a very large number of times (10,000, in this case), results in a distribution of values of ϕ_m (figure 3.8).

Assuming that this distribution is normal, the mean, $\phi_m = 0.5933$ can be cal-

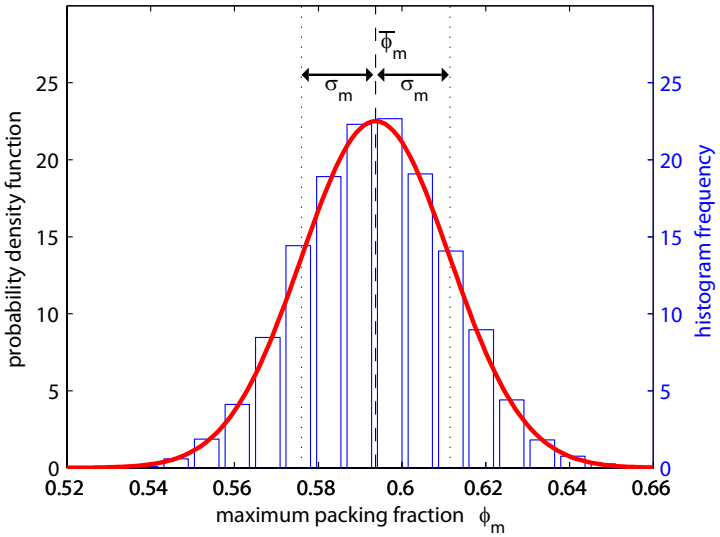

Figure 3.8: Histogram of fitted ϕ_m values. Red curve is the scaled probability density function, assuming that the ϕ_m values form a normal distribution.

culated (which is very close to the value calculated from a least squares fit to the original data, $\phi_m = 0.5934$), and a standard deviation, $\sigma_m = 0.0177$. Thus it is possible to estimate the potential error in the value of ϕ_m.

3.5 Discussion

3.5.1 Reference viscosity of three-phase suspensions

In figure 3.4, all suspensions that contain bubbles have a higher reference viscosity than a two-phase particle suspension with the same particle volume fraction. Conceptually, this is equivalent to saying that, for a given particle suspension, the viscosity increases if some of the suspending liquid is replaced with bubbles. This is intuitive, because bubbles in the low-capillarity regime increase suspension viscosity.

Recasting the data in terms of ϕ_b^* and ϕ_p^* yields figure 3.9. It is evident from this plot that the effect of *adding* bubbles to a particle suspension (or growing bubbles in a particle suspension) depends upon the initial particle volume fraction ϕ_p^*. For dilute particle suspensions ($\phi_p^* \lesssim 0.25$), adding bubbles increases the suspension viscosity; whereas, for more concentrated particle suspensions ($\phi_p^* \gtrsim 0.25$), adding bubbles decreases suspension viscosity.

These relationships are more clearly demonstrated by figure 3.10. The plot shows that the rheology of a particle suspension becomes increasingly sensitive to

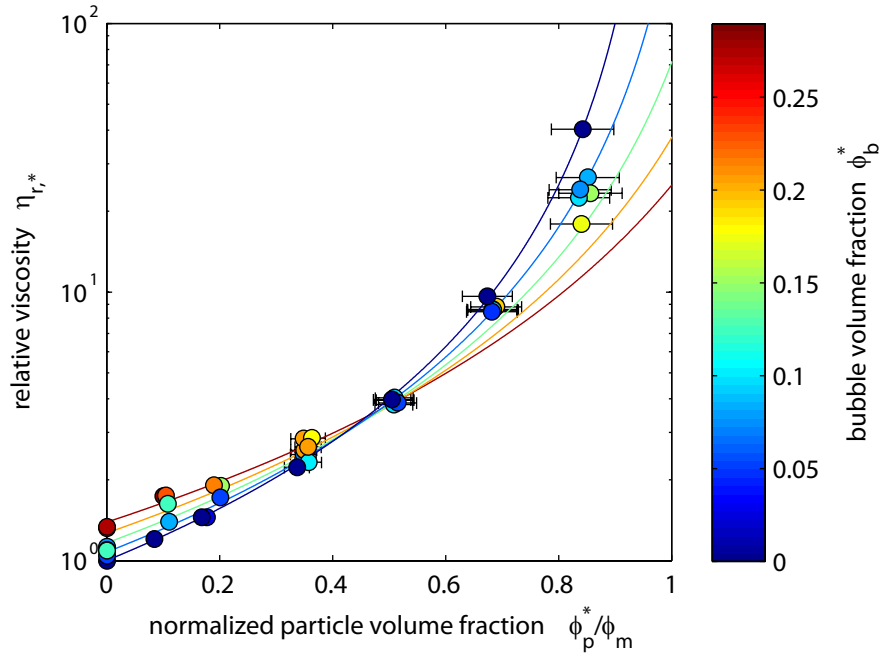

Figure 3.9: Three phase data from figure 3.4 recast in terms of ϕ_b^* and ϕ_p^*. Solid lines are the three-phase model (equation 3.2) contoured in ϕ_b^*. Error bars (1σ) are shown when larger than the data points.

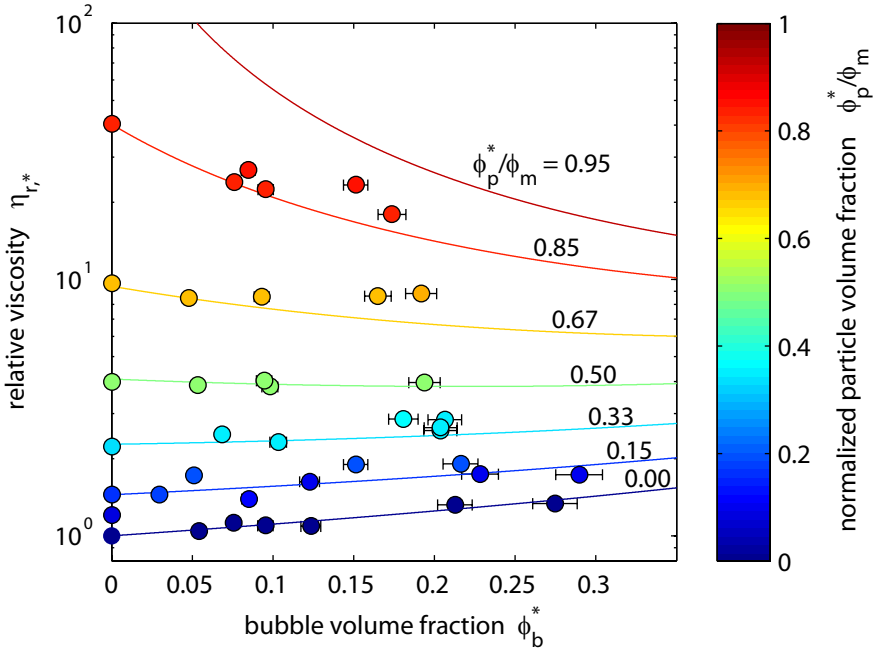

Figure 3.10: Relative viscosity $\eta_{r,*}$ against ϕ_b^*. Datapoints are shaded according to ϕ_p^*/ϕ_m. Solid curves are the three-phase model (equation 3.2) for representative values of ϕ_p^*/ϕ_m contoured according to the same scale. Error bars (1σ) are shown when larger than the data points.

the addition of a small volume fraction of bubbles as its particle volume fraction approaches the maximum packing fraction. The physical explanation for this behaviour is straightforward, and relies on two competing processes. As discussed above, the addition of low capillarity (i.e. spherical) bubbles to a fluid increases its viscosity. For dilute particle suspensions, this is the dominant trend, hence the data show an increase in reference viscosity with increasing bubble content for $\phi_p^* \lesssim 0.25$. Opposing this is a 'dilution' effect, in which the addition of bubbles to a suspension of particles moves the particles further apart; this decreases the particle volume fraction ϕ_p, reduces the impact that particle–particle interactions have on suspension rheology, and reduces suspension viscosity. This process dominates for concentrated particle suspensions; indeed, because the Maron-Pierce relationship is a power law, the higher the initial particle volume fraction, the greater the impact the same dilution with bubbles will have.

It is also clear from these figures that the data agree well with the proposed three-phase model (equation 3.2). The model predicts the relative viscosity to within ±20 % for all but three of the samples, and within ±10 % for the majority (figure 3.11). Furthermore, there is no strong systematic trend relating the discrepancy to either ϕ_b^* or ϕ_p^*. It is noted that a close agreement between model and data is found despite the fact that some samples violate the model assumption that bubbles are small compared with particles (section 3.2). In all samples the majority (by number) of the bubbles are smaller than the particles and so it makes sense to choose the bubble suspension as the effective medium. However, the average bubble radius is between 0.20 and 0.97 times the average particle radius and the bubble volume-mean-radius (section 3.3.3) is between 0.57 and 2.4 times the particle volume-mean-radius indicating that the 'typical' bubble in many samples is comparable in size to the particles.

The largest discrepancy between the model and data occurs when both ϕ_p^* and ϕ_b^* are large: the model then tends to underpredict the reference viscosity in such samples. This discrepancy is probably caused by bubble-particle interactions, which are not captured in the simple approach of combining two-phase equations. Further work is needed to formulate a model that captures such interactions.

3.5.1.1 Will increasing bubble volume fraction increase or decrease reference viscosity?

For a given bubble and particle volume fraction, it is useful to know the effect of the addition of further bubbles (or the growth of existing bubbles). Depending on the

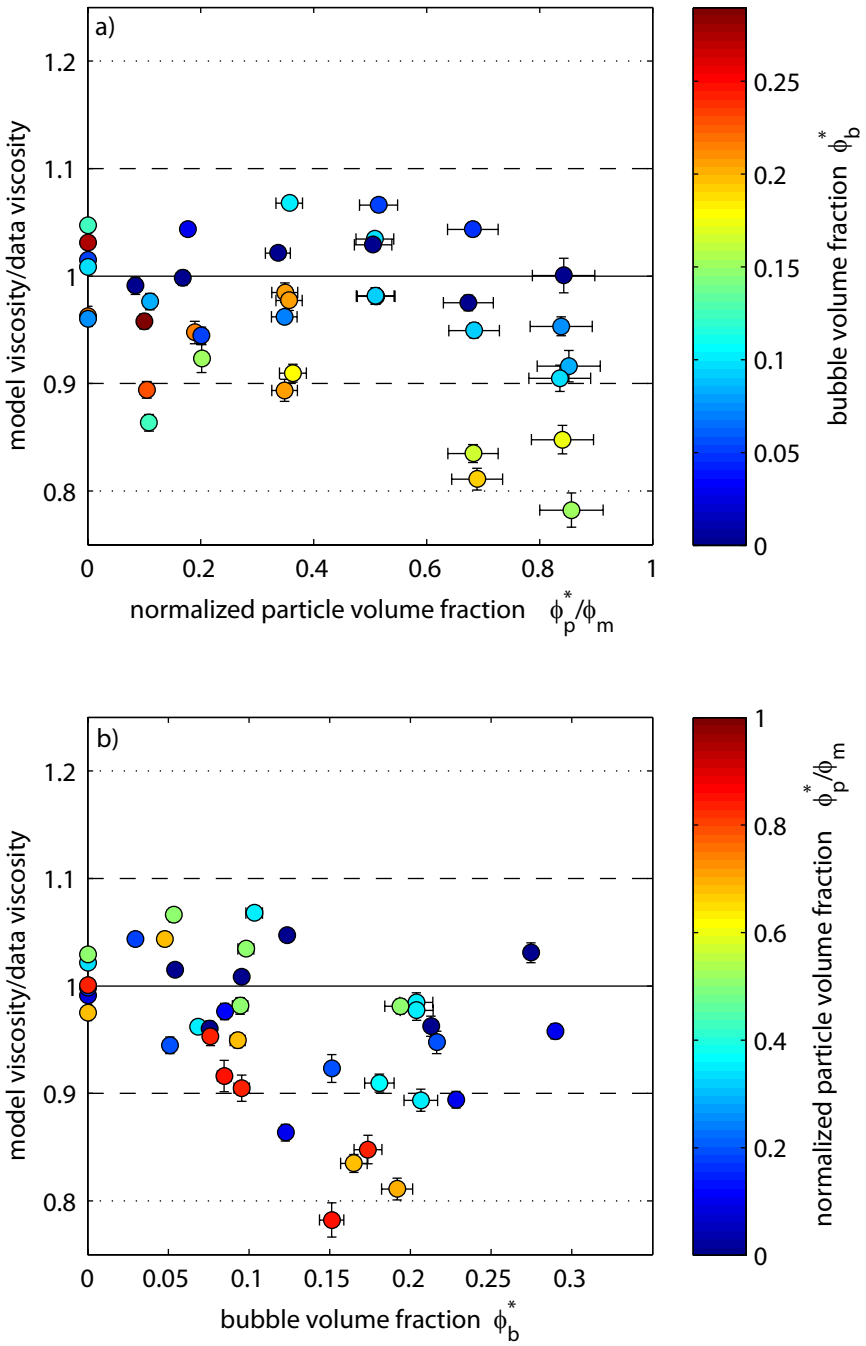

Figure 3.11: Comparison between $\eta_{r,*}$ predicted by the model (equation 3.2) and $\eta_{r,*}$ calculated from experimental data, against a) ϕ_p^*/ϕ_m, shaded for ϕ_b^*, and b) ϕ_b^*, shaded for ϕ_p^*/ϕ_m. Error bars (1σ) are shown when larger than the data points. The solid line indicates a perfect match between model and data; the dashed and dotted lines respectively indicate $\pm 10\%$ and $\pm 20\%$ discrepancy.

intial bubble and particle volume fractions, this may cause an increase in viscosity, a decrease in viscosity, or a decrease followed by an increase. At some point in between, the addition of an infinitesimally small volume of bubbles will cause no

change in viscosity; this will be the points at which:

$$\frac{\partial \eta_{r,*}}{\partial \phi_b^*} = 0. \tag{3.15}$$

By finding the root of this equation, it is possible to determine the location of the regime divide between bubbles causing an increase in viscosity, and bubbles causing a decrease in viscosity.

Expanded, the differential equation becomes:

$$\frac{\partial \eta_{r,*}}{\partial \phi_b^*} = \frac{1-\phi_p^*}{\left(1-\frac{\phi_p^*(1-\phi_b^*)}{\phi_m}\right)^2\left(1-\phi_p^*(1-\phi_b^*)-\phi_b^*\right)^2} - \frac{2\phi_p^*}{\phi_m\left(1-\frac{\phi_b^*}{1-\phi_p^*(1-\phi_b^*)}\right)\left(1-\frac{\phi_p^*(1-\phi_b^*)}{\phi_m}\right)^3}, \tag{3.16}$$

and the root is:

$$\phi_b^* = \frac{\sqrt{(9-8\phi_m)(\phi_p^*)^2}+4(\phi_p^*)^2-3\phi_p^*}{4(\phi_p^*)^2}; \tag{3.17}$$

an explicit solution cannot be found for ϕ_p^*. Equation 3.17 is plotted in figure 3.12. For all suspensions with bubble and particle volume fractions to the left of the black curve, the addition of bubbles will lead to an increase in reference viscosity. An example is shown by the blue trajectory, for a fluid that begins with no suspended particles or bubbles. To the right of the black curve, addition of bubbles will initially lead to a decrease in reference viscosity. An example is shown by the red trajectory, for a fluid with an initial particle volume fraction $\phi_p^* = 0.5$. If enough bubbles are added that the suspension reaches the black curve, viscosity will begin to increase again. In order to determine the effect of adding some volume of bubbles to a suspension, both the initial bubble volume fraction and particle volume fraction must be known.

This effect, for an initially bubble-free suspension, is demonstrated clearly by the data (figure 3.13). For a particle-free suspension, addition of bubbles will always lead to a viscosity increase compared to the bubble-free suspension (equivalent to the blue trajectory in figure 3.12); on the other hand, the addition of bubbles to a concentrated suspension always leads to a viscosity decrease (equivalent to the red trajectory in figure 3.12).

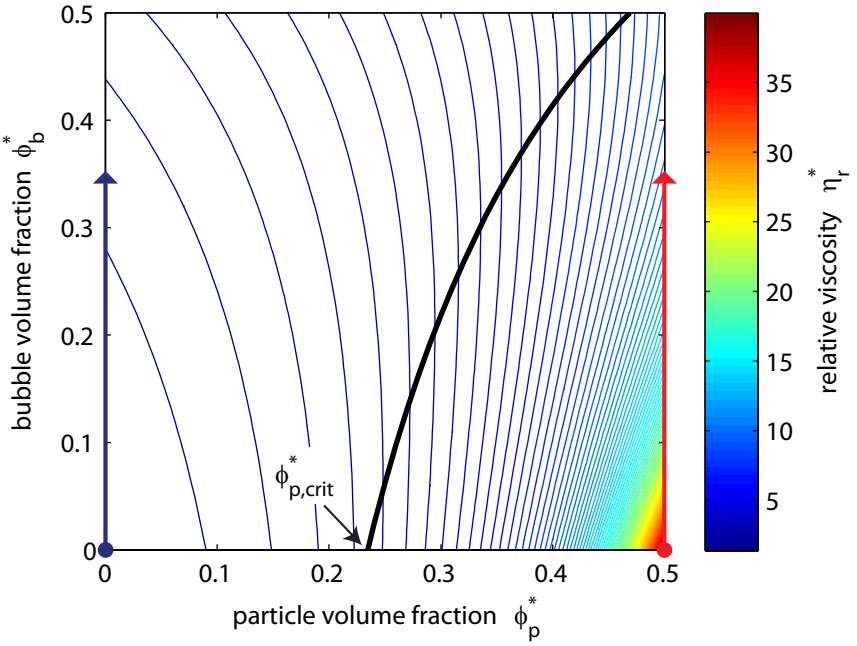

Figure 3.12: Contours of $\eta_{r,*}$ for the relevant range of ϕ_p^* and ϕ_b^*. The black curve is equation 3.17, and the point $\phi^*_{p,\text{crit}}$ is the point at which addition of bubbles to an initially bubble-free suspension will switch from increasing to decreasing viscosity. The blue trajectory shows an increase in viscosity as bubbles are added to a particle-free suspension; the red trajectory shows a decrease in viscosity as bubbles are added to a particle-rich suspension.

3.5.2 Flow index of three-phase suspensions

Reference viscosity provides only a partial description of the rheology of a shear-thinning suspension; for a practical rheological model, the flow index n is also required (equation 2.9). Figure 3.14 re-casts the flow index data shown in figure 3.5, plotting them against ϕ_b^* and ϕ_p^*/ϕ_m.

Figure 3.14a shows clearly that shear thinning is observed for all suspensions, even those containing only bubbles. The data indicate a linear relationship between n and ϕ_b for particle-free suspensions, in the low-capillarity regime, such that shear thinning becomes more pronounced as bubble volume fraction increases:

$$n = 1 - 0.334\phi_b \tag{3.18}$$

(note that $\phi_b = \phi_b^*$ when $\phi_p = 0$). Bubble suspensions are known to be strongly shear thinning in the range $0.1 \lesssim Ca \lesssim 10$ but, at lower and higher capillary number, current models predict that shear thinning is negligible (see figure 2.1 and section 2.2.2), which makes this result surprising. One potential explanation is that, despite

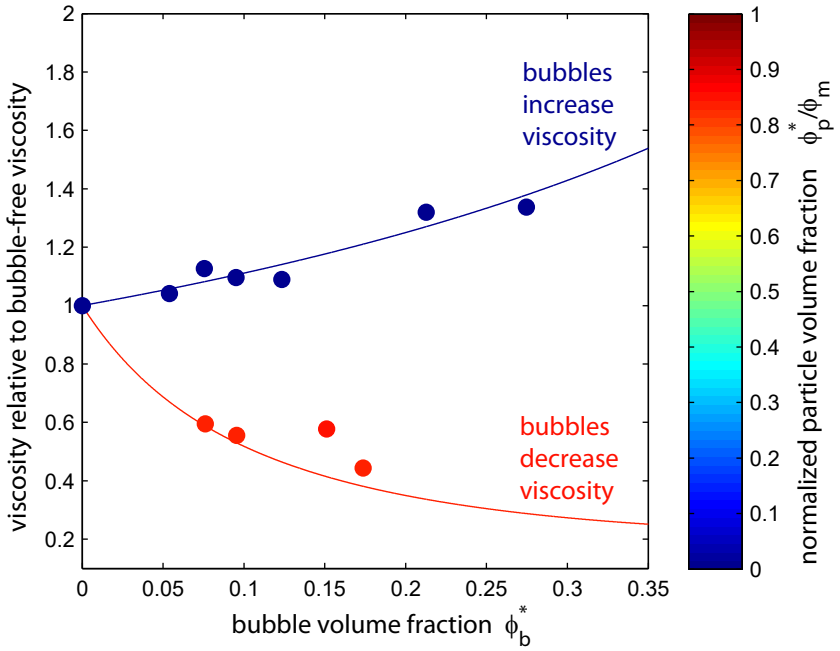

Figure 3.13: Relative viscosity $\eta_{r,*}$ compared to relative viscosity of bubble-free suspension $\eta_{r,*,\phi_b^*=0}$, for a particle-free suspension (blue datapoints and model curve) and a particle-rich suspension (red datapoints and model curve).

the data filtering methodology (section 3.3.3), there are a small number of very large bubbles in the samples, larger than those measured in the sample images, which have a correspondingly long relaxation time and, as a consequence, have a capillary number in the transitional regime. An alternative explanation is that the current model for bubble suspension rheology (equation 2.4) is inadequate for non-dilute suspensions. That model can be derived from the theoretical treatment of Frankel and Acrivos (1970) (Llewellin et al., 2002b), which is analytically exact in the limit of a dilute suspension (in which bubble–bubble interactions can be neglected) and in the limit of small bubble deformations. It is possible that bubble–bubble interactions in non-dilute samples act to introduce shear thinning — this would be consistent with the finding that shear thinning becomes more pronounced as bubble volume fraction increases. Further experimental work would be required to underpin a more detailed investigation of this phenomenon.

Superimposed on the decrease in flow index due to increasing bubble volume fraction is the effect of increasing particle volume fraction, shown most clearly in figure 3.14b. This relationship is non-linear, and appears to follow the empirical model proposed by Mueller et al. (2010) (equation 2.14 with $r_p = 1$ for spherical particles). For bubble-free suspensions — comparable to those investigated by Mueller — there

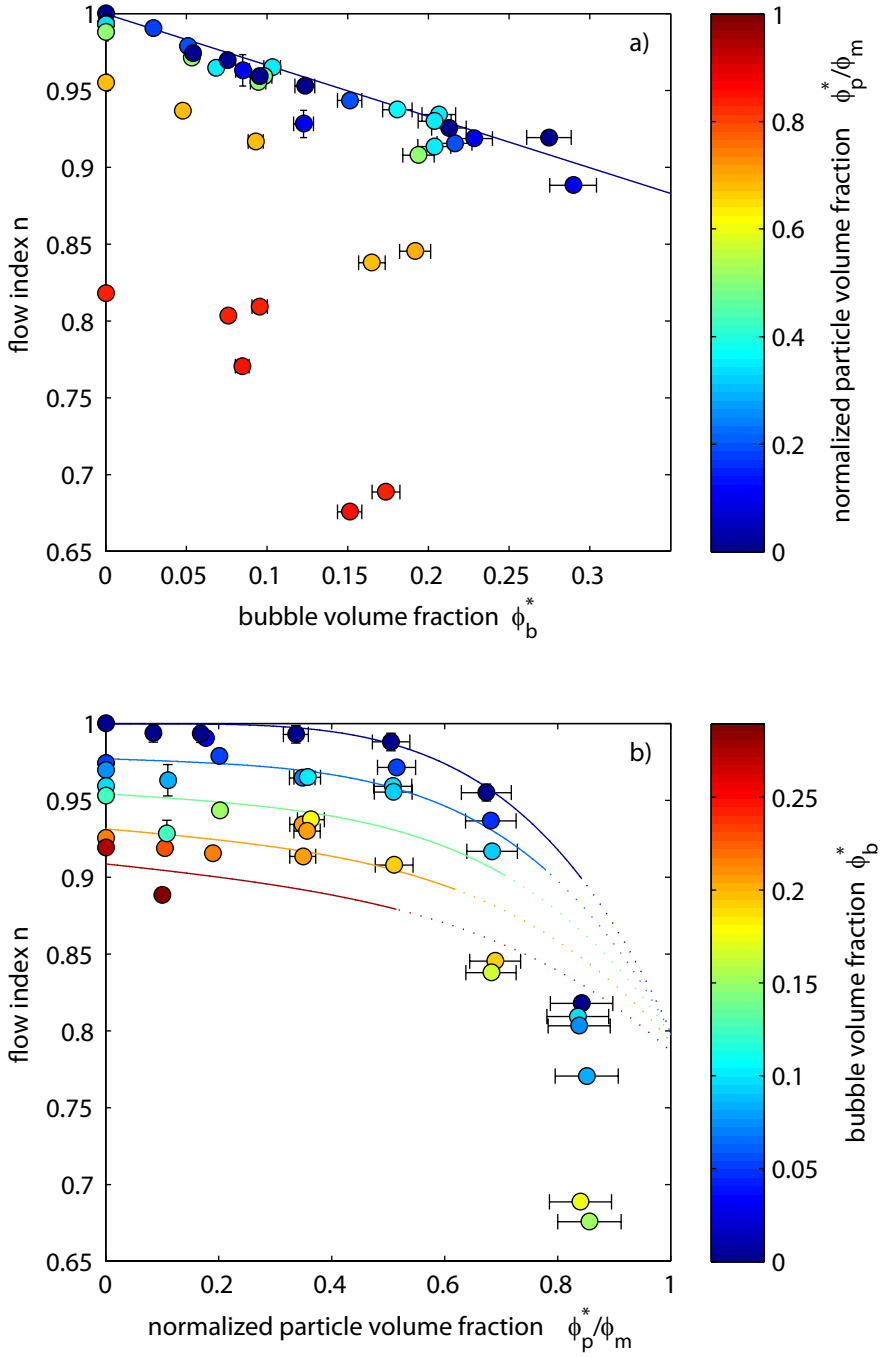

Figure 3.14: Flow index n against a) ϕ_b^*, shaded according to ϕ_p^*/ϕ_m, and b) ϕ_p^*/ϕ_m, shaded according to ϕ_b^*. Error bars (1σ) are shown when larger than data points. In a) solid line shows the linear relationship between n and ϕ_b^* for $\phi_p^* = 0$ (equation 3.18). In b) curves, contoured for ϕ_b^*, plot equation 3.19; solid over the range of particle volume fractions for which the total suspended fraction $\phi_s < 0.5$, and dotted outside this range.

is excellent agreement between data and model for $\phi_p/\phi_m < 0.8$, which is consistent with the limits of applicability given by Mueller et al. (2010).

The combined effect of bubbles and particles on the flow index appears to be a simple superposition of these two effects: the flow index of a pure fluid is 1, and is reduced by some amount dependent on bubble volume fraction, and again by some amount dependent on particle volume fraction. Consequently, the following purely empirical model is proposed for the flow index for suspensions of spherical particles:

$$n = 1 - 0.2\left(\frac{\phi_p}{\phi_m}\right)^4 - 0.334\phi_b. \tag{3.19}$$

Curves of this model for various bubble volume fractions are shown in figure 3.14b, and indicate that the model is valid for all samples with a total suspended fraction $\phi_s \lesssim 0.5$. The model agrees with the data to within $\pm 5\%$ for all samples below this cut-off. Note that this cut-off is drawn empirically from the data and has no theoretical basis.

3.5.3 Extensions to the model

3.5.3.1 Non-spherical particles

For suspensions of non-spherical, non-smooth particles, equation 2.13 can be used to calculate the expected maximum packing fraction. This value can then be incorporated into equation 3.2, so that the reference viscosity can be corrected for variations in particle aspect ratio and rugosity. Experiments with non-spherical particles in three-phase suspensions have not been performed here, so this has not yet been validated. However, based on the well-understood behaviour of two-phase particle suspensions, and the conceptual framework of an effective medium, which is used to explain our model, it is expected that this extension of the model will be valid.

The aspect ratio may also be included in equation 3.19 in a manner analogous to equation 2.14:

$$n = 1 - 0.2r_p\left(\frac{\phi_p}{\phi_m}\right)^4 - 0.334\phi_b. \tag{3.20}$$

As such, more elongate particles would be expected to give a lower flow index than spherical particles, and the fluid would therefore be more shear thinning. Although equation 2.14 is established in the literature, no conceptual model exists with which to explain the empirically derived equation 3.19. As such, without experiments to validate equation 3.20, it is not possible to be confident about its range of applicability: this equation remains only a proposal.

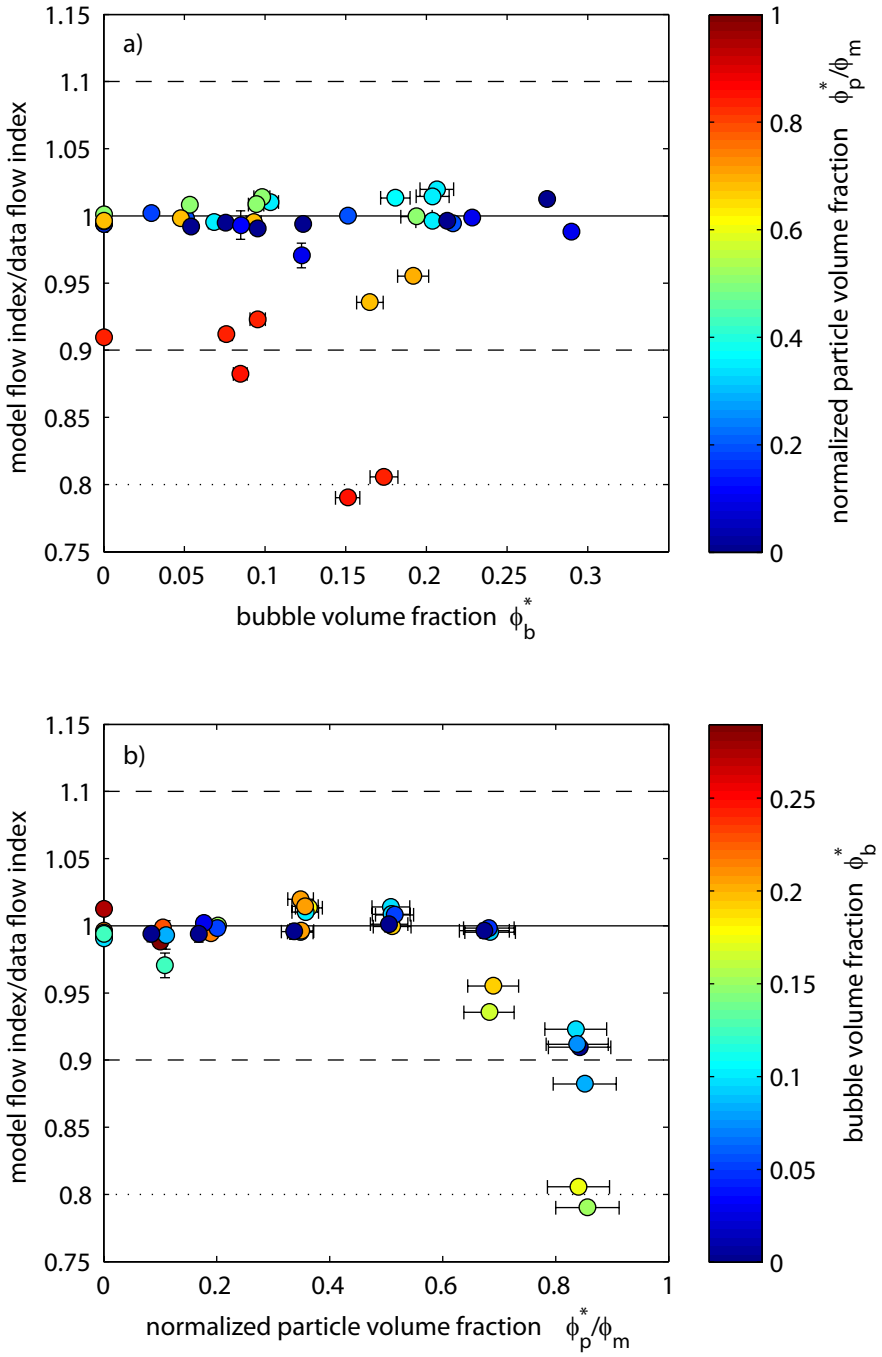

Figure 3.15: Comparison between n predicted by the model (equation 3.19) and n calculated from experimental data, against a) ϕ_b^*, shaded for ϕ_p^*/ϕ_m, and b) ϕ_p^*/ϕ_m, shaded for ϕ_b^*. Error bars (1σ) are shown when larger than the data points. The solid line indicates a perfect match between model and data; the dashed and dotted lines respectively indicate $\pm 10\%$ and $\pm 20\%$ discrepancy.

3.5.3.2 High capillarity bubbles

In section 3.2, it was noted that in the high capillarity regime, equation 2.6 could be used rather than equation 2.5, in formulating the three-phase model. The three-

phase equation would then become:

$$\eta_{r,*} = (1 - \phi_b)^{5/3} \left(1 - \frac{\phi_p}{\phi_m}\right)^{-2}; \tag{3.21}$$

this model is shown in figure 3.16.

Figure 3.16 demonstrates that in the high bubble capillarity regime, it is expected that any addition of bubbles to, or growth of bubbles in, a crystal-bearing suspension will lead to a decrease in viscosity. Suspensions that begin with higher crystal volume fraction will show a larger decrease in viscosity for the addition of a given volume of bubbles.

In the experiments, at the highest strain rates, the larger bubbles in many samples will have been in the high bubble capillarity regime. However, the majority of bubbles, usually much smaller, will have been either in the low capillarity regime, or in the transitional regime. As such, it is not possible to simply filter out the low capillarity data in a similar manner to that described in section 3.3.3 for filtering out high capillarity data. This means that this study does not have the data necessary to validate the proposed adaptation of the three-phase equation.

The model for the control of bubble and particle volume fractions on flow index, at low capillarity, was based entirely on empirical data. As such, no comparable model is proposed here for how the flow index depends on bubble volume fraction in the high capillarity regime.

3.5.3.3 Bubbles which are larger than the particles

In section 3.2, a continuous medium concept was used to formulate the three-phase viscosity equation. This concept requires that the bubbles are smaller than the particles, such that the particles do not interact with individual bubbles, only a bubbly continuous medium. A similar argument could be made for a system in which the particles are smaller than the bubbles: then the bubbles could be considered to be suspended in a particle suspension. In this case, equations 3.5 and 3.6 would be used to define the bubble and particle volume fractions in the model, leading to

$$\eta_{r,*} = (1 - \phi_b^*)^{-1} \left(1 - \frac{\phi_p^*}{\phi_m}\right)^{-2} \tag{3.22}$$

becoming the equation for the reference viscosity of the system with low capillarity bubbles, and

$$\eta_{r,*} = (1 - \phi_b^*)^{5/3} \left(1 - \frac{\phi_p^*}{\phi_m}\right)^{-2} \tag{3.23}$$

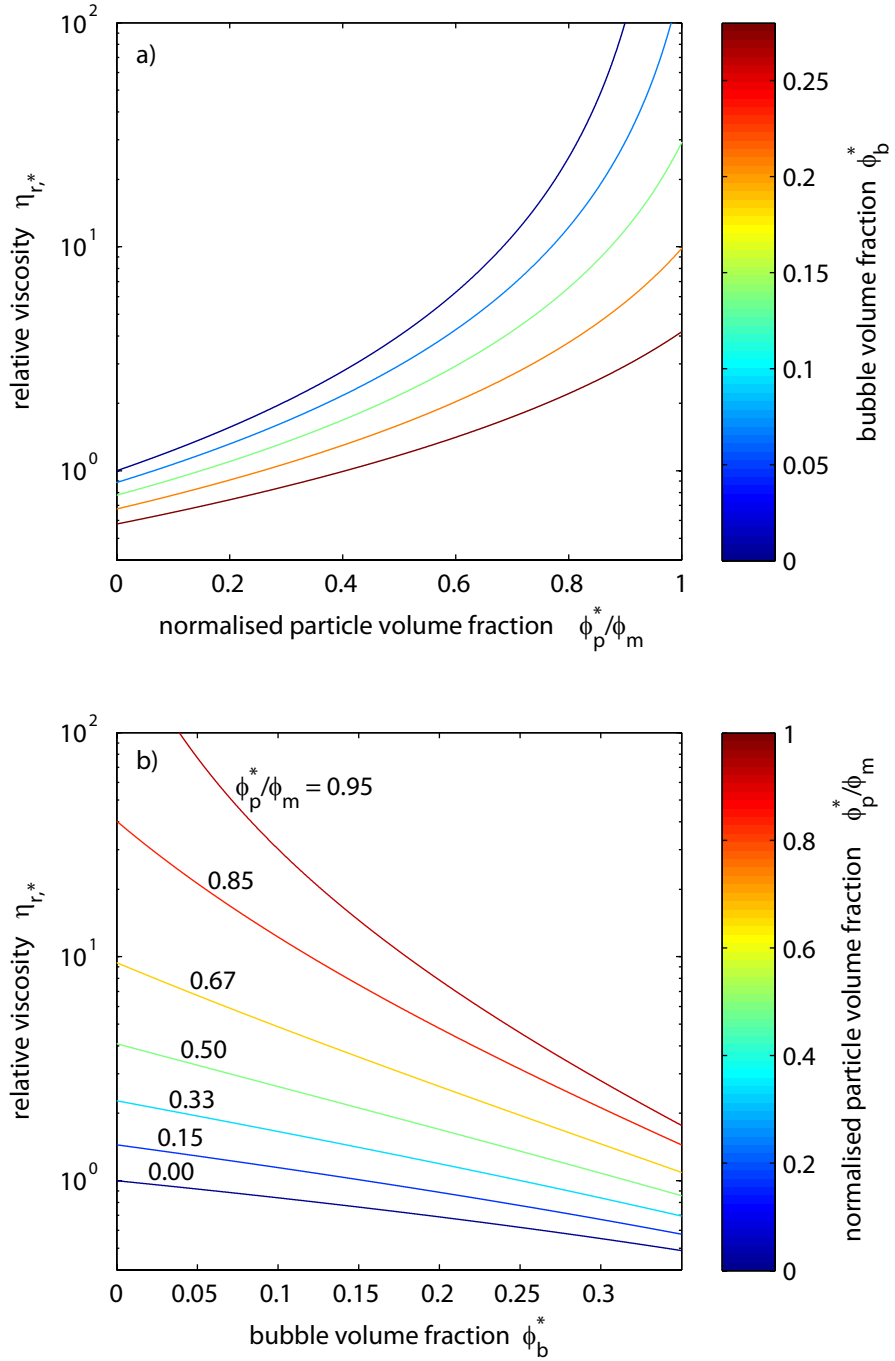

Figure 3.16: Relative viscosity $\eta_{r,*}$ of a high capillarity three-phase suspension against a) ϕ_p^*/ϕ_m, shaded for ϕ_b^* and b) ϕ_b^*, shaded for ϕ_p^*/ϕ_m. The curves show the model predictions from equation 3.21.

for high capillarity bubbles. These proposed equations are shown in figure 3.17. The effect of bubbles on the viscosity of a three-phase suspension is predicted to be much reduced if the bubbles are larger than the particles. Low capillarity bubbles

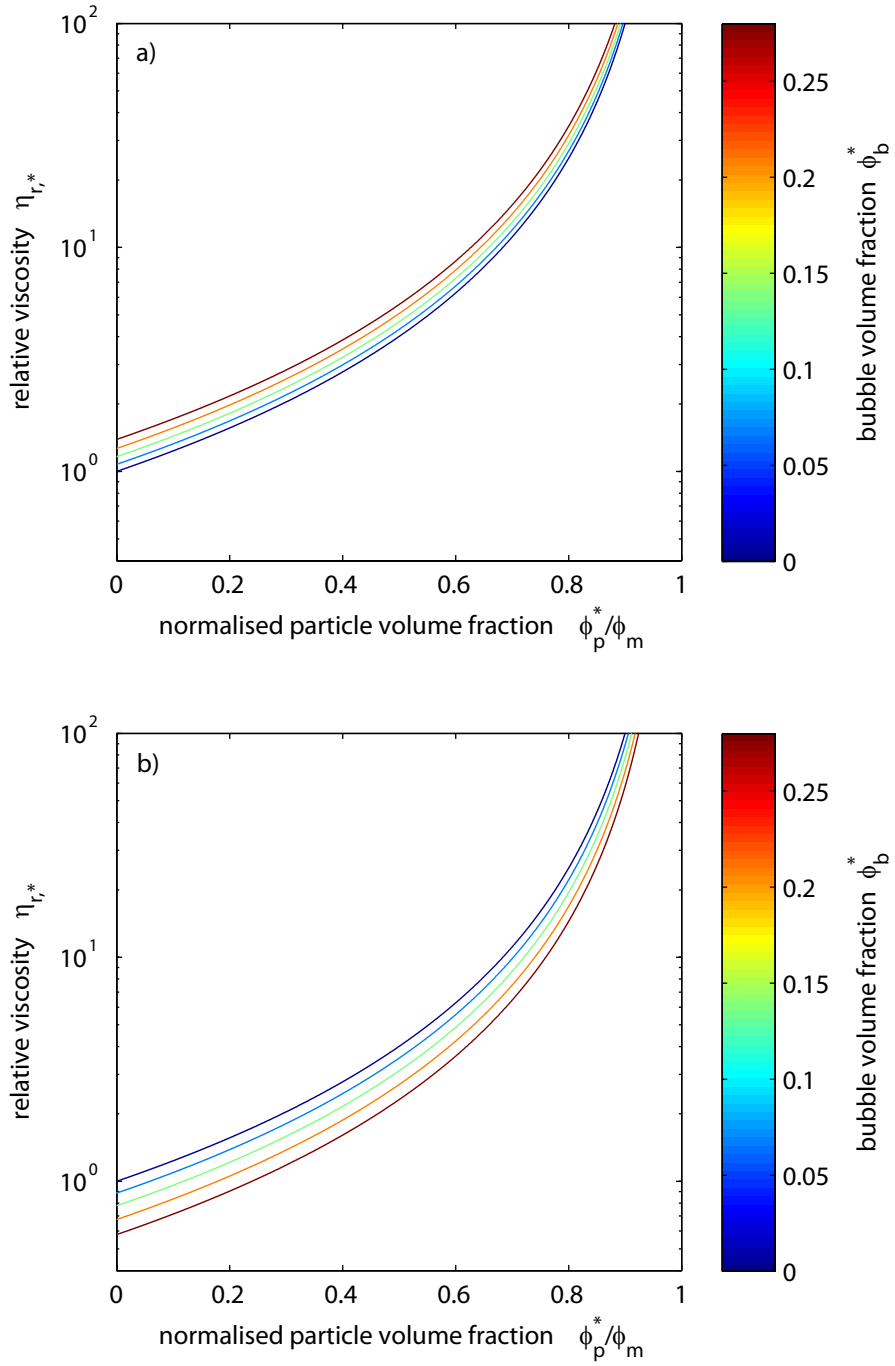

Figure 3.17: Relative viscosity $\eta_{r,*}$ of a three-phase suspension in which the bubbles are larger than the particles, against ϕ_p^*/ϕ_m, shaded for ϕ_b^*, for a) low capillarity bubbles, and b) high capillarity bubbles. The curves show the model predictions from equations 3.22 and 3.23.

always increase the suspension viscosity; high capillarity bubbles always reduce the viscosity. The total change in viscosity is much lower than in the case where bubbles are smaller than particles.

The majority of bubbles used in the experiments described in section 3.3 are smaller than the particles; a small number are comparable in size to the particles. It is therefore not possible to validate equations 3.22 and 3.23 using these data. Further experiments in which bubbles were all larger than the particles would be required.

3.6 Applying the model to natural magmatic systems

3.6.1 Additional complexities of a natural system

These analogue experiments are ideal for characterizing the fundamental processes that are understood to occur in magmatic systems. Rather than attempting to simulate the full range of processes in the natural system, the aim here is to eliminate complexity while retaining control on the key parameters which govern specific aspects of the system's behaviour. This makes it possible to isolate the effects of changing bubble and crystal volume fractions from other potentially dependent parameters in the natural system.

In the analogue system, smooth, spherical particles and insoluble bubbles were used in a well-characterized Newtonian fluid. It was possible to control the temperature and pressure of the experiment, and it was assumed that the bubble and crystal fractions did not change over the duration of the experiment.

However, in order to relate the results of these experiments to specific natural magmas, aspects of the system that did not exist — or were unimportant — in the analogue system must be accounted for. These additional complexities include: changing crystal population (volume fraction, aspect ratio, and size distribution) as the system evolves; changing bubble population (volume fraction, size distribution, capillary numbers) as volatiles become saturated in the melt and bubbles nucleate and grow; and temporally and spatially varying melt viscosity as volatiles exsolve, and the temperature, pressure, and composition changes. In order to track changes in viscosity over the lifetime of a natural system, it is necessary to understand how parameters such as pressure, temperature, and time affect crystallization and bubble growth, which in turn affect the bulk magma viscosity.

Many of these can be accounted for either within the model or by extending it to include parameters such as the aspect ratio of the crystals. However, there are other controls that are not so easily accounted for. For example, crystals in a magmatic

suspension tend to form chains or clusters (Philpotts et al., 1998) rather than acting individually, and have the potential to intergrow. These processes are less well understood, and their affects on viscosity calculations are not easily quantified. In addition, the magma as a whole may not act as a closed system (Edmonds, 2008). If gas is lost over time, for example if the magma becomes permeable (at a gas fraction around 30% Blower, 2001; Candela, 1991), or crystal-melt segregation occurs (Costa et al., 2006; Vigneresse et al., 1996), then the bulk properties of the system will not be appropriate for calculating the rheology of a small parcel of melt.

3.6.2 Implications of the model

The model presented here captures the first order physical processes involved in magma flow, with caveats given in section 3.6.1. It can therefore be used to understand the implications and importance of bubbles in controlling the flow of a crystal-rich lava or magma.

3.6.2.1 Lava flows

The majority of lavas have low crystal content (Marsh, 1981), and, as discussed in section 2.5.3, it is often observed that, with increasing crystal content (i.e. viscosity), lava morphology changes from pāhoehoe to ʻaʻā in basaltic systems (Peterson and Tilling, 1980). With the exception of lava domes, lavas with crystal contents above 50% are extremely rare (Marsh, 1981) due to their increasingly high viscosity. The results presented here indicate that for lavas with crystal content higher than about 30% the addition of bubbles can significantly lower their viscosities.

This leads to two suppositions: bubbly lavas with crystal contents higher than 50% may exist; and the pāhoehoe-ʻaʻā transition may occur at higher crystal contents for bubbly lavas than for non-bubbly lavas (see figure 3.18). In chapter 5, observations of extremely crystal-rich pāhoehoe lavas at Volcán Llaima, Chile, will be discussed. These lavas are some of the most crystal-rich known to exist, and flowed as both pāhoehoe and ʻaʻā in close proximity, indicating that they were close to the pāhoehoe-ʻaʻā transition. The lavas also form some unusual landforms, which can be related to their rheology.

The evolution of the physical properties of a less crystal-rich lava may also cause considerable changes in its flow behaviour and morphology. Quenched lava samples from Kīlauea, Hawaiʻi, are used to track the variations in dissolved volatile content and crystal populations as lava flowed away from the vent. Degassing-induced crystallization created several simultaneous changes in properties that control viscosity,

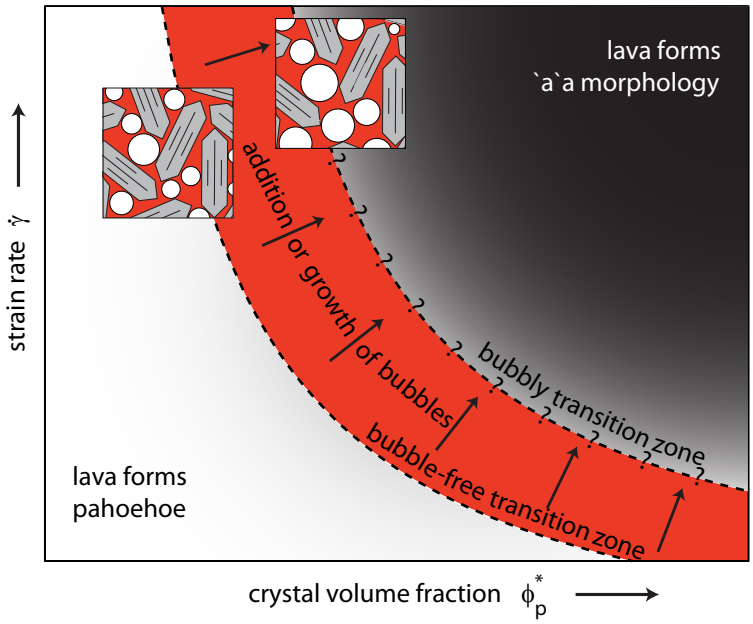

Figure 3.18: Schematic diagram showing the relationship between strain-rate and crystal volume fraction, split into regimes in which pāhoehoe or ‘a‘ā morphology form. This figure demonstrates how bubbly lava may be able to flow at higher strain rates and crystal fractions than bubble-free lava. The concept will be explored in detail in chapter 5.

and the model is used in chapter 6 to understand these changes and their control on morphology.

3.6.2.2 Magma reservoir state

Many large magma bodies are thought to spend a large proportion of their lifetimes as locked magma mushes (e.g. Cooper and Kent, 2014; Cashman and Giordano, 2014). A key question in volcanology is how these magma bodies — stored with crystal fractions at or above the maximum packing fraction — can mobilize and erupt in a short period of time. The model described here provides a simple, intuitive mechanism through which magma mushes can mobilize.

Although the experiments in this chapter only cover the range $0 \leq \phi_p^*/\phi_m \lesssim 0.85$, it can be postulated that similar results may be expected as ϕ_p^* approaches ϕ_m. If the pattern observed here continues, the addition of a small volume of bubbles will cause an increasingly large reduction in the viscosity of the suspension as the crystal fraction increases. The model (equation 3.2) predicts that for a crystal-rich fluid that is initially jammed (with $\phi_p^* = \phi_m$), adding bubbles — or creating a decrease in bulk crystal fraction such that $\phi_p < \phi_m$ — will allow the fluid to begin to flow.

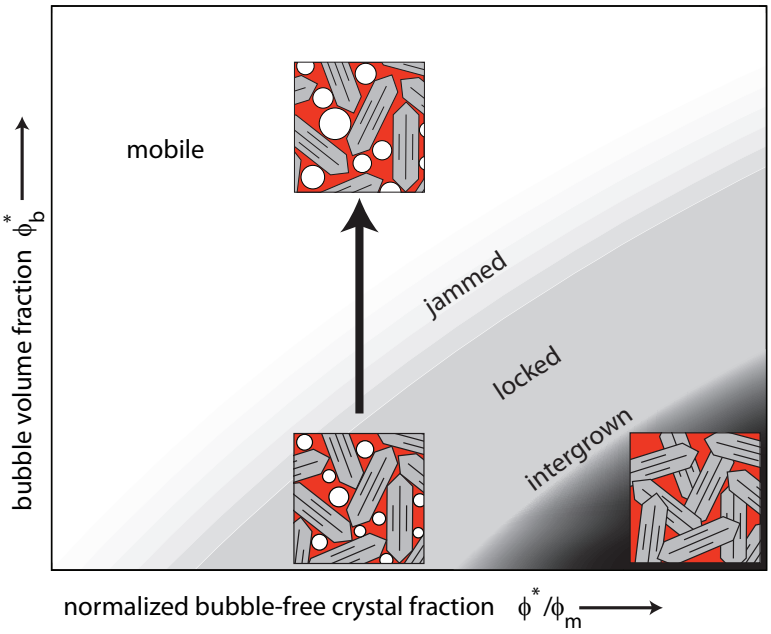

Figure 3.19: Schematic diagram showing bubble fraction against crystal fraction, and the ranges in which a suspension will contain intergrown, locked, or jammed crystals, or will be mobile and able to flow. The black arrow indicates the mobilization of an initially jammed or locked magma, through the growth of bubbles. The concept will be explored in detail in chapter 4.

This concept is demonstrated in figure 3.19.

In chapter 4, the results of analogue experiments that demonstrate this process are presented, and how realistic this mechanism may be in nature is discussed in detail. In order for this mechanism to work, bubbles must be able to grow in the interstitial melt in the mush, and the various inter-dependent properties of the magma must not act to increase viscosity more rapidly than the growing bubbles reduce viscosity. The circumstances in which bubble growth is expected to mobilize a magma are discussed in more detail in chapter 4.

3.6.3 How important are bubbles?

Many existing magma flow models work with the assumption that the crystals are the only important phase in determining viscosity, and that bubbles can be neglected. The model and experiments presented in this chapter demonstrates that in a three-phase suspension, bubbles can also have a significant affect on rheology. However, it may be the case that it is not always important to account for the — relatively complex — effects of bubbles. For example, at crystal fractions around 0.25 to 0.3, the addition of bubbles has very little effect on the viscosity.

The model can be used to quantify the importance of bubbles at various strain rates that are reasonable for magmatic systems. The difference in viscosity at a given strain rate calculated based on using a two-phase equation only, compared to using our three-phase equation, is shown in figure 3.20. This figure demonstrates that the likely error introduced by neglecting to account for the effect of bubbles on viscosity in any flowing system depends strongly on the strain rate it experiences,

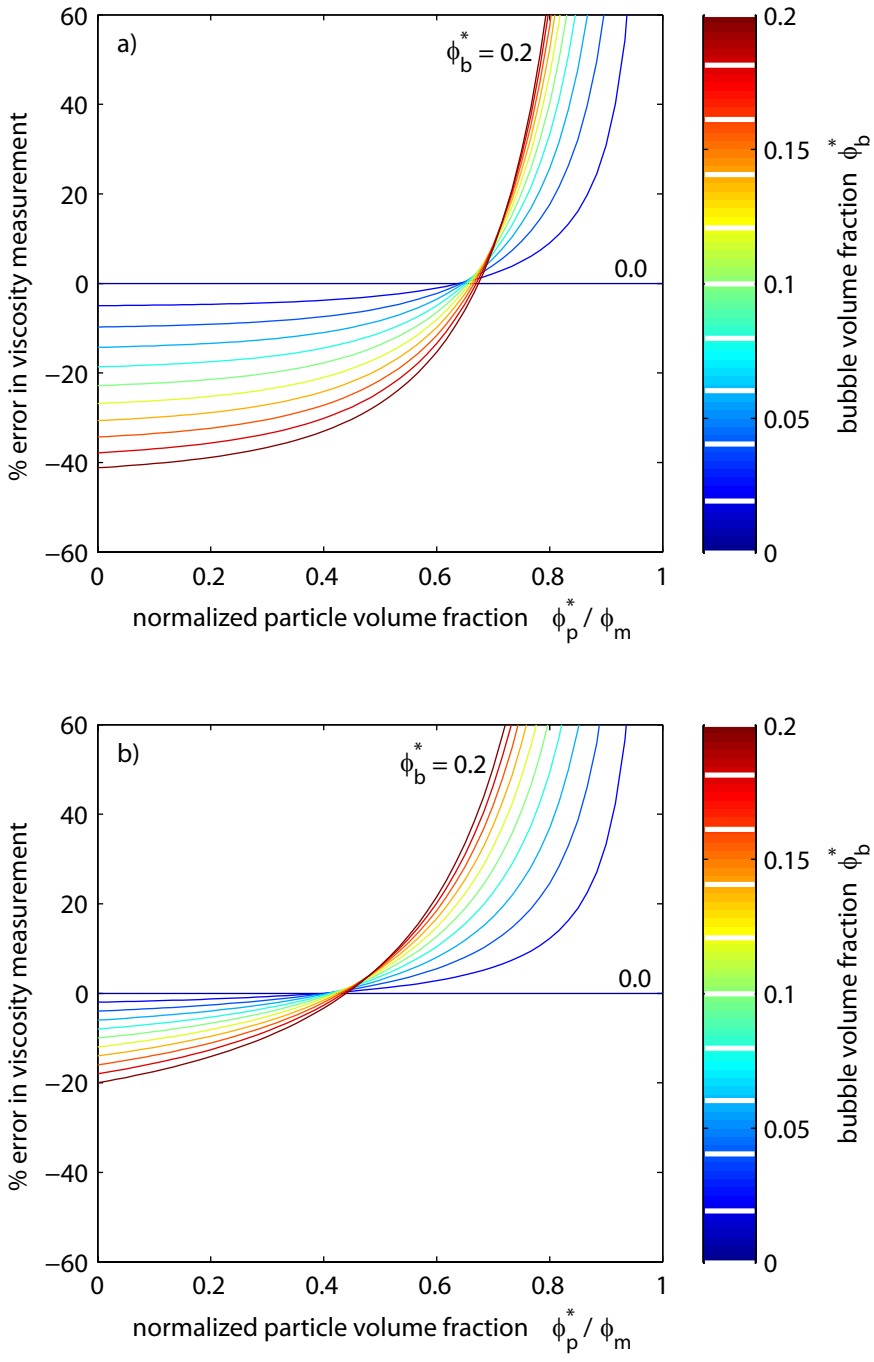

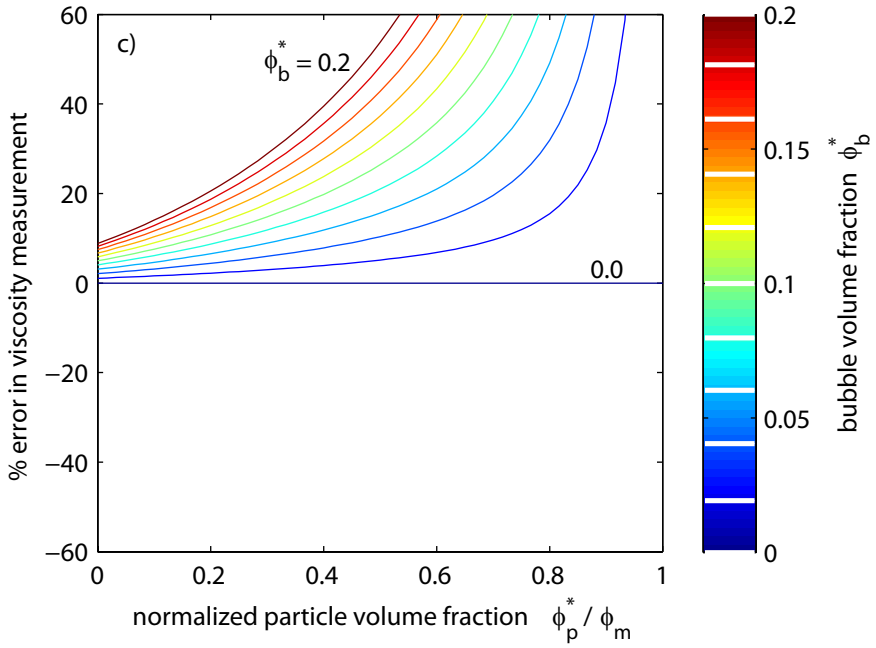

Figure 3.20: Percentage error in the viscosity estimate between using the three-phase model and ignoring the presence of bubbles, against ϕ_p^*/ϕ_m, shaded for ϕ_b^*. a) for strain rate of 0.01 s^{-1}, b) for strain rate of 1 s^{-1}, c) for strain rate of 100 s^{-1}.

and the volume of bubbles and crystals it contains.

In general, if the volume fraction of both bubbles and particles is low, the inclusion of the effect of bubbles will only change the outcome of a viscosity calculation by a small percentage. However, as the particle fraction approaches ϕ_m, neglecting even a very small percentage of bubbles can lead to a very large error.

3.7 Conclusions

These results demonstrate that the proposed three-phase rheological model (equation 3.2) based on an effective medium approach is in close agreement with experimental data over the full range ($0 \leq \phi_b^* \lesssim 0.3$ and $0 \leq \phi_p^*/\phi_m \lesssim 0.85$) investigated. The experiments involved spherical particles and steady flow in the low capillarity regime; hence, the model's validity is only demonstrated subject to these restrictions. The model's applicability is, however, potentially much broader (though extensions to the model require further experimental validation).

Mueller et al. (2011) demonstrate that the Maron-Pierce relationship (equation 2.11) is valid for suspensions of non-spherical particles when ϕ_m is calculated as a function of particle shape (equation 2.13). Adopting this methodology for equa-

tion 3.2 broadens its applicability to natural systems, in which particles are rarely spherical.

The low capillarity assumption can also be adapted. Substituting equation 2.6 for equation 2.5 in the formulation of equation 3.2 yields a three-phase model suitable for high-capillarity flows. This version of the model predicts that the addition of bubbles will always reduce the reference viscosity of a three-phase suspension, even when particle concentration is low. At high particle concentrations, the reduction in viscosity is much more dramatic than in the low capillarity case.

Removing the assumption of steady flow is more challenging because, whilst the rheology of bubble suspensions in unsteady flow is well known (Llewellin et al., 2002b; Llewellin and Manga, 2005), there is no adequate model for particle suspensions in unsteady flow.

The model developed in this study assumes that bubbles are small compared with particles, although the experimental data demonstrate that the model remains valid when bubbles and particles are comparable in size. Further experiments are required, however, to determine the rheology of suspensions in which bubbles are large compared with particles.

The proposed model for the flow index of three-phase suspensions (equation 3.19) also provides good agreement with experimental data for which $\phi_s \lesssim 0.5$. Since this model is purely empirical, the relationship between the coefficients found here and the physical properties of the material is not clear: without a physical explanation for the occurrence of shear thinning in bubble and particle suspensions, more work is still needed.

Taken as a whole, the model presented in this chapter is relevant for a wide range of magmatic systems, which commonly contain both bubbles and crystals. The results of this model imply that crystal-rich lavas may be able to flow more fluidally when they contain bubbles, and crystal-rich magmatic mushes may become mobile when bubbles grow in the interstitial melt. They also imply that complicated feedbacks may affect the viscosity of a lava as its physical properties evolve. These examples are the focus of chapters 4, 5, and 6, in which the importance of using a three-phase model when considering the flow of many magmatic fluids will be emphasised.

Chapter 4

Mobilization of a magma mush

4.1 Introduction

This chapter will focus on the eruptibility of extremely crystal-rich magmas, a topic that was introduced in chapter 2.5.2. At the end of chapter 3, it was proposed that the three-phase rheology model provided an explanation for the mobilization and eruption of large volumes of previously jammed magma mush. In this chapter, this model for mush mobilization will be presented in detail, and experiments will be described which demonstrate the fundamental processes involved.

Although the analogue experiments strongly support the model, the range of its applicability to natural magma reservoirs is key for emphasizing its use in volcanological settings. Discussion of the experimental results will therefore be followed by an extended discussion of how the model can be applied to natural magmas. Instead of focusing on a particular natural system, a hypothetical generalized magma reservoir will be introduced. This allows the general features and implications of the model to remain the focus of discussion, rather than the specifics of parameters relating to any given case study. It will be demonstrated that, in some circumstances, the mobilization model implies that the magma mush will become mobile and eruptible, whereas in others, the model predicts that the magma will remain jammed and uneruptible, as may be expected from the geological record in which many magmas evolve to form plutons rather than eruptions.

4.2 A model for mobilizing magma mush

It is proposed here that a jammed or locked crystal mush may be effectively mobilized through the *in situ* growth of small bubbles. The fundamental mechanism is simple

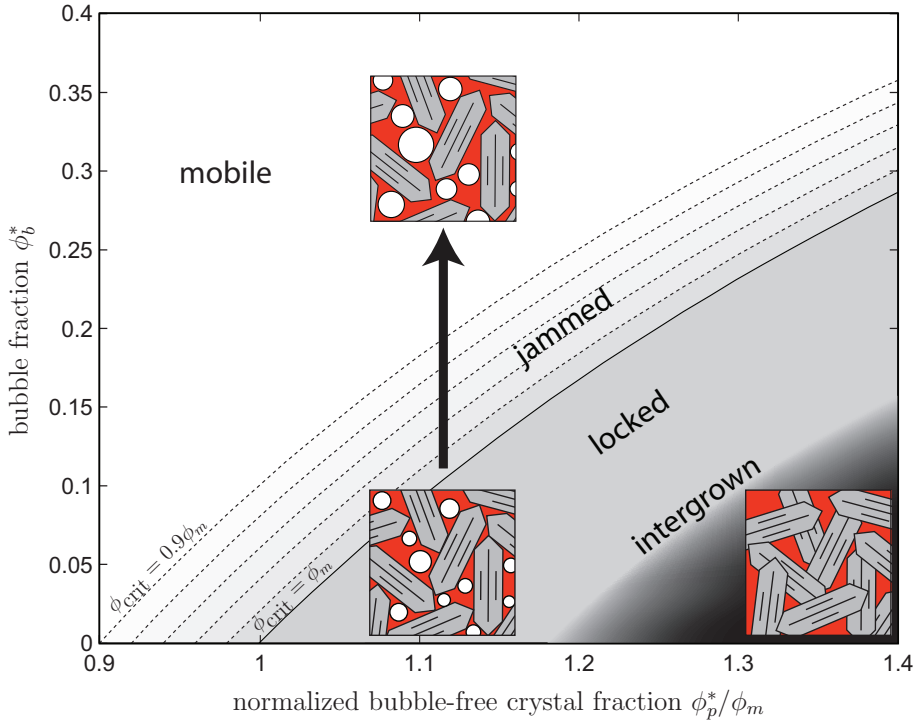

Figure 4.1: Mobility regimes, dependent on bubble fraction and initial crystal fraction. For $\phi_p < \phi_{\text{crit}}$ the magma is mobile; this is the case when $\phi_b^* > 1 - \phi_{\text{crit}}/\phi_p^*$. For $\phi_p \geq \phi_m$ the magma is locked; for $\phi_{\text{crit}} \geq \phi_p \geq \phi_m$ the magma is jammed. Bubble growth moves a magma in the direction of the arrow, and can mobilize a locked or jammed magma. If the crystals are strongly intergrown, then bubble nucleation or growth may be hindered and mobilization suppressed.

and intuitive: growth of bubbles pushes the crystals apart, reducing the bulk crystal fraction in the magma; when the crystal fraction falls below ϕ_{crit}, the magma can flow. Experiments by Pistone et al. (2013) using natural magmas show that the presence of bubbles in a crystal-rich magma strongly reduces its viscosity, supporting this conceptual model.

A magma is jammed while $\phi_p \geq \phi_{\text{crit}}$, and so the minimum fraction of bubbles that must grow in order to mobilize a magma with a given initial crystal fraction and critical crystal fraction is $\phi_{b,\text{min}}^* = 1 - \phi_{\text{crit}}/\phi_p^*$ (figure 4.1). Note that a locked magma ($\phi_p \geq \phi_m$) may also be mobilized via this mechanism, as long as the crystals are not strongly intergrown.

Once the magma is mobilized, its rheology will evolve with changing ϕ_b and ϕ_p according to the model presented in chapter 3. As the bubble fraction continues to grow (ϕ_b^* increases), the crystal fraction (ϕ_p) will be decreasing, leading to a reduction in the bulk viscosity.

4.3 Experiments

The hypothesis — that a jammed suspension will become mobile when the fraction of bubbles grows to a value such that $\phi_p < \phi_{\text{crit}}$ — was tested by performing rheometry on a three-phase, analogue suspension of air bubbles and spherical particles in a Newtonian liquid. The rheometry was performed under variable confining pressure, which in turn allowed the bubble fraction in the particle-rich suspension to be varied, and mimicks bubble growth in a magma mush. It should be noted that pressure changes were used in these experiments only to control the bubble volume fraction: the experimental pressures were not intended to be comparable to magmatic pressures. One advantage of using analogue materials and methods is that the fundamental effect of changing bubble fraction can be isolated from inter-related processes — such as nucleation, exsolution, volatile-dependent melt viscosity, and crystallization — that operate in a magma mush. Consequently, the experiments are designed to test only the fundamental process that underpins the model and eliminate the complexity associated with the natural magmatic system (section 2.4), not to simulate magma chamber processes in general.

4.3.1 Samples

The sample was prepared by adding a known mass of particles (in this case ballotini — spherical glass beads — with diameters 75 to 150 μm) to a known mass of Newtonian silicone oil (with viscosity 59.84 Pa s at experimental temperature 20°C). The mixture was then aerated with an electric hand-whisk. The initial bubble-free particle fraction was calculated, using the ballotini and oil densities, to be $\phi_p^* = 0.6000 \pm 0.0006$. Similarly, the bubble fraction was calculated, from volume measurements pre- and post-aeration, to be $\phi_b^* = 0.10 \pm 0.03$. A portion of the resulting suspension was used for the rheometric experiment, and an equal volume was reserved for imaging.

4.3.2 Rheometry

The apparent viscosity η of the first portion of the sample was measured using an Anton Paar MCR301 rheometer with pressure cell CC25/Pr150/ In/A1/SS. The sensor system was a purpose-made vane-spindle (six blades, 11.5 mm radius, 16 mm length) in a cylindrical cup (12.5 mm radius) (figure 4.2a). Since the sensor system was custom-made for these experiments, the conversion factors from torque to stress, and rotation rate to strain rate, cannot be calculated analytically (although

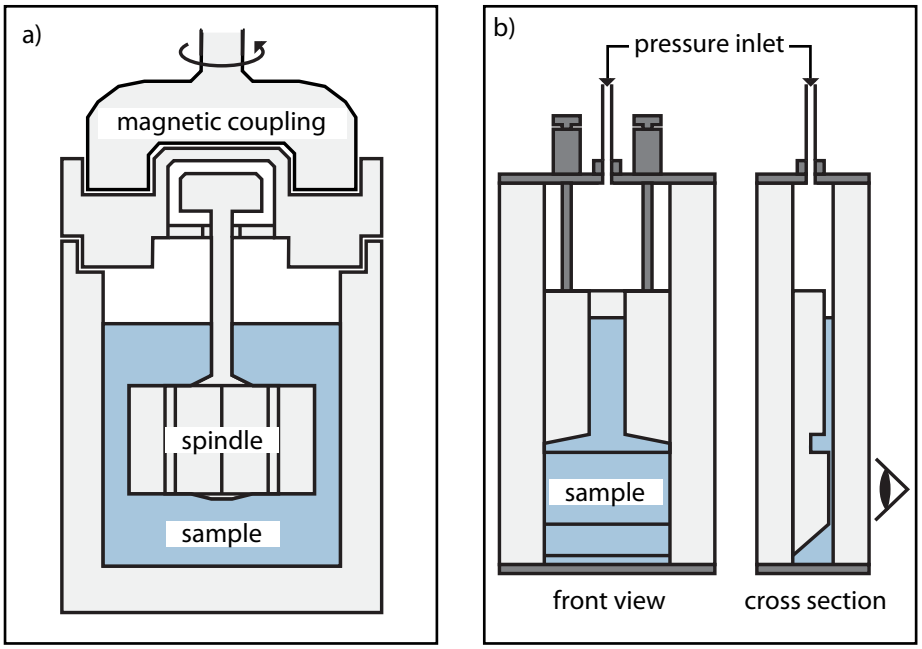

Figure 4.2: a) Sketch of rheometer internal geometry, showing cylindrical cup and vane spindle, inside pressurized cell (not to scale). b) The 'imaging cell' used to photograph samples held under the same pressure conditions as those in the opaque rheometer (not to scale).

approximations can be derived following Barnes and Carnali (1990)). Instead, the ratio of torque to rotation rate was calibrated for viscosity by performing flow curves of incrementally increasing then decreasing torque on two silicone oils with strictly Newtonian viscosities $\mu = 60.3\,\mathrm{Pa\,s}$ and $\mu = 816.7\,\mathrm{Pa\,s}$, respectively. The pressure-dependence of the viscosity of the silicone oil was found to be very small: viscosity increased by around 4% as pressure increased by a factor of four, as shown in figure 4.3. Throughout the experiment, temperature — measured by a thermocouple built into the sensor system — was maintained at $20.000 \pm 0.003°\mathrm{C}$ and no shear heating was observed.

In parallel with the rheometer was a transparent imaging cell (figure 4.2b), with internal geometry designed to mimic the rheometer sensor system, containing more of the same sample. This allowed the second portion of the sample to be imaged and volume changes to be observed in the bubbles as pressure changed (examples at 2 and 1 bars are shown in figure 4.4). Due to expansion of bubbles in the whole sample outside the field of view, there was significant movement of the sample between pressure steps. As a result, the number of bubbles that could be tracked from one step to the next was limited. Some coalescence was observed, but no bubbles were seen to nucleate during the course of the experiment. The material in the imaging cell was not subjected to rheometric shearing during the experiments. The bubble

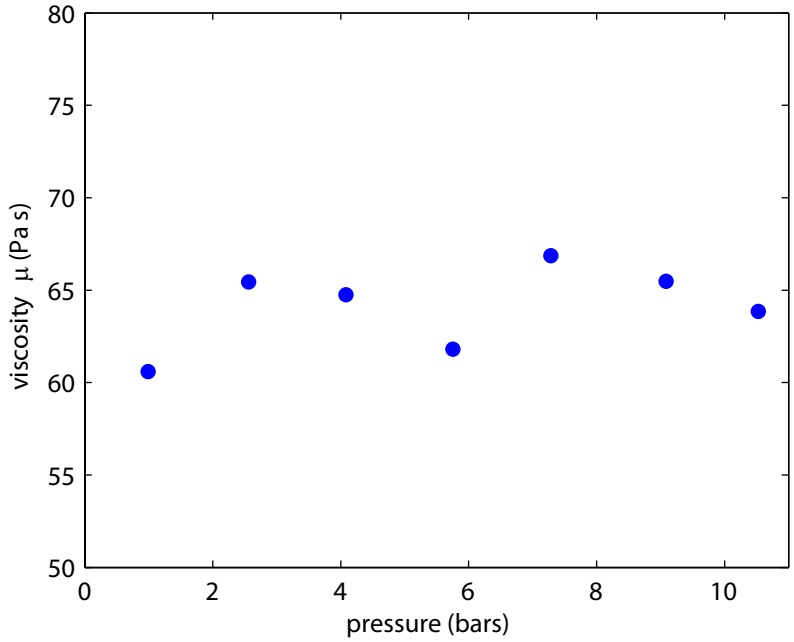

Figure 4.3: Measurements of the viscosity of pure silicone oil plotted against pressure.

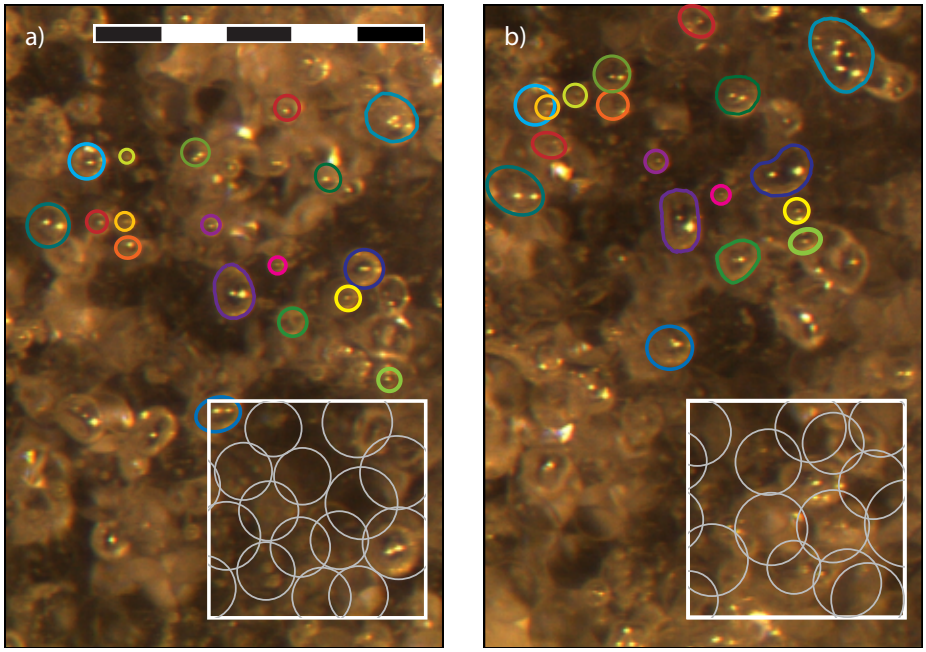

Figure 4.4: Photographs of the sample in the imagining cell, at a) 2 bars, and b) 1 bar. The bubbles are clearly visible, appearing as brighter spherical and elongate objects, and a number have been tracked between images: same bubble, same colour. The particles are very difficult to make out, tending to appear as faint arcs in the darker parts of the image; those in a selected region in each figure are circled in grey. The scale bar is 500 μm, and the depth of view is approximately 0.5 mm.

fraction under pressure P was calculated, assuming the isothermal ideal gas law, as: $\phi_b^* = P_0\phi_{b0}^*/(P(1-\phi_{b0}^*)+P_0\phi_{b0}^*)$, where ϕ_{b0}^* is the bubble fraction at reference pressure P_0. Experimental uncertainty in ϕ_b^* was $\pm 30\%$, but note that this was a systematic uncertainty due to the error on the measurement of the bubble fraction at pressure P_0 — random errors were expected to be small. Pressures and corresponding bubble (ϕ_b^*) and particle (ϕ_p) volume fractions are summarized in table 4.1.

Pressure	Bubble fraction ϕ_b^*	Particle fraction ϕ_p
4.0	0.027	0.584
3.8	0.028	0.583
3.7	0.029	0.582
3.5	0.031	0.581
3.3	0.033	0.580
3.0	0.035	0.579
2.9	0.037	0.578
2.7	0.040	0.576
2.5	0.043	0.574
2.2	0.047	0.572
2.0	0.052	0.569
1.8	0.057	0.566
1.6	0.064	0.562
1.4	0.073	0.556
1.2	0.084	0.550
1.0	0.100	0.540

Table 4.1: List of experimental pressures, and corresponding bubble and particle volume fractions, rounded to three decimal places.

Once the sample was placed in the rheometer and imaging cell the system was pressurized to 4 bars, using argon, and controlled with a pressure regulator. A constant shear stress was then imposed on the sample by setting the torque on the vane spindle to a value of 5 mN m throughout, and the rotation rate of the vane spindle was recorded by the rheometer every second. Every hundred seconds, the pressure was reduced manually by roughly 0.2 bars as rapidly as possible (typically in less than 10 seconds). This step duration was chosen to be short enough that particles did not sink more than one particle radius during each step. This was repeated until ambient pressure was reached.

The duration of the experiment was short enough that bubble rise was negligible, and the bubble volume fractions were not high enough for the development of permeability. As such, it is expected that very few bubbles were lost during the experiment.

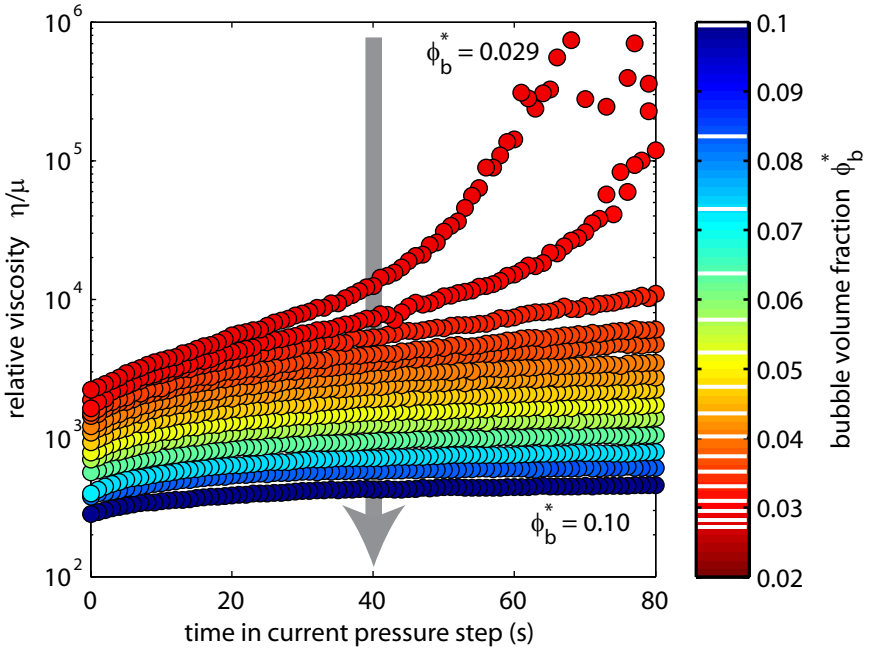

Figure 4.5: The relative apparent viscosity of the sample at a given pressure and bubble fraction, plotted against time in the relevant isobaric run. The grey arrow indicates the effect of increasing bubble fraction through bubble growth.

4.3.3 Results

Figure 4.5 plots the relative viscosity of the sample ($\eta_r = \eta/\mu$, where η is the suspension viscosity and μ is the liquid viscosity) over time, for isobaric runs at pressures between 3.7 bars ($\phi_b^* = 0.029$) and 1 bar ($\phi_b^* = 0.100$). For the highest pressure shown in figure 4.5, the viscosity of the sample increases dramatically over the course of the isobaric run (note logarithmic scale). Towards the end of this run, very small or negative rotation rates are observed, indicating that the sample viscosity is above the rheometer's range. The same pattern is seen for the next highest pressure (3.5 bars, $\phi_b^* = 0.031$). Runs at 4.0 bars ($\phi_b^* = 0.027$) and 3.8 bars ($\phi_b^* = 0.028$) yield even higher viscosities, but these are not shown because of very large scatter, indicating viscosities above the rheometer's range. By contrast, the viscosities for runs at 3.3 bars ($\phi_b^* = 0.033$) and lower tend towards finite values, indicating that the sample is flowing as a viscous liquid (although it should be noted that the run at 3.3 bars may not have reached steady state).

Figure 4.6 shows the cumulative strain γ in the sample over time, for four isobaric runs: 4.0 bars ($\phi_b^* = 0.027$); 3.7 bars ($\phi_b^* = 0.029$); 3.3 bars ($\phi_b^* = 0.033$); and 2.9 bars ($\phi_b^* = 0.037$). Each curve starts at $\gamma = 0$ at the time when the pressure

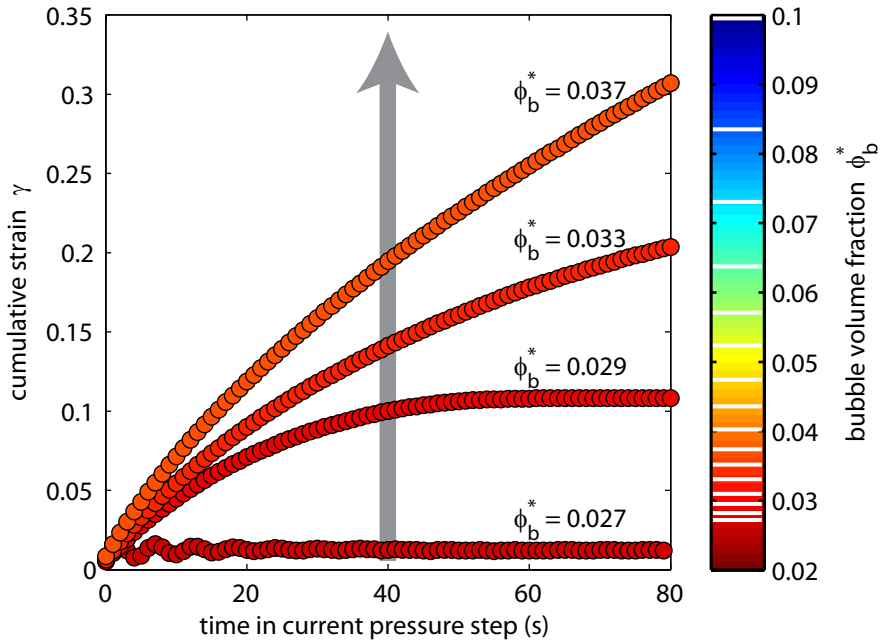

Figure 4.6: The cumulative strain in an isobaric run, plotted against time, for four selected pressures (4.0, 3.7, 3.3, and 2.9 bars), coloured according to bubble volume fraction ϕ_b^* at that pressure. The grey arrow indicates the effect of increasing bubble fraction through bubble growth.

reaches its new value following a pressure drop. The strain is approximated following Barnes and Carnali (1990). The viscosity drops considerably in response to the decompression at the end of each isobaric run. This is particularly noticeable for runs in which the sample was jammed at the end of the run — in these cases, the sample flows briefly in response to the pressure drop, before jamming again. In figure 4.6, the plot for 4.0 bars ($\phi_b^* = 0.027$) demonstrates that the sample is essentially static throughout the run — the cumulative strain shows decaying oscillations around a small, fixed value of γ. When pressure is dropped to 3.7 bars ($\phi_b^* = 0.029$), the sample deforms slightly over 40–50 seconds, then stops deforming once a small strain (around 0.1) is reached. At pressures of 3.3 and 2.9 bars ($\phi_b^* = 0.033$ and $\phi_b^* = 0.037$) the strain does not reach a constant value; rather it tends towards constant strain rate ($\dot{\gamma}$).

4.4 Discussion

Although the data in section 4.3.3 are presented in terms of pressures and the corresponding bubble volume fractions, it is important to emphasise that these pressure changes are purely used to control the bubble volume fraction: they are not intended

to replicate magmatic pressures. In this discussion, the focus is therefore on particle fraction and corresponding bubble fraction, rather than pressure and corresponding bubble fraction.

At the highest particle fractions (not shown in figure 4.5), $\phi_p = 0.584$ ($\phi_b^* = 0.027$) and $\phi_p = 0.583$ ($\phi_b^* = 0.028$), the viscosity of the sample was beyond the rheometer's measurable range. This has two potential implications: it is possible that the yield stress for these particle fractions was higher than the applied stress, and so the sample was unable to flow; equally, it is possible that the viscosity was simply too high to be measured. In either case, the sample can definitely be viewed as jammed at these high particle fractions. This is supported by the observation that no strain accumulates during these runs (figure 4.6).

As the particle fraction was reduced as a result of bubble growth, a slightly different pattern was observed. For runs with $\phi_p = 0.583$ ($\phi_b^* = 0.029$) and $\phi_p = 0.581$ ($\phi_b^* = 0.031$), the sample is able to flow briefly, but the rheometer indicates increasingly high viscosities towards the end of the run. This is supported both by the measurable viscosities for these runs in figure 4.5, and the accumulation of a finite amount of strain in figure 4.6. This can be interpreted to show that bubble growth — resulting from the pressure drop — pushes the jammed particles apart, allowing some flow; after a small strain the particles come back into contact, jamming the suspension once again. The amount of strain is very small, indicating that although the suspension is able to move very slightly in response to the bubble growth, it is unable to truly flow, and is still jammed.

At lower particle fractions, the sample flows with a measurable viscosity throughout the run (figure 4.5) and approaches a constant rate of accumulation of strain by the end of the run (figure 4.6). These observations indicate viscous flow of a mobile suspension.

It is concluded that the sample is jammed when the particle fraction $\phi_p \geq 0.581$ ($\phi_b^* \leq 0.031$), and mobile when $\phi_p = 0.580$ ($\phi_b^* \geq 0.033$), giving $\phi_c \approx 0.581$ ($\phi_{b,\min}^* \approx 0.032$). The maximum packing fraction for a monodisperse suspension of smooth spheres under shear is $\phi_m = 0.633$ (Mueller et al., 2010), which is higher than the highest particle fraction ($\phi_p = 0.584$) achieved in these experiments at 4 bars pressure. The implication of the experimental observations is that $\phi_{\text{crit}} < \phi_m$, as expected; in this case, the sample becomes mobile at $\phi_{\text{crit}} \approx 0.917\phi_m$.

For runs in which the viscosity approached a fixed, finite value, the final measurement of the run was taken as an approximation to that value. These values are plotted in figure 4.7, which demonstrates the transition from immobile to mobile suspension as bubbles grow and the subsequent reduction in viscosity observed with

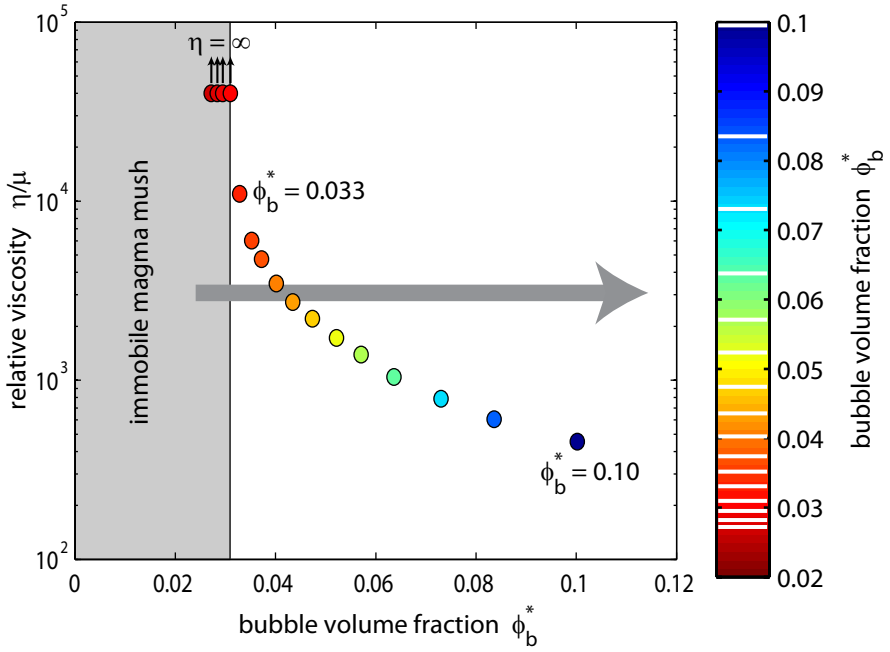

Figure 4.7: The asymptotic (long time) relative viscosity for each bubble fraction (pressure). Bubble fractions at which the suspension is immobile are indicated by the grey area. The grey arrow indicates the effect of increasing bubble fraction through bubble growth.

increasing bubble fraction.

4.5 Applying the model to a “typical” magma mush

The nucleation and growth of bubbles requires that the melt phase must become saturated in volatile species (typically H_2O and CO_2 are the most important). Nucleation and growth of bubbles is promoted by decompression, heating, or crystallization of anhydrous crystal phases in the magma reservoir. An additional consequence of bubble growth is that the bulk density of the magma decreases. The growth of bubbles, therefore, can both unjam the magma and provide the buoyancy required to initiate its eruption (Blake, 1984). In many natural systems, however, mushes do not erupt in their entireity — some undergo segregation, erupting only the crystal-poor portions, and others never erupt at all (Cashman and Giordano, 2014). Here the circumstances in which bubble growth is likely to lead to eruption are discussed, along with conditions under which bubble growth is either insufficient to mobilize the magma or is unable to occur.

4.5.1 Conditions in the reservoir

Instead of attempting to explain any one particular eruption, this discussion is framed around a hypothetical magma mush, using typical parameters from well-studied magma reservoirs to inform the discussion. A number of scenarios are introduced, in which the mush may or may not erupt. This demonstrates the range of applicability of the model, and conditions under which bubble growth will fail to trigger an eruption, in addition to those in which the magma is mobilized.

4.5.1.1 Pressure

Current understanding of the structure of magma reservoirs indicates that many are formed from numerous lenses of melt, with a pressure difference of up to 130 MPa (Cashman and Giordano, 2014) within a single magma reservoir. Therefore magmatic conditions may vary considerably with depth. This discussion will therefore focus on pockets of magma crystallizing at different depths and pressures within a single hypothetical magma system.

Bachmann and Bergantz (2006) consider a range of pressures from 100-400 MPa when modelling the Fish Canyon Tuff reservoir. This range encompasses numerous other calculated magma chamber pressures (e.g. Cerro Galán, Argentina (Folkes et al., 2011); Bishop Tuff, USA (Gualda and Ghiorso, 2013); Lund Tuff, USA (Maughan et al., 2002)), and is therefore adopted for this investigation. Two extreme scenarios to consider are a "shallow" reservoir at 100 MPa (≈3.8 km depth for country rock density 2.7 kg m^{-3}), and a "deep" reservoir at 400 MPa (≈15.1 km depth).

4.5.1.2 Temperature

Temperature may vary within a magma reservoir, and may also change over time. In this hypothetical scenario, a reservoir temperature of 720°C will be considered, again based on the Fish Canyon Tuff (Bachmann and Bergantz, 2003), and supported by similar values from other reservoirs (e.g. Bishop Tuff, USA (Gualda and Ghiorso, 2013); Lund Tuff, USA (Maughan et al., 2002); eruptions from Mount Hood, USA (Cooper and Kent, 2014)).

4.5.1.3 Pre-eruptive crystallinity

It has been suggested that many magma reservoirs spend a significant portion of their lifetimes with crystal contents high enough that they would have been rheologically

immobile (e.g. Cooper and Kent, 2014). In the literature, values of 0.5 to 0.6 have been suggested for pre-eruptive crystallinity (e.g. Bachmann and Bergantz, 2006), and a typical value of $\phi_p = 0.55$ will be used here.

4.5.1.4 Maximum packing fraction

The aspect ratios of phenocrysts in natural magmas are variable, but commonly less than 5 (e.g. Mock and Jerram, 2005). Values around 2 seem typical, based on photomicrographs (e.g. as discussed for Volcán Llaima lavas that contain plagioclase (40-50%) and olivine (6-7%) in chapter 5.4, and for the Fish Canyon Tuff magma, containing predominantly feldspars (30-40%), quartz (3-5%), hornblende (3-5%) and biotite (3-5%), in Bachmann et al. (2002)). Using equation 2.13, the maximum packing fraction for a magma with aspect ratios around $r_p = 2$ is $\phi_m = 0.526$.

Based on the crystallinity and maximum packing fraction in this hypothetical magma chamber, and the model presented in section 4.2, at least $\phi^*_{b,\min} = 4.36$ vol.% bubbles must grow in order for the magma to become mobile such that $\phi_p < \phi_m$ and hence $\eta < \infty$. Further growth of bubbles would then lead to a reduction in viscosity, as described in chapter 3.

4.5.1.5 Composition

The composition of a magma controls its melt viscosity and density. Composition is highly variable in natural systems, and may vary throughout the course of a single eruption, between different eruptions, and between different volcanoes. As a basis for discussion, the major oxide composition of rhyolitic glass in crystal-rich Fish Canyon magma will be used (table 4.2, from Bachmann et al., 2002).

SiO_2	TiO_2	Al_2O_3	FeO	MnO	MgO	CaO	Na_2O	K_2O	P_2O_5	F_2O_{-1}
77.28	0.13	13.23	0.66	0.03	0.07	0.56	3.60	4.41	0.01	0

Table 4.2: Composition of rhyolitic glass from crystal-rich Fish Canyon Tuff (Table 7, Bachmann et al., 2002) normalized to 100% anhydrous.

4.5.1.6 Water content

Magma reservoirs contain a wide range of water contents, depending primarily on their composition and tectonic setting. The water content in rhyolitic systems typically ranges from 2-5 wt.% (e.g. Anderson et al., 2000).

4.5.2 Calculation procedure

Calculating the viscosity of a magma requires a large number of inputs, which were given in section 4.5.1. For each hypothetical magma reservoir, the following procedure is used to calculate the viscosity of the magma at a range of dissolved volatile contents, in order to assess whether or not the magma will become mobile. It is important to note that throughout these calculations, it is assumed that bubbles are able to exsolve and grow, and are not limited by the volume of the magma chamber. This is equivalent to the unconstrained sample volume in the experiments, and the limitations of this approach are discussed more in section 4.5.7.

The first step in calculating the viscosity of the magma is to calculate the viscosity of the interstitial melt. The equations of Giordano et al. (2008) are used for this purpose, and are described here for convenience. The viscosity is found using:

$$\log \mu = A + \frac{B}{T(\mathrm{K}) - C}, \tag{4.1}$$

and the parameters A, B, and C are given by:

$$A = -4.55, \tag{4.2}$$

$$B = \sum_{i=1}^{7} [b_i M_i] + \sum_{j=1}^{3} [b_{1j} M_{1j}], \tag{4.3}$$

and

$$C = \sum_{i=1}^{6} [c_i N_i] + [c_{11} N_{11}], \tag{4.4}$$

where the coefficients b_i, b_{1j}, c_i and c_{11} and combinations of oxides (in mol%) M_i, M_{1j}, N_i, N_{11} are listed in table 4.3. In order to draw useful comparisons between models, the melt viscosity is normalised to the initial melt viscosity μ_0; in all cases, as the dissolved water content decreases the melt viscosity increases more and more rapidly as the water content approaches zero.

The volume of bubbles produced must then be calculated based on changes in the dissolved volatile content. First, the molar density of water at the appropriate pressure and temperature is calculated, using the equations of Pitzer and Sterner (1994), described here for convenience. The molar density is found by solving (using

coefficient	value	M/N	corresponding oxides
b_1	159.6	M_1	SiO_2 + Ti_2O
b_2	-173.3	M_2	Al_2O_3
b_3	72.1	M_3	FeO(T) + MnO + P_2O_5
b_4	75.7	M_4	MgO
b_5	-39.0	M_5	CaO
b_6	-84.1	M_6	Na_2O + H_2O + F_2O_{-1}
b_7	141.5	M_7	H_2O + F_2O_{-1} + ln(1 + H_2O)
b_{11}	-2.43	M_{11}	(SiO_2 + TiO_2)*(FeO(T) + MnO + MgO)
b_{12}	-0.91	M_{12}	(SiO_2 + TiO_2 + Al_2O_3)*(Na_2O + K_2O + H_2O)
b_{13}	17.6	M_{13}	(Al_2O_3)*(Na_2O + K_2O)
c_1	2.75	N_1	SiO_2
c_2	15.7	N_2	TiO_2 + Al_2O_3
c_3	8.3	N_3	FeO(T) + MnO + MgO
c_4	10.2	N_4	CaO
c_5	-12.3	N_5	Na_2O + K_2O
c_6	-99.5	N_6	ln(1 + H_2O + F_2O_{-1})
c_{11}	0.30	N_{11}	(Al_2O_3 + FeO(T) + MnO + MgO + CaO - P_2O_5)* (Na_2O + K_2O + H_2O + F_2O_{-1}

Table 4.3: Coefficients and combinations of oxides for equations 4.3 and 4.4, from Giordano et al. (2008).

MATLAB's "solve" function) the equation:

$$P/RT = \rho + c_1\rho^2 - \rho^2\left[\frac{c_3 + 2c_4\rho + 3c_5\rho^2 + 4c_6\rho^3}{(c_2 + c_3\rho + c_4\rho^2 + c_5\rho^3 + c_6\rho^4)^2}\right] + c_7\rho^2\exp(-c_8\rho) + c_9\exp(-c_{10}\rho), \quad (4.5)$$

where P is the pressure, T is the temperature, R is the gas constant, ρ is the molar density, and each coefficient c_i is a polynomial in temperature:

$$c_i = c_{i,1}T^{-4} + c_{i,2}T^{-2} + c_{i,3}T^{-1} + c_{i,4} + c_{i,5}T + c_{i,6}T^2. \quad (4.6)$$

The coefficients fitted by Pitzer and Sterner (1994) are given in table 4.4. This molar density is then used to calculate the volume of water exsolved, which is in turn used in combination with the melt density (calculated using Pering (2013), which is based on Bottinga and Weill (1970)) to calculate the volume fractions ϕ_b, ϕ_b^*, ϕ_p and ϕ_p^*.

It is assumed that the bubbles in this magma are in the low capillarity regime. Although this assumption may not be true once the magma starts moving (and the shear rate increases, increasing the capillarity — equation 2.2), it will provide an upper bound on the viscosity. As the bubbles shift into the high capillarity regime,

i	$c_{i,1}$	$c_{i,2}$	$c_{i,3}$	$c_{i,4}$	$c_{i,5}$	$c_{i,6}$
1	0	0	0.24657688E+6	0.51359951E+2	0	0
2	0	0	0.58638965	-0.28646939E-2	0.31375577E-4	0
3	0	0	-0.6278380E+1	0.14791599E-1	0.35779579E-3	0.15432925E-7
4	0	0	0	-0.42719875	-0.16325155E-4	0
5	0	0	0.56654978E+4	-0.16580167E+2	0.76560762E-1	0
6	0	0	0	0.10917883	0	0
7	0.38878656E+13	-0.13494878E+9	0.30916564E+6	0.75591105E+1	0	0
8	0	0	-0.65537898E+5	0.18810675E+3	0	0
9	-0.14182435E+14	0.18165390E+9	-0.19769068E+6	-0.23530318E+2	0	0
10	0	0	0.92093375E+5	0.12246777E+3	0	0

Table 4.4: Coefficients c_i for equations 4.5 and 4.6, from Pitzer and Sterner (1994).

it is expected that the viscosity would drop more dramatically than predicted here — thus the results given in the following sections are likely to be minimum estimates of the viscosity drop expected due to the growth of bubbles.

The analogue experiments presented in chapter 3 validated an equation for the viscosity of a three-phase suspension in which:

- the bubbles are smaller than the particles
- the bubbles are in the low capillarity regime.

This relationship (equation 3.2) is repeated here for convenience:

$$\eta_{r,*} = (1 - \phi_b)^{-1} \left(1 - \frac{\phi_p}{\phi_m}\right)^{-2}, \tag{4.7}$$

and is used to calculate the relative viscosity of the magma, based on the bubble and crystal fractions calculated earlier. Based on equation 2.1, the absolute viscosity can then be calculated:

$$\eta_* = \eta_{r,*}\mu. \tag{4.8}$$

In order to present this information, the bubble and crystal volume fractions, and melt and magma viscosities are plotted against dissolved volatile content. At high dissolved volatile content, few or no bubbles have grown; as the dissolved volatile content decreases, an increasing volume of bubbles are assumed to grow, leading to changes in the volume fractions and viscosities. In some circumstances, this growth will be sufficient to render the magma mobile; in others, it will either be insufficient, or prevented altogether by the solubility of water in the melt.

The conditions used for the various hypothetical magma reservoirs are summarized in table 4.5.

Name of model	Pressure (MPa)	Total water (wt.%)	Melt water at 55% crystallinity (wt.%)	equilibrium solubility (wt.%)
shallow, wet	100	5	11.1	4.29
deep, wet	400	5	11.1	10.47
deep, dry	400	2	4.44	10.47

Table 4.5: Conditions for each hypothetical magma reservoir.

4.5.3 Anhydrous crystallization in a shallow, wet magma reservoir

Many silicic magmatic systems crystallize predominantly anhydrous crystal phases such as feldspars and quartz. In some, volatiles may become sufficiently saturated in the melt as a result that they begin to exsolve (second boiling). In this first example, the magma reservoir is assumed to be shallow (100 MPa) and wet (5 wt.% water).

Based on these initial conditions, if 55 vol.% anhydrous phases have crystallized, then the water concentration in the remaining melt would be 11.1 wt.%. At 100 MPa and 720°C, the solubility of water in rhyolite is approximately 4.29 wt.% (using Newman and Lowenstern, 2002). If bubbles of water are able to nucleate and grow, the dissolved water content would be reduced from 11.1 wt.% to 4.29 wt.%. It should be noted that in reality, a magma is unlikely to reach this degree of supersaturation without exsolving some volatiles - the exsolution process would likely be concurrent with crystallization. However, if no bubbles escape, the same total volume will be produced whether exsolution happens incrementally or in one go. The important quantity for this model is the total volume of water exsolved, and so the problem is simplified here by assuming exsolution to a given water content happens in a single stage. The method for calculating the effect of a given amount of exsolution is detailed in section 4.5.2. The expected bubble and crystal volume fractions produced in this hypothetical reservoir are plotted against the remaining dissolved water content in figure 4.8a.

Assuming that there is negligible volume change in the melt, the total resulting bubble volume fraction will be $\phi_b^* = 0.177$, with $\phi_p = 0.453$, when the melt has reached equilibrium solubility (4.29 wt.%). Since the growth of this volume of bubbles is sufficient to drop the crystal volume fraction below the maximum packing fraction, the magma may become mobile.

However, counteracting the reduction in bulk magma viscosity due to bubble growth is an increase in the melt viscosity due to decreasing dissolved water content, calculated as described in section 4.5.2. Figure 4.8b demonstrates how these two effects interact: once the magma is mobilized, growth of bubbles leads to a decrease in the magma viscosity, however just before reaching equilibrium solubility, the bulk viscosity begins to increase again due to increasing melt viscosity. If further exsolution were to occur past equilibrium, the magma viscosity would continue to increase, and would make flow extremely unlikely. At this point, the magma would be essentially immobile again, due to high melt viscosity rather than being jammed.

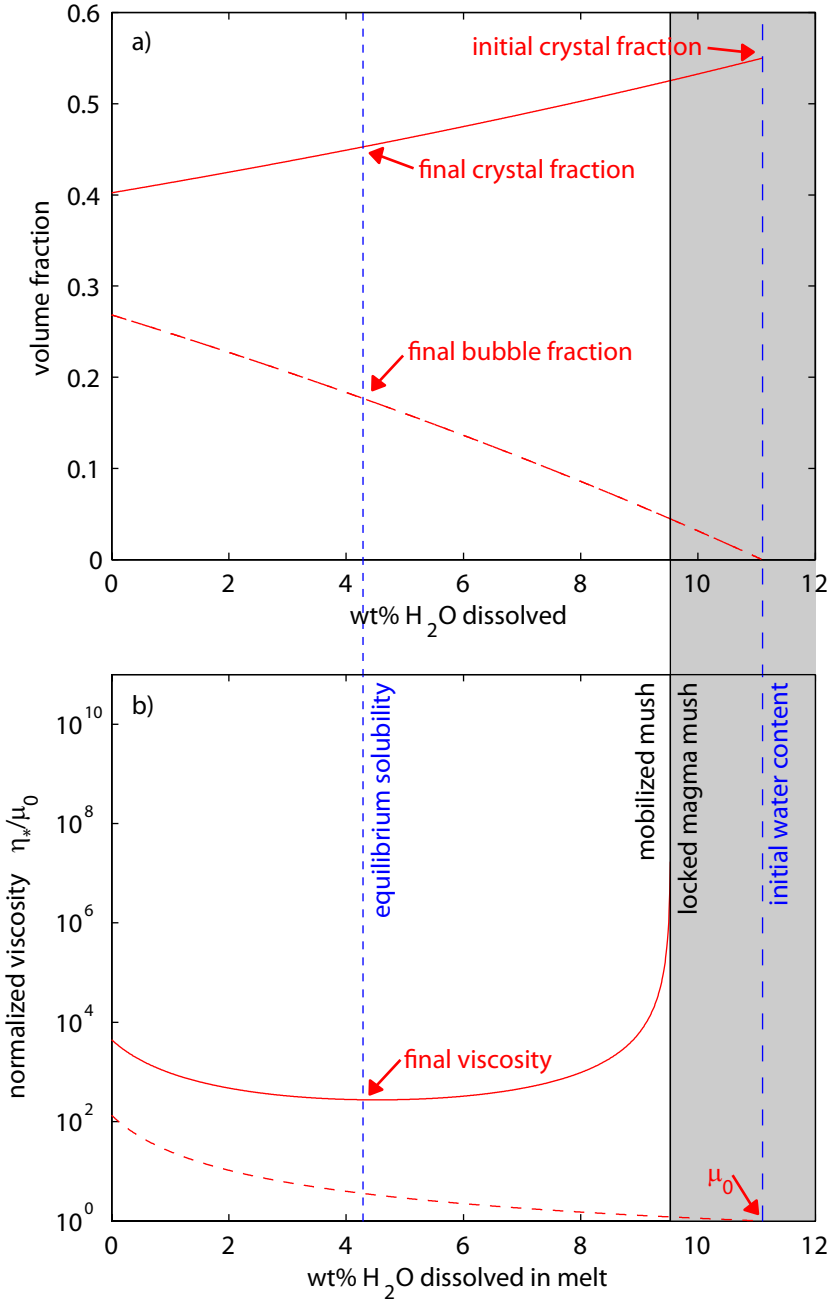

Figure 4.8: Magma evolution with dissolved water for a shallow (100 MPa), wet (5 wt.% H_2O) rhyolite magma chamber. a) Crystal fraction (ϕ_p, solid red curve), bubble fraction (ϕ_b^*, dashed red curve); b) melt viscosity (μ/μ_0, dashed red curve), bulk magma viscosity (η_*/μ_0, solid red curve, from equation 3.2) against dissolved water. Grey region indicates locked magma. Blue dashed line is water content at 55% crystals; bubbles exsolve and grow until melt reaches equilibrium solubility (dotted blue line), at which point magma becomes mobile.

4.5.4 Anhydrous crystallization in a deep, wet magma reservoir

If the same magma was present in a deeper reservoir, volatile exsolution due to anhydrous crystallization may not have the same effect. At 400 MPa, the solubility

of water is much higher — 10.47 wt.% in the hypothetical rhyolitic magma (using Newman and Lowenstern, 2002). Again following the process described in section 4.5.2, the volume of bubbles exsolved and corresponding viscosity changes can be assessed in this situation.

Due to the higher water solubility, a much smaller volume of bubbles will grow before equilibrium saturation is reached (figure 4.9a). This will happen before the volume fraction of bubbles is sufficient to mobilize the mush: despite bubble growth, the mush will remain immobile (figure 4.9b). Although further anhydrous crystallization would increase the dissolved water content further, and lead to more exsolution, the crystals are more likely to be intergrown. By calculating the water content remaining in the melt as crystallization continues, once the magma has crystallized to 66%, the resulting water content would be just sufficient that exsolution until the melt reaches its equilibrium solubility would produce enough bubbles to mobilize the mush. However, at 66% crystals, the mush will have a significant mechanical strength. Should bubbles begin to exsolve at this point, it is unlikely that they would be able to disaggregrate the intergrown crystals.

4.5.5 Anhydrous crystallization in a deep, dry magma reservoir

A second counterpoint to the example presented in section 4.5.3 is a deep magma chamber (400 MPa) with a lower initial dissolved volatile content (2 wt.% water). As in section 4.5.4, the equilibrium solubility of water will be much higher than in the shallow case. The water concentration produced by anhydrous crystallization to 55% crystals will be much lower, however, at only 4.44 vol.%. This is considerably lower than the solubility of water in the reservoir, and so no bubbles will exsolve at all (figure 4.10). In this case, the mush is highly unlikely to ever be mobilized through this mechanism.

4.5.6 Other scenarios

4.5.6.1 Temperature perturbations

In many cases, both published numerical models (e.g. Burgisser and Bergantz, 2011; Bachmann and Bergantz, 2006; Huber et al., 2010) and petrological evidence (e.g. Bachmann and Bergantz, 2003; Murphy et al., 2000) indicate a small pre-eruptive temperature rise within magma reservoirs, often due to the addition of a recharge magma. This temperature rise may partially melt the mush, reducing the crystal

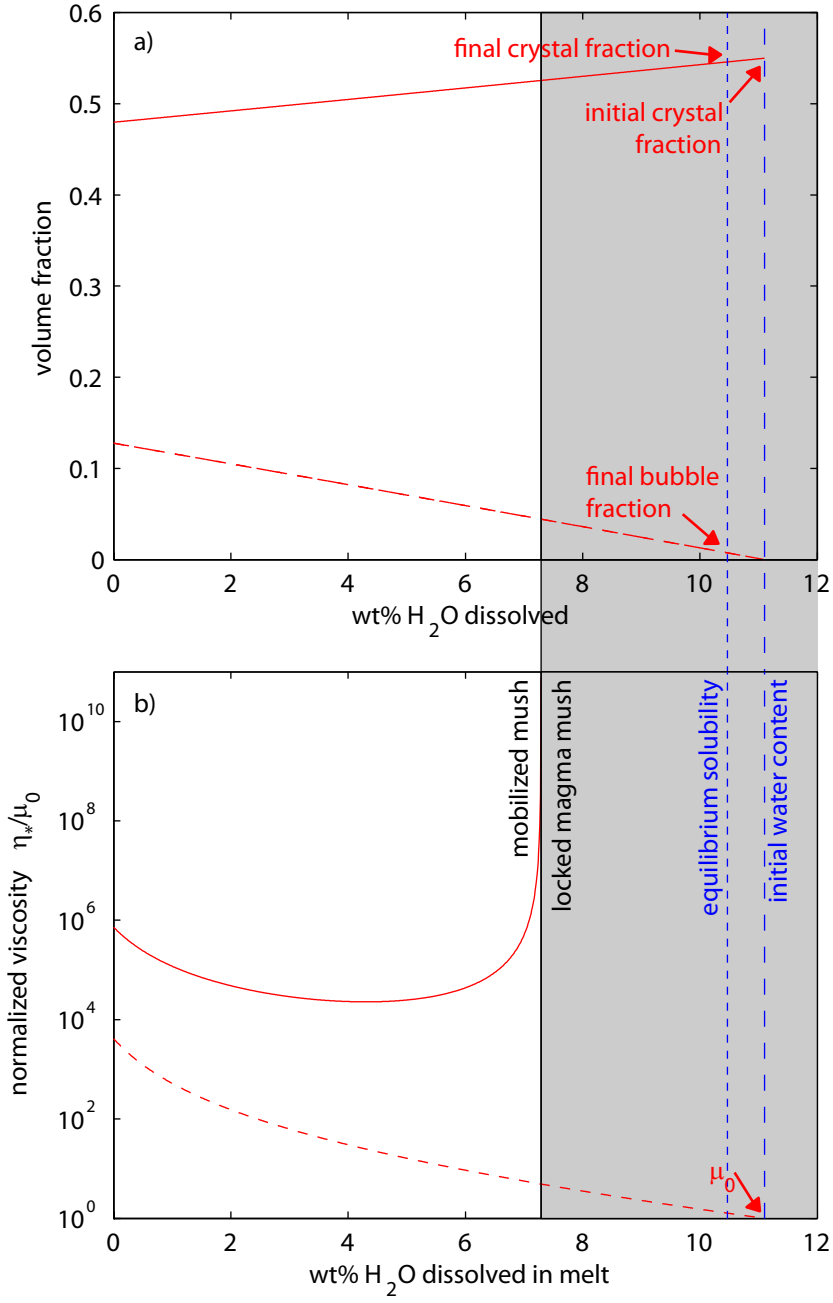

Figure 4.9: Magma evolution with dissolved water for a deep (400 MPa), wet (5 wt.% H_2O) rhyolite magma chamber. a) Crystal fraction (ϕ_p, solid red curve), bubble fraction (ϕ_b^*, dashed red curve); b) melt viscosity (μ/μ_0, dashed red curve), bulk magma viscosity (η_*/μ_0, solid red curve, from equation 3.2) against dissolved water. Grey region indicates locked magma. Blue dashed line indicates water content at 55% crystals. Bubbles exsolve and grow until melt reaches equilibrium solubility (dotted blue line); magma does not become mobile.

fraction, potentially leading to the addition of anhydrous material to the melt, and decreasing the dissolved water fraction. A temperature rise will also reduce the

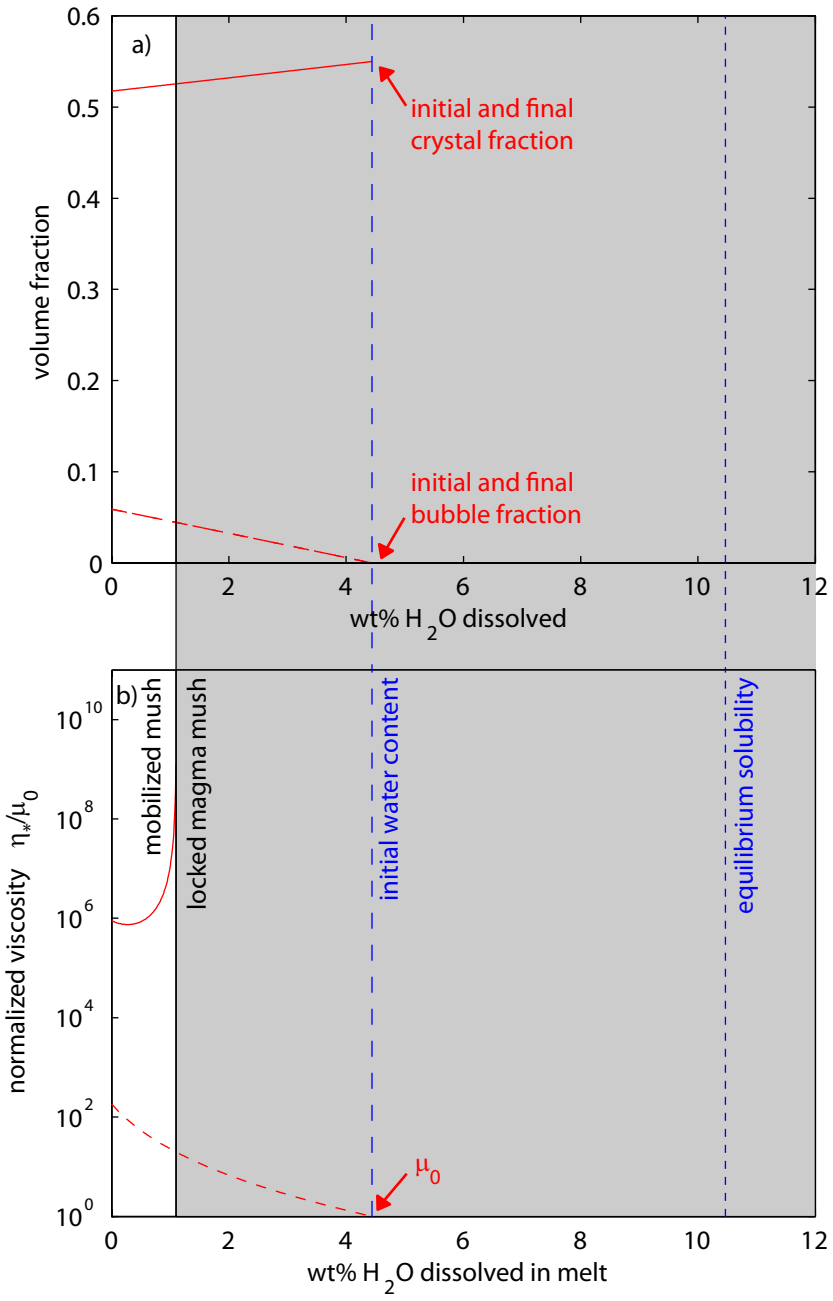

Figure 4.10: Magma evolution with dissolved water for a deep (400 MPa), dry (2 wt.% H_2O) rhyolite magma chamber. a) Crystal fraction (ϕ_p, solid red curve), bubble fraction (ϕ_b^*, dashed red curve); b) melt viscosity (μ/μ_0, dashed red curve), bulk magma viscosity (η_*/μ_0, solid red curve, from equation 3.2) against dissolved water. Grey region indicates locked magma. Blue dashed line indicates water content at 55% crystals; this is lower than equilibrium solubility (dotted blue line), so no bubbles will exsolve.

water solubility in the melt (e.g. Burnham and Jahns, 1962), however this effect is small: for example, a 40°C rise in temperature (as has been suggested by Bachmann

and Bergantz, 2003) in the magma in section 4.5.3 would reduce the water solubility from 4.29 wt.% to 4.16 wt.% (Newman and Lowenstern, 2002), creating a bubble fraction of only $\phi_b^* = 0.005$. The balance between the various factors controlling viscosity would also need to be accounted for, for each specific situation.

4.5.6.2 Bubble growth due to pressure decrease

The solubility of dissolved volatiles is also reduced by decreasing pressure (e.g. Burnham and Jahns, 1962). In the event of a catastrophic pressure drop, for example due to edifice collapse (Pinel and Jaupart, 2005; Cassidy et al., 2015), decompression has been inferred to have led to volatile exsolution and bubble growth (e.g. Manconi et al., 2009) and contributed to triggering the eruption by lowering the bulk magma density. This would act in concert with the model presented here in which the magma viscosity could be significantly lowered through the growth of bubbles, allowing an immobile magma to rapidly become mobilized.

Once a magma is mobilized, or if it is close to jamming but still mobile, convection within the reservoir or conduit may also lead to bubble exsolution. In this case, the growth of bubbles will act to reduce viscosity and make eruption easier.

4.5.6.3 Bubble growth due to shaking

It has been observed that there is a statistically significant correlation between large earthquakes and eruptions (Linde and Sacks, 1998; Manga and Brodsky, 2006). The majority of mechanisms for triggering eruptions due to earthquakes involve bubbles nucleating, growing, or rising (Manga and Brodsky, 2006), or foam collapsing (Namiki et al., 2016), and similar processes have been inferred in groundwater systems (Crews and Cooper, 2014). If this occurs in a crystal-rich magmatic system, the drop in viscosity may be sufficient to mobilize the magma, depending on how close to the jamming fraction the magma was, and what volume of bubbles grows.

4.5.7 Complications

The discussion in this chapter has presumed that exsolved volatiles remain within the magma. Percolation theory suggests that permeability develops once the bubble fraction in a crystal-rich fluid reaches around 31 vol.% (Candela, 1991). This is significantly higher than the volume suggested by the model that is needed to mobilize magmas at or slightly higher than the jamming fraction, so it is likely that a mobilized magma would be able to erupt before becoming permeable. However,

if the overpressure due to buoyancy in the reservoir is not high enough to trigger an eruption prior to permeability development, the magma may then lose enough bubbles that it ceases to be eruptible.

A second potential complication is that the experiments in section 4.3 were carried out in constant pressure conditions, with the volume of the sample unconstrained. The model in section 4.5 made the same assumption. In a magma reservoir, the volume is unlikely to be able to expand to accommodate the full volume of bubbles that could exsolve from the magma. This means that the volume of bubbles is likely to be less than predicted based solely on the initial reservoir pressure, and the exsolution of bubbles is likely to lead to overpressure.

Even in a volume confined system, however, bubble growth may be accommodated. Magma is mostly incompressible (Spera, 1984), but a magma reservoir as a whole may be heterogeneous and contain slightly variable fractions of bubbles. Compression of magma (and bubbles) in one region of the chamber may allow for bubble growth in another region. Once bubble growth has led to mobilization, and an eruption has been triggered, it would then be possible for decompression to occur elsewhere in the reservoir, potentially leading to a runaway process.

A further complication relates to the timescales of the experiments, compared to the lifetime of a magma reservoir. The experiments were run over a short enough time that, even in a pure fluid, settling of particles and rise of bubbles would be negligible. However, in a natural magma reservoir, the timescales are much longer; this is offset to some extent by the higher melt viscosity and length scales, and by the high crystal content hindering settling. However, despite indications that some magma resevoirs may accumulate a large volume of melt over centuries or less (Charlier et al., 2007; Gualda and Ghiorso, 2013) it is likely that some crystal-bubble-melt segregation will occur, as evidenced by zoned magma chambers (, e.g.)Cashman2014. Segregation is likely to have two effects on the processes inferred in this model. Firstly, bubble rise could promote bubble loss from the system, leading to a reduction in the total bubble volume available to mobilize the magma. Secondly, crystal-poor regions are more likely to be capable of eruption than crystal-rich regions. As such, it may be expected that a run-away eruption process, may be triggered by mobilization of the comparatively crystal-poor upper region of a reservoir.

4.6 Mobilization or pluton formation?

The analysis presented in section 4.5 shows that in a comparatively wet and shallow magma reservoir, second boiling could lead to mobilization. Second boiling, temper-

ature increase, pressure decrease, and shaking are all processes that favour bubble growth and mobilization. Nonetheless, the existence of plutons testifies that not all magma mushes are erupted, so what factors influence whether a mush is mobilized, or a pluton is formed?

Pluton formation will result if the fraction of exsolved bubbles never reaches a value that is sufficient to push ϕ_p below ϕ_{crit}, as in the examples of deeper magma reservoirs presented in sections 4.5.4 to 4.5.5. This type of situation is favoured by multiple factors: high pressure in the magma reservoir such that the bubble fraction produced by exsolution of a given quantity of gas is small (e.g. section 4.5.4); low initial water content in the melt such that the quantity of exsolved gas is small or the melt only becomes saturated at very high crystal fractions (e.g. section 4.5.5); crystallization of hydrous crystal phases; and highly anisometric crystals (i.e. $r_p \ll 1$ or $r_p \gg 1$) such that ϕ_m, and hence also ϕ_{crit}, are low. Another factor that could mitigate against mobilization is the intergrowth of crystals prior to vesiculation, which could form a framework with sufficient strength to prevent relative motion of the crystals as bubbles grow (Costa et al., 2006). In this case the melt could be expelled from the crystal framework (filter pressing — Sisson and Bacon, 1999), but the crystalline portion of the reservoir would remain uneruptible.

Another circumstance in which pluton formation will occur is when the whole of the magma chamber is not mobilized. As discussed above, bubble growth may occur in one region of a magma reservoir at the expense of other regions in order to conserve volume. An eruption may then fail to fully evacuate the magma reservoir, which would explain observations that plutons do not always represent liquid compositions (Gelman et al., 2014; Lee and Morton, 2015).

Even if a magma is mobilized through the addition of bubbles, it will only flow if a stress is imposed. This may come from the increased buoyancy of bubbly magma, or through external stresses. However, if these are not sufficient to cause an eruption, the magma may pass through a "window" of mobility and cease to be mobile as crystals continue to grow.

4.7 Conclusions

In order for any highly crystalline mush to become mobile, its crystal fraction must first be reduced below a critical value, ϕ_{crit}. Experiments with analogue materials have demonstrated that the growth of bubbles is sufficient to mobilize an initially jammed suspension. In the context of a natural model magma reservoir, the calculations developed here demonstrate that under some conditions the magma may

become mobile, while under other conditions bubble growth may be insufficient, or may not occur at all.

This new model is consistent with existing models of eruption triggers and provides a unifying, underlying mechanism for magma mobilization. Previous models have suggested underplating by recharge magma, decompression related to changing tectonic stresses, and seismic shaking as potential triggers for mobilization. Each of these mechanisms has the potential to induce vesiculation, either through heating (underplating), which is also likely to promote mobilization through crystal melting, through decompression (tectonic stress), or through rarefaction (seismic shaking). Furthermore, vesiculation may occur in the absence of external triggers, through second boiling. The model presented here postulates that it is the vesiculation event that renders the magma mobile, regardless of the trigger: the growth of bubbles pushes the crystals apart, decreasing the effective crystal fraction below a critical value. The bubbles may also provide the buoyancy to drive the eruption of the mobile magma.

All magmas at depth contain dissolved volatiles and, at some point in their lifetime, the growth of bubbles — whether externally or internally triggered — may cause or assist mobilization. The model presented here provides the framework to determine whether, for a given magma composition and volatile content, a known pressure-temperature-time pathway would lead to bubble exsolution, growth, and subsequent magma mobilization, or to viscous death and pluton formation.

Chapter 5

Emplacement and morphology of a crystal-rich basaltic lava flow field

5.1 Introduction

The morphology that a lava flow will produce is primarily controlled by its rheology, as discussed in section 2.5.3. This chapter will further address the topic of lava flow morphology, focussing on one particularly crystal-rich lava (Bouvet de Maisonneuve et al. (2012) quote a value of 64% phenocrysts) effused during the 1780 eruption at Volcán Llaima, Chile. This lava formed a compound flow field including both ‘a‘ā and pāhoehoe— despite its high crystallinity — and exhibits a range of larger-scale morphological features of interest.

Lavas with such high crystal content are rare (Marsh, 1981), and it was suggested in section 3.6.2 that bubbles may be required for crystal-rich lava to flow, and that the presence of bubbles may allow a lava that would otherwise flow as ‘a‘ā to flow as pāhoehoe. These concepts will be explored here, and the expected viscosity of the lava at Volcán Llaima will be calculated using the model introduced in chapter 3 and compared to the viscosity of lavas at Kīlauea and Mount Etna. This will allow their respective propensities for producing pāhoehoe versus ‘a‘ā to be assessed.

5.2 Volcán Llaima

Volcán Llaima (figure 5.1) is located in Chile's Southern Volcanic Zone, and is one of the largest and most active volcanoes in Chile. Over 50 eruptions have occurred since 1640 AD (Bouvet de Maisonneuve et al., 2012), although the historical record is poor prior to 1850 (Dzierma and Wehrmann, 2010). Historical activity on Volcán

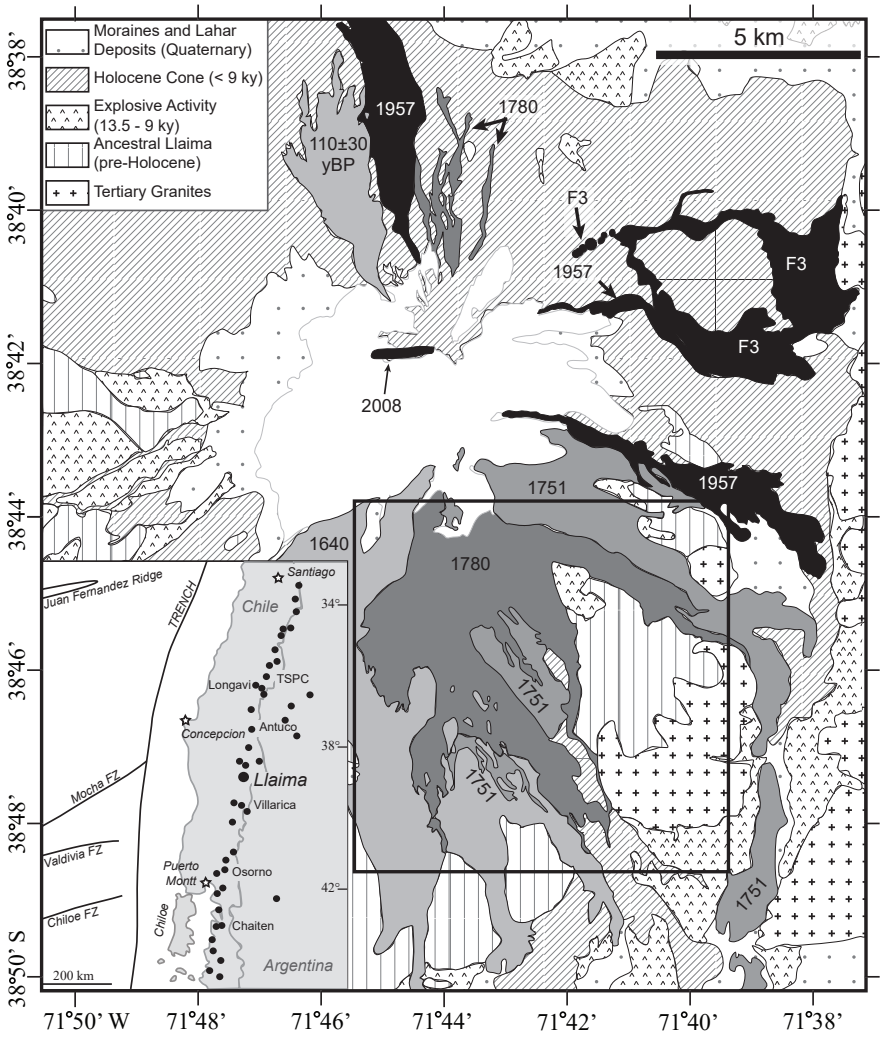

Figure 5.1: Geological map of Volcán Llaima, after Bouvet de Maisonneuve et al. (2012), showing the various lava flows in shades of grey. The inset shows the location of Volcán Llaima within Chile's Southern Volcanic Zone, along with other volcanic centres (black spots), fault zones (FZ), and the subduction trench (TRENCH). The box shows the region examined in more detail, in figure 5.2.

Llaima has been dominated by basalt to basaltic-andesite Strombolian eruptions both near the summit and on the flanks. These eruptions have built numerous cinder cones and have erupted lavas that mantle much of the edifice, particularly on the southern flank. The most recent eruption was in 2008-2009. All of the samples taken by Bouvet de Maisonneuve et al. (2012) for recent eruptions at Volcán Llaima plot along the boundary between basalt and basaltic andesite on a total alkali-silica (TAS) diagram. It is assumed that the composition of the 1780 lava is similar.

Lavas form the largest volume erupted product on Volcán Llaima, and are commonly crystal rich, with an average of at least 34 vol.% crystals on a vesicle-free basis

(for the three eruptions studied by Bouvet De Maisonneuve et al., 2013), rising to 64 vol.% in the most extreme examples (Bouvet de Maisonneuve et al., 2012).

The 1780 eruption on Volcán Llaima has not been studied in detail and the only known historical record of this eruption comes from Jesuit missionaries, who noted that the eruption lasted 10 years (Hugo Moreno, pers. comm. 2014). Despite their age, the 1780 lavas are well-preserved on the flanks and glassy margins are still present in some parts of the flow. By contrast, the preceeding 1751 lava has no preserved glass, and was extensively eroded, apparently by lahars, prior to the 1780 eruption. The upper region of the 1780 lava flow is obscured by snow for much of the year, and was partially covered by scoria from the 2008-2009 eruptions.

The 1780 eruption produced a compound flow field (Walker, 1971), comparable to those typically produced by Mount Etna, Italy, and sharing a number of features in common. However, Volcán Llaima is less extensively studied than Mount Etna, and a number of the features described in this chapter have not been discussed in detail before.

5.3 Features of the compound flow field

A range of volcanic landforms occur across the 1780 flow field (figure 5.2). These were investigated in detail during fieldwork.

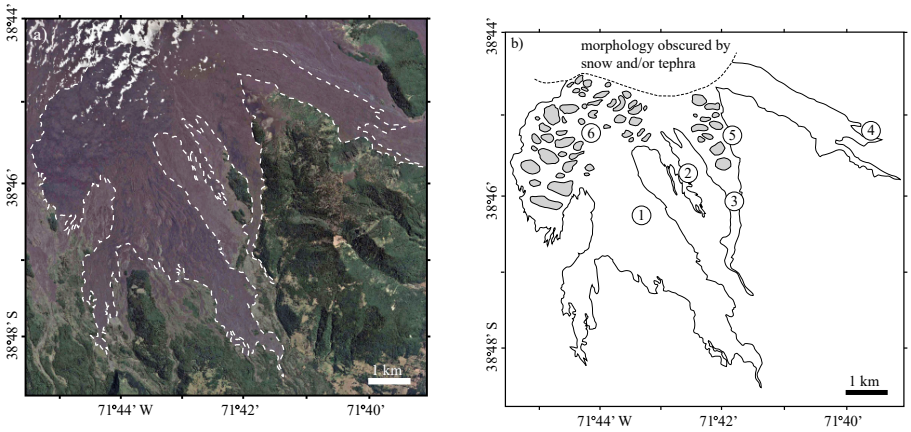

Figure 5.2: a) Aerial image of the 1780 lava flow field, with the outline marked by dashed white lines. b) Outline of the 1780 lava flow field, showing key features and locations discussed in this study. Grey outlines indicate the summits of ʻaʻā mounds. 1: Channelized ʻaʻā. 2: Slabby ʻaʻā and pāhoehoe. 3: pāhoehoe. 4: Transitions between ʻaʻā and pāhoehoe. 5: ʻaʻā mounds observed in detail. 6: ʻaʻā mounds observed from a distance and interpreted from aerial imagery.

Figure 5.3: Typical ‘a‘ā channel in the region around location 1.

5.3.1 ‘A‘ā channels

The region around location 1 (figure 5.2) contains many overlapping ‘a‘ā channels (figure 5.3. The current regional slope in this location is 8-10° and rarely up to 15-20°, and the most proximal ‘a‘ā flows are around 5 km from the vent. Levees can exceed 5-10 m height and the channels are typically 10-30 m wide; some reach 80 m wide. The wider flows tend to be longer and may extend up to 3 km in length, however the overlapping nature of the channels makes them difficult to trace individually. It is common to find stacked channels, and overspills from the levees locally fed subsidiary ‘a‘ā flows up to 300 m long.

In some channels, the lava has drained out of the channel and the internal structure of the levees is exposed. Although the outer carapace of the levees is formed from clinker breccia, the interior margins have a more complex structure. This consists of sub-vertical walls composed of alternating sheets of massive and brecciated lava, running parallel to the channel. The massive lava is almost avesicular; the few vesicles present show a weak foliation parallel to the channel. The material also appears fresh and is dark grey to black. The brecciated material is much less well consolidated, and is formed of oxidised fragments of clinker, ash, and agglutinated clinker (i.e. lava balls).

5.3.2 Pāhoehoe

Lava flows with exclusively pāhoehoe morphology are very rare in the 1780 flow field, but flows with patches of pāhoehoe morphology are fairly common. In a number of locations (e.g. location 2 in figure 5.2, where the regional slope is 6-8°) the ‘a‘ā is slabby, and in some places includes scratched pāhoehoe surfaces up to 2 m^2 in area. In many places, the slabs do not appear to have been moved far by the ‘a‘ā. These features are most common where the ‘a‘ā flows are thinner, and have not developed channels. Occasionally, regions of the larger ‘a‘ā channels are predominantly slabby.

In addition, at location 3 (figure 5.2), there are small, thin (less than 3 m thick), overlapping flows of ‘a‘ā, slabby ‘a‘ā and pāhoehoe. This compound flow is confined to a valley, the base of which has a slope of 6-8°. These individual flows generally cannot be followed for more than 50 m downslope, and commonly override each other. Pāhoehoe is most commonly preserved at the margins of the main flow,

where it has not been overridden by later flows.

5.3.3 Transitional lava

At the distal end of the eastern limb of the 1780 flow field (location 4 on figure 5.2), the palaeotopography is consistently shallow, with a slope of 4-6°. In this region, the lava morphology switches downslope between ʻaʻā and pāhoehoe several times, over a distance of around 400 m (figure 5.4). The breakout of pāhoehoe and the progressive transition to ʻaʻā was examined in detail at one location, and the same sequence was observed to be repeated at least three times downslope.

The initial transition from ʻaʻā to pāhoehoe occurs at the front of an 8 m high ʻaʻā lobe. A slab-crusted pāhoehoe flow (Guest and Stofan, 2005) emerges from near the base of the ʻaʻā lobe. This flow widens from 1 m to 2 m over the first 15 m, and extends as a well-confined channel flow, with solid rubbly levees, for around 50 m. The lava surface shows scratch marks within 1 m of the breakout. The height of the preserved flat surface is approximately level with the top of the levees.

As the channel continues downslope, the surface begins to break into imbricated slabs. For a further 10 m, the channel shape is still apparent, but becomes increasingly disrupted until it transitions into a thicker, wider, slabby ʻaʻā flow, and then a clinkery ʻaʻā flow for a further 50 m, with thickness increasing from 2 m to 8 m over the length of the flow. From the front of this next ʻaʻā lobe, a second flat-topped break-out occurs, which is the same thickness as the initial pāhoehoe breakout upstream. The sequence of flow and breakup followed by break-out is then repeated (figure 5.4c).

5.3.4 ʻAʻā mounds

The field term "ʻaʻā mounds" is used to refer to features that are found in two regions of the 1780 flow field marked 5 and 6 on figure 5.2. Location 5 was examined in detail and location 6 at reconnaissance level. Figure 5.5 highlights the key features of the mounds.

5.3.4.1 Characteristic features of ʻaʻā mounds

5.3.4.1.1 Summit

The summit of each ʻaʻā mound is defined by a broadly flat region (average slope <5°), which forms a local topographic high, typically 100-200 m above the base of the mound. The summits are roughly circular and range from 100 to 400 m in

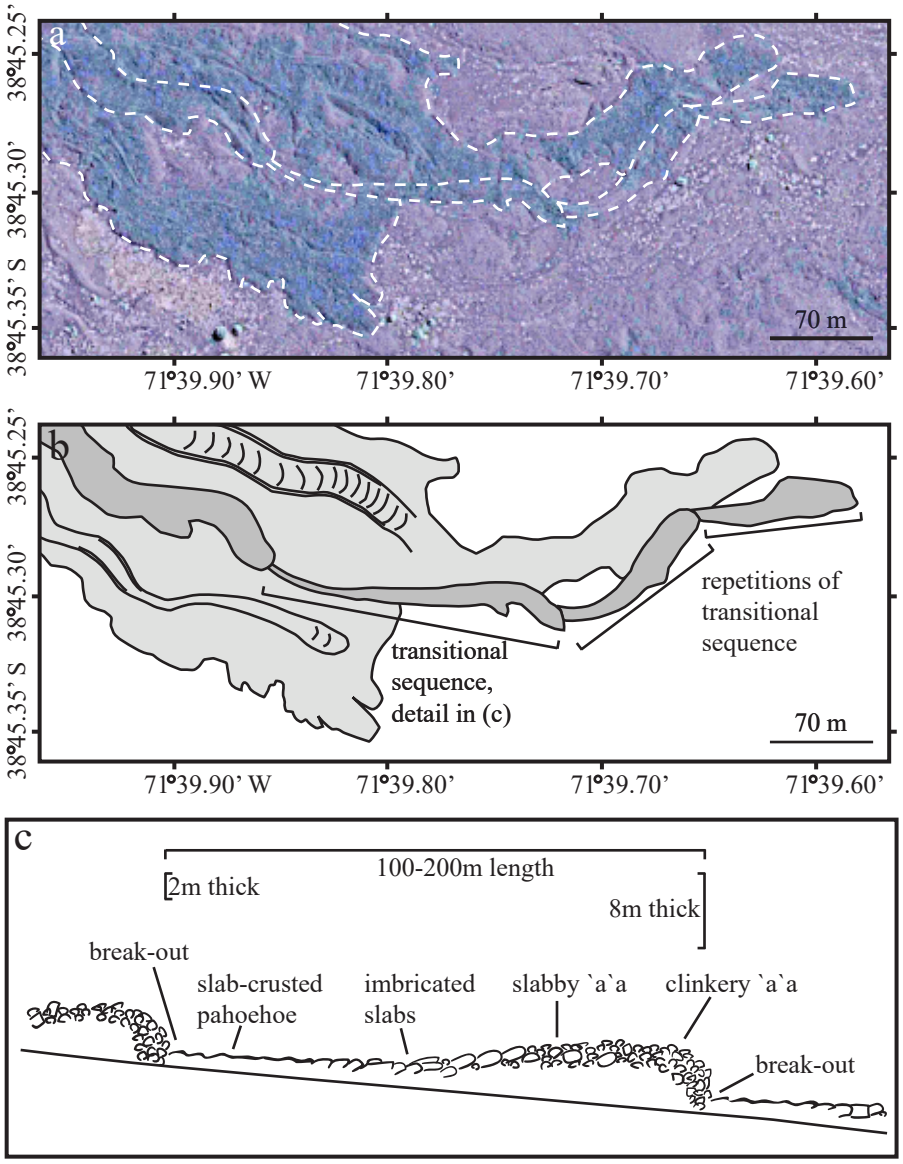

Figure 5.4: a) Aerial image of the region in which repeated slab-crusted pāhoehoe flows occur (location 4 on Figure 2), with the outline of the 1780 flow marked by dashed white lines. b) Map of the 1780 lava, based on the image in (a). Pale grey indicates 1780 ʻaʻā lava flows; dark grey indicates the transitional lavas, which appear to overlie all other 1780 flows in this region. c) Overview cross-section sketch, highlighting the key features in the transition from slab-crusted pāhoehoe break-out to clinkery ʻaʻā. This sequence repeats at least three times along the same flow.

diameter. In aerial imagery (figure 5.2a), the summit regions are clearly visible and appear more reflective than the surrounding flanks.

Each summit is covered with numerous randomly-oriented elongate tumuli (e.g. figure 5.5c), up to 10 m high, 10-30 m long, and 5-20 m wide. The tumuli are closely spaced such that little of the summit is left undisrupted. The tumuli are often

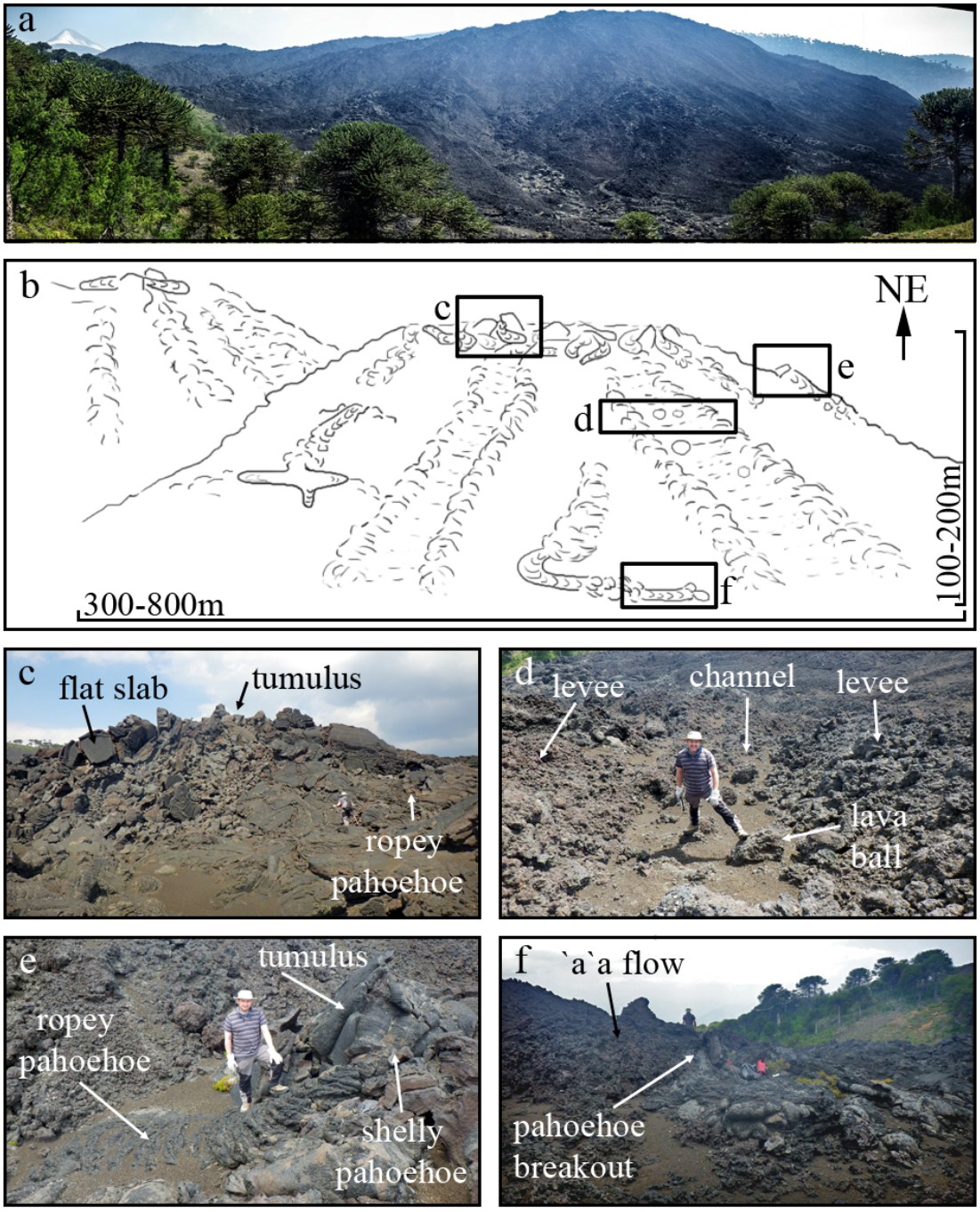

Figure 5.5: a) Panorama photo of an ‘a‘ā mound that was examined in detail. Further mounds can be seen in the distance, at the left of the image. b) Overview sketch highlighting the key features of a typical ‘a‘ā mound, based loosely on the image in (a); the locations of photos c-f are indicated. c) Summit tumulus, with part of a rotated flat slab visible at the left. d) Looking downslope, down the centre of a leveed ‘a‘ā flow. e) pāhoehoe breakout from a flank tumulus. f) pāhoehoe breakout from an ‘a‘ā flow at the base.

associated with small squeeze-ups of ropey pāhoehoe, which rarely extend more than 5 m from their sources. Some tumuli show multiple generations of squeeze-ups.

The predominant lava morphology on the summit is short (<15 m) and narrow (<1 m) pāhoehoe flows with well-developed surface ropes. These flows follow local downslope directions, which are highly variable due to the close spacing of the tumuli. There are regions of flat, smooth lava, up to 10 m wide, often with deep ropes near the margins, which appear to be contiguous with the pāhoehoe flows. Flat slabs that are uplifted and rotated by tumuli reveal cross sections through vesicular upper crust up to 4 m thick. Within the slabs are layers, 10-20 cm thick, of variably shaped vesicles: small, spherical vesicles contrast with larger irregularly shaped vesicles, which are often elongated parallel to the flat surfaces of the slabs. The interiors of the slabs show poorly-developed columnar jointing.

5.3.4.1.2 Flanks

Away from the flat summit region, the typical slope angle on the ʻaʻā mounds increases smoothly, but rapidly, towards the flanks, which have a maximum slope angle of 30-35° (figure 5.5a). Two intermediate, annular zones are identified. The first is immediately adjacent to the summit region, up to 100 m in width for most mounds, and has slope angles that are 5-10°. It is characterized by pāhoehoe flows that predominantly flowed towards the flanks, and by an absence of flat slabs. The second is immediately adjacent to the first, 100 to 200 m in width for most mounds, and has a slope angle of 10-30°. It is characterized by intermingled pāhoehoe and slabby, transitional ʻaʻā flows that also flowed away from the summit. Within this latter zone the proportion of pāhoehoe lava decreases, while the proportion of ʻaʻā increases, towards the flanks.

The steepest portions of the ʻaʻā mound flanks are composed almost exclusively of ʻaʻā, the majority of which appears to be sourced from the summit region. As the ʻaʻā becomes well developed away from the summit, it forms channels up to 8 m wide, with rubbly levees (figure 5.5d). The lava surface in the channels is typically 1-2 m lower than the levees and contains numerous lava balls, 0.2-1 m in diameter.

Scattered across the flanks are tumuli (figure 5.5e) up to 10 m across, which have uplifted the ʻaʻā flows. In some instances the tumuli now represent local topographic highs, in others the tumuli form humps on the flanks - in both cases the tumuli locally deflect the flank upwards by around 5-10 m, measured perpendicular to the main flank slope. Many tumuli have breakout flows that extend more than 30 m downslope. The breakout flows are typically shelly pāhoehoe adjacent to the

breakout point, but transition into ropey pāhoehoe within 10m; they then break up and transition into ‘a‘ā at distances of 20-30 m from their tumulus source.

5.3.4.1.3 Base

Near the base of the mound the slope of the flanks decreases to <5°. The proportion of pāhoehoe increases as the slope angle decreases until ‘a‘ā and pāhoehoe are present in roughly equal proportions. ‘A‘ā and pāhoehoe flows overlap considerably in this region, and it is generally difficult to trace any flow for more than 20 m.

Where the source of the pāhoehoe flows can be traced, they are sourced from breakouts in ‘a‘ā flows on the flanks that reach the base of the mound (figure 5.5f). In some cases, these pāhoehoe flows then break up, and transition into slabby ‘a‘ā and then ‘a‘ā. Most do not extend more than 20 m, and many form lobate flows with multiple toes. The sources of other pāhoehoe flows are not clear, as they are overridden by both ‘a‘ā and pāhoehoe.

In some places the pāhoehoe lavas form flat regions up to 10 m wide, apparently as a result of ponding within pre-existing depressions. In some cases, this ponded pāhoehoe then overflows and feeds another flow.

5.3.4.1.4 Petrography

The 1780 lava was sampled at a number of locations, from ‘a‘ā, pāhoehoe and transitional lavas, and all samples have certain features in common. The lava contains phenocrysts of plagioclase feldspar and olivine in a variably crystalline matrix (figure 5.6). X-ray computed tomography (XRCT) was used to measure the bulk crystal and bubble volume fractions, and gather large-scale information about the crystal

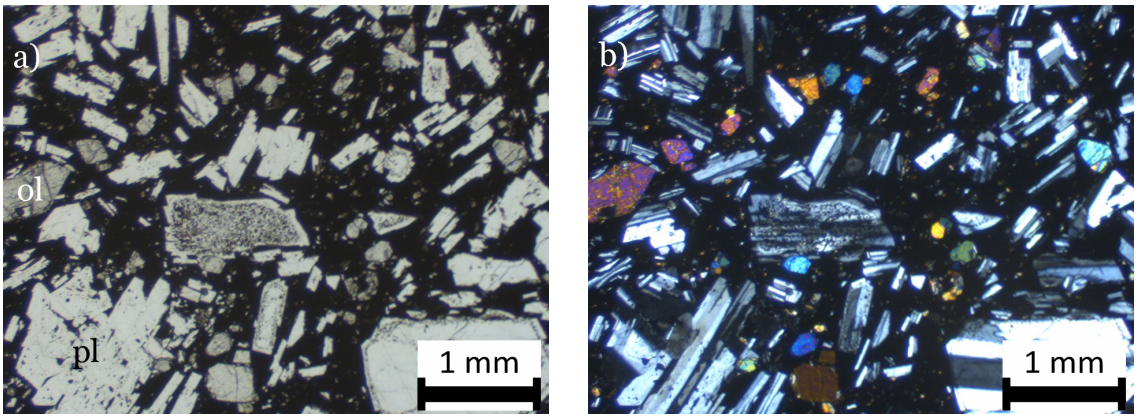

Figure 5.6: Representative thin section (from sample 2a-6) of the 1780 lava, in a) plane polarized light, and b) cross polarized light. Plagioclase (pl) and olivine (ol) phenocrysts are labelled.

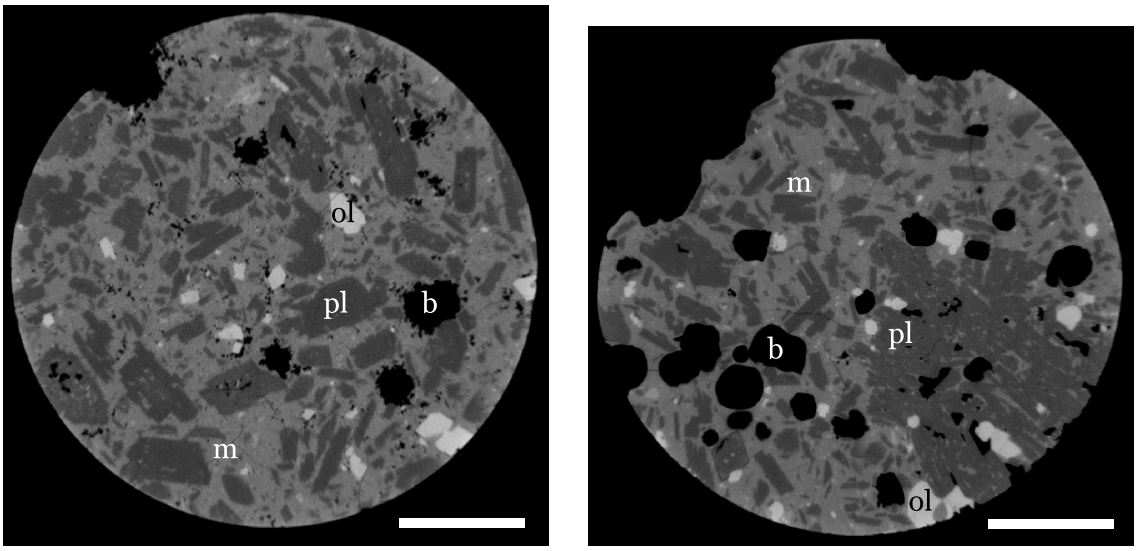

Figure 5.7: XRCT scan of a) 2a-6 and b) 2a-7, showing typical crystallinity and bubble populations. Bubbles (b) appear black, olivines (ol) are off-white crystals, plagioclase (pl) phenocrysts are darker grey, and the microcrystalline matrix (m) is paler grey. In both images, the scale bar is 2 mm.

textures. A summary of XRCT results is shown in table 5.1. The phenocrysts together comprise 49-53% of the solid volume. This is somewhat lower than the value

Sample	Description	Location	ϕ_b^*	ϕ_p^*	$\phi_{p,plag}^*$	$\phi_{p,ol}^*$
2a-6	pāhoehoe toe	5	0.12	0.52	0.46	0.06
2a-7	pāhoehoe	5	0.24	0.53	0.46	0.07
2a-8	‘a‘ā	5	0.14	0.49	0.42	0.07

Table 5.1: Analysis of phase abundances using XRCT. ϕ_b^* is the vesicle fraction in the whole sample; ϕ_p^* is the crystal fraction in the solid (as defined in section 3.2.1). $\phi_{p,plag}^*$ and $\phi_{p,ol}^*$ are the fractions of plagioclase feldspar and olivine in the solid, respectively.

presented in Bouvet de Maisonneuve et al. (2012), who quote a crystallinity of 64% for their 1780 lava sample. In addition to the XRCT analsis, thin sections were used to gather more detailed petrographic information — unless otherwise stated, all information given comes from the thin sections.

Plagioclase phenocrysts make up 42-46% of the solid volume, based on XRCT scans (figure 5.7), and are up to 4 mm in length. The smaller plagioclase crystals (up to 1 mm in length) are lath-shaped and un-zoned (see figure 5.6). Larger plagioclase phenocrysts, however, commonly show zoning, which may be complex, and are more likely to have a less simple shape (larger crystals in figure 5.6, and figures 5.8 and 5.9). Some of these larger crystals appear to be intergrown. Bands of melt inclusions associated with the zoning are common in these larger crystals (figure

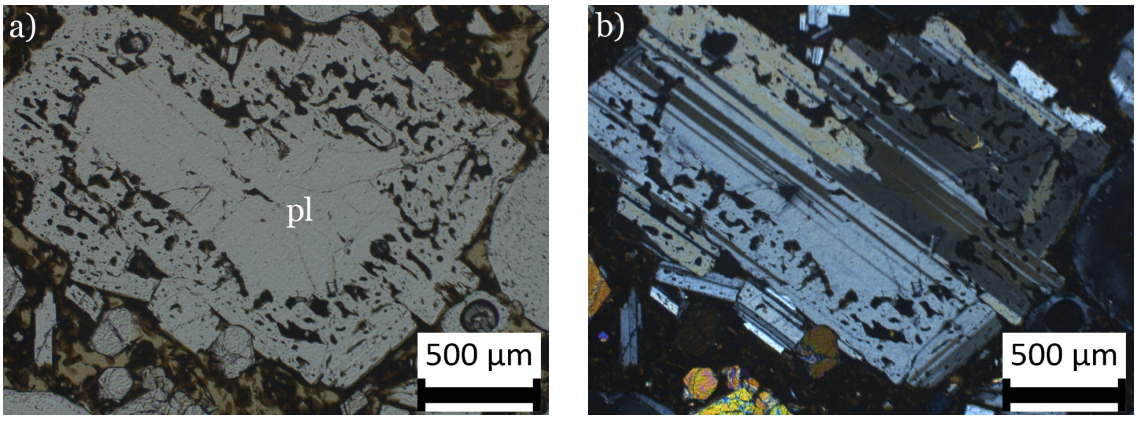

Figure 5.8: Large plagioclase (pl) phenocryst showing complex shape, with inclusion-free core and melt inclusion-rich rim (from sample 2a-7), in a) plane polarized light, and b) cross polarized light.

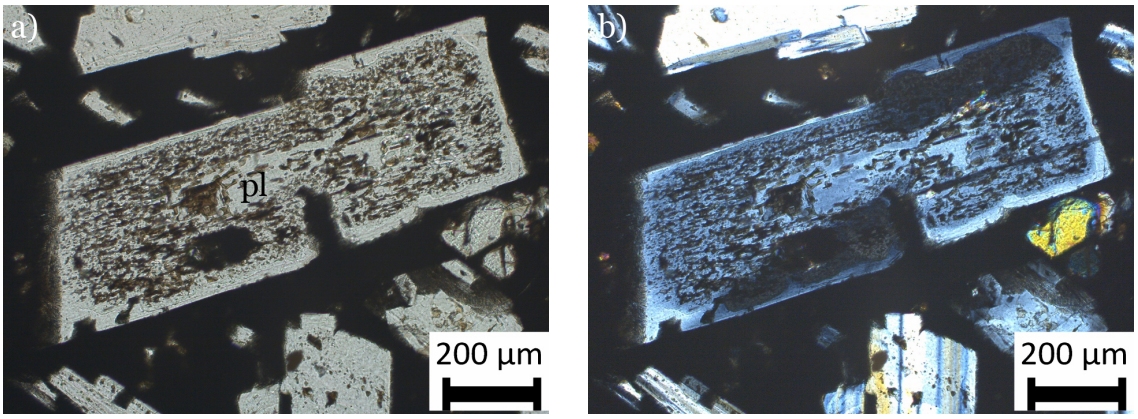

Figure 5.9: Large plagioclase (pl) phenocryst with melt inclusion-rich core and narrow inclusion-free rim (from sample 1-3Pa), in a) plane polarized light, and b) cross polarized light.

5.8), and in some the cores have a sieve texture, which contrasts with inclusion-free rims (figure 5.9).

These melt inclusion-rich bands and cores indicate (potentially multiple) melting and resorption events. Bouvet De Maisonneuve et al. (2013) found that these textural variations corresponded to compositional variations, and suggested that the crystals in the Volcán Llaima magma reservoir experienced sporadic changes in their crystallization environment. In particular, Bouvet De Maisonneuve et al. (2013) found that repeated recharge events, with mafic magma injected into the crystallizing reservoir, would lead to periodic increases in temperature, and could create the observed textures.

Olivine phenocrysts make up 6-7% of the solid volume, from the XRCT scans. These are rarely euhedral, commonly occurring as rounded crystals less than 200 μm diameter and in clusters of 200-700 μm crystals (figure 5.10). Some rare isolated

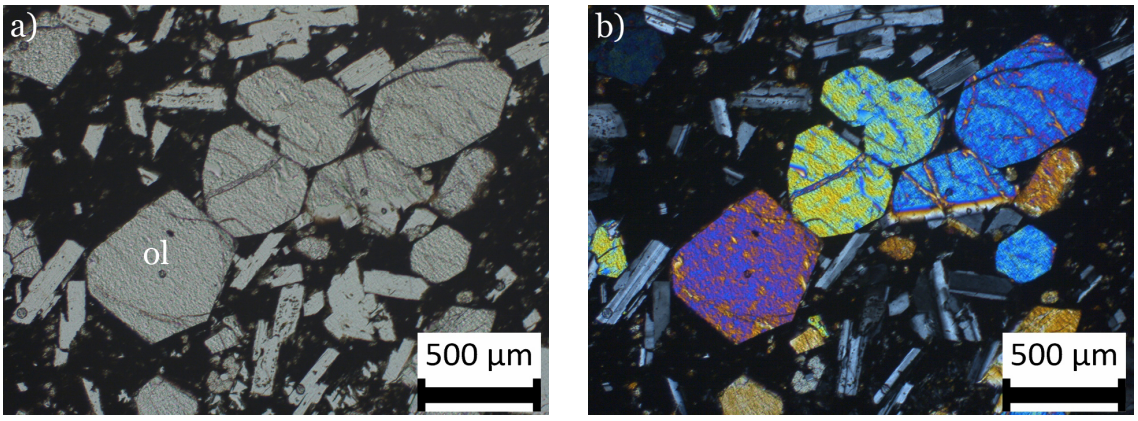

Figure 5.10: Cluster of euhedral and rounded olivine (ol) phenocrysts (from sample 2a-6), in a) plane polarized light, and b) cross polarized light.

crystals, around 1 mm across, show signs of resorption (figure 5.11) or reaction rims

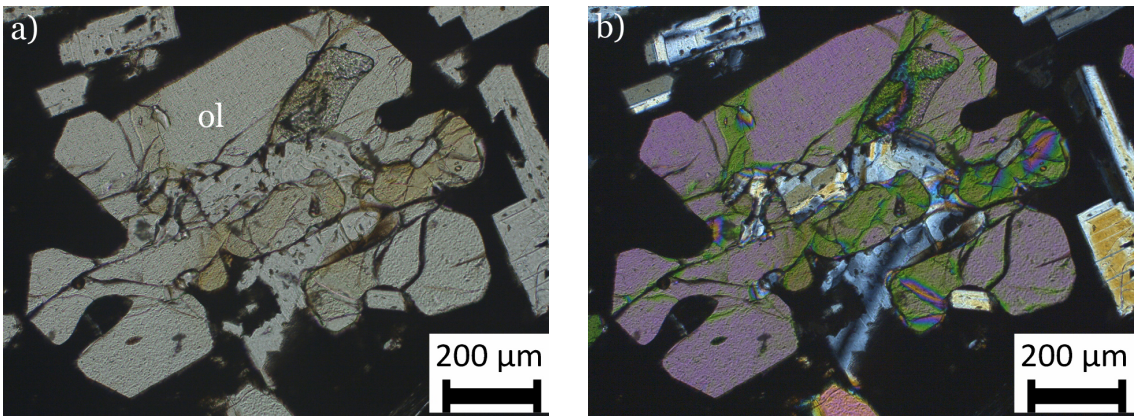

Figure 5.11: Olivine (ol) phenocryst with resorbed margin in the form of embayments (from sample 1-3Pa), in a) plane polarized light, and b) cross polarized light.

(figure 5.12).

Similarly to the plagioclase phenocrysts, olivines also show evidence of changes in their crystallization environment. The resorption event affecting the olivines only appears to alter the outer rim of some crystals: there is no sign of the internal zoning seen in plagioclase. The variability in the olivine textures — some crystals are euhedral, some show deep embayments, and some have reaction rims — has been interpreted by Bouvet De Maisonneuve et al. (2013) to represent a population of olivines sampled from different depths in a resevoir, affected to different extents by a recharge event.

In some samples, XRCT scans show clusters of rounded olivines, 500 μm to 1 mm diameter, surrounded by a network of large intergrown sieve-textured plagioclase

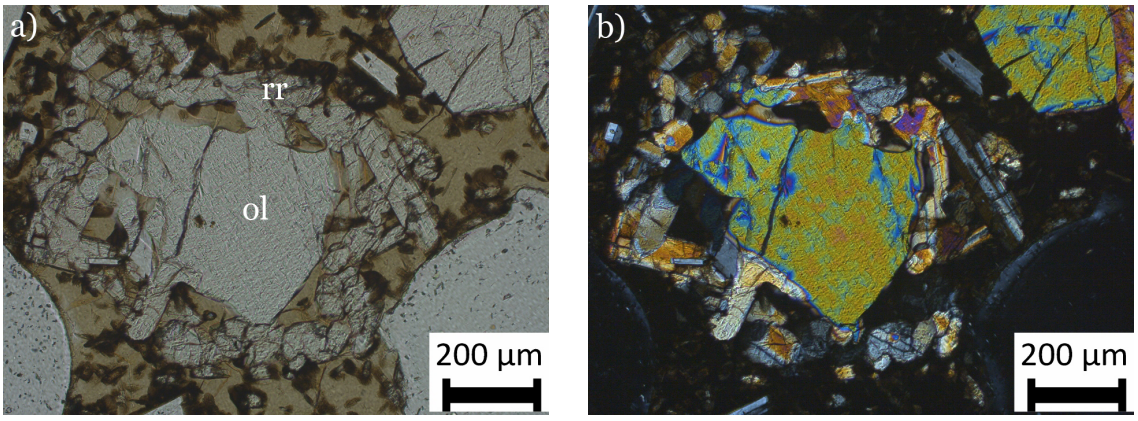

Figure 5.12: Olivine (ol) phenocryst surrounded by a reaction rim (rr) (from sample 2a-7), in a) plane polarized light, and b) cross polarized light.

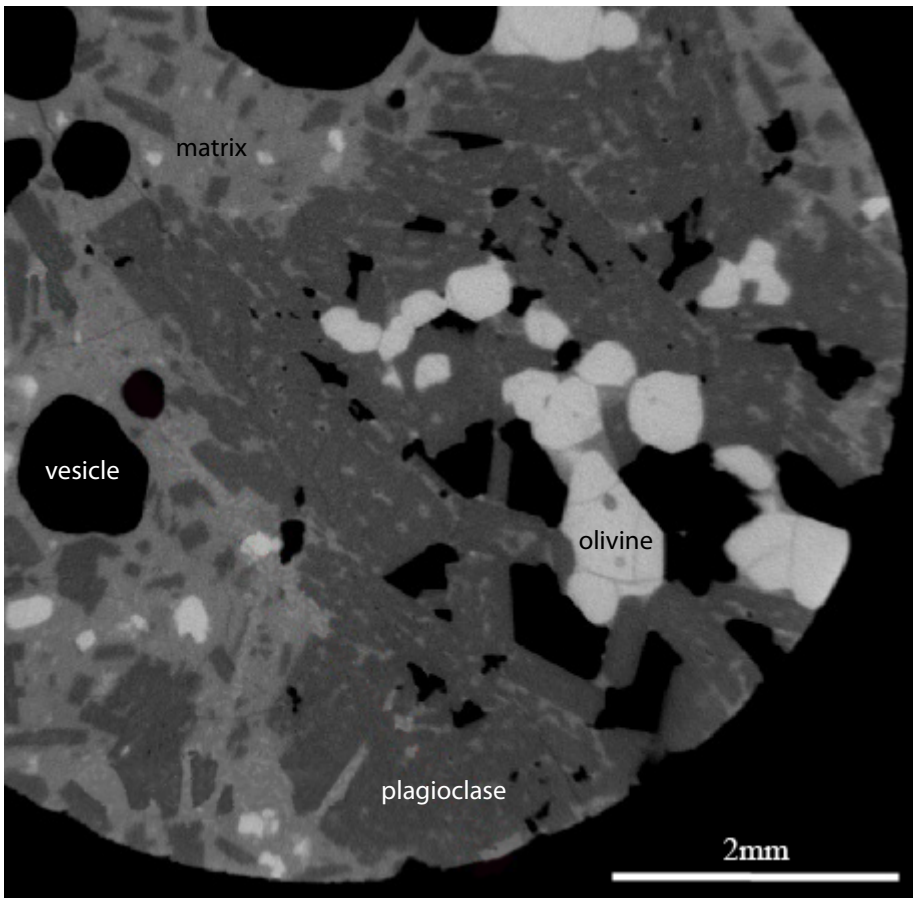

Figure 5.13: XRCT scan cross-section of sample 2a-7, showing cluster of rounded olivine phenocrysts (off-white crystals) surrounded by intergrown and inclusion-rich plagioclase phenocrysts (darker grey crystals) and microcrystalline matrix (pale grey).

phenocrysts (figure 5.13); these clusters were not encountered in thin section.

The microlite fraction in these rocks is variable. Some samples have a glassy matrix, and in others the matrix is wholly crystalline. However, it is difficult to tell how representative this is of the true microlite content during lava flow, as glass would typically only have formed at the surface of the flows, and the glassiest material has since been weathered away across much of the 1780 lava.

The bubble fraction is considerably more variable than the crystallinity, ranging from 12 to 24% in the samples that were analysed. Bubble sizes range from less than 50 μm to 2 mm. The bubble populations within a single sample may also be quite complex - some bubbles are rounded, while others have crenulated margins, which may be representative of tearing of the melt in response to stress as the lava cooled, or of dissolution by a corrosive vapour phase.

Combined, the crystal textures imply that the magma in the reservoir may have experienced multiple recharge events prior to eruption, although there may not have been sufficient time between the final recharge and eruption for conditions in the reservoir to become homogenized (Bouvet De Maisonneuve et al., 2013). It is likely that the majority of the resulting changes to crystal shapes will have occurred within the magma reservoir - as such, the observed crystal cargo in the lava flows is unlikely to have changed significantly during ascent and eruption, and this cargo can be used to model the rheology of the lava.

5.3.4.2 Interpretation

5.3.4.2.1 Formation of the summit features of the ‘a‘ā mounds

The flat slabs observed at the summit of the ‘a‘ā mounds indicate that lava ponded. Disruption of the surface by tumuli, and resurfacing by later squeeze-up pāhoehoe flows sourced from them, mean that it is not possible to determine whether there was a single pond that was continuous across the whole summit area or several discrete ponds that formed within local depressions.

The numerous tumuli indicate that the summits of the mounds underwent a period, or periods, of inflation following ponding (Walker, 1991). The inflation was sufficient to rotate many large (5 m wide, 4 m thick) slabs to a near vertical orientation. Based on the crust thickness-time relationship of Hon et al. (1994), it is calculated that there must have been at least 3-4 months of cooling during the formation of the summit tumuli. The squeeze-ups and short lava flows sourced from the tumuli support the interpretation that the tumuli were produced by pressurization of a core of molten lava beneath them (Anderson et al., 2012). The morphology of the mounds' summits allow us to build a clear interpretation only of the final stages

of the processes that formed them — presumably evidence of earlier processes is buried beneath the preserved surface.

5.3.4.2.2 Formation of flank and base features of the ʻaʻā mounds

Two possible interpretations of the tumuli found on the flanks of the mounds may be considered. The first is that they are summit tumuli, preserved from a time when the mound was lower. In this scenario they would have formed at the summit margin, and escaped being overridden by later ʻaʻā as the mound grew. However, the flank tumuli distort the flanks much more than any of the summit tumuli. On the summit, tumuli tend to create a vertically oriented bulge, whereas on the flanks, the bulge has a radial component as well. In addition, there are no other features preserved from when the mound was lower — the resurfacing by ʻaʻā has been complete everywhere else. The second, preferred, interpretation is that the interior of the mound became pressurized, and that the extent of pressurization was enough to force lava out through the flanks, overcoming the strength of that material, and producing the tumuli. This mechanism would also explain the pāhoehoe at the base that cannot be traced back to a parent ʻaʻā flow. These breakouts are cognate with the "seeps" identified at Kīlauea (Hawaiʻi) by Patrick and Orr (2012); they are distinct from breakouts formed from an active lava surface, such as those at the summit or from a lava flow.

5.3.4.2.3 Controls on the distribution of ʻaʻā and pāhoehoe

In all places where a flow's origin can be confidently identified, the most proximal part of the flow has pāhoehoe morphology. This includes breakouts from tumuli on the summit and the flank, breakouts from ʻaʻā flows, and breakouts from the ponded lava. Not one ʻaʻā flow can be traced back to a breakout, but many can be traced back to a pāhoehoe flow source. This suggests that the lava breaks out from the mounds exclusively or almost exclusively as pāhoehoe (as per Wolfe et al., 1988; Jurado-Chichay and Rowland, 1995).

In the flat summit regions, the lavas are entirely pāhoehoe; on the steepest slopes they are predominantly ʻaʻā; around the flat base they are mostly pāhoehoe again. Rapid transitions from pāhoehoe to ʻaʻā on the flanks of the mound are associated with breaks in slope, at which lava from the summit or from a flank tumulus meets a steeper slope. Transitions from ʻaʻā to pāhoehoe occur where the lava reaches the base of the mound, encountering a much shallower slope. Thus, the morphology that develops appears to be correlated with — and controlled by — the angle of the

slope on which it flows (Peterson and Tilling, 1980). Previous studies (e.g. Rowland and Walker, 1990; Pinkerton and Sparks, 1976) have found that both viscosity and volumetric flow rate together control lava morphology: here it is concluded that the lava building the mounds at Volcán Llaima has viscosity such that a small increase in flow rate, caused by an increase in slope, was enough to trigger the transition to ʻaʻā.

5.3.4.2.4 Formation of the ʻaʻā mounds

The majority of the visible lava on each mound appears to have been sourced from its summit region, and flowed as ʻaʻā down the flanks. Each mound forms a local topographic high, and all the mounds are several kilometres from the main 1780 vent. In order to flow out of the summit of each mound, lava must have travelled downslope from the main vent and then flowed up into and out of each mound — the summit regions effectively form secondary, superficial vents.

Features that have some of the same characteristics as the ʻaʻā mounds have been observed on long-lived flow fields on Kīlauea, Hawai'i, where they are called "rootless shields" (Kauahikaua et al., 2003; Patrick and Orr, 2012). They normally form over a well-established lava tube, and are built by repeated overflows of lava from a pond, so that the shield becomes higher and larger over time (Kauahikaua et al., 2003). The Kīlauea rootless shields also form local topographic high points, 20-30 m higher than the surrounding lava surface, and up to 700 m wide (Patrick and Orr, 2012). Throughout their lifetimes they commonly have an ephemeral lava pond in the summit region, but this often appears to have been disrupted towards the end of the eruption. Features characteristic of overpressure, such as tumuli and hornitos, are common at rootless shields (Tim Orr, pers. comm., 2015). Observations made while the rootless shields were active show that the entire system — from the main vent, through all the mounds, to the distal end of the flow field — can be active simultaneously for several months (Kauahikaua et al., 2003).

The term "rootless mounds" is chosen to describe the features observed at Volcán Llaima, by analogy to the rootless shields on Kīlauea. This identification is based on the following common features: (1) both types of edifice form a local topographic high, which is built by repeated overflows from a lava pond; and (2) they do not directly overlie the primary volcanic vent: the lava may flow for several kilometres before reaching the rootless mound.

There are some notable morphological differences between rootless mounds and rootless shields. Rootless shields are low aspect-ratio shield edifices composed en-

tirely of pāhoehoe lava. Rootless mounds at Volcán Llaima are steep sided and are mantled by ‘a‘ā lavas. It is proposed that this is primarily due to the differences in the viscosity of the lavas that constructed the two edifice types. Collectively, these different types of rootless formation can be referred to as “rootless edifices”.

Similar features are also found on Mount Etna. Guest et al. (1984, 2012) describe flat topped terraces of lava up to 300 m wide and 150 m high that step down the flank of the volcano. They have flanks mantled with ‘a‘ā and pāhoehoe, and summits covered by tumuli, squeeze-ups, and short pāhoehoe flows. This description matches closely those at Volcán Llaima and it is tentatively suggested that the rootless mounds are cognate with these “terraces”. Another group of features called megatumuli, or tumulus complexes, are similar, but with a more domed shape and are indicative of significant inflation (Guest et al., 1984). Guest et al. (1984) interpret the megatumuli to have developed from terraces. The terraces and megatumuli on Mount Etna have one feature that is not observable at Volcán Llaima— a well-mapped feeder tube system. The lava tubes explored by Guest et al. (1984) clearly fed lava flowing from the terraces and megatumuli, and it is likely that a similar system of tubes existed at Volcán Llaima. The system at Volcán Llaima is either deep enough to have not collapsed, or perhaps never drained of lava.

Combining the observations at Volcán Llaima, the observations of Guest et al. (1984, 2012) at Mount Etna, and an understanding of the processes that build rootless shields on Kīlauea (Kauahikaua et al., 2003; Patrick and Orr, 2012) allows the sequence of formation of an individual rootless mound to be postulated (figure 5.14). Stage 1: lava that had erupted from a vent higher up on a volcano’s flanks stalls and ponds, possibly in a local depression, or attempts to spread out on reaching a shallower slope (figure 5.14a) (Wilson and Parfitt, 1993; Guest et al., 2012). Stage 2: the pond continues to be fed by the flow, and once the capacity of the region containing the pond is reached, lava breaks out, and overflows (figure 5.14b). This overflowing lava initially forms pāhoehoe, but transitions to ‘a‘ā as it reaches the steeper slope at the edge of the pond. Stage 3: if the effusion rate is not high enough to sustain a flow, the breakout simply builds up the mound, rather than allowing lava to continue to flow out of the pond. Further breakouts build the mound incrementally, and the pond becomes raised above the surrounding lava field, armoured and flanked by lava that had previously overspilled (figure 5.14c). As the mound grows, the flanks steepen and the summit widens. Although the summit may have initially started as a single pond of lava, it may have evolved into a more complex system, in which overflows from the pond are preceded by inflation and tumuli formation. Stage 4: thermal erosion within the mound may result in

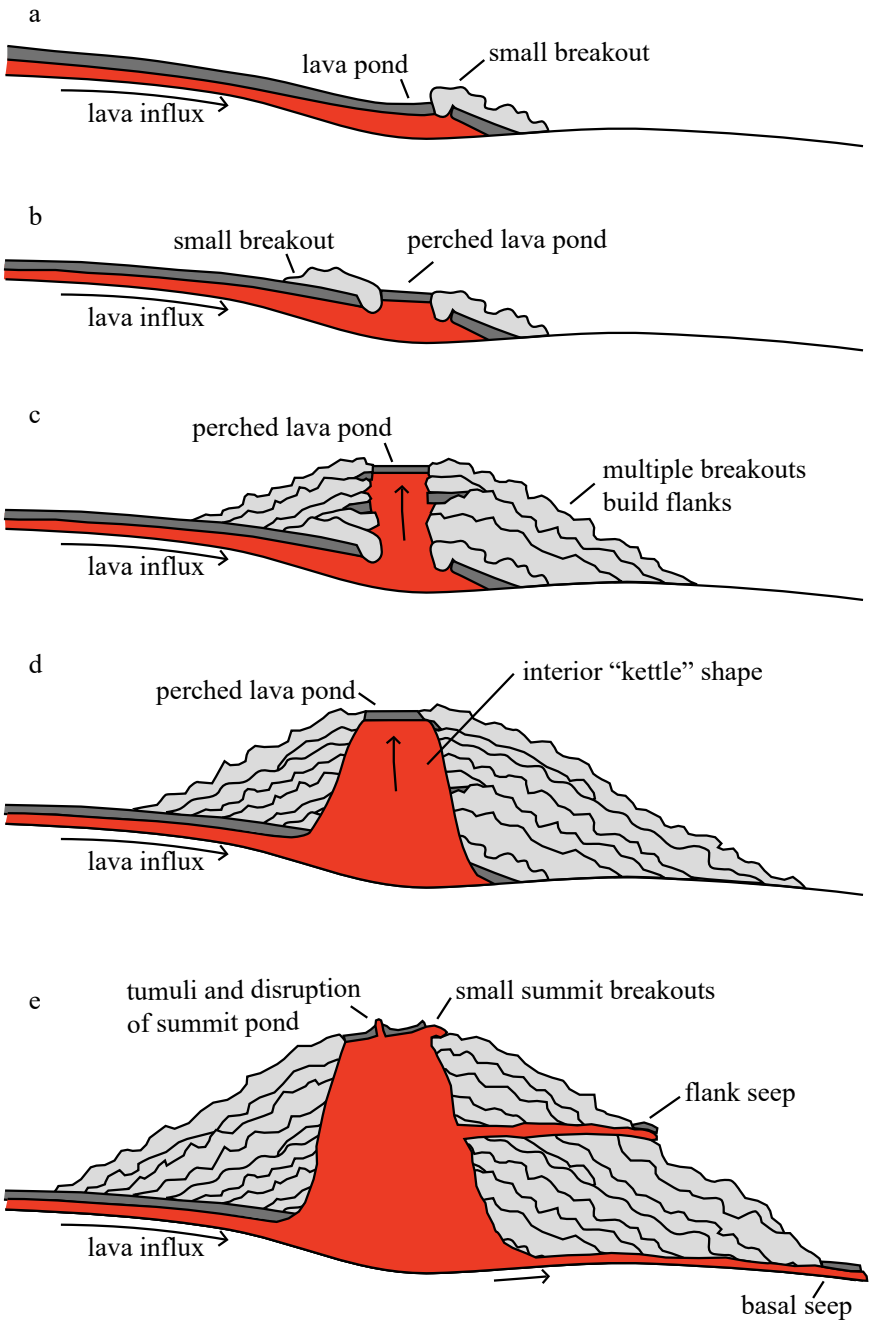

Figure 5.14: Hypothesised sequence of formation of a rootless mound. See main text in section 5.3.4.2.4 for a detailed commentary.

the formation of an interior "kettle" shape, based on observations of rootless shields at Kīlauea (figure 5.14d). Stage 5: eventually the height of the mound is such that the magmastatic pressure of lava contained within it is enough to overcome the strength of the flanks, leading to seeps on the flanks and at the base; the final phase

of inflation at the summit fails to produce overflows (figure 5.14e).

At Volcán Llaima, the rootless mounds are spread over an area of at least 6 km^2, and there is a difference in elevation of around 550 m from the top to the bottom of the rootless mound field. However, the order of formation of the mounds within the field is unclear. It is possible that, once a mound is breached at the base, the lava is then able to flow through that seep, so that more distal mounds formed after the proximal mounds. This was the case in the 2007-2008 phase of shield building on Kīlauea (Patrick and Orr, 2012). Rootless shields have also been observed to form at lava tube breakouts on Kīlauea, both after a pause in the eruption in 1999 and over continuously active lava tubes in 2001-2002 (Kauahikaua et al., 2003). It is also possible that all the mounds were active at the same time, similar to each of the rootless shield fields already mentioned (Kauahikaua et al., 2003; Patrick and Orr, 2012). Another potential sequence of formation is that the most distal mound formed first and as it built up the lava became backed up in the system until it was able to break out closer to the main vent, so that the sequence of mounds propagated back towards the vent. It might be possible to distinguish the order of mound formation if the saddles between the mounds were sufficiently well exposed; however, at Volcán Llaima, the saddles that were investigated were mantled with complex pāhoehoe and ʻaʻā flows that had interacted and defied simple interpretation.

5.4 Discussion

One of the key controls on lava flow morphology is its rheology (e.g. Peterson and Tilling, 1980). The discussion will therefore begin by comparing the likely rheology of the lavas at Volcán Llaima with those at Kīlauea and Mount Etna.

5.4.1 Rheology of crystal-rich lava

The rheology of a lava depends on its suspended crystal and bubble content (section 2.2), as well as the viscosity of the interstitial melt phase (section 2.4). By examining each parameter that influences viscosity, it is possible to estimate the apparent viscosity of the crystal-rich lava at Volcán Llaima, and compare it to values of viscosity from the literature for lava at Kīlauea and Mount Etna.

In a two phase fluid containing bubbles and liquid, the addition of bubbles may increase or decrease the bulk fluid viscosity relative to the bubble-free liquid viscosity depending on capillary number Ca (according to equations 2.5 and 2.6, respectively). For a two phase fluid containing crystals and liquid, the addition of crystals always

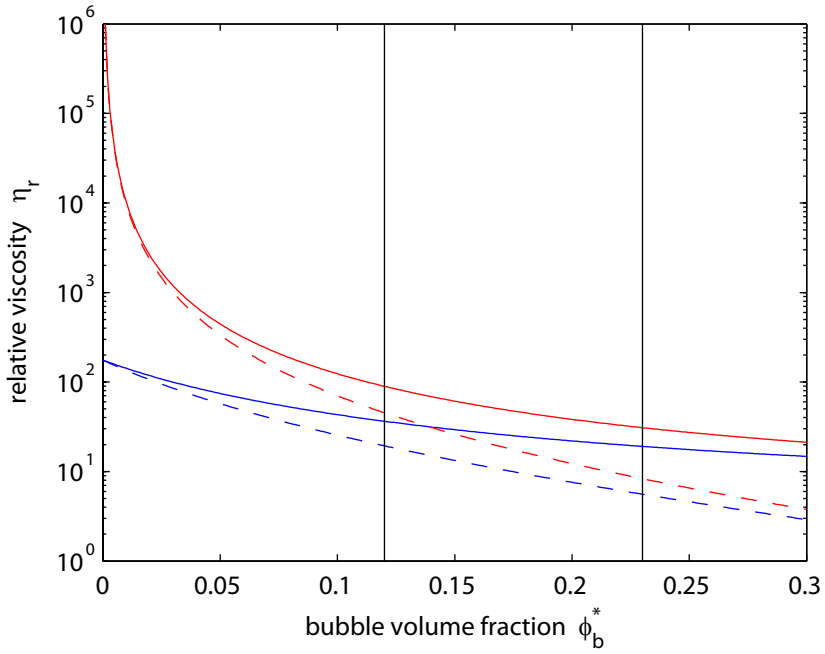

Figure 5.15: Expected relative viscosity plotted against bubble fraction. Red curves are for the highest measured crystallinity, 53% ($\phi_p^* = 0.53$); blue curves are for the lowest measured crystallinity, 49% ($\phi_p^* = 0.49$). Solid lines are for low capillarity bubbles; dashed lines are for high capillarity bubbles. The vertical dark lines indicate the lowest and highest bubble fractions measured in the 1780 lava ($0.12 \leq \phi_b^* \leq 0.23$, as given in table 5.1.

increases the bulk fluid viscosity relative to the crystal-free liquid viscosity (according to equation 2.11). Based on a qualitative inspection of photomicrographs of samples from Volcán Llaima in figures 5.6 to 5.12, it is estimated that the aspect ratio of the majority of the phenocrysts in the 1780 lava is around 2. Using equation 2.13, the maximum packing fraction of these crystals is approximately 0.53. The crystal content of the lava at Volcán Llaima (49-53 vol.%) is therefore at the maximum packing fraction, or very near it and subject to a large yield stress. Based purely on this crystal content, the lava should have been jammed and unable to flow.

The model and experiments discussed in chapter 3 provide a three-phase equation with which to postulate the expected viscosity of the bubble- and crystal-bearing lavas at Volcán Llaima. Using equation 3.2 for low capillarity bubbles, and 3.21 for high capillarity bubbles, the dependence of viscosity on bubble content can be plotted for the highest and lowest crystal fractions measured in samples collected from Volcán Llaima, and for both low and high capillarity bubbles (figure 5.15).

Clearly in both capillarity regimes, it is expected that the addition of bubbles will lead to a reduction in viscosity. The range of bubble fractions measured in the lava and a lack of knowledge of the strain rates experienced by the lava make

it difficult to place a single value on the viscosity. Instead, it is suggested that the viscosity would have been a factor of between 5 (for the lowest crystal content, highest bubble fraction, and high capillarity bubbles) and 90 (for the highest crystal content, lowest bubble content, and low capillarity bubbles) times higher than the viscosity of the melt alone. In any case, the expected viscosity is much lower for the three phase lava than it would have been for bubble-free lava.

In order to calculate apparent viscosity, rather than relative viscosity, it is necessary to know the viscosity of the suspending melt. This is controlled by a number of factors, including melt composition, water content, and temperature (section 2.4). The model of Giordano et al. (2008) is used, along with the highest and lowest silica content glass compositions given in table 1 of Bouvet de Maisonneuve et al. (2012) (table 5.2). These are combined with the corresponding water content (2.31wt.% and 0wt.%, respectively) and temperature (1004°C and 1152°C, respectively) (Bouvet De Maisonneuve et al., 2013). From these values, it is estimated that the erupted melt at Volcán Llaima would have had a viscosity in the range 10^2 to $4x10^3$ Pa s.

SiO_2	TiO_2	Al_2O_3	FeO	MnO	MgO	CaO	Na_2O	K_2O	P_2O_5	F_2O_{-1}
57.03	1.32	15.54	9.5	0.17	3.34	7.97	3.55	1.21	0	0
52.02	1.23	15.36	10.9	0.2	5.29	9.67	4.33	0.74	0	0

Table 5.2: Composition of basalt to basaltic andesite glass from recent eruption at Volcán Llaima (table 1 of Bouvet De Maisonneuve et al., 2013), normalized to 100% anhydrous.

Combining this pure melt viscosity with the relative viscosities calculated for the observed bubble and crystal fractions in the 1780 lava, the lava is estimated to have had a viscosity in the range $5x10^2$ to $3.6x10^5$ Pa s. This range of absolute viscosity values can be compared to observed lava viscosities at Mount Etna and Kīlauea in order to understand their variable propensities for producing pāhoehoe or ‘a‘ā flows. Shaw (1969) provides a Newtonian viscosity value of 190 Pa s for Hawaiian basalt at 1150°C (which is the typical temperature of near-vent lavas on Kīlauea (Helz et al., 2003)); for cooler or more crystalline lavas, the yield stress becomes appreciable, and Bingham viscosity up to 3700 Pa s is found (Moore, 1987). For Mount Etna basalt, Pinkerton and Norton (1995) also found that the lava was Newtonian above 1120°C with viscosity around 150 Pa s. Cooler and more crystalline lavas were found to have rheology matching a power law fluid, with viscosities at unit strain rate up to 8625 Pa s (Pinkerton and Sparks, 1978; Pinkerton and Norton, 1995; Gauthier, 1973).

These ranges of viscosity are plotted in figure 5.16 alongside the regions in which

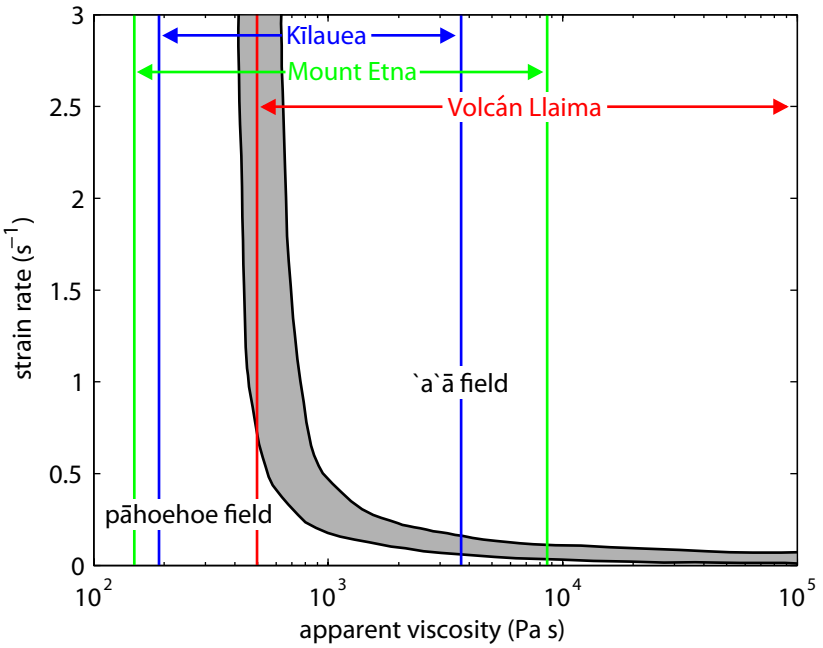

Figure 5.16: Diagram showing the relationship between strain-rate, lava viscosity, and lava flow morphology, after Hon et al. (2003). The shaded region indicates the transition zone between pāhoehoe and ‘a‘ā, which was determined by Hon et al. (2003) and others, based on field observations; the pāhoehoe field is found at low viscosities and strain rates; the ‘a‘ā field is found at high viscosities and strain rates. The vertical lines indicate the observed lava viscosity ranges at Kīlauea (blue), Mount Etna (green), and Volcán Llaima (red).

pāhoehoe and ‘a‘ā flow morphology will form, adapted here from Hon et al. (2003). Lavas from all three volcanoes span a wide range of possible viscosities, and at different viscosity and strain-rate it is possible to produce both pāhoehoe and ‘a‘ā at each. However, the ‘a‘ā field is much larger for lavas from Volcán Llaima than those from Kīlauea and Mount Etna, indicating that, under similar conditions of emplacement, lavas from Volcán Llaima are more likely to form ‘a‘ā.

5.4.2 Comparison with other rootless lava structures

5.4.2.1 Kīlauea

The main differences between the rootless shields on Kīlauea and the rootless mounds on Volcán Llaima are the shapes of the edifices that they build, and the morphology of lava as it overflows. At Kīlauea, the shields are wide and flat, with average slopes no more than 7° (based on heights and widths given by Kauahikaua et al. (2003)), and are composed exclusively of fluidal pāhoehoe lava. At Volcán Llaima, on the other hand, the mounds are taller, with average slopes of 20-25°, and the flanks are

composed predominantly of ʻaʻā. It seems that the lava rheology may hold the key to these differences.

Lava from Kīlauea tends to be erupted as low viscosity (190 Pa s, Shaw, 1969) basalt (45-53 wt.% SiO_2, Jackson et al., 2012) with a very low phenocryst fraction (Cashman et al., 1999). It typically flows as pāhoehoe for many kilometres before cooling and microlite crystallization cause it to transition to ʻaʻā (Cashman et al., 1999). In some locations, a sharp steepening in slope can also cause a transition to ʻaʻā (Peterson and Tilling, 1980). However, this normally only occurs after many kilometres of flow, when the lava has been primed for the transition by the crystallization of microlites. The Kīlauea rootless shields are proximal, fed by a long-lived lava tube system, and so they produce pāhoehoe that remains pāhoehoe as it flows away from the shield (Patrick and Orr, 2012; Kauahikaua et al., 2003). The potential morphological evolution of the lava is evident from figure 5.16: on eruption, the lava has viscosity close to the left-most blue line, and significant increases in viscosity and strain rate are necessary before the lava would cross into the transition zone.

At Volcán Llaima, the lava is basalt to basaltic andesite (51-56 wt.% SiO_2, Bouvet De Maisonneuve et al., 2013), and the 1780 lava has a very high crystal fraction — both the melt viscosity (10^2 to $4x10^3$ Pa s) and the bulk magma viscosity ($5x10^2$ to $3.6x10^5$ Pa s) are higher than at Kīlauea. As discussed above, the presence of bubbles in the lava appears to have been a key factor in allowing it to erupt as pāhoehoe. However, on eruption, the lava may be inferred to have been much closer to the pāhoehoe-ʻaʻā transition than lava at Kīlauea, as indicated in Figure 14, and was more susceptible to changing morphology when slope angle, and therefore strain rate, changed. Thus the lava at Volcán Llaima formed pāhoehoe as it initially overspilt from its pond, but as the slope steepened, it transitioned to ʻaʻā. This allowed it to build up steeper-sided mounds through repeated overflows.

5.4.2.2 Mount Etna

Many lavas at Mount Etna (49-53 wt.% SiO_2, Lanzafame et al., 2013) are crystal rich, and at least one of the flow fields known to have produced terraces contained 29% phenocrysts (Guest et al., 2012). It is possible that crystallinity is one factor that increases the likelihood that this type of feature — rootless mounds and terraces or megatumuli — will form.

Another common factor between the specific eruptions at Volcán Llaima and Mount Etna that produced rootless mounds or lava terraces is their longevity. The flow that produced these features on Mount Etna in 1614-1624 lasted 10 years,

which is considerably longer than most Etnean eruptions (Guest et al., 1984). The 1780 flow on Volcán Llaima also lasted 10 years, although it is difficult to compare with other eruptions at Volcán Llaima due to poor historical records. It is possible that these features are limited to long-lived lava flow fields with a correspondingly well-established lava tube network.

5.4.2.3 Vesuvius

Rittmann (1962) described lava morphologies at Vesuvius that are reminiscent of rootless mounds:

> "In the level ground of the Valle dell'Inferno, the dammed-up Vesuvius lava built dome-shaped hillocks 50-70 m in height, best designated rootless flow-domes. The lava flowing down the outer slopes of Vesuvius in its thick-walled, tube-like tunnels was under high hydrostatic pressure, causing it to break through the solidified crust which had formed over the more level parts of the flow in the valley below. The now viscous lava welled out from the rents in contorted masses; these in turn acquired a congealed crust which was further ruptured to emit fresh masses of contorted plastic lava. In this manner the hillocks grew steadily higher, so long as the hydrostatic pressure behind the lava and the strength of the walls of the feeding tunnels allowed the process to continue."

This text has been included as a quote to highlight the similarites between the orginal description of rootless flow domes and the rootless mounds described in this chapter; re-writing the quote would have added an extra level of description, biased towards an interpretation of the rootless flow domes as rootless mounds. Although there is no mention of a perched lava pond, and it is unclear how high the rootless flow domes grew, their mechanism of formation seems similar to features at Volcán Llaima and elsewhere.

5.4.3 Synthesis of lava morphology features on Volcán Llaima

Lava from the 1780 eruption of Volcán Llaima may form a variety of morphological features: ʻaʻā, pāhoehoe, transitional features, and rootless mounds. However, one property is consistent everywhere: fresh breakouts produce pāhoehoe lavas. The lava then rarely flows as pāhoehoe for more than 50 m before breaking up and transitioning into ʻaʻā.

It may be inferred that the lava flows in a well-insulated tube prior to emerging at a downslope vent, such that it does not cool significantly (Helz et al., 2003). When the lava breaks out — either close to the main vent, or from a rootless source — it carries a high volume fraction of phenocrysts, and is able to flow as fluidal pāhoehoe due to the presence of bubbles. The rapid transition to ʻaʻā may result from an increase in viscosity, or from an increase in strain rate.

In the case of the transitional features seen at location 4, it appears that a change in viscosity is responsible for the transition. As the lava moves away from a breakout, it cools, degases, loses bubbles through outgassing, and crystallizes microlites. All of these processes lead to an increase in viscosity. The lava continues flowing on the same slope, but reaches the transition between pāhoehoe and ʻaʻā as a result of this viscosity increase. Once the flow forms a substantial carapace — whether pāhoehoe, slabby pāhoehoe, or ʻaʻā clinker — the interior becomes insulated again, allowing lava to flow through it without significant cooling. Thus the flow is able to break out again downslope as pāhoehoe, repeating the cycle.

In the case of the rootless mounds seen at locations 5 and 6, it appears that a change in strain rate is dominantly responsible for the transition. The lava reaches a break in slope when it moves off the summit of a rootless mound and onto the steeper flanks. The resulting increase in strain rate causes it to transition to ʻaʻā. Lava in the interior of a flow that reaches the edge of a mound, and transitions to ʻaʻā to flow down the flank, may then remain insulated and hot enough to break out as pāhoehoe again once the flow reaches the shallower slope at the base.

Lava flowing down the slopes of Vesuvius broke out when the tubes reached flatter ground (Rittmann, 1962). At Mount Etna, the breakouts were interpreted to occur in part due to the steep slope, maintaining a high hydrostatic pressure on lava in the tubes (Guest et al., 1984), and often formed on reaching a break in slope (Guest et al., 2012). The slopes of Volcán Llaima are similarly steep, and sharp breaks in slope occur on the current ground surface in many locations often due to the presence of erosional gullies cut by lahars. It is probable that the combination of steep slopes and breaks in slope are factors that favour the breakouts and ponding that must occur to trigger the building of rootless mounds.

5.4.4 Hazards associated with rootless edifices

One further aspect of rootless edifice growth that has not been touched on previously is the hazard implications of such features. During the 2007-2008 eruption of Kīlauea, in which multiple rootless shields formed, the shields collapsed on a num-

ber of occasions (Patrick and Orr, 2012). These collapses released large volumes of lava and produced fast-moving ʻaʻā lava flows — a significant contrast to the slowly advancing pāhoehoe flows normally produced during this eruption. Similarly, Guest et al. (1984) suggest that ʻaʻā flows associated with the 1614-1624 eruption of Mount Etna may have burst out from the front of a terrace. Storage and sudden release of large volumes of mobile lava from potentially unstable edifices is therefore an aspect of these features that would need to be considered for hazard assessment should they form during a contemporary eruption.

5.5 Conclusions

The 1780 lava flow field on Volcán Llaima displays a wide range of lava morphologies. The erupted lava was constantly close to the pāhoehoe-ʻaʻā transition: a small change in either strain rate or viscosity was enough to cause a transition at a number of locations. This flow field also produced newly described features - rootless mounds - that are comparable to rootless shields on Kīlauea, terraces and megatumuli on Mount Etna, and rootless flow domes on Vesuvius. This family of rootless edifices shares many features in common, while their differences depend on lava viscosity. Rootless edifices never form the dominant landform at any of these volcanoes, and occur only in a minority of eruptions at a single volcano.

Controls on the formation of rootless mounds, and similar shields at Kīlauea, Mount Etna, and Vesuvius, include the crystallinity of the lava, the eruption duration, and the presence of steep slopes and breaks in slope. Rootless edifices are not common enough to determine which of these characteristics are necessary to trigger their formation.

Chapter 6

Progressive degassing and crystallization of a Kīlauean lava

6.1 Introduction

Lava rheology is controlled by a number of inter-dependent factors (chapter 2.4). Understanding the evolution of these factors during an eruption is important for predicting the rheology of the lava, which in turn allows its likely flow style and associated hazards to be determined. Unlike at Volcán Llaima, where the predominant lava morphology is ʻaʻā, at Kīlauea the majority of vent proximal lava is pāhoehoe (Clague et al., 2000; Orr et al., 2013). Transitions to ʻaʻā tend to occur only after several kilometres of flow, although this depends on volumetric flow rate (MacDonald, 1953; Peterson and Tilling, 1980). Exceptions occur, however, particularly during periods of high lava flux (MacDonald, 1953; Kauahikaua et al., 2003) when vent proximal lava may begin flowing as ʻaʻā.

In this chapter, measurements of crystal and bubble populations and dissolved volatile contents are made for active lavas at a range of distances from the vent. This leads to an understanding of how the degassing of various species influenced the crystallization of the lava. In turn, this is combined with the three-phase viscosity model presented in chapter 3, to calculate the changes in lava rheology as it flowed away from the vent.

6.2 Kīlauea and the Pāhoa lava crisis

Kīlauea is the youngest and currently most active volcano on the Big Island of Hawaiʻi (figure 6.1). It has been continuously active since January 1983, and the

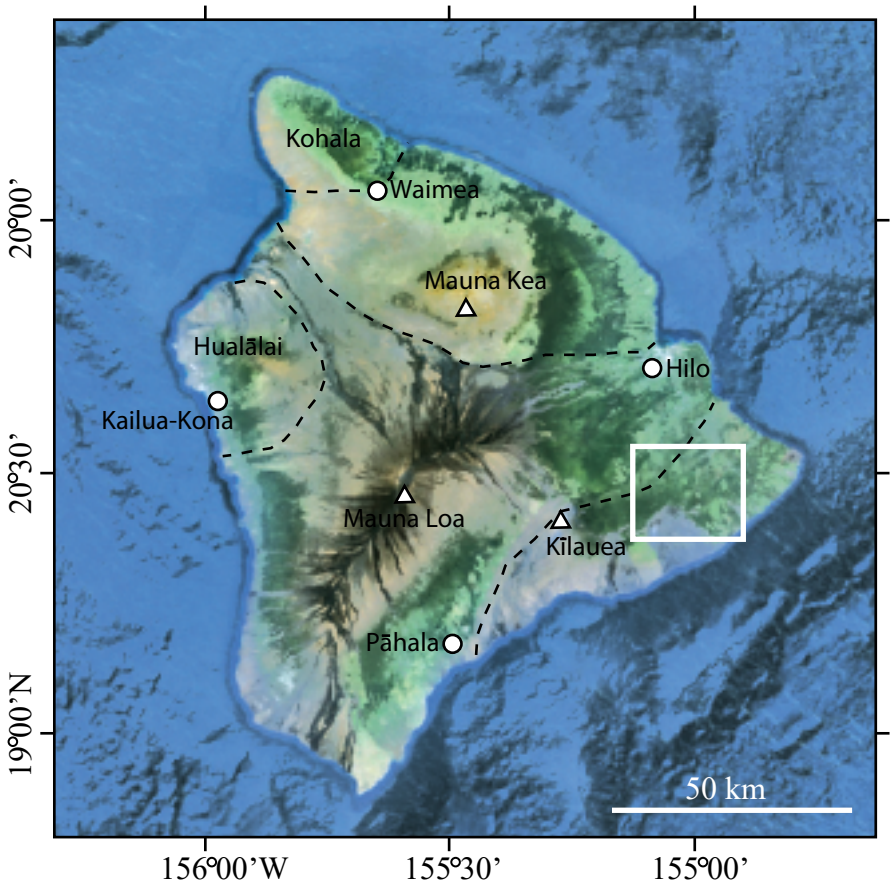

Figure 6.1: Aerial image of the Big Island, sourced from Google Earth. The location of the Pāhoa flows, samples, and figure 6.2 is shown by the white box.

historical record prior to this lists 61 eruptions since 1823 (Global Volcanism Program, 2016), in addition to many mentioned in earlier Hawaiian oral history (e.g. U.S. Geological Survey, 2009). This historical activity has been dominated by persistent activity at the Halema'uma'u crater, building of large pāhoehoe flow fields, and sporadic fountaining (e.g. Heliker et al., 2003; Poland et al., 2014). Between 1983 and 2014, much of the activity on Kīlauea was along the East Rift Zone, primarily at Pu‘u ‘Ō‘o (Orr et al., 2013), and most of the lava flowed towards the south. Flows with prolonged duration entered the ocean approximately 12km from the vent.

The most recent phase of activity on Kīlauea started on 27th June 2014. Lava flowed east and north east from Pu‘u ‘Ō‘o— in contrast to the majority of flows over the previous two decades — towards the town of Pāhoa and the Puna district. This region is home to around 10,000 residents, who rely on a single tarmacked highway to access the rest of the island (Poland et al., 2016). The initial direction of lava flow indicated that it would cross this highway, and cut off the power supply to the

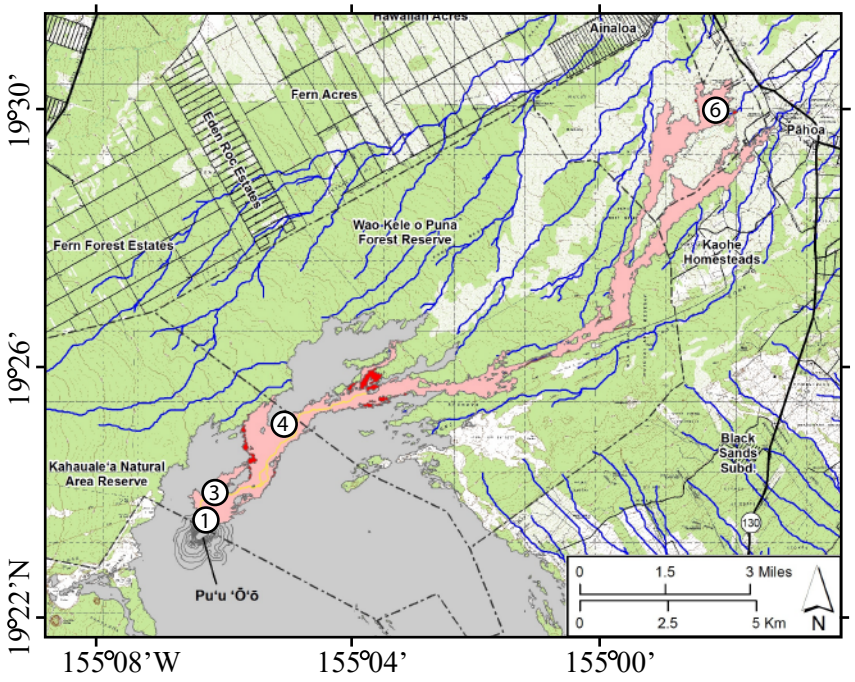

Figure 6.2: Map of Pāhoa lava flows. Pink shows outline of lava flow on 10th March 2015; red shows lava produced between 10th March and 1st April 2015 (from U.S. Geological Survey, 2015). Numbers in circles indicate locations of samples.

district.

On the way from the vent at Pu'u 'Ō'o to Pāhoa, the lava flowed through forested areas, causing fires and smoke. The average ground slope in this area is 1-2° and the lava typically followed lines of steepest descent, although it was sometimes diverted by previously unrecognized ENE-trending cracks (Poland et al., 2016).

Over the months of the eruption, a lava tube developed that extended from the vent all the way to the flow front. Although lava threatened to engulf the town multiple times, the flows always stopped - just short. Each time this occurred, the most distal lobe of lava became inactive and lava broke out from the tube closer to the vent.

There are several possible explanations for why this might have happened, and the one that will be examined here is that some intrinsic physical property of the lava changed as it progressed away from the vent such that continued flow of lava at the flow front near Pāhoa was not rheologically favourable. It is particularly important to understand the factors controlling how far this lava flowed, because this has implications for the hazards faced by local communities.

6.2.1 Samples

Samples were collected from a number of locations along the 27th June lava flow, in January and March 2015. Where possible, a range of quench methods were used and lava was sampled directly from the active flow.

The most proximal sample (site 1 on figure 6.2) was collected from very near a vent that had continued to feed more distal flows for several months, and as a result had cooled naturally and probably considerably more slowly than other samples. This sample was taken from a cold, solidified shelly pāhoehoe surface. There was extensive hydrothermal alteration in this area, and although material with the freshest appearance possible was chosen for sampling it is unlikely that this sample was truly pristine. As a result, most of the quantitative analyses presented in section 6.4 do not include this sample.

The second most proximal samples were collected from an active breakout on 5th March 2015, approximately 0.8 km down flow from the vent (site 3 on figure 6.2, and figure 6.3). The lava flowed as smooth, lobate pāhoehoe, and was sampled using a spade. Separate samples of the lava were quenched in several ways: by total immersion in water, by partial immersion in water, and in air. In addition, samples were taken from a naturally cooled lava toe, estimated to be between 1 hour and 1

Figure 6.3: Site 3 with smooth, lobate pāhoehoe. Quench samples were taken from this active breakout, which was 1.5 m wide at the point of break out.

day old.

The third group of samples were also collected on the 5th of March, from a fresh breakout approximately 3.6 km down flow from the vent (site 4 on figure 6.2). The pāhoehoe lava in this location appeared "gnarly" and "pasty", in stark contrast to the smooth fluidal pāhoehoe sampled at site 3. The active lava was again sampled with a spade, and quenched as for site 3. A naturally cooled lava toe, estimated to be between 1 hour and 1 day old, was also sampled.

The final group of samples were collected on the 13th January 2015, from a fresh breakout approximately 21.1 km down flow from the vent (site 6 on figure 6.2, and figure 6.4). The appearance of the lava at this location was similar to that at site 4 - gnarly and pasty, and it appeared considerably more viscous than the lava at site 3. The surface texture on this lava was similar to shark-skin pāhoehoe (Wentworth and MacDonald, 1953). Another set of variably quenched shovel samples were collected from the active lava, along with a lava toe, estimated to be less than 1 hour old. The toe cooled naturally until being cooled with water for transportation.

Figure 6.4: Site 6, with gnarly, pasty pāhoehoe. Quench samples were taken from this active breakout, which was 15cm wide at the point of break out.

6.3 Methods

In order to constrain the parameters that affect lava viscosity, a number of analyses were performed on the samples; a summary is given in table 6.1, where details of the various methods used are presented. All lavas from the June 27th flow are basaltic

Site	Sample	Quench type	TGA?	FTIR?	SEM?	Vesicularity
1	sp01	natural	yes	yes	yes	no
3	sp07	total water	yes	yes	yes	yes
3	sp03	partial water	yes	no	no	no
3	sp08	air	yes	no	no	no
3	sp09	natural	yes	yes	no	no
4	sp11	total water	yes	yes	yes	yes
4	sp10	partial water	yes	yes	no	no
4	sp13	air	yes	no	no	no
4	sp14	natural	yes	yes	no	no
6	s07	total water	yes	yes	yes	yes
6	s06	partial water	yes	no	no	no
6	s10	air	yes	no	no	no
6	s09	natural	yes	yes	no	no

Table 6.1: List of samples and techniques applied to each sample.

($SiO_2 \approx 51$, Tim Orr, pers. comm., 2016), and contain phenocrysts of plagioclase and pyroxene, both in isolation and aggregated together in glomerocrysts. The proportion of bubbles and crystals visibly changes from the most proximal to the most distal samples, as does the proportion of each sample with a glassy matrix, although this does depend on quench method in addition to distance from vent.

6.3.1 Vesicularity

The method of Houghton and Wilson (1989) was used to measure the vesicularity of the most quenched samples from each site. This method involves measuring the mass of a sample clast in air, and comparing it to the mass of the sample in water, when wrapped with parafilm to prevent vesicles from filling with water (Archimedes principle). Applying a correction for the mass of parafilm in water allows the specific gravity $S.G.$ to be calculated for each sample:

$$S.G. = \frac{(W_c)air}{(W_c)air + (W_s)water - (W_{c+s})water}, \tag{6.1}$$

where $(W_c)air$ is the mass of the clast in air, $(W_s)water$ is the mass in water of the parafilm used to wrap the clast, and $(W_{c+s})water$ is the mass of the parafilm-wrapped clast in water. This allows the clast density ρ_c to be calculated:

$$\rho_c = \frac{S.G.}{\rho_{water}} \tag{6.2}$$

where ρ_{water} is the density of water, $1000\,\mathrm{kg\,m^{-3}}$. From this, the vesicularity ϕ_b^* can be calculated:

$$\phi_b^* = \frac{\rho_{DRE} - \rho_c}{\rho_{DRE}} \tag{6.3}$$

where ρ_{DRE} is the density of the "dense rock equivalent", i.e. the density of a completely bubble-free sample. In this case, the dense rock equivalent was calculated to be $2622\,\mathrm{kg\,m^{-3}}$, using Pering (2013) and the composition of lava from the June 27th flow collected in December 2014 (table 6.2).

SiO_2	TiO_2	Al_2O_3	FeO	MnO	MgO	CaO	Na_2O	K_2O	P_2O_5
50.84	2.38	13.83	11.08	0.17	7.01	10.95	2.35	0.41	0.22

Table 6.2: Composition of June 27th lava flow, sampled in December 2014 (Tim Orr, pers.comm., 2016).

Repeating this method on a large number of clasts from the same sample allows a density histogram to be produced. Due to limitations on the available volume of sampled material, 13-15 fragments were analysed for each site. Although Houghton and Wilson (1989) recommend using their method on 30 or more fragments, to produce a density histogram, they note that the average vesicularity and standard deviation do not tend to change once at least 10 fragments have been analysed. As such, 13-15 should be sufficient in this case.

6.3.2 Scanning electron microscope (SEM)

A Hitachi SU-70 FEG SEM was used to capture backscattered electron (BSE) images of polished thin sections of the samples. For each sample, a montage of 140 images (covering an area of around 10 mm x 10 mm at 120 x magnification) was captured (figure 6.5).

The resolution on the individual images was high enough to clearly see acicular microlites 5 microns wide. Crystal populations were measured manually: the outlines of the crystals were traced in ImageJ, as shown in figure 6.6, and measurements of each crystal's area, Feret width (minimum crystal dimension) and Feret length

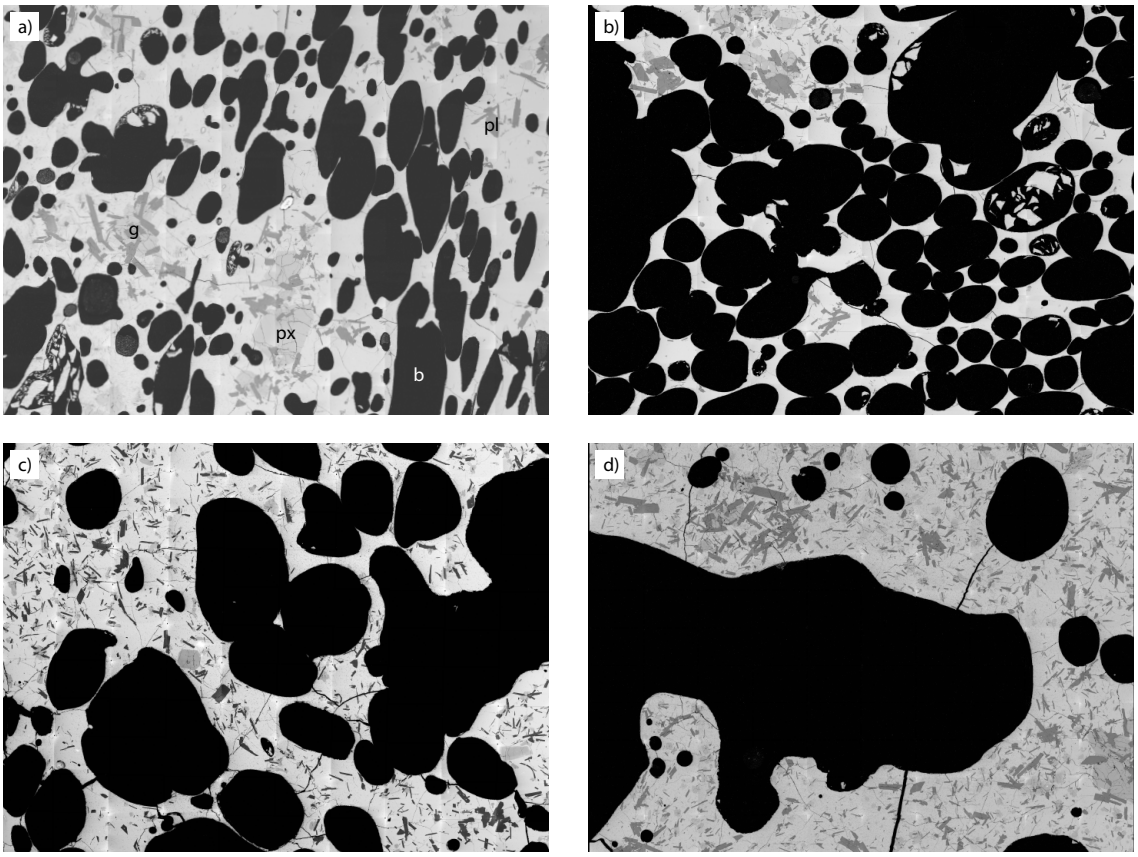

Figure 6.5: SEM montage images showing plagioclase (pl) and pyroxene (px) crystals and glomerocrysts (g) and bubbles (b) for the most rapidly quenched sample at a) site 1 sample sp01, b) site 3 sample sp07, c) site 4 sample sp11, and d) site 6 sample s07. Each montage (consisting of 140 images) is approximately 10 mm wide.

(maximum crystal dimension) were made. This was done using the high resolution images that contributed to the montages in figure 6.5, and counting continued until at least 500 isolated plagioclase crystals had been measured in each sample.

6.3.3 Thermogravimetric analysis (TGA)

Thermogravimetric analysis (TGA) consists of measuring the mass lost from a crushed sample as it is heated (as demonstrated by Applegarth et al., 2013). Volatiles that have been either adsorbed to the surface of the sample or dissolved within the sample at higher temperature are released over a range of temperatures. This method allows quantification of the mass of volatiles within the sample. The heat flow is measured using differential scanning calorimetry (DSC) alongside the mass changes. This allows the identification of internal physical changes, such as when the sample crosses the glass transition, and when crystals melt or grow. The DSC

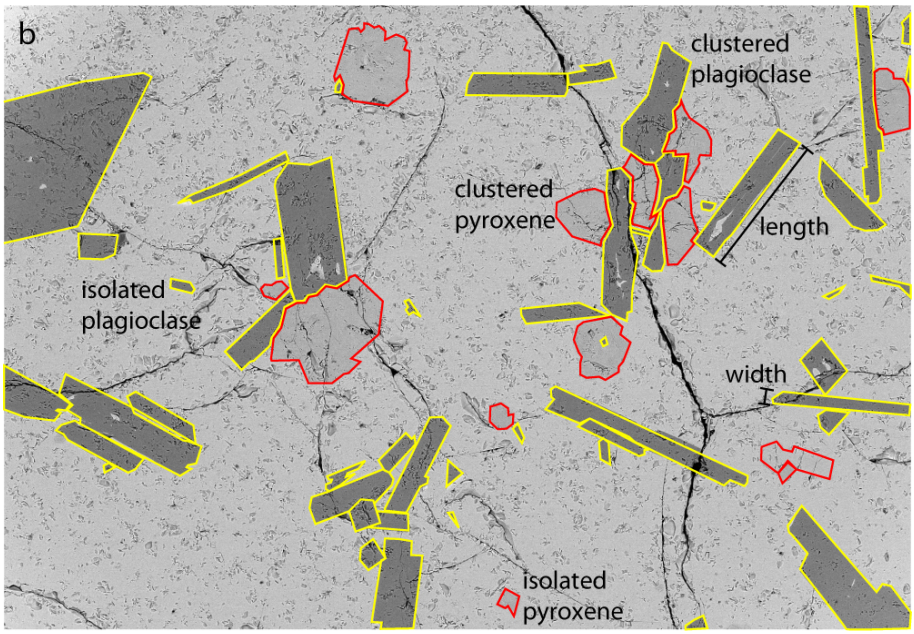

Figure 6.6: Outlined crystals in ImageJ, from the quenched site 6 sample. The image is approximately 1mm wide.

measurements are not used in this study.

A Netzsch STA449C Jupiter was used to collect simultaneous weight loss (TGA) and heat flow data (DSC). The weight signal calibration routine included measurement of internal standards for absolute values at 25°C and scanning calibration over the temperature range 25-1400°C using inert alumina standards of known weight, in order to create a buoyancy calibration. This is sensitive to the sample volume, and potential effects of sample oxidation if the furnace is contaminated by oxygen. A purge with oxygen-free nitrogen was used to minimize this source of uncertainty. Weight loss for each sample was characterized over the temperature range 25-1250°C, at a heating rate of 10°C per minute. Due to the low volatile concentrations of the samples (the maximum measured was 0.26 wt.%), a double heating routine was used, with the weight signal from the second heating used as an improved baseline. This method assumes that all volatiles were lost in the first heating so that no degassing occurs on the second heating, which has been shown to be appropriate (Tuffen et al., 2012; Applegarth et al., 2013). Combined uncertainties in the total weight loss measurements are approximately 0.03 wt.%, based on the adequacy of the second heating baseline, oxidation, and repeatability.

6.3.4 Fourier transform infrared spectroscopy (FTIR)

For samples indicated in table 6.1, Fourier transform infrared spectroscopy (FTIR) was used to measure the water content in double polished wafers, 50-120 μm thick. Clusters of crystals were avoided during these measurements, however small isolated crystals were unavoidable: the water contents from the raw data $\Phi_{H_2O,measured}$ have been re-calculated to account for the fraction of small isolated crystals $\phi_{isolated}$, giving the true water content of the glass: $\Phi_{H_2O,glass}$

$$\Phi_{H_2O,glass} = \frac{\Phi_{H_2O,measured}}{1 - \phi_p^*(\phi_{isolated})}, \tag{6.4}$$

and then for the bulk crystal fraction, giving the water fraction of the bulk sample $\Phi_{H_2O,bulk}$:

$$\Phi_{H_2O,bulk} = \Phi_{H_2O,glass}(1 - \phi_p^*), \tag{6.5}$$

so that the reported values are directly comparable to the TGA measurements.

The FTIR used for these measurements was the Thermo Nicolet IR interferometer at Lancaster University with a Continuum Analytical microscope, KBr beamsplitter, MCT-A detector and 100 μm square aperture. 128 spectra were collected at 4 cm^{-1} spectral resolution within the mid-IR range of 4000-1000 cm^{-1}, with a 12-point linear baseline correction used to quantify absorption peaks at 3550 cm^{-1} (-OHT) and 1630 cm^{-1} (H2Om). Sample thickness was determined using reflectance fringes (von Aulock et al., 2014). Sources of error include uncertainty in sample thickness, absorption coefficients and peak quantification (von Aulock et al., 2014) and typically combine to create uncertainty of 10%.

6.4 Results

6.4.1 Bubble populations

Bubble fractions calculated using the vesicularity method presented in section 6.3.1 for each of the fully water quenched samples are plotted against down flow distance from the vent, in figure 6.7. These measurements show clearly the significant reduction in bubble fraction with distance.

In addition, the bubble shapes change with distance, as can be seen in the SEM images in figure 6.5. The most proximal sample contains bubbles that appear to be spheroidal. With increasing distance, the bubble shapes become more distorted and large, non-spheroidal bubbles become more common. In all cases, the smallest

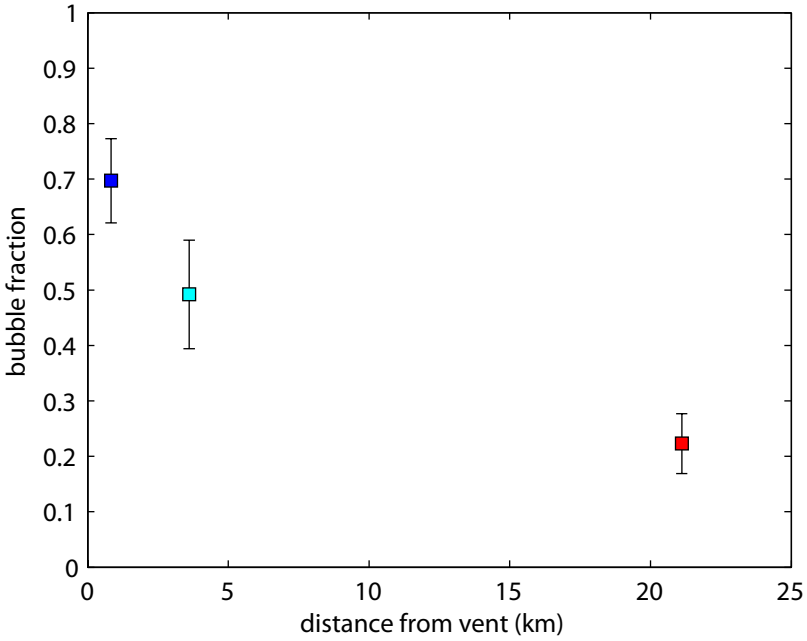

Figure 6.7: Plot of total bubble fraction using vesicularity method against distance from vent. Site 3, sample sp07 is shown in dark blue; site 4, sample sp11 is shown in pale blue; and site 6, sample s07 is shown in red. The error bars indicate the standard deviation from 13-15 measurements for each site.

bubbles appear to be closer to spherical; the limit above which bubbles lost their sphericity was a radius of approximately 0.1 mm.

6.4.2 Crystal populations

All samples contain phenocrysts and microphenocrysts of plagioclase feldspar and pyroxene. These are often found in clusters of significantly intergrown crystals (glomerocrysts), and are also found in apparent isolation. The higher resolution SEM images used to create the montages in figure 6.5 were used to measure the size and aspect ratio of crystals. The most numerous type of crystal in any sample was always isolated plagioclase, followed by clustered plagioclase, clustered pyroxene, and isolated pyroxene (one example image is shown in figure 6.8).

The observed crystal populations and textures change both with distance from the vent and with type of quench. The crystal population that most closely represents the crystal cargo of flowing lava is likely to be captured by the most rapidly quenched samples: for site 1, this is naturally cooled sample sp01; for sites 3, 4 and 6, these are totally water quenched samples sp07, sp11, and s07 (figure 6.5; see figure 6.2 for sample locations). As a result of being naturally cooled rather

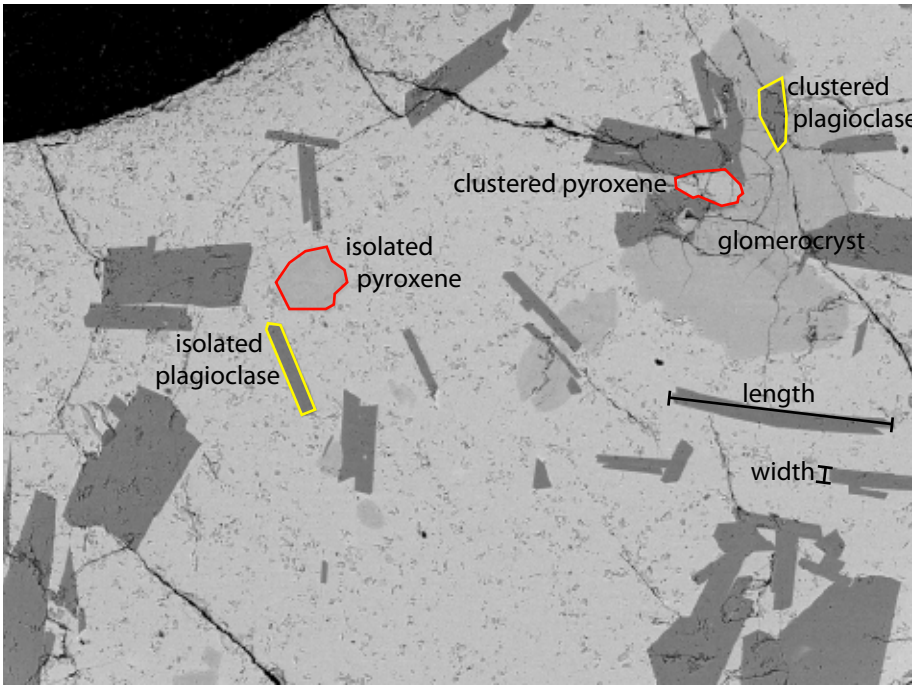

Figure 6.8: Examples of clustered (glomerocryst) and isolated plagioclase and pyroxene crystals, from the fully water quenched site 6 sample. The image is approximately 1 mm wide.

than quenched, the site 1 sample contains relatively little clean glass, and it can be difficult to confidently distinguish microlites that grew during cooling from microlites and microphenocrysts carried by the lava while it flowed. The totally water quenched samples from the remaining sites contain clean glass with no sign of microlite growth, and can be used to understand how the crystal cargo changed as the lava flowed away from the vent.

From the SEM montage images (figure 6.5), it is clear that the crystal fraction (ϕ_p^*) increases with distance from the vent. This increase was quantified by measuring the area, length, and width of individual crystals in the higher resolution images (e.g. figure 6.8) in ImageJ: crystal fractions based on area measurements are plotted in figure 6.9.

In addition to the bulk increase in crystal fraction, there are more subtle changes in the characteristics of the crystal population with distance from the vent. Since crystal size measurements (i.e. length and width, as shown in figure 6.8) were made using two-dimensional thin sections, it is necessary to account for the true three-dimensional shapes and sizes of the crystals. CSDCorrections (Higgins, 2000) is a piece of software designed to calculate the three-dimensional crystal population that could have produced an observed two-dimensional crystal population. This software is commonly used in volcanological applications (e.g. Higgins and Meilleur,

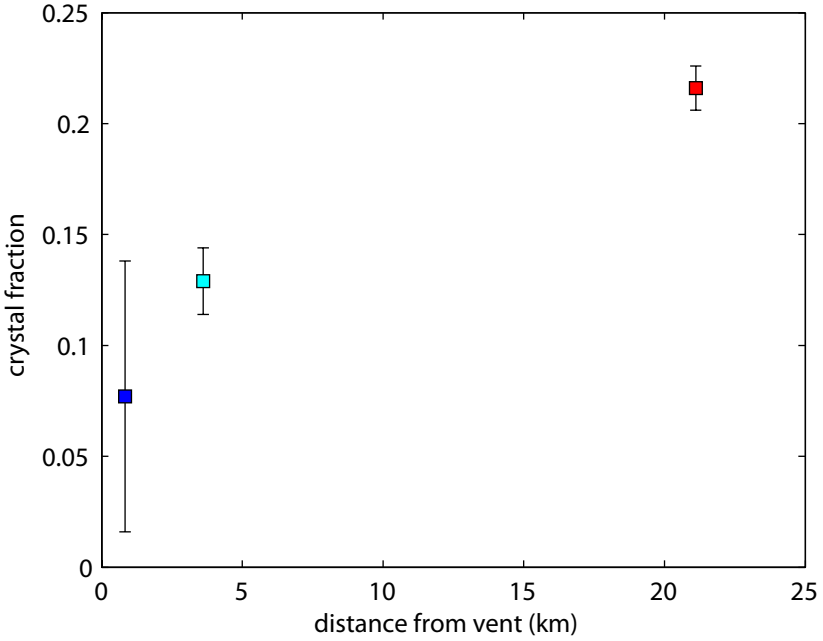

Figure 6.9: Plot of total crystal area fraction against distance from vent. Site 3, sample sp07 is shown in dark blue; site 4, sample sp11 is shown in pale blue; and site 6, sample s07 is shown in red. Error bars show standard deviations based on repeated measurements of an area of 5.7 mm^2 (equivalent to 8 high resolution SEM images, which is visually a roughly representative area for each sample). The large standard deviation for site 3 is due to the heterogeneties created by the clustered crystals; in other samples, this effect is reduced due to the larger fraction of non-clustered crystals.

2009; Vona et al., 2013; McClinton et al., 2014), and the crystal size distributions resulting from inputting observed two-dimensional size distributions in these lavas are shown in figure 6.10. Both the shift to larger crystal sizes and the increase in crystal fraction with increasing distance from vent are clear. This trend is seen in all four groups of crystals.

In order to calculate the effect of crystals on rheology, two parameters are needed: the volume fraction and the maximum packing fraction, which in turn is affected by aspect ratio and particle roughness. The volume fraction will be the same whether crystals are dealt with in isolation or as part of clusters; the aspect ratio and roughness are not. The glomerocrysts tend to be more equidimensional than isolated crystals, but have a higher rugosity. The former factor will tend to increase the maximum packing fraction, while the latter will tend to reduce it, compared to the smooth, more elongate isolated crystals.

Dealing with a polydisperse population of crystals in general is never trivial, and typically results in a complicated effective medium method, in which the smallest

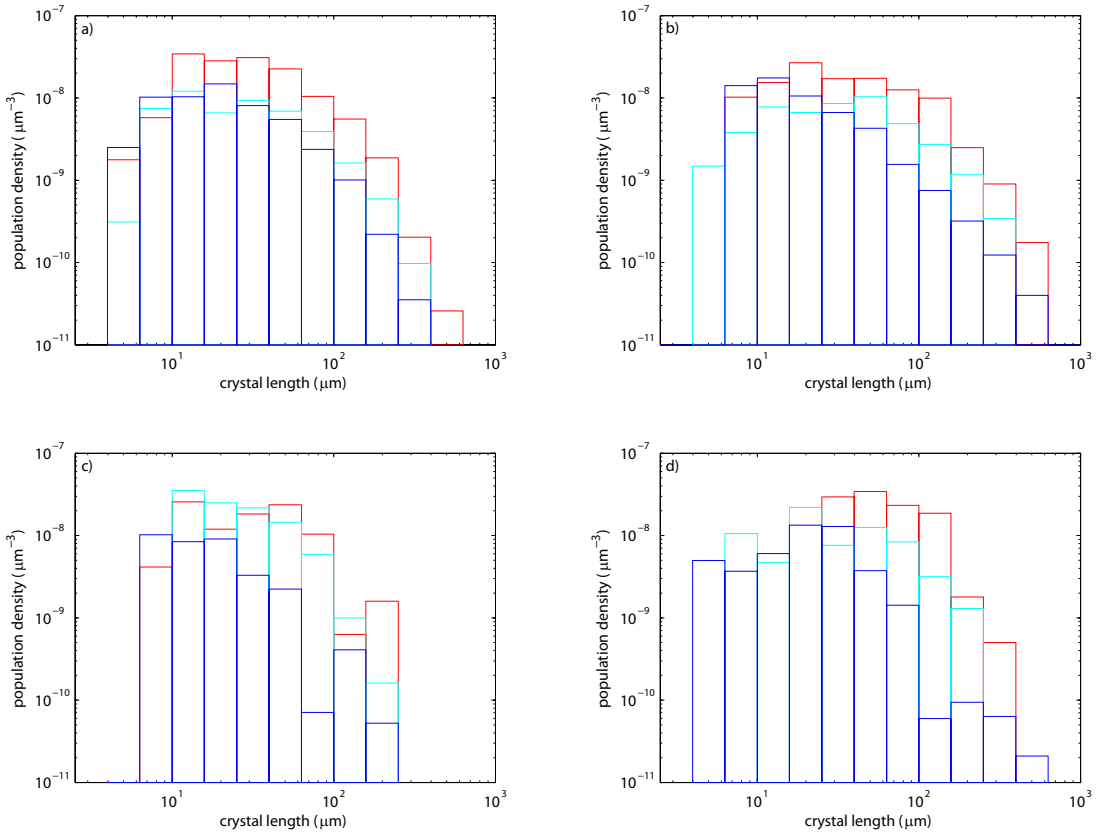

Figure 6.10: Number of crystals per unit bubble-free volume (population density) in each crystal length interval, as calculated from CSDCorrections. a) isolated plagioclase, b) clustered plagioclase, c) isolated pyroxene, and d) clustered pyroxene. Site 3, sample sp07 is shown in dark blue; site 4, sample sp11 is shown in pale blue; and site 6, sample s07 is shown in red.

crystals are considered first and additional populations of increasingly large crystals are then added. This level of complexity is probably unnecessary here: the crystal sizes vary by less than an order of magnitude, which is typically quoted as the minimum size difference needed for a continuous medium method to be justified (Farris, 1968). As a result, instead of considering the effects of the different crystal populations independently, the crystals that compose the glomerocrysts have been treated as individuals, rather than clusters. Although this is a simplification, it does seem justified here, as discussed above.

6.4.3 Volatile content

FTIR measurements (figure 6.11) show that the dissolved water content in the glass increases slightly with distance from the vent, although there is significant overlap in the errors. The measured water contents are close to the atmospheric solubility

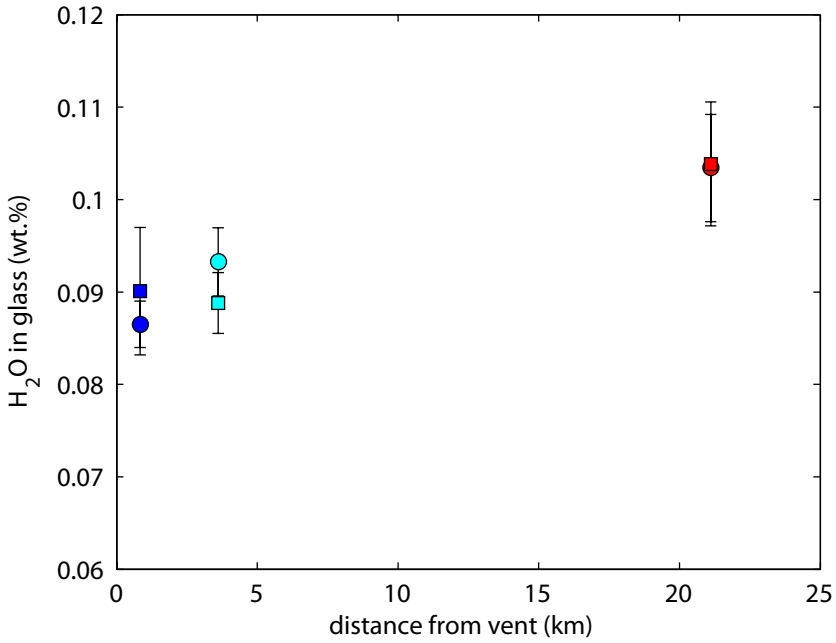

Figure 6.11: Water content (wt.% H_2O) in the glass $\Phi_{H_2O,glass}$, measured using FTIR, against distance from vent. Site 3 is shown in dark blue, site 4 is shown in pale blue, and site 6 is shown in red. Squares indicate totally water quenched samples, and circles indicate naturally cooled samples. Error bars represent standard deviation from 7-13 repeat measurements.

value for water in a basaltic melt (0.11 wt.% at 1200°C Dixon et al., 1995), and comparable to those found by Carey et al. (2013) for earlier lavas at Kīlauea. The bulk water content in the sample (figure 6.12) does not change with distance from the vent.

Mass loss measured using TGA tells a more complicated story. The amount of mass lost above 500°C (i.e. magmatic mass loss as opposed to adsorbed surface water) does vary with distance from the vent, as shown in figure 6.13. Although there is significant scatter, the most proximal samples all show greater mass loss than increasingly distal samples.

6.5 Discussion

6.5.1 Volatile content variations

The bulk FTIR measurements are between 0.077 and 0.083 wt.% H_2O for all samples, and the one standard deviation error bars shown in figure 6.12 overlap. However, the water content in the glass increases gradually with distance from the vent, from

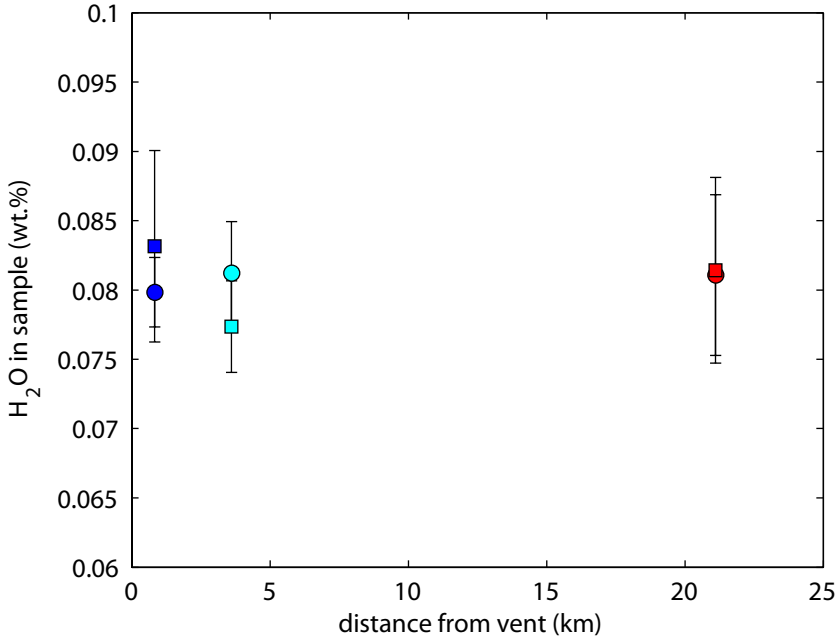

Figure 6.12: Water content (wt.% H_2O) in the bulk sample $\Phi_{H_2O,bulk}$, measured using FTIR, against distance from vent. Site 3 is shown in dark blue, site 4 is shown in pale blue, and site 6 is shown in red. Squares indicate totally water quenched samples, and circles indicate naturally cooled samples.

around 0.088 wt.% to 0.104 wt.%. The simple explanation for the discrepancy between these results is that as the crystal fraction increased with distance from vent (figure 6.9), the residual melt fraction decreased, and the volatiles became concentrated in the melt. Contemporaneously with this, the temperature of the melt would have been decreasing, resulting in a gradual increase in the solubility of water, allowing the water to remain in the melt rather than being exsolved, and leading to a decrease in the bulk water content. This process has been shown to account for increasing dissolved water content in silicic melts as they cool (Liu et al., 2005; Ryan et al., 2015).

The TGA measurements of mass loss from the bulk samples show a much wider range of weight loss than the FTIR bulk measurements, from 0.077 to 0.259 wt.% (figure 6.13). Although some of the mass loss measured by the TGA must be due to the loss of water — as measured by the FTIR — this does not explain the full extent of the mass loss. Figure 6.14 shows the discrepancy between the bulk mass loss measured by TGA and the bulk water content measured by FTIR, for samples in which both types of analysis were made. For the most distal samples the water content explains the majority of the TGA mass loss, but for the most proximal

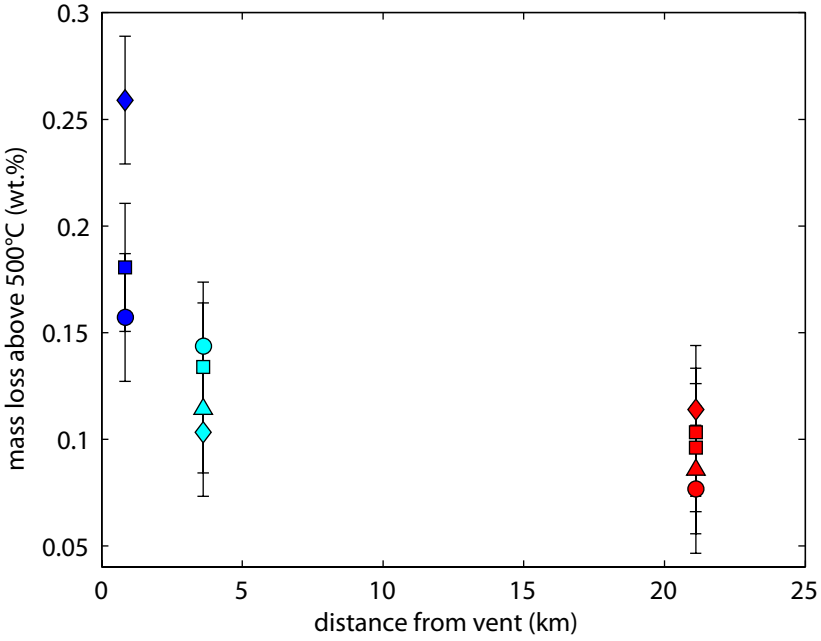

Figure 6.13: Mass loss (wt.%) from crushed sample during heating, measured using TGA, against distance from vent. Site 3 is shown in dark blue, site 4 is shown in pale blue, and site 6 is shown in red. Squares indicate totally water quenched samples, diamonds indicate partially water quenched samples, triangles indicate air quenched samples, and circles indicate naturally cooled samples.

Volcano	S (wt.%)	Cl (wt.%)	F (wt.%)	Total (wt.%)
Kīlauea [a]	0.0065-0.014	0.0051-0.0155	0.03-0.04	0.0416-0.0633
Kīlauea [b]	0-0.02			0-0.02
Mauna Loa[c]	0.0068-0.0373	0.0064-0.0119	0.0260-0.0527	0.0392-0.102

Table 6.3: Mass fractions of sulphur, chlorine, and fluorine in subaerial lavas from Kīlauea ([a] Swanson, 1973); Halema‘uma‘u, Kīlauea ([b] Helz et al., 2014); and Mauna Loa ([c] Davis et al., 2003)

samples there is as much as 0.097 wt.% mass loss in addition to the measured mass of water.

A hypothesis that would explain this discrepancy is that the samples contain other volatiles in addition to water. These would be lost as the sample is heated during the TGA measurements, and so would contribute to the measured mass loss, but would not be detected by the FTIR technique. Therefore the difference between the TGA mass loss and the FTIR water content would provide a measure of the mass of these additional volatiles.

Sulphur, chlorine, and fluorine measurements from subaerially erupted lava from Kīlauea (Swanson, 1973; Helz et al., 2014) and Mauna Loa (Davis et al., 2003) are summarized in table 6.3. The total mass provided by these additional volatiles is

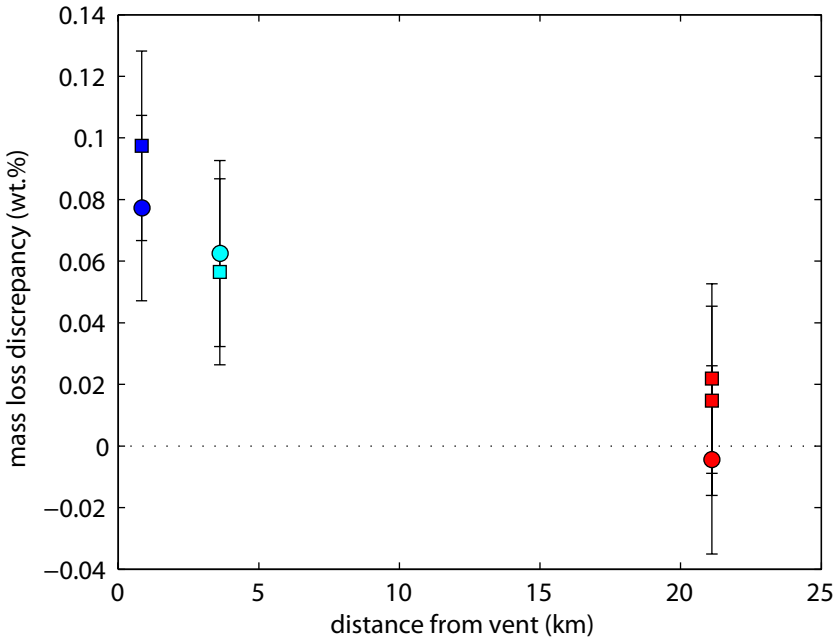

Figure 6.14: Difference between mass loss measured by TGA and H_2O content measured by FTIR. Site 3 is shown in dark blue, site 4 is shown in pale blue, and site 6 is shown in red. Squares indicate totally water quenched samples, and circles indicate naturally cooled samples. The dashed black line is zero — where the TGA mass loss would be the same as the water content measured by FTIR.

comparable to the range of excess masses measured by the TGA (up to 0.097 wt.%), therefore it seems plausible that the presence of these volatiles in addition to water explains the high TGA mass loss values.

6.5.2 Degassing and crystallization history

The FTIR measurements of water content (0.0883-0.104 wt.%) indicate that within 0.83 km of the vent (site 3) the water content had equilibrated to approximately atmospheric values (Dixon et al., 1995). If the excess mass loss measured by TGA is due to a combination of sulphur, chlorine and fluorine, an explanation is needed for why these species did not also equilibrate to atmospheric values as rapidly.

Exsolution is limited by the rate at which volatiles can diffuse through a melt. Based on typical eruptive temperatures from Kīlauea (≈1155°C Helz et al., 2003), and the measured water concentrations (≈ 0.09 wt.%), the diffusivity of water (D_{H_2O}) and sulphur (D_S) can be calculated using equations provided by Zhang

et al. (2007):

$$\ln \frac{D_{H_2O_t}}{C_w} = -8.56 - \frac{19110}{T}, \ln D_S = -8.21 - \frac{27692 - 651.5C_w}{T} \tag{6.6}$$

where C_w is the dissolved water content in wt.% (equations 18 and 31, respectively). Under these conditions, the diffusivity of water is $D_{H_2O} = 2.7 \times 10^{-11}\,\mathrm{m^2\,s^{-1}}$, and the diffusivity of sulphur is over an order of magnitude lower, at $D_S = 1.1 \times 10^{-12}\,\mathrm{m^2\,s^{-1}}$. Therefore if water had become equilibrated to atmospheric pressures within an upper limit 0.83 km of the vent it is expected that sulphur would be equilibrated within an upper limit of 20.4 km, assuming a constant flow rate. Without more samples in between sites 4 and 6, or closer to the vent, it is difficult to calculate more precisely how far the lava would have flowed before sulphur became equilibrated.

Rapid exsolution of water to reach atmospheric equilibrium tends to cause undercooling in Hawaiian lavas (Lipman et al., 1985; Crisp and Baloga, 1994; Applegarth et al., 2013), leading to rapid crystallization. Further and continuing crystallization is also likely to have been caused by the gradual decrease in lava temperature with distance, although this is commonly small for well-insulated tube-fed lava flows (e.g. Helz et al., 2003). Thus two factors likely control the increasing crystallinity with distance observed here: undercooling due to volatile exsolution and temperature decrease over time and distance.

6.5.3 Evolution of lava rheology and morphology

The first step towards calculating the lava viscosity at Kīlauea is to calculate the melt viscosity. The model of Giordano et al. (2008) accounts for melt composition, including water and fluorine contents, but does not account for chlorine and sulphur, which have comparably minor influences on viscosity. From the measurements shown in table 6.3, fluorine typically accounts for just over half the total mass of fluorine, chlorine and sulphur together. In order to estimate the fluorine content of the samples from the Pāhoa lava flows, it is therefore assumed that half the "excess" mass loss shown in figure 6.14 is due to fluorine. Estimates of fluorine in the glass for each sample location are given in table 6.4. The composition of lava collected from the June 27th flow in December 2014 (table 6.2) is used for the remaining compositional input required for the model. The temperature is also needed for this viscosity model; this can be estimated based on typical eruptive temperatures ($\approx 1155\,^\circ$C Helz et al., 2003), rates of temperature drop in lava tubes (typically $\approx 0.6\,^\circ$C /km Thornber, 2001; Helz et al., 2003; Riker et al., 2009), and the distance

Property	Site 3	Site 4	Site 6
Distance from vent km	0.83	3.61	21.1
Crystallinity ϕ_p^*	0.077	0.129	0.216
Mean aspect ratio	5.1	4.9	4.5
Bubble fraction	0.697	0.492	0.223
Assumed temperature ($\circ$C)	1154.5	1152.8	1142.3
FTIR water in glass (wt.%)	0.0883	0.0910	0.1036
Excess mass loss (wt.%)	0.0947	0.0683	0.0136
Assumed fluorine in glass (wt.%)	0.0473	0.0342	0.0068

Table 6.4: Key properties required to calculate viscosity.

down flow at which each sample was collected (table 6.4). Results of the melt viscosity calculations are given in table 6.5 and shown in figure 6.15. The decreases

Property	Site 3	Site 4	Site 6
Melt viscosity μ (Pa s)	85.4	89.1	113
Relative viscosity (low Ca) $\eta_{r,*}$	4.91	3.99	4.87
Bulk viscosity (low Ca) η (Pa s)	419	356	548
Relative viscosity (high Ca) $\eta_{r,*}$	0.203	0.656	2.49
Bulk viscosity (high Ca) η (Pa s)	17.4	58.5	280

Table 6.5: Viscosities calculated for each location, for the melt and for low and high capillarity bubbles.

in fluorine content and temperature with distance both lead to an increase in melt viscosity; this competes with the slight increase in dissolved melt water content with temperature and distance, which would reduce the melt viscosity.

In this calculation, it has been assumed that lava temperature depends entirely on the distance travelled along the — very well insulated — lava tube. This is likely to be accurate for breakouts that occur directly from the tube, but once lava has broken out its temperature will decrease much more rapidly. As such, by the point at which a breakout was sampled, its viscosity could have dropped by several degrees, compared to its initial breakout temperature. Unfortunately, the distance at each site that the breakout travelled before being sampled was not measured in the field; as a result, it is not possible to quantify the post-breakout temperature drop. A range of post-breakout distances would potentially explain the observed visual increase in viscosity with distance: for more distal sites, the tube may not be so well established and insulated, and the breakout may have travelled further from the tube prior to being sampled. Since a range of viscosities and strain rates can produce the same lava morphology, it is not possible to uniquely identify viscosity

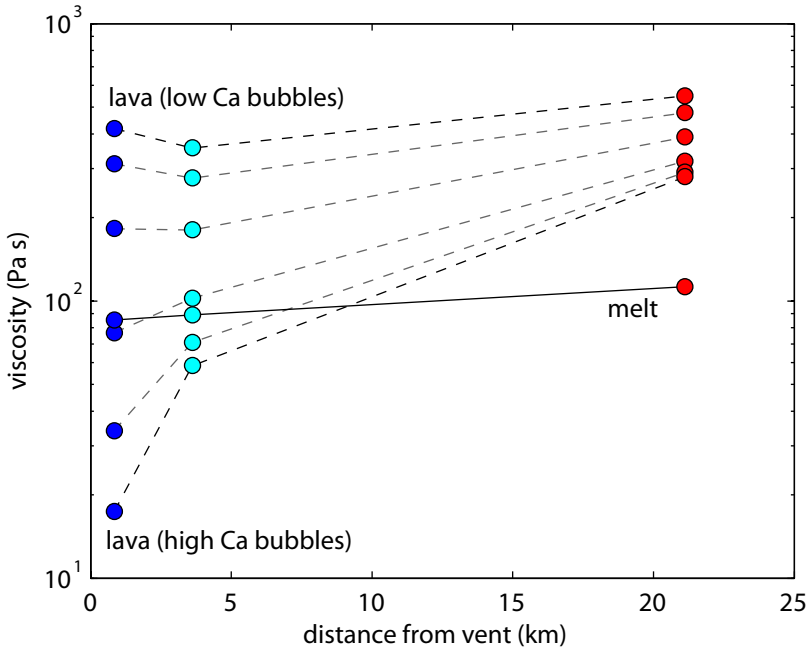

Figure 6.15: Calculated melt (solid line) and bulk (dashed lines) viscosities. Site 3 is shown in dark blue, site 4 is shown in pale blue, and site 6 is shown in red. The bulk viscosities are calculated based on the two extremes of low and high capillarity bubbles (black dashed lines), and using equation 6.8 for intermediate capillarities (grey dashed lines; Ca = 0.5, 1, 2, 4).

based on observations of morphology.

In order to calculate the bulk lava viscosity, the two suspended phases (crystals and bubbles) must be considered. Unlike the experimental samples used in chapter 3, the lavas here clearly contain bubbles that are significantly larger than the crystals. The appropriate form of the three-phase equation can therefore be formulated by considering a bubble suspension in which the continuous medium is a particle suspension, as discussed in section 3.5.3.3.

In order to determine which variant of the equation to use, it is also necessary to calculate the capillary number appropriate for bubbles in this suspension. Using equation 2.2, repeated here for convenience:

$$Ca = \frac{\mu a \dot{\gamma}}{\Gamma}, \tag{6.7}$$

where μ is the melt viscosity, a is the bubble radius, $\dot{\gamma}$ is the strain rate, and Γ is the surface tension. As shown in figure 6.15, all samples have μ 85-113 Pa s; from figure 6.5, typical bubble radii in the proximal samples are $a \approx 1$ mm; and Khitarov et al. (1979) provides $\Gamma \approx 0.1$-$0.4\,\mathrm{N\,m^{-1}}$. Lava toes were typically observed to be around 1 m wide and 10 cm tall, and advanced at around $10\,\mathrm{cm\,s^{-1}}$: strain rates were likely

to be in the range $\dot{\gamma} \approx 0.1 - 1\,\mathrm{s}^{-1}$. Using these values, the capillary number of an average sized bubble in these lavas is likely to have been in the range 0.01 to 0.61. This implies that while smaller than average bubbles are likely to have been in the low capillarity regime, larger than average bubbles may have reached the high capillarity regime.

As such, equation 2.4 will be used as the bubble suspension component of the appropriate three-phase relative viscosity equation:

$$\eta_{r,*} = \left(\eta_{r,\infty} + \frac{\eta_{r,0} - \eta_{r,\infty}}{1 + \left(\frac{6}{5}Ca\right)^2}\right)\left(1 - \frac{\phi_p^*}{\phi_m}\right)^{-2}. \tag{6.8}$$

where

$$\eta_{r,0} = (1 - \phi_b^*)^{-1} \tag{6.9}$$

$$\text{and} \qquad \eta_{r,\infty} = (1 - \phi_b^*)^{\frac{5}{3}}. \tag{6.10}$$

The relative viscosity values for the low and high capillarity limits (based on a three phase viscosity in which the bubble suspension component is given by $\eta_{r,0}$ and $\eta_{r,*}$ respectively) given by this equation are provided in table 6.5. Equation 6.8 can be used to calculate the reference viscosity $\eta_* = \mu\eta_{r,*}$, for various capillarities, as plotted in figure 6.15.

Since a model for the flow index of suspensions in which bubbles are larger than particles and in either capillarity regime does not exist, only the shear thinning effect of the crystals will be accounted for here (using equation 2.14). The apparent viscosity of the lava will therefore be given by:

$$\eta = \eta_* \dot{\gamma}^{n-1}, \tag{6.11}$$

which is plotted in figure 6.16. It can be seen from this figure that the lava at the most distal site (site 6) would have been in or close to the pāhoehoe-ʻaʻā transition, no matter what capillarity regime the bubbles were in. However, the more proximal sites (sites 3 and 4) show a much wider range of viscosities, depending on the strain rate. This is because the bubble fraction is much larger in these samples, and so the difference between low and high capillarity is much more significant.

In the samples, a range of bubble sizes are present - the bubbles are not all 1 mm radius, as assumed in the calculations for figure 6.16. Larger bubbles will enter the high capillarity regime at lower strain rates, leading to the decrease in viscosity occuring at lower strain rates. Similarly, smaller bubbles will enter the

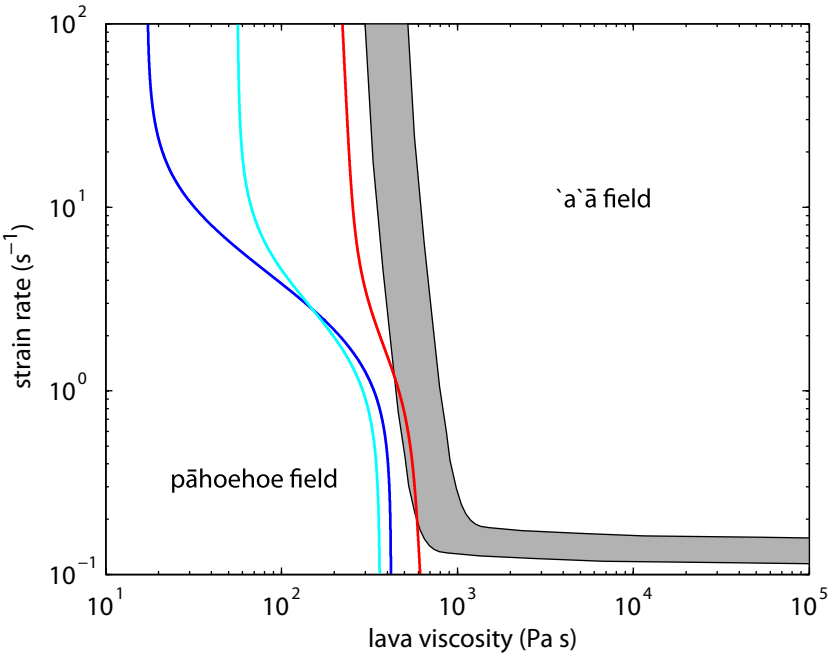

Figure 6.16: Diagram showing the relationship between strain rate, lava viscosity, and lava flow morphology, after Hon et al. (2003). The shaded region indicates the transition zone between pāhoehoe and ‘a‘ā; the pāhoehoe field is found at low viscosities and strain rates; the ‘a‘ā field is found at high viscosities and strain rates. Site 3 is shown in dark blue, site 4 is shown in pale blue, and site 6 is shown in red. Strain rate-viscosity relationship is calculated for typical bubbles of 1 mm radius, and a surface tension of 0.2 N m^{-1} (within the range found by (Khitarov et al., 1979)).

high capillarity regime at higher strain rates.

In the field it was observed that the lava at site 3 appeared to be considerably less viscous than the lava at site 4. From figure 6.16, this implies that the bubbles (at site 3, at least) are likely to have been in the high capillarity regime, such that the viscosity would have been lower than at site 4, even for the strain rates observed (0.1-1 s^{-1}). In order for the bubbles to have been dominated by high capillarity behaviour, the bubble sizes would have had to be slightly larger than those estimated from the SEM images in figure 6.5. This could be the case if either the bubbles imaged were not representative of the flowing lava, or if a smaller number of large bubbles controlled the overall capillarity of the suspension.

There are a large number of factors that influenced the viscosity of the Pāhoa lava. Figure 6.17 shows how these break down. If the bubbles were in the low capillarity regime, it can be seen that the loss of low capillarity bubbles reduces the viscosity down flow. This reduction would be just overcome by the growth of crystals and increase in melt viscosity, leading to the overall slight increase in viscosity

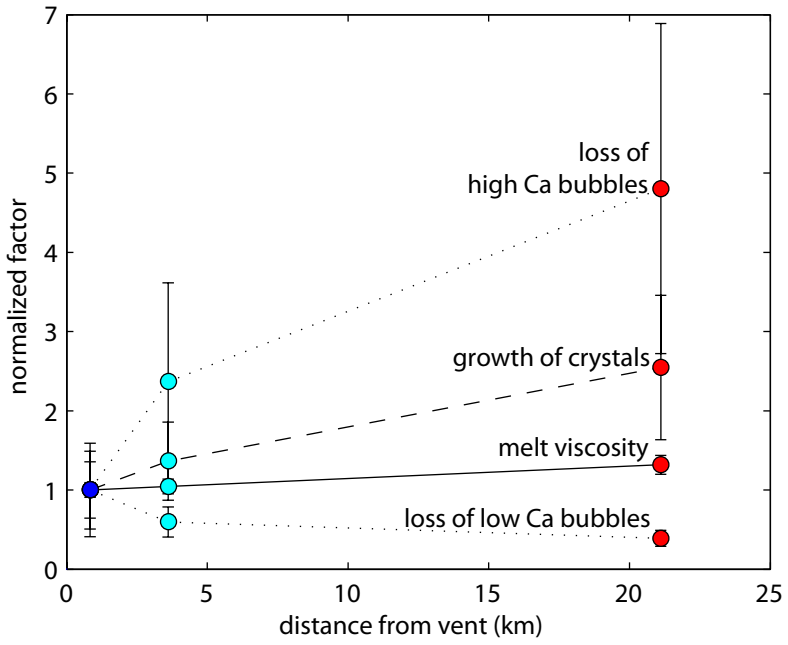

Figure 6.17: Influence of different factors on viscosity. Each factor is normalized to 1 at site 3. The increase in melt viscosity is smaller than the changes in the other factors. Crystallization leads to a large increase in viscosity, while loss of bubbles may decrease viscosity (for high capillarity bubbles) or increase viscosity (for low capillarity bubbles). Site 3 is shown in dark blue, site 4 is shown in pale blue, and site 6 is shown in red. The errors shown are based on propagation of errors on measured values.

shown for the low capillarity extreme in figure 6.15. If the bubbles were in the high capillarity regime, on the other hand, loss of these bubbles would significantly increase the viscosity down flow. This increase is greater than the increases due to crystal growth and melt viscosity increase, and leads to the even larger change in viscosity seen in the high capillarity extreme in figure 6.15. In this case, the transition to higher viscosities is driven more by outgassing than by crystallization or degassing.

6.6 Conclusions

Observations and samples from active lava flows on Hawai‘i have been used to constrain the factors that influence lava rheology. Measurements of the mass of dissolved volatile phases (H_2O, S, Cl, F) were used to calculate the viscosity of the basaltic melt. Crystal size distribution and aspect ratio measurements, along with bubble fractions — and capillarity — were used to calculate the influence of the suspended phases on viscosity.

The FTIR measurements indicate that water degassed at or near the vent, so that the dissolved water content reached atmospheric saturation levels very rapidly. The bulk water content remained the same throughout the flow, although water became concentrated in the melt due to crystallization; this was possible due to the slight increase in solubility during cooling. Dissolved water content is a strong control on melt viscosity, and the slight increase in dissolved water in the melt was accounted for in the viscosity calculations. Slower diffusing volatiles (e.g. F, Cl, S) took longer to reach equilibrium, and TGA measurements show that their mass decreased with distance from the vent. The mass of each species could not be determined from the TGA measurements, so the mass of S (which has an effect on viscosity) was estimated based on the proportions measured in other Hawaiian lavas. Undercooling caused by volatile exsolution at the vent, combined with temperature reduction with distance from the vent, led to crystallization as the lava flowed away from the vent.

The combination of changing volatile contents, decreasing bubble fraction, and increasing crystallinity caused an order of magnitude increase in viscosity in this lava from vent to flow tip. The relationship between strain rate and viscosity can be calculated using equations for the viscosity (from chapter 3) and flow index (equation 2.14), and compared to the expected pāhoehoe and ‘a‘ā fields (figure 6.16). Both the low and high capillarity regimes predict an increase in viscosity from the proximal sites (sites 3 and 4) to the distal site (6). This explains why the lava transitioned from smooth, fluidal pāhoehoe near the vent, to a more gnarly, pasty pāhoehoe at greater distances.

Chapter 7

Synthesis and conclusions

7.1 The importance of rheology in the volcanic system

Using the experimental results presented in chapters 3 and 4, this thesis has demonstrated how three-phase rheology affects the volcanic system through three case studies (in chapters 4, 5 and 6, and indicated on figure 7.1). There are many other parts of the volcanic system in which multi-phase rheology is important however. Beginning with a fresh intrusion into a crystallizing magma reservoir and ending with lava flowing on the surface, this discussion will serve as a synthesis of the topics considered in the thesis and put them into context.

7.1.1 In the magma reservoir

There is extensive evidence that magma reservoirs are built up over time by repeated injections of magma (Coleman et al., 2004). Commonly, this recharge magma is more volatile-rich (less degassed), and less crystalline than the reservoir into which it is intruded (Huppert et al., 1982; Bouvet De Maisonneuve et al., 2013; Myers et al., 2014). In some cases, there is evidence that the magmas mixed completely prior to eruption (e.g. Kent et al., 2010). In others, enclaves of one are included as xenoliths in the other (e.g. Eichelberger, 1980; Barclay et al., 2010). There are also different scales on which mixing and mingling occurs — for example, two magmas may exchange phenocrysts, but not become homogenised on a microscopic scale. The degree to which mixing between the two magmas occurs depends strongly on the viscosity contrast between them (Campbell and Turner, 1985; Blake and Campbell, 1986; Blake and Ivey, 1986). In addition, the ability of a magma reservoir to convect

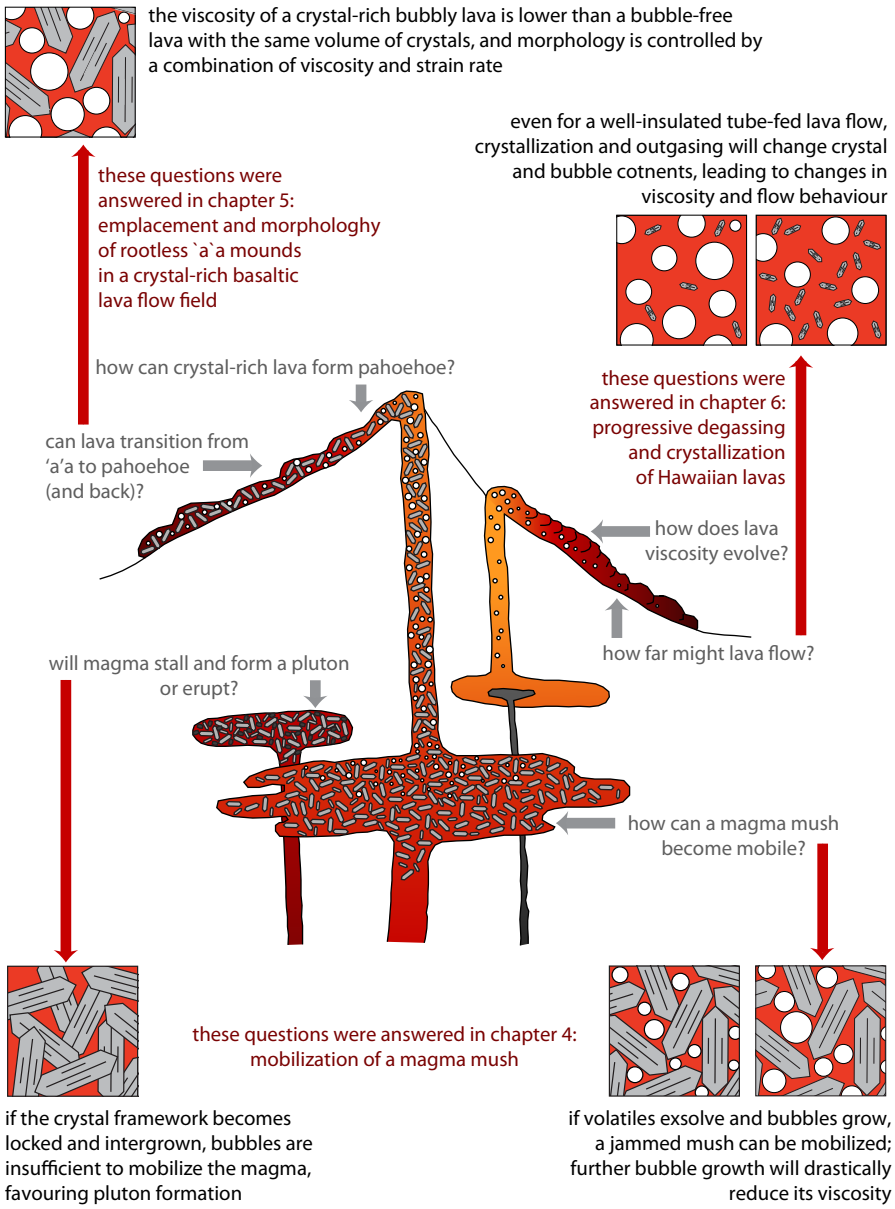

Figure 7.1: Schematic sketch — not to scale — of a volcanic system, showing the locations and processes investigated in this thesis in which rheology plays a key role.

(an efficient way of mixing magmas) depends on viscosity.

The link between plutons and large volcanic eruptions has been disputed in the literature (Bachmann et al., 2007; Mills and Coleman, 2013). Some plutons are thought to represent magma that stalled in the crust and never erupted (as in the examples presented in sections 4.5.4 and 4.5.5); other plutons are thought to be the residual mush left behind when more mobile portions of the reservoir erupted (Lipman, 2007; Gelman et al., 2014). In some cases, it is thought that the magma reservoir may have been almost completely evacuated during an eruption, leaving

no magma behind to form a pluton (Zimmerer and McIntosh, 2012). These different scenarios will in part be controlled by the rheology of a crystallizing magma. If the magma erupts before a significant fraction of crystals has formed — or if the magma reservoir becomes segregated, with a crystal-free cap overlying a more crystalline region — the viscosity may not be a limiting factor. On the other hand, if the crystal fraction approaches the maximum packing fraction for that crystal shape, the increasing viscosity and yield strength will prevent the magma from being eruptible (shown by the red curves in figure 7.2). The case studies presented in chapter 4 demonstrate one mechanism through which a crystal-rich magma may become mobile, through the growth of bubbles (shown by the blue curves in figure 7.2).

7.1.2 In the conduit

In order to ascend to the surface, a mobile magma must form a dyke or use an existing conduit. During ascent, the magma will not experience a uniform strain-rate and so the non-Newtonian rheology of a magma carrying suspended crystals or bubbles must be considered. This will affect the flow velocity profile across the conduit and consequently, the rate at which the bulk of the magma is able to ascend, and potentially the fragmentation depth (as demonstrated by Llewellin et al. (2002a); Llewellin and Manga (2005) for a bubble-bearing magma, and Caricchi et al. (2007) for a crystal-bearing magma). Viscosity is a primary control on the ability of bubbles to rise and coalesce, and for permability development (Klug and Cashman, 1996). Brittle fragmentation occurs when the magma crosses the glass transition — and this depends on melt viscosity as well (Papale, 1999; Webb and Dingwell, 1990). Therefore many of the processes that dictate how a magma will erupt are controlled by viscosity.

Throughout the ascent of the magma, conditions (e.g. pressure, temperature, melt composition) will be changing. As a result, the magma may crystallize, volatiles may exsolve, and bubbles may grow. All of these processes affect the rheology of the magma, much as they were shown to affect the rheology of an evolving lava flow, in chapter 6. Existing conduit flow models typically take into account crystallization or bubble growth during ascent, but not both. Using the model presented in chapter 3 for the rheology of three-phase suspensions, it should be straightforward to incorporate the effects of both crystallization and bubble growth into such models. Section 3.6.3 discussed the degree to which including bubbles in a viscosity model affects the predicted rheology of a suspension: in the high strain rate environment found along the margins of a conduit, the shear thinning effect created by bubbles

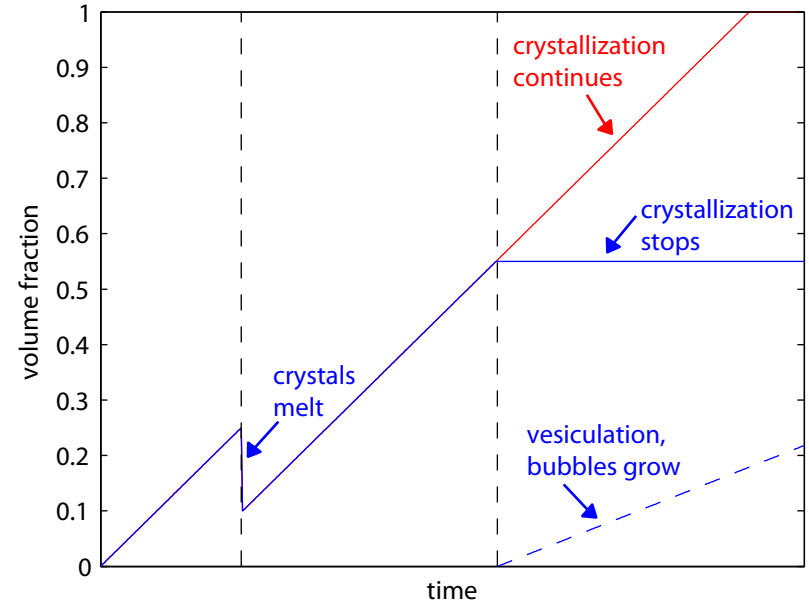

(a)

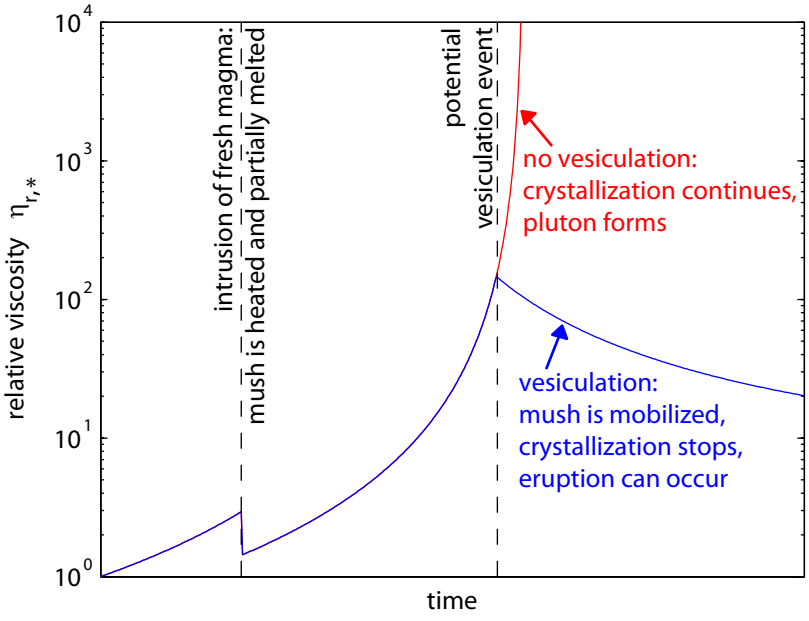

(b)

Figure 7.2: Hypothetical magma reservoir a) bubble (dashed line) and crystal (solid lines) volume fractions and b) viscosity. Red curve indicates magma which crystallizes completely forming a pluton. Blue curve indicates magma undergoing volatile exsolution and bubble growth (black dashed line); crystallization halts, and viscosity drops as a result of bubble growth. Effect of reduction in crystallinity due to hotter aphyric recharge magma is also shown (black dashed line).

becomes particularly important. In addition, increasing strain rates may cause a transition to high bubble capillarity and further reduce the expected viscosities. Neglecting one of the suspended phases present in the conduit could therefore have implications for the results drawn from conduit flow models. Caricchi et al. (2007) found, for example, that fragmentation may occur over 2 km closer to the surface when shear thinning fluids are modelled instead of Newtonian fluids.

7.1.3 On the surface

If a magma erupts effusively, the morphology that it produces is strongly dependent on its rheology, as discussed in chapters 5 and 6 (MacDonald, 1953; Peterson and Tilling, 1980). The results of chapter 5 demonstrated that even at unusually high crystal fractions lava could still flow fluidally, due to the presence of bubbles. This has implications for inferences drawn from lavas: many authors assume that pāhoehoe can only flow with a low crystal content (e.g. Lanzafame et al., 2013). Clearly, this must be re-assessed, and the influence of bubbles must be accounted for.

The study of Volcán Llaima in chapter 5, and comparisons to other volcanoes in section 5.4.2, suggested that eruption duration may be a key control on the ability of a given volcanic field to build certain volcanic structures. Instead of covering an extensive area, the 1780 eruption of Volcán Llaima built 200 m high rootless ‘a‘ā mounds. This eruption is thought to have lasted 10 years, comparable to that which built lava terraces at Mount Etna in 1614 (Guest et al., 1984). On the other hand, similarly crystal-rich lavas at Volcán Villarrica, 80 km south of Volcán Llaima, have historically only formed very short duration eruptions and lack any sign of rootless edifice formation (Mike Dungan, pers. comm., 2016). It appears that time and volume of magma produced, in addition to rheology, are controlling factors on whether or not a rootless edifice may form.

In a less crystal-rich example, progress towards higher viscosity lava morphology was controlled more by outgassing than crystallization in the Kīlauean lava analysed in chapter 6. Here, a number of factors were found to control viscosity — including bubble fraction, crystal fraction, crystal sizes, water content, melt composition, and temperature — and the interplay between them was deemed to be complex. By examining each component individually their contributions to changes in the viscosity can be calculated, and the overall change in viscosity can be predicted.

7.2 Conclusions

This thesis has filled an important gap in knowledge by providing a constitutive equation for calculating the rheology of three-phase suspensions. Although the equation is only validated for low capillarity bubbles and a total suspended fraction less than 0.5, the theoretical framework used to derive the model allows for a number of plausible extensions makes it widely applicable to natural magmas.

Using this framework for calculating three-phase rheology, three applications to volcanic processes have demonstrated how important it is to include the effects of bubbles on rheology in addition to the effects of particles. In particular, the exsolution of volatiles and/or expansion of bubbles lead to rheological changes that may explain why some highly crystal-rich mushes are able to erupt, and how some crystal-rich magmas are able to flow as pāhoehoe. Tracking the evolution of various lava properties is also shown to be vitally important for assessing how lava flows are likely to change with distance from the vent, and throughout an eruption.

In summary, this thesis has:

1. provided a framework for calculating the viscosity of a three-phase suspension,
2. experimentally validated this three-phase viscosity equation for suspensions at low bubble capillarity, where the bubbles are smaller than the particles,
3. demonstrated how the growth of bubbles in a particle-rich suspension can lead to flow,
4. shown that an immobile crystal mush could become mobile through the growth of bubbles,
5. described unusual morphologies in crystal-rich lava at Volcán Llaima, and explained how their formation was controlled by their rheology, and
6. examined how changes in lava properties during flow can lead to changes in viscosity, and therefore morphology.

7.3 Future directions

One limitation of the experiments in chapter 3 is that they cover a limited range of the possible bubble and crystal fractions. The ternary diagram in figure 7.3 shows the range of possible bubble, crystal, and fluid fractions, and the range that

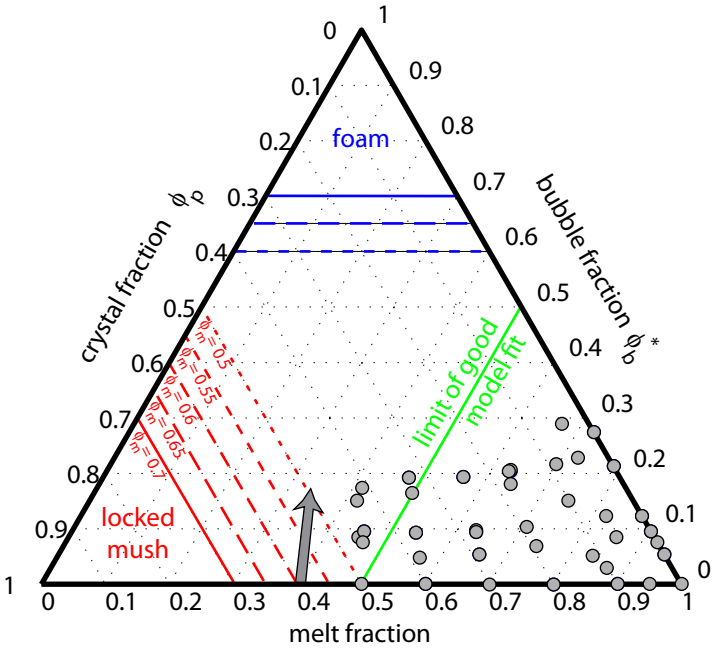

Figure 7.3: Ternary diagram showing the proportions of crystals, bubbles, and melt in a sample. Experiments from chapter 3 are shown by the grey circles, and the trajectory of the sample in the mobilization experiment from chapter 4 is shown by the grey arrow. The limit of the three-phase rheology equation ($\phi_s \leq 0.5$) is shown by the green line. High bubble fraction suspensions are foams (blue); high crystal fractions are mush mush or intergrown crystals and eventually solid rock (red).

has been covered by experiments. The three-phase rheology equations are found to be valid for total suspended fractions less than 0.5 (shown by green line in figure 7.3), and the highest bubble fraction investigated is 0.3. The limitation on bubble fraction is experimental: it is easy to produce suspensions with a low bubble fraction, or foams with a high bubble fraction (shown in blue in figure 7.3), which behave quite differently to low volume fraction suspensions, but there is a range of bubble fractions in between which are difficult to produce. As such, these bubble fractions have not been investigated in detail before. The cut-off for the model, at suspended fraction less than 0.5, is likely due to microscopic interactions between bubbles and particles. The three-phase equations treat the bubble and crystal fractions in isolation. While this is justifiable for low volume fractions, at higher fractions it is implausible that the phases exist without interactions. An improved understanding of these interactions may lead to an extra term in the equations, which depends on some combination of the bubble and crystal fractions.

In section 3.5.3, a number of extensions to the three-phase model were proposed but not experimentally validated. These include suspensions involving non-spherical

particles; high capillarity bubbles; and bubbles which are larger than the particles. Valuable future work would be to carry out systematic analogue experiments to test each of these extensions, and demonstrate the range of values for which they are applicable.

For example, throughout chapters 4 to 6, the model is applied to natural magmas and lavas in which the particles are not spherical. However, although it is well understood how to account for particle aspect ratio variations in two-phase (particle-fluid) suspensions (Mueller et al., 2010, 2011), further experiments would be required to validate use of the equation with three phases.

Similarly, the high capillarity version of the model is based on knowledge of the viscosity of two-phase (bubble-fluid) suspensions (Llewellin and Manga, 2005). The data used in chapter 3 include some measurements in which a minority of the bubble population would be in the high capillarity regime, but these measurements are not sufficient for an analysis similar to that carried out for low capillarity bubbles. A further experimental campaign, using larger bubbles, more viscous fluids, or higher strain-rates, would be needed to collect enough high capillarity data.

In section 3.5.2, an empirical relationship between flow index and bubble and crystal fractions was found. The part of this relationship influenced by crystal fraction was comparable to that found by Mueller et al. (2010), but the part influenced by the bubble fraction has not previously been observed. Although this empirically derived equation allows predictions of flow index to be made, it is not clear why this form of equation is found. An improved understanding of the causes of shear thinning in two-phase suspensions is probably required before the three-phase relationship can be understood. In addition, this equation is probably only valid for low capillarity bubbles — and without an understanding of the fundamental processes that cause the suspension to be shear thinning, a model for the flow index of a high capillarity bubble suspension cannot be proposed. However, if further experiments were carried out with high capillarity bubbles, another equation for the flow index could be empirically derived.

The bulk of the research on suspensions assumes that they deform in a homogeneous manner. However, experiments on natural samples demonstrate that they do not (Caricchi et al., 2007; Pistone et al., 2012). Experiments in general only allow snap-shots of the system to be viewed — in the example of natural experiments, the end product is commonly quenched and sectioned in order to view its internal structure. In situ measurements of deforming suspensions would be needed to quantify the heterogeneity developed during flow.

Chapter 8

Bibliography

Allan, A. S. R., Morgan, D. J., Wilson, C. J. N., and Millet, M. A. (2013). From mush to eruption in centuries: assembly of the super-sized Oruanui magma body. *Contributions to Mineralogy and Petrology*, 166(1):143–164.

Anderson, A. T., Davis, A. M., and Lu, F. (2000). Evolution of Bishop Tuff rhyolitic magma based on melt and magnetite inclusions and zoned phenocrysts. *Journal of Petrology*, 41(3):449–473.

Anderson, S., Smrekar, S. E., and Stofan, E. R. (2012). Tumulus development on lava flows: insights from observations of active tumuli and analysis of formation models. *Bulletin of Volcanology*, 74:931–946.

Applegarth, L. J., Tuffen, H., James, M. R., Pinkerton, H., and Cashman, K. V. (2013). Direct observations of degassing-induced crystallization in basalts. *Geology*, 41:243–246.

Avard, G. and Whittington, A. G. (2012). Rheology of arc dacite lavas: experimental determination at low strain rates. *Bulletin of Volcanology*, 74:1039–1056.

Bachmann, O. and Bergantz, G. W. (2003). Rejuvenation of the Fish Canyon magma body: A window into the evolution of large-volume silicic magma systems. *Geology*, 31(9):789–792.

Bachmann, O. and Bergantz, G. W. (2006). Gas percolation in upper-crustal silicic crystal mushes as a mechanism for upward heat advection and rejuvenation of near-solidus magma bodies. *Journal of Volcanology and Geothermal Research*, 149(1-2):85–102.

Bachmann, O. and Bergantz, G. W. (2008). The magma reservoirs that feed supereruptions. *Elements*, 4:17–21.

Bachmann, O., Dungan, M. A., and Lipman, P. W. (2002). The Fish Canyon magma body, San Juan volcanic field, Colorado: Rejuvenation and eruption of an upper-crustal batholith. *Journal of Petrology*, 43(8):1469–1503.

Bachmann, O., Oberli, F., Dungan, M. A., Meier, M., Mundil, R., and Fischer, H. (2007). 40Ar/39Ar and UPb dating of the Fish Canyon magmatic system, San Juan Volcanic field, Colorado: Evidence for an extended crystallization history. *Chemical Geology*, 236:134–166.

Bagdassarov, N. S., Dingwell, D. B., and Webb, S. L. (1994). Viscoelasticity of crystal- and bubble-bearing rhyolite melts. *Physics of the Earth and Planetary Interiors*, 83:83–99.

Baker, D. R. and Alletti, M. (2012). Fluid saturation and volatile partitioning between melts and hydrous fluids in crustal magmatic systems: The contribution of experimental measurements and solubility models. *Earth-Science Reviews*, 114:298–324.

Barclay, J., Herd, R. A., Edwards, B. R., Christopher, T., Kiddle, E. J., Plail, M., and Donovan, A. (2010). Caught in the act: Implications for the increasing abundance of mafic enclaves during the recent eruptive episodes of the Soufrière Hills Volcano, Montserrat. *Geophysical Research Letters*, 37:L00E09.

Barnes, H. A. and Carnali, J. O. (1990). The vane-in-cup as a novel rheometer geometry for shear thinning and thixotropic materials. *Journal of Rheology*, 34(6):841–866.

Begue, F., Deering, C. D., Gravley, D. M., Kennedy, B. M., Chambefort, I., Gualda, G. A. R., and Bachmann, O. (2014). Extraction, storage and eruption of multiple isolated magma batches in the paired Mamaku and Ohakuri eruption, Taupo Volcanic Zone, New Zealand. *Journal of Petrology*, 55(8):1653–1684.

Best, M. G., Christiansen, E. H., and Blank, R. H. (1989). Oligocene caldera complex and calc-alkaline tuffs and lavas of the Indian Peak volcanic field, Nevada and Utah. *Geological Society of America Bulletin*, 101(8):1076–1090.

Bi, D., Zhang, J., Chakraborty, B., and Behringer, R. P. (2011). Jamming by shear. *Nature*, 480:355–358.

Blake, S. (1984). Volatile oversaturation during the evolution of silicic magma chambers as an eruption trigger. *Journal of Geophysical Research*, 89:8237–8244.

Blake, S. and Campbell, I. (1986). The dynamics of magma-mixing during flow in volcanic conduits. *Contributions to Mineralogy and Petrology*, 94:72–81.

Blake, S. and Ivey, G. N. (1986). Magma-mixing and the dynamics of withdrawal from stratified reservoirs. *Journal of Volcanology and Geothermal Research*, 27:153–178.

Blower, J. D. (2001). Factors controlling permeability-porosity relationships in magma. *Bulletin of Volcanology*, 63(7):497–504.

Bottinga, Y. and Weill, D. F. (1970). Densities of liquid silicate systems calculated from partial molar volumes of oxide components. *American Journal of Science*, 269:169–182.

Bottinga, Y. and Weill, D. F. (1972). The viscosity of magmatic silicate liquids: A model for calculation. *American Journal of Science*, 272:438–475.

Bouvet de Maisonneuve, C., Dungan, M. A., Bachmann, O., and Burgisser, A. (2012). Insights into shallow magma storage and crystallization at Volcán Llaima (Andean Southern Volcanic Zone, Chile). *Journal of Volcanology and Geothermal Research*, 211-212:76–91.

Bouvet De Maisonneuve, C., Dungan, M. A., Bachmann, O., and Burgisser, A. (2013). Petrological insights into shifts in eruptive styles at Volcan Llaima (Chile). *Journal of Petrology*, 54(2):393–420.

Burgisser, A. and Bergantz, G. W. (2011). A rapid mechanism to remobilize and homogenize highly crystalline magma bodies. *Nature*, 471:212–215.

Burgisser, A., Bergantz, G. W., and Breidenthal, R. E. (2005). Addressing complexity in laboratory experiments: the scaling of dilute multiphase flows in magmatic systems. *Journal of Volcanology and Geothermal Research*, 141(3-4):245–265.

Burnham, C. and Jahns, R. (1962). A method for determining the solubility of water in silicate melts. *American Journal of Science*, 260:721–745.

Campbell, I. and Turner, J. S. (1985). Turbulent mixing between fluids with different viscosities. *Nature*, 313:39–42.

Candela, P. A. (1991). Physics of aqueous phase evolution in plutonic environments. *American Mineralogist*, 76:1081–1091.

Carey, R. J., Manga, M., Degruyter, W., Gonnermann, H., Swanson, D. A., Houghton, B. F., Orr, T. R., and Patrick, M. (2013). Convection in a volcanic conduit recorded by bubbles. *Geology*, 41(4):395–398.

Caricchi, L., Burlini, L., Ulmer, P., Gerya, T., Vassalli, M., and Papale, P. (2007). Non-Newtonian rheology of crystal-bearing magmas and implications for magma ascent dynamics. *Earth and Planetary Science Letters*, 264:402–419.

Caricchi, L., Giordano, D., Burlini, L., Ulmer, P., and Romano, C. (2008). Rheological properties of magma from the 1538 eruption of Monte Nuovo (Phlegrean Fields, Italy): An experimental study. *Chemical Geology*, 256:158–171.

Cashman, K. V. and Giordano, G. (2014). Calderas and magma reservoirs. *Journal of Volcanology and Geothermal Research*, 288:28–45.

Cashman, K. V. and Sparks, R. S. J. (2013). How volcanoes work: A 25 year perspective. *Geological Society of America Bulletin*, 125(5-6):664–690.

Cashman, K. V., Thornber, C. R., and Kauahikaua, J. P. (1999). Cooling and crystallization of lava in open channels, and the transition of pahoehoe lava to 'a'a. *Bulletin of Volcanology*, 61:306–323.

Cassidy, M., Watt, S. F. L., Talling, P. J., Palmer, M. R., Edmonds, M., Jutzeler, M., Manga, M., Coussens, M., Gernon, T., Taylor, R. N., Michalik, A., Inglis, E., Breitkreuz, C., Le Friant, A., Ishizuka, O., Boudon, G., Mccanta, M. C., Adachi, T., Hornbach, M. J., Colas, S. L., Endo, D., Fujinawa, A., Kataoka, K. S., Maeno, F., Tamura, Y., and Wang, F. (2015). Rapid onset of mafic magmatism facilitated by volcanic edifice collapse. *Geophysical Research Letters*, 42:4778–4785.

Castruccio, A., Rust, A. C., and Sparks, R. S. J. (2010). Rheology and flow of crystal-bearing lavas: Insights from analogue gravity currents. *Earth and Planetary Science Letters*, 297:471–480.

Champallier, R., Bystricky, M., and Arbaret, L. (2008). Experimental investigation of magma rheology at 300 MPa: From pure hydrous melt to 76 vol.% of crystals. *Earth and Planetary Science Letters*, 267:571–583.

Chang, C. and Powell, R. L. (1994). Effect of particle size distributions on the rheology of concentrated bimodal suspensions. *Journal of Rheology*, 38(1):85–98.

Charlier, B. L. A., Bachmann, O., Davidson, J. P., Dungan, M. A., and Morgan, D. J. (2007). The Upper Crustal Evolution of a Large Silicic Magma Body: Evidence from Crystal-scale Rb Sr Isotopic Heterogeneities in the Fish Canyon Magmatic System, Colorado. *Journal of Petrology*, 48(10):1875–1894.

Chevrel, M. O., Platz, T., Hauber, E., Baratoux, D., Lavallée, Y., and Dingwell, D. B. (2013). Lava flow rheology: A comparison of morphological and petrological methods. *Earth and Planetary Science Letters*, 384:109–120.

Cimarelli, C., Costa, A., Mueller, S., and Mader, H. M. (2011). Rheology of magmas with bimodal crystal size and shape distributions: Insights from analog experiments. *Geochemistry, Geophysics, Geosystems*, 12(7):1–14.

Clague, D. A., Moore, J. G., and Reynolds, J. R. (2000). Formation of submarine flat-topped volcanic cones in Hawai'i. *Bulletin of Volcanology*, 62(3):214–233.

Coleman, D. S., Gray, W., and Glazner, A. F. (2004). Rethinking the emplacement and evolution of zoned plutons: Geochronologic evidence for incremental assembly of the Tuolumne Intrusive Suite, California. *Geology*, 32(5):433–436.

Cooper, K. M. and Kent, A. J. R. (2014). Rapid remobilization of magmatic crystals kept in cold storage. *Nature*, 506:480–483.

Costa, A., Blake, S., and Self, S. (2006). Segregation processes in vesiculating crystallizing magmas. *Journal of Volcanology and Geothermal Research*, 153:287–300.

Crews, J. B. and Cooper, C. A. (2014). Experimental evidence for seismically initiated gas bubble nucleation and growth in groundwater as a mechanism for coseismic borehole water level rise and remotely triggered seismicity. *Journal of Geophysical Research: Solid Earth*, 119:7079–7091.

Crisp, J. and Baloga, S. M. (1994). Influence of crystallization and entrainment of cooler material on the emplacement of basaltic aa lava flows. *Journal of Geophysical Research*, 99:11819–11831.

Davis, M. G., Garcia, M. O., and Wallace, P. (2003). Volatiles in glasses from Mauna Loa Volcano, Hawai'i: implications for magma degassing and contamination, and growth of Hawaiian volcanoes. *Contributions to Mineralogy and Petrology*, 144:570–591.

De Silva, S. L. and Gregg, P. M. (2014). Thermomechanical feedbacks in magmatic systems: Implications for growth, longevity, and evolution of large caldera-forming magma reservoirs and their supereruptions. *Journal of Volcanology and Geothermal Research*, 282:77–91.

Delaney, G. W. and Cleary, P. W. (2010). The packing properties of superellipsoids. *EPL (Europhysics Letters)*, 89:34002.

Dingwell, D. B. (1996). Volcanic dilemma: flow or blow? *Science*, 273:1054–1055.

Dingwell, D. B., Romano, C., and Hess, K.-U. (1996). The effect of water on the viscosity of a haplogranitic melt under P-T-X conditions relevant to silicic volcanism. *Contributions to Mineralogy and Petrology*, 124:19–28.

Dixon, J. E., Stolper, E. M., and Holloway, J. R. (1995). An experimental study of water and carbon dioxide solubilities in mid-ocean ridge basaltic liquids. Part II: applications to degassing. *Journal of Petrology*, 36(6):1607–1631.

Donev, A., Cisse, I., Sachs, D., Variano, E. A., Stillinger, F. H., Connelly, R., Torquato, S., and Chaikin, P. M. (2004). Improving the density of jammed disordered packings using ellipsoids. *Science*, 303:990–993.

Dzierma, Y. and Wehrmann, H. (2010). Eruption time series statistically examined: Probabilities of future eruptions at Villarrica and Llaima Volcanoes, Southern Volcanic Zone, Chile. *Journal of Volcanology and Geothermal Research*, 193:82–92.

Edmonds, M. (2008). New geochemical insights into volcanic degassing. *Philosophical Transactions of the Royal Society A: Mathematical and Physical Sciences*, 366:4559–4579.

Eichelberger, J. C. (1980). Vesiculation of mafic magma during replenishment of silicic magma reservoirs. *Nature*, 288:446–450.

Einstein, A. (1906). Eine neue Bestimmung der Molekuldimensionen. *Annalen der Physik*, 19:289–306.

Ewart, A. (1976). Mineralogy and chemistry of modern orogenic lavas - some statistics and implications. *Earth and Planetary Science Letters*, 31:417–432.

Farris, R. J. (1968). Prediction of the viscosity of multimodal suspensions from unimodal viscosity data. *Journal of Rheology*, 12:281–301.

Fernandez, N., Mani, R., Rinaldi, D., Kadau, D., Mosquet, M., Lombois-Burger, H., Cayer-Barrioz, J., Herrmann, H. J., Spencer, N. D., and Isa, L. (2013). Microscopic mechanism for shear thickening of non-Brownian suspensions. *Physical Review Letters*, 111:108301.

Folkes, C. B., de Silva, S. L., Schmitt, A. K., and Cas, R. A. F. (2011). A reconnaissance of U-Pb zircon ages in the Cerro Galán system, NW Argentina: Prolonged magma residence, crystal recycling, and crustal assimilation. *Journal of Volcanology and Geothermal Research*, 206:136–147.

Frankel, N. A. and Acrivos, A. A. (1970). The constitutive equation for diulte emulsions. *Journal of Fluid Mechanics*, 44:65–78.

Frazer, R. E., Coleman, D. S., and Mills, R. D. (2014). Zircon U-Pb geochronology of the Mount Givens Granodiorite: Implications for the genesis of large volumes of eruptible magma. *Journal of Geophysical Research: Solid Earth*, 119:2907–2924.

Fulcher, G. S. (1925). Analysis of recent measurements of the viscosity of glasses. *Journal of the American Ceramic Society*, 8:339–355.

Gauthier, F. (1973). Field and laboratory studies of the rheology of Mount Etna lava. *Philosophical Transactions of the Royal Society A: Mathematical and Physical Sciences*, 274:83–98.

Gelman, S. E., Deering, C. D., Bachmann, O., Huber, C., and Gutiérrez, F. J. (2014). Identifying the crystal graveyards remaining after large silicic eruptions. *Earth and Planetary Science Letters*, 403:299–306.

Giordano, D. and Dingwell, D. B. (2003). Non-Arrhenian multicomponent melt viscosity: a model. *Earth and Planetary Science Letters*, 208:337–349.

Giordano, D., Romano, C., Papale, P., and Dingwell, D. B. (2004). The viscosity of trachytes, and comparison with basalts, phonolites, and rhyolites. *Chemical Geology*, 213:49–61.

Giordano, D., Russell, J. K., and Dingwell, D. B. (2008). Viscosity of magmatic liquids: A model. *Earth and Planetary Science Letters*, 271:123–134.

Global Volcanism Program (2016). Kilauea. *http://volcano.si.edu/volcano.cfm?vn=332010*, 2016-03-21.

Gottsmann, J., Lavallée, Y., Martí, J., and Aguirre-Díaz, G. (2009). Magma-tectonic interaction and the eruption of silicic batholiths. *Earth and Planetary Science Letters*, 284:426–434.

Gualda, G. A. R. and Ghiorso, M. S. (2013). The Bishop Tuff giant magma body: an alternative to the Standard Model. *Contributions to Mineralogy and Petrology*, 166:755–775.

Guest, J. and Stofan, E. R. (2005). The significance of slab-crusted lava flows for understanding controls on flow emplacement at Mount Etna, Sicily. *Journal of Volcanology and Geothermal Research*, 142:193–205.

Guest, J. E., Duncan, A. M., Stofan, E. R., and Anderson, S. (2012). Effect of slope on development of pahoehoe flow fields: Evidence from Mount Etna. *Journal of Volcanology and Geothermal Research*, 219-220:52–62.

Guest, J. E., Wood, C., and Greeley, R. (1984). Lava tubes, terraces and mega-tumuli on the 1614-24 pahoehoe lava flow field, Mount Etna, Sicily. *Bulletin of Volcanology*, 47(3):635–648.

Hale, A. J., Wadge, G., and Mühlhaus, H. B. (2007). The influence of viscous and latent heating on crystal-rich magma flow in a conduit. *Geophysical Journal International*, 171:1406–1429.

Hammond, W. C. and Humphreys, E. D. (2000). Upper mantle seismic wave attenuation: Effects of realistic partial melt distribution. *Journal of Geophysical Research*, 105(B5):10975–10986.

Hansen, S., Thurber, C., Mandernach, M., Haslinger, F., and Doran, C. (2003). Seismic velocity and attentuation structure of the East Rift Zone and South Flank of Kilauea volcano, Hawai‘i. *Bulletin of the Seismological Society of America*, 94:1430–1440.

Harris, A. J. L. and Allen, J. S. (2008). One-, two- and three-phase viscosity treatments for basaltic lava flows. *Journal of Geophysical Research*, 113:B09212.

Heliker, C., Swanson, D. A., and Takahashi, T. J., editors (2003). *The Pu‘u ‘Ō‘ō-Kūpaianaha eruption of Kilauea Volcano, Hawai‘i: the first 20 years.* U.S. Geol. Surv. Prof. Paper 1676.

Helz, R. T., Clague, D. A., Sisson, T. W., and Thornber, C. R. (2014). Petrologic insights into basaltic volcanism at historically active Hawaiian volcanoes. In Poland, M. P., Takahashi, T. J., and Landowski, C. M., editors, *Characteristics of Hawaiian Volcanoes*, pages 237–293. U.S. Geol. Surv. Prof. Paper 1801.

Helz, R. T., Heliker, C., Hon, K., and Mangan, M. T. (2003). Thermal efficiency of lava tubes in the Pu‘u ‘Ō‘ō-Kūpaianaha eruption. In Heliker, C., Swanson, D. A., and Takahashi, T. J., editors, *The Pu‘u ‘Ō‘ō-Kūpaianaha eruption of Kilauea Volcano, Hawai‘i: the first 20 years.*, pages 237–293. U.S. Geol. Surv. Prof. Paper 1676.

Herschel, W. H. and Bulkley, R. (1926). Konsistenzmessungen von Gummi-Benzollsungen. *Kolloid Zeitschrift*, 39:291–300.

Hess, K.-U. and Dingwell, D. B. (1996). Viscosities of hydrous leucogranitic melts: A non-Arrhenian model. *American Mineralogist*, 81:1297–1300.

Higgins, M. D. (2000). Measurement of crystal size distributions. *American Mineralogist*, 85:1105–1116.

Higgins, M. D. and Meilleur, D. (2009). Development and emplacement of the Inyo Domes Magmatic Suite, California: Evidence from geological, textural (CSD) and geochemical observations of ash and lava. *Journal of Volcanology and Geothermal Research*, 186(3-4):280–292.

Hon, K., Gansecki, C., and Kauahikaua, J. (2003). The transition from ʻaʻā to pāhoehoe crust on flows emplaced during the Puʻu ʻŌʻō-Kūpaianaha eruption. In Heliker, C., Swanson, D. A., and Takahashi, T. J., editors, *The Puʻu ʻŌʻō-Kūpaianaha eruption of Kilauea Volcano, Hawaiʻi: the first 20 years.*, pages 89–103. U.S. Geol. Surv. Prof. Paper 1676.

Hon, K., Kauahikaua, J. P., Denlinger, R., and Mackay, K. (1994). Emplacement and inflation of pahoehoe sheet flows: Observations and measurements of active lava flows on Kilauea Volcano, Hawaii. *Geological Society of American Bulletin*, 106:351–370.

Hoover, S. R., Cashman, K. V., and Manga, M. (2001). The yield strength of subliquidus basalts - experimental results. *Journal of Volcanology and Geothermal Research*, 107:1–18.

Houghton, B. F. and Wilson, C. J. N. (1989). A vesicularity index for pyroclastic deposits. *Bulletin of Volcanology*, 51:451–462.

Huber, C., Bachmann, O., and Manga, M. (2010). Two competing effects of volatiles on heat transfer in crystal-rich magmas: Thermal insulation vs defrosting. *Journal of Petrology*, 51(4):847–867.

Hulme, G. (1974). The interpretation of lava flow morphology. *Geophysical Journal International*, 39:361–383.

Huppert, H. E., Sparks, R. S. J., and Turner, J. S. (1982). Effects of volatiles on mixing in calc-alkaline magma systems. *Nature*, 297:554–557.

Hurwitz, S. and Navon, O. (1994). Bubble nucleation in rhyolitic melts: Experiments at high pressure, temperature, and water content. *Earth and Planetary Science Letters*, 122:267–280.

Jackson, M. G., Weis, D., and Huang, S. (2012). Major element variations in Hawaiian shield lavas: Source features and perspectives from global ocean island basalt (OIB) systematics. *Geochemistry, Geophysics, Geosystems*, 13(9):Q09009.

Jeffery, G. B. (1922). The motion of ellipsoidal particles immersed in a viscous fluid. *Proceedings of the Royal Society A: Mathematical, Physical and Engineering Sciences*, 102:161–179.

Jellinek, A. M., Kerr, R. C., and Griffiths, R. W. (1999). Mixing and compositional stratification produced by natural convection. 1. Experiments and their application to Earth's core and mantle. *Journal of Geophysical Research: Solid Earth*, 104(B4):7183–7201.

Jurado-Chichay, Z. and Rowland, S. K. (1995). Channel overflows of the Pohue Bay flow, Mauna Loa, Hawai'i: examples of the contrast between surface and interior lava. *Bulletin of Volcanology*, 57:117–126.

Justet, L. and Spell, T. L. (2001). Effusive eruptions from a large silicic magma chamber: the Bearhead Rhyolite, Jemez volcanic field, NM. *Journal of Volcanology and Geothermal Research*, 107:241–264.

Kauahikaua, J., Sherrod, D. R., Cashman, K. V., Heliker, C., Hon, K., Mattox, T. N., and Johnson, J. A. (2003). Hawaiian lava-flow dynamics during the Pu'u'Ō'ō-Kūpaianaha eruption: A tale of two decades. In Heliker, C., Swanson, D. A., and Takahashi, T. J., editors, *The Pu'u 'Ō'ō-Kūpaianaha eruption of Kilauea Volcano, Hawai'i: the first 20 years.*, pages 63–87. U.S. Geol. Surv. Prof. Paper 1676.

Kent, A. J. R., Darr, C., Koleszar, A. M., Salisbury, M. J., and Cooper, K. M. (2010). Preferential eruption of andesitic magmas through recharge filtering. *Nature Geoscience*, 3(9):631–636.

Khitarov, N. I., Lebedev, E. B., Dorfman, A. M., and Bagdasarov, N. S. (1979). Effect of temperature, pressure and volatile components upon the surface-tension of basaltic melt. *Geokhimiya*, 10:1427–1438.

Klug, C. and Cashman, K. V. (1996). Permeability development in vesiculating magmas: implications for fragmentation. *Bulletin of Volcanology*, 58:87–100.

Koleszar, A. M., Kent, A. J. R., Wallace, P. J., and Scott, W. E. (2012). Controls on long-term low explosivity at andesitic arc volcanoes: Insights from Mount Hood, Oregon. *Journal of Volcanology and Geothermal Research*, 219-220:1–14.

Kushiro, I. (1976). Changes in viscosity and structure of melt of NaAlSi2O6 composition at high pressures. *Journal of Geophysical Research*, 81(35):6347–6350.

Kushiro, I., Yoder, H. S., and Mysen, B. O. (1976). Viscosities of basalt and andesite melts at high pressures. *Journal of Geophysical Research*, 81(35):6351–6356.

Lanzafame, G., Mollo, S., Iezzi, G., Ferlito, C., and Ventura, G. (2013). Unraveling the solidification path of a pahoehoe "cicirara" lava from Mount Etna volcano. *Bulletin of Volcanology*, 75:703.

Lee, C.-T. A. and Morton, D. M. (2015). High silica granites: Terminal porosity and crystal settling in shallow magma chambers. *Earth and Planetary Science Letters*, 409:23–31.

Lejeune, A.-M. and Richet, P. (1995). Rheology of crystal-bearing silicate melts: An experimental study at high viscosities. *Journal of Geophysical Research*, 100(B3):4215–4229.

Lesher, C. E. and Spera, F. J. (2015). Thermodynamic and transport properties of silicate melts and magma. In Sigurdsson, H., Houghton, B., Rymer, H., Stix, J., and McNutt, S., editors, *The Encyclopedia of Volcanoes.*, pages 113–141. Elsevier.

Linde, A. T. and Sacks, I. S. (1998). Triggering of volcanic eruptions. *Nature*, 395:888–890.

Lipman, P. W. (2007). Incremental assembly and prolonged consolidation of Cordilleran magma chambers: Evidence from the Southern Rocky Mountain volcanic field. *Geosphere*, 3:42–70.

Lipman, P. W., Banks, N. G., and Rhodes, J. M. (1985). Degassing-induced crystallization of basaltic magma and effects on lava rheology. *Nature*, 314:435–438.

Liu, Y., Zhang, Y., and Behrens, H. (2005). Solubility of H2O in rhyolitic melts at low pressures and a new empirical model for mixed H2O-CO2 solubility in rhyolitic melts. *Journal of Volcanology and Geothermal Research*, 143:219–235.

Llewellin, E. W., Mader, H. M., and Wilson, S. D. R. (2002a). The constitutive equation and flow dynamics of bubbly magmas. *Geophysical Research Letters*, 29(24):2170.

Llewellin, E. W., Mader, H. M., and Wilson, S. D. R. (2002b). The rheology of a bubbly liquid. *Proceedings of the Royal Society A: Mathematical, Physical and Engineering Sciences*, 458:987–1016.

Llewellin, E. W. and Manga, M. (2005). Bubble suspension rheology and implications for conduit flow. *Journal of Volcanology and Geothermal Research*, 143:205–217.

Longpre, M. A., Klugel, A., Diehl, A., and Stix, J. (2014). Mixing in mantle magma reservoirs prior to and during the 2011-2012 eruption at El Hierro, Canary Islands. *Geology*, 42(4):315–318.

MacDonald, G. A. (1953). Pāhoehoe, ʻaʻā, and block lava. *American Journal of Science*, 251:161–191.

Macedonio, G., Neri, A., Martí, J., and Folch, A. (2005). Temporal evolution of flow conditions in sustained magmatic explosive eruptions. *Journal of Volcanology and Geothermal Research*, 143:153–172.

Mackenzie, J. K. (1950). Elastic constants of a solid containing spherical holes. *Proceedings of the Royal Society B*, 63:2–11.

Mader, H. M., Llewellin, E. W., and Mueller, S. (2013). The rheology of two-phase magmas : a review and analysis. *Journal of Volcanology and Geothermal Research*, 257:1–51.

Manconi, A., Longpre, M. A., Walter, T. R., Troll, V. R., and Hansteen, T. H. (2009). The effects of flank collapses on volcano plumbing systems. *Geology*, 37(12):1099–1102.

Manga, M. and Brodsky, E. (2006). Seismic triggering of eruptions in the far field: Volcanoes and geysers. *Annual Review of Earth and Planetary Sciences*, 34:263–291.

Mangan, M. T., Cashman, K. V., and Swanson, D. A. (2014). The dynamics of Hawaiian-style eruptions: A century of study. In Poland, M. P., Takahashi, T. J., and Landowski, C. M., editors, *Characteristics of Hawaiian Volcanoes*, pages 323–354. U.S. Geol. Surv. Prof. Paper 1801.

Maron, S. H. and Pierce, P. E. (1956). Application of Ree-Eyring generalized flow theory to suspensions of spherical particles. *Journal of Colloid Science*, 11:80–95.

Marsh, B. D. (1981). On the crystallinity, probability of occurrence, and rheology of lava and magma. *Contributions to Mineralogy and Petrology*, 78:85–98.

Maughan, L. L., Christiansen, E. H., Best, M. G., Gromme, C. S., Deino, A. L., and Tingey, D. G. (2002). The Oligocene Lund Tuff, Great Basin, USA: a very large volume monotonous intermediate. *Journal of Volcanology and Geothermal Research*, 113:129–157.

McClinton, J. T., White, S. M., Colman, A., Rubin, K., and Sinton, J. M. (2014). The role of crystallinity and viscosity in the formation of submarine lava flow morphology. *Bulletin of Volcanology*, 76(9):854.

Mills, R. D. and Coleman, D. S. (2013). Temporal and chemical connections between plutons and ignimbrites from the Mount Princeton magmatic center. *Contributions to Mineralogy and Petrology*, 165:961–980.

Mock, A. and Jerram, D. A. (2005). Crystal size distributions (CSD) in three dimensions: Insights from the 3D reconstruction of a highly porphyritic rhyolite. *Journal of Petrology*, 46(8):1525–1541.

Moore, H. J. (1987). Preliminary estimates of the rheological properties of 1984 Mauna Loa lava. In Decker, R., Wright, T., and Stauffer, P. H., editors, *Volcanism in Hawaii*, pages 1569–1588. U.S. Geol. Surv. Prof. Paper 1350.

Mueller, S., Llewellin, E. W., and Mader, H. M. (2010). The rheology of suspensions of solid particles. *Proceedings of the Royal Society A: Mathematical, Physical and Engineering Sciences*, 466:1201–1228.

Mueller, S., Llewellin, E. W., and Mader, H. M. (2011). The effect of particle shape on suspension viscosity and implications for magmatic flows. *Geophysical Research Letters*, 38:L13316.

Murphy, M. D., Sparks, R. S. J., Barclay, J., Carroll, M. R., and Brewer, T. S. (2000). Remobilization of andesite magma by intrusion of mafic magma at the Soufriere Hills Volcano, Montserrat, West Indies. *Journal of Petrology*, 41(1):21–42.

Myers, M. L., Geist, D. J., Rowe, M. C., Harpp, K. S., Wallace, P., and Dufek, J. (2014). Replenishment of volatile-rich mafic magma into a degassed chamber drives mixing and eruption of Tungurahua volcano. *Bulletin of Volcanology*, 76:872.

Namiki, A., Rivalta, E., Woith, H., and Walter, T. R. (2016). Sloshing of a bubbly magma reservoir as a mechanism of triggered eruptions. *Journal of Volcanology and Geothermal Research*, 320:156–171.

Newman, S. and Lowenstern, J. B. (2002). Volatile Calc: a silicate melt-H2O-CO2 solution model written in Visual Basic for excel. *Computers & Geosciences*, 28:597–604.

Orr, T. R., Heliker, C., and Patrick, M. R. (2013). The ongoing Puu Oo-Kupaianaha eruption of Kilauea Volcano, Hawai i. *U.S. Geological Survey*, Fact Sheet.

Ostwald, W. (1925). Concerning the function rate of the viscosity of dispersion systems: IV. *Kolloid Zeitschrift*, 36:248–250.

Papale, P. (1999). Strain-induced magma fragmentation in explosive eruptions. *Nature*, 397:425–428.

Papale, P., Neri, A., and Macedonio, G. (1998). The role of magma composition and water content in explosive eruptions. 1. Conduit ascent dynamics. *Journal of Volcanology and Geothermal Research*, 87:75–93.

Patrick, M. R. and Orr, T. R. (2012). Rootless shield and perched lava pond collapses at Kilauea Volcano, Hawai'i. *Bulletin of Volcanology*, 74(1):67–78.

Pering, T. (2013). Matlab codes for volcanology - magma density. *https://vhub.org/resources/2790*.

Peterson, D. W., Holcomb, R. T., Tilling, R. I., and Christiansen, R. L. (1994). Development of lava tubes in the light of observations at Mauna Ulu, Kilauea Volcano, Hawaii. *Bulletin of Volcanology*, 56:343–360.

Peterson, D. W. and Tilling, R. I. (1980). Transition of basaltic lava from pahoehoe to aa, Kilauea volcano, Hawaii: Field observations and key factors. *Journal of Volcanology and Geothermal Research*, 7:271–293.

Petford, N. (2003). Rheology of granitic magmas during ascent and emplacement. *Annual Review of Earth and Planetary Sciences*, 31:399–427.

Phan-Thien, N. and Pham, D. C. (1997). Differential multiphase models for polydispersed suspensions and particulate solids. *Journal of Non-Newtonian Fluid Mechanics*, 72:305–318.

Phillips, J. and Woods, A. W. (2002). Suppression of large-scale magma mixing by melt-volatile separation. *Earth and Planetary Science Letters*, 204:47–60.

Philpotts, A. R., Shi, J., and Brustman, C. (1998). Role of plagioclase crystal chains in the differentiation of partly crystallized basaltic magma. *Nature*, 395:343–346.

Pinel, V. and Jaupart, C. (2005). Some consequences of volcanic edifice destruction for eruption conditions. *Journal of Volcanology and Geothermal Research*, 145:68–80.

Pinkerton, H. and Norton, G. E. (1995). Rheological properties of basaltic lavas at sub-liquidus temperatures: laboratory and field measurements on lavas from Mount Etna. *Journal of Volcanology and Geothermal Research*, 68:307–323.

Pinkerton, H. and Sparks, R. S. J. (1976). The 1975 sub-terminal lavas, Mount Etna: A case history of the formation of a compound lava field. *Journal of Volcanology and Geothermal Research*, 1:167–182.

Pinkerton, H. and Sparks, R. S. J. (1978). Field measurements of the rheology of lava. *Nature*, 276:383–385.

Pinkerton, H. and Stevenson, R. J. (1992). Methods of determining the rheological properties of magmas at sub-liquidus temperatures. *Journal of Volcanology and Geothermal Research*, 53:47–66.

Pistone, M., Caricchi, L., Ulmer, P., Burlini, L., Ardia, P., Reusser, E., Marone, F., and Arbaret, L. (2012). Deformation experiments of bubble- and crystal-bearing magmas: Rheological and microstructural analysis. *Journal of Geophysical Research*, 117:B05208.

Pistone, M., Caricchi, L., Ulmer, P., Reusser, E., and Ardia, P. (2013). Rheology of volatile-bearing crystal mushes: Mobilization vs. viscous death. *Chemical Geology*, 345:16–39.

Pitzer, K. S. and Sterner, S. M. (1994). Equations of state valid continuously from zero to extreme pressures for H2O and CO2. *The Journal of Chemical Physics*, 101(4):3111–3116.

Polacci, M., Cashman, K. V., and Kauahikaua, J. P. (1999). Textural characterization of the pahoehoe - 'a'a transition in Hawaiian basalt. *Bulletin of Volcanology*, 60:595–609.

Poland, M. P., Orr, T. R., Kauahikaua, J. P., Brantley, S. R., Babb, J. L., Patrick, M. R., Neal, C. A., Anderson, K. R., Antolik, L., Burgess, M., Elias, T., Fuke, S., Fukunaga, P., Johanson, I. A., Kagimoto, M., Kamibayashi, K., Lee, L., Miklius, A., Million, W., Moniz, C., Okubo, P. G., Sutton, A. J., Takahashi, T. J., Thelen, W. A., Tollett, W., and Trusdell, F. A. (2016). The 2014-2015 Pahoa lava flow crisis at Kilauea Volcano, Hawai'i: Disaster avoided and lessons learned. *GSA Today*, 26(2):4–10.

Poland, M. P., Takahashi, T. J., and Landowski, C. M., editors (2014). *Characteristics of Hawaiian Volcanoes*. U.S. Geol. Surv. Prof. Paper 1801.

Riker, J. M., Cashman, K. V., Kauahikaua, J. P., and Montierth, C. M. (2009). The length of channelized lava flows: Insight from the 1859 eruption of Mauna Loa Volcano, Hawaii. *Journal of Volcanology and Geothermal Research*, 183:139–156.

Rittmann, A. (1962). *Volcanoes and their activity.* Wiley (New York, London).

Robert, G., Whittington, A. G., Stechern, A., and Behrens, H. (2013). The effect of water on the viscosity of a synthetic calc-alkaline basaltic andesite. *Chemical Geology*, 346:135–148.

Rowland, S. K. and Walker, G. P. L. (1990). Pahoehoe and aa in Hawaii: volumetric flow rate controls the lava structure. *Bulletin of Volcanology*, 52:615–628.

Rudge, J. F., Holness, M., and Smith, G. C. (2008). Quantitative textural analysis of packings of elongate crystals. *Contributions to Mineralogy and Petrology*, 156(4):413–429.

Rust, A. C. and Manga, M. (2002). Effects of bubble deformation on the viscosity of dilute suspensions. *Journal of Non-Newtonian Fluid Mechanics*, 104:53–63.

Ryan, A. G., Russell, J. K., Nichols, A. R. L., Hess, K.-U., and Porritt, L. A. (2015). Experiments and models on H2O retrograde solubility in volcanic systems. *American Mineralogist*, 100:774–786.

Sehlke, A., Whittington, A. G., Robert, B., Harris, A., Gurioli, L., and Médard, E. (2014). Pahoehoe to ‘a‘a transition of Hawaiian lavas: an experimental study. *Bulletin of Volcanology*, 76:876.

Shaw, H. R. (1969). Rheology of basalt in the melting range. *Journal of Petrology*, 10(3):510–535.

Shaw, H. R., Wright, T. L., Peck, D. L., and Okamura, R. (1968). The viscosity of basaltic magma: An analysis of field measurements in Makaopuhi lava lake, Hawaii. *American Journal of Science*, 266:225–264.

Sierou, A. and Brady, J. F. (2002). Rheology and microstructure in concentrated noncolloidal suspensions. *Journal of Rheology*, 46(5):1031–1056.

Singh, A. and Nott, P. R. (2000). Normal stresses and microstructure in bounded sheared suspensions via Stokesian Dynamics simulations. *Journal of Fluid Mechanics*, 412:279–301.

Sisson, T. W. and Bacon, C. R. (1999). Gas-driven filter pressing in magmas. *Geology*, 27(7):613–616.

Spera, F. J. (1984). Some numerical experiments on the withdrawal of magma from crustal reservoirs. *Journal of Geophysical Research*, 89(B10):8222–8236.

Swanson, D. A. (1973). Pahoehoe flows from the 1969-1971 Mauna Ulu eruption, Kilauea volcano, Hawaii. *Bulletin of the Geological Society of America*, 84:615–626.

Tanner, R. I., Qi, F., and Dai, S. (2013). Scaling the normal stresses in concentrated non-colloidal suspensions of spheres. *Rheologica Acta*, 52:291–295.

Taylor, G. I. (1932). The viscosity of a fluid containing small drops of another fluid. *Proceedings of the Royal Society A*, 138:41–48.

Taylor, G. I. (1934). The formation of emulsions in definable fields of flow. *Proceedings of the Royal Society A: Mathematical, Physical and Engineering Sciences*, 146:501–523.

Thornber, C. R. (2001). Olivine-liquid relations of lava erupted by Kilauea volcano from 1994 to 1998: Implications for shallow magmatic processes associated with the ongoing east-rift-zone eruption. *The Canadian Mineralogist*, 39:239–266.

Truby, J. M., Mueller, S., Llewellin, E. W., and Mader, H. M. (2015). The rheology of three-phase suspensions at low bubble capillary number. *Proceedings of the Royal Society A: Mathematical, Physical and Engineering Sciences*, 471:20140557.

Tuffen, H., Owen, J., and Applegarth, L. J. (2012). Measurement of volatile concentrations in volcanic glasses using thermogravimetric analysis: comparison with micro-analytical methods. In Abbasi, A. and Giesen, N., editors, *EGU General Assembly Conference Abstracts*, volume 14 of *EGU General Assembly Conference Abstracts*, page 11347.

U.S. Geological Survey (2009). Introduction to Kilauea Volcano, Hawai'i. *http://hvo.wr.usgs.gov/kilauea/*, 2016-01-27.

U.S. Geological Survey (2015). HVO Maps. *http://hvo.wr.usgs.gov/maps/*, 2015-06-04.

Vigneresse, J. L., Barbey, P., and Cuney, M. (1996). Rheological transitions during partial melting and crystallization with application to felsic magma segregation and transfer. *Journal of Petrology*, 37(6):1579–1600.

Vogel, D. H. (1921). Temperaturabhängigkeitsgesetz der Viskosität von Flüssigkeiten. *Phys. Zeit.*, 22:209–223.

von Aulock, F. W., Kennedy, B. M., Schipper, C. I., Castro, J. M., Martin, D. E., Oze, C., Watkins, J. M., Wallace, P. J., Puskar, L., Begue, F., Nichols, A. R. L., and Tuffen, H. (2014). Advances in Fourier transform infrared spectroscopy of natural glasses: From sample preparation to data analysis. *Lithos*, 206-207:52–64.

Vona, A., Romano, C., Giordano, D., and Russell, J. K. (2013). The multiphase rheology of magmas from Monte Nuovo (Campi Flegrei, Italy). *Chemical Geology*, 346:213–227.

Walker, G. P. L. (1971). Compound and simple lava flows and flood basalts. *Bulletin Volcanologique*, 35:579–590.

Walker, G. P. L. (1991). Structure, and origin by injection of lava under surface crust, of tumuli, "lava rises", "lava-rise pits", and "lava inflation clefts" in Hawaii. *Bulletin of Volcanology*, 53:546–558.

Webb, S. L. and Dingwell, D. B. (1990). Non-Newtonian rheology of igneous melts at high stresses and strain rates: Experimental results for rhyolite, andesite, basalt, and nephelinite. *Journal of Geophysical Research*, 95(B10):15695–15701.

Wentworth, C. K. and MacDonald, G. A. (1953). Structures and forms of basaltic rocks in Hawaii. *Geological Survey Bulletin*, 994:1–98.

Whittington, A. G., Hellwig, B. M., Behrens, H., Joachim, B., Stechern, A., and Vetere, F. (2009). The viscosity of hydrous dacitic liquids: implications for the rheology of evolving silicic magmas. *Bulletin of Volcanology*, 71:185–199.

Wilson, L. and Parfitt, E. A. (1993). The formation of perched lava ponds on basaltic volcanoes: the influence of flow geometry on cooling-limited lava flow lengths. *Journal of Volcanology and Geothermal Research*, 56:113–123.

Wolfe, E. W., Neal, C. A., Banks, N. G., and Duggan, T. J. (1988). Geological observations and chronology of eruptive events. In Wolfe, E. W., editor, *The Pu'u 'Ō'ō eruption of Kilauea Volcano, Hawai'i; episodes 1 through 20, January 3, 1983, through June 8, 1984.*, pages 1–98. U.S. Geol. Surv. Prof. Paper 1463.

Wotzlaw, J.-F., Schaltegger, U., Frick, D. A., Dungan, M. A., Gerdes, A., and Gunther, D. (2013). Tracking the evolution of large-volume silicic magma reservoirs from assembly to supereruption. *Geology*, 41(8):867–870.

Zarraga, I. E., Hill, D. A., and Leighton, D. T. (2000). The characterization of the total stress of concentrated suspensions of noncolloidal spheres in Newtonian fluids. *Journal of Rheology*, 44(2):185–220.

Zhang, Y., Xu, Z., Zhu, M., and Wang, H. (2007). Silicate melt properties and volcanic eruptions. *Reviews of Geophysics*, 45:1–27.

Zimmerer, M. J. and McIntosh, W. C. (2012). An investigation of caldera-forming magma chambers using the timing of ignimbrite eruptions and pluton emplacement at the Mt. Aetna caldera complex. *Journal of Volcanology and Geothermal Research*, 245-246:128–148.

Appendix A

Published work

PROCEEDINGS A

rspa.royalsocietypublishing.org

Research

Cite this article: Truby JM, Mueller SP, Llewellin EW, Mader HM. 2015 The rheology of three-phase suspensions at low bubble capillary number. *Proc. R. Soc. A* **471**: 20140557. http://dx.doi.org/10.1098/rspa.2014.0557

Received: 22 July 2014
Accepted: 28 October 2014

Subject Areas:
volcanology, materials science

Keywords:
rheology, particle suspension, bubble suspension, analogue experiments, three phase

Author for correspondence:
J. M. Truby
e-mail: j.m.truby@durham.ac.uk

Electronic supplementary material is available at http://dx.doi.org/10.1098/rspa.2014.0557 or via http://rspa.royalsocietypublishing.org.

THE ROYAL SOCIETY PUBLISHING

The rheology of three-phase suspensions at low bubble capillary number

J. M. Truby[1], S. P. Mueller[2], E. W. Llewellin[1] and H. M. Mader[3]

[1]Department of Earth Sciences, Durham University, Durham DH1 3LE, UK
[2]Institute of Geosciences, Johannes Gutenberg University Mainz, 55099 Mainz, Germany
[3]School of Earth Sciences, University of Bristol, Bristol BS8 1RJ, UK

We develop a model for the rheology of a three-phase suspension of bubbles and particles in a Newtonian liquid undergoing steady flow. We adopt an 'effective-medium' approach in which the bubbly liquid is treated as a continuous medium which suspends the particles. The resulting three-phase model combines separate two-phase models for bubble suspension rheology and particle suspension rheology, which are taken from the literature. The model is validated against new experimental data for three-phase suspensions of bubbles and spherical particles, collected in the low bubble capillary number regime. Good agreement is found across the experimental range of particle volume fraction ($0 \leq \phi_p \lesssim 0.5$) and bubble volume fraction ($0 \leq \phi_b \lesssim 0.3$). Consistent with model predictions, experimental results demonstrate that adding bubbles to a dilute particle suspension at low capillarity increases its viscosity, while adding bubbles to a concentrated particle suspension decreases its viscosity. The model accounts for particle anisometry and is easily extended to account for variable capillarity, but has not been experimentally validated for these cases.

1. Introduction

Multiphase suspensions of particles and/or bubbles in a continuous liquid phase are common in nature and industry; examples include magma, oil, concrete,

foodstuffs, cosmetics, pharmaceuticals, biological fluids and nanofluids. Characterizing, modelling and controlling the flow of these suspensions requires a constitutive rheological model, encapsulating the viscosity of the suspension as a function of the properties of the suspending liquid, the volume fraction and properties of the suspended phase(s), and the flow conditions.

The rheology of two-phase suspensions (bubbles-in-liquid *or* particles-in-liquid, where the liquid is Newtonian) has been the subject of extensive experimental and theoretical research for more than a century. In recent years, significant advances have been made and two-phase constitutive equations are now available which have been validated against experimental data for a wide range of conditions (see [1] for a recent review). By contrast, considerably less research has been directed at understanding the rheology of three-phase suspensions (where bubbles *and* particles are suspended in a liquid) primarily owing to the complexity of the problem. Phan-Thien & Pham [2] present a theoretical treatment—discussed later in §3—which has been applied in studies of multiphase magma (e.g. [3,4]), but has not been experimentally validated. Experimental investigation of the rheology of three-phase suspensions appears to be confined to studies of bubble- and crystal-bearing magmas (e.g. [4,5]); these experiments and materials are complex and the resulting data are not well-suited to the validation of three-phase rheological models. Constraining three-phase rheology therefore remains an important, yet outstanding, problem in multiphase fluids research.

Here, we build on published two-phase constitutive equations to generate a three-phase model, by using an 'effective-medium' method in which the bubble suspension is treated as a continuous medium which suspends the particles; this carries the implicit assumption that the bubbles are small compared with the particles. We validate the model against new experimental data for three-phase suspensions of bubbles and spherical particles in the low-capillarity regime (in which flow is steady and bubble deformation is small).

2. Rheology of two-phase suspensions

The rheology of a strictly Newtonian fluid is completely described by its viscosity μ. The viscosity is the ratio of the deforming stress and associated strain-rate which, for rheometric flow, is given by $\mu = \tau/\dot{\gamma} = \text{const.}$, where τ is the shear stress and $\dot{\gamma}$ is the shear strain-rate. When bubbles or solid particles are added to a Newtonian liquid, the resulting suspension has non-Newtonian rheology. In the simplest case, this means that the ratio of stress and strain-rate is a function of strain-rate and is termed the apparent viscosity $\eta = \tau/\dot{\gamma} = f(\dot{\gamma})$. The viscosity of a suspension is often reported as the relative viscosity η_r, which is the apparent viscosity of the suspension at some strain-rate, normalized by the viscosity of the liquid phase

$$\eta_r = \frac{\eta}{\mu}. \tag{2.1}$$

In the following subsections, we briefly review the constitutive equations for two-phase suspensions that provide the building blocks for the three-phase rheological model presented later in §3. The subscript 'b' refers to bubbles suspensions, the subscript 'p' refers to particle suspensions.

(a) Bubble suspension rheology

When a bubble suspension flows, viscous stresses cause the bubbles to deform. If the flow is 'steady' the bubbles reach an equilibrium deformation, which is described by the bubble capillary number

$$Ca = \lambda\dot{\gamma}, \tag{2.2}$$

where λ is the bubble relaxation time [6–8]. The relaxation time describes the characteristic timescale over which the bubble adjusts towards a new equilibrium deformation in response to a

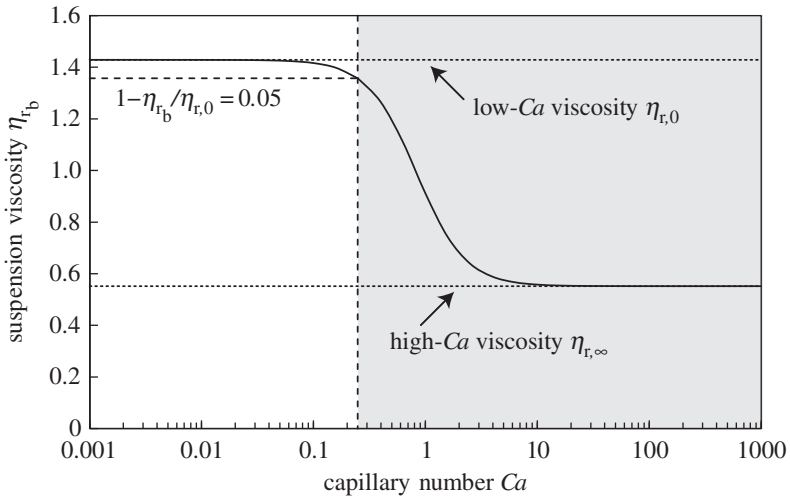

Figure 1. Normalized bubble suspension viscosity η_{r_b} as a function of capillary number *Ca* for $\phi_b = 0.3$ (solid line). Short-dashed lines show the asymptotic values of η_{r_b} at low and high capillary number. Long-dashed line shows the capillary number that we define as the upper limit of the low-capillarity region ($Ca \geq 0.248$ for $\phi_b = 0.3$); we discard experimental data collected above this value, in the shaded region, as discussed in §4*c*.

change in the strain environment; it is given by

$$\lambda = \frac{\mu a}{\Gamma}, \tag{2.3}$$

where a is the bubble's equivalent spherical radius and Γ is the liquid–gas surface tension. The flow is steady if the condition $\lambda \ll \dot{\gamma}/\ddot{\gamma}$ has been satisfied for time $t \gg \lambda$ [7].

For steady flow, the relative viscosity η_{r_b} of a bubble suspension is given by Rust & Manga [8] and Mader *et al.* [1]

$$\eta_{r_b} \equiv \frac{\eta_b}{\mu} = \eta_{r,\infty} + \frac{\eta_{r,0} - \eta_{r,\infty}}{1 + ((6/5)Ca)^2}, \tag{2.4}$$

where η_b is the apparent viscosity of the bubble suspension, and $\eta_{r,0}$ and $\eta_{r,\infty}$ are, respectively, the relative viscosity of the bubble suspension at low and high *Ca*. For non-dilute suspensions $\eta_{r,0}$ and $\eta_{r,\infty}$ are given by Llewellin & Manga [9] and Mader *et al.* [1]

$$\eta_{r,0} = (1 - \phi_b)^{-1} \tag{2.5}$$

and

$$\eta_{r,\infty} = (1 - \phi_b)^{5/3}, \tag{2.6}$$

where ϕ_b is the bubble volume fraction. These expressions, which reduce in the dilute limit (as $\phi_b \to 0$) to the well-known theoretical models of Taylor [10] ($\eta_{r,0} = 1 + \phi_b$) and Mackenzie [11] ($\eta_{r,\infty} = 1 - 5\phi_b/3$), show that bubbles increase suspension viscosity at low *Ca* and decrease suspension viscosity at high *Ca*. Equation (2.4) is plotted in figure 1, which demonstrates that the transition between the asymptotic viscosity regions at low and high capillarity occurs over a fairly narrow range of *Ca*, centred on $Ca \approx 1$. Consequently, equations (2.5) and (2.6) can be used to calculate bubble suspension viscosity for all *Ca*, except over the narrow transitional region; we define an approximate upper bound to the low *Ca* region later in §4*c*.

Equations (2.2)–(2.6) are relevant for monodisperse bubble suspensions at low and moderate bubble volume fractions ($\phi_b \lesssim 0.5$) [7]. Most bubble suspensions are polydisperse to some extent, resulting in a range of bubble relaxation times; hence also a range of capillarities for a given strain-rate. In this work, we restrict our analysis to suspensions in the low-capillarity limit, where equation (2.5) is sufficient to describe the viscosity of a bubble suspension regardless of its bubble size distribution. For the more general case of intermediate capillarity, a more sophisticated

approach is required, in which the contribution of each bubble size fraction to the viscosity of the bulk suspension is linearly superposed; this approach is described in detail in Mader *et al.* [1]. Bubble suspensions are visco-elastic even when dilute, and elastic behaviour becomes more pronounced as bubble volume fraction increases; visco-elastic rheology is neglected in this work because elastic behaviour is not manifest in steady flow [7].

(b) Particle suspension rheology

Particle suspensions commonly show non-Newtonian behaviour when non-dilute, including shear-thinning (e.g. [12]), shear-thickening (e.g. [13,14]) and non-zero normal stress differences (e.g. [15,16]). When shear-thinning behaviour is observed, the rheology of a particle suspension is often described using the model of Herschel & Bulkley [17]

$$\tau = \tau_0 + K\dot{\gamma}^n, \tag{2.7}$$

where τ_0 is the yield stress, K is the consistency and n is the flow index ($n < 1$ when the suspension is shear-thinning). The yield stress is non-zero only for highly concentrated suspensions, hence it is often neglected, reducing equation (2.7) to a power-law [18]

$$\eta_\mathrm{p} = K\dot{\gamma}^{n-1}, \tag{2.8}$$

where η_p is the apparent viscosity of the suspension. Although in common usage (e.g. [4,19,20]), this approach has the limitation that the consistency has fractional units of Pa s^n and is therefore not amenable to non-dimensionalization when $n \neq 1$; this issue is discussed in detail in Mader *et al.* [1] and Mueller *et al.* [20]. In this work, we address this limitation by introducing a characteristic timescale t_c of a shear-thinning suspension, against which the strain-rate can be non-dimensionalized, giving

$$\eta_\mathrm{p} = \eta_*(t_\mathrm{c}\dot{\gamma})^{n-1}, \tag{2.9}$$

where η_* is a 'reference viscosity' of the suspension — i.e. the apparent viscosity at strain-rate $\dot{\gamma} = 1/t_\mathrm{c}$. No satisfactory microphysical explanation for shear-thinning has yet been proposed for suspensions of the sort considered in this work, in which the particles are not subject to Brownian motion (high Peclet number), are strongly coupled to the flow (low Stokes number) and in which inertial effects can be neglected (low particle Reynolds number) [19]. Consequently, there is no physical model from which t_c can be computed *a priori*. However, Mueller *et al.* [19,20] find empirically that the theoretical model of Maron & Pierce [21]

$$\eta = \mu\left(1 - \frac{\phi_\mathrm{p}}{\phi_\mathrm{m}}\right)^{-2} \tag{2.10}$$

accurately captures the rheology of diverse particle suspensions (with variable ϕ, μ and particle aspect ratio) when the consistency is identified with the viscosity; i.e. under the assumption $K \equiv \eta$. This is equivalent to finding that the characteristic timescale $t_\mathrm{c} = 1$ s, and making the identity $\eta_* \equiv \eta$ in equations (2.9) and (2.10). This allows us to link these two equations while maintaining strict dimensional consistency, giving

$$\eta_{\mathrm{r},*} = \left(1 - \frac{\phi_\mathrm{p}}{\phi_\mathrm{m}}\right)^{-2}, \tag{2.11}$$

where we define $\eta_{\mathrm{r},*}$ as the relative reference viscosity

$$\eta_{\mathrm{r},*} \equiv \frac{\eta_*}{\mu}. \tag{2.12}$$

We propose that this approach is a useful improvement over that adopted by Mueller *et al.* [19,20], Vona *et al.* [4] and Mader *et al.* [1], which included the pragmatic, but inexact, non-dimensionalization $K_\mathrm{r} = K/\mu$. Numerically, the values of K_r and $\eta_{\mathrm{r},*}$ are identical when $t_\mathrm{c} = 1$ s (as is indicated empirically) so the results of those earlier studies can be transferred directly into this new framework.

The maximum packing fraction in equations (2.10) and (2.11) is a function of particle shape and roughness; Mader *et al.* [1] give the following equation for ϕ_m:

$$\phi_m = \phi_{m_1} \exp\left[-\frac{(\log_{10} r_p)^2}{2b^2}\right], \tag{2.13}$$

where r_p is the particle aspect ratio. For smooth particles $\phi_{m_1} = 0.66$ and $b = 1.08$, and for rough particles $\phi_{m_1} = 0.55$ and $b = 1.00$; these values are empirically determined.

Mueller *et al.* [19] report that the flow index n for a particle suspension is a function of the particle volume fraction ϕ_p and the particle aspect ratio. They present a purely empirical relationship

$$n = 1 - 0.2 r_p \left(\frac{\phi_p}{\phi_m}\right)^4, \tag{2.14}$$

which is valid for $\phi_p/\phi_m \leq 0.8$.

3. A model for the rheology of three-phase suspensions

Equation (2.11) gives the relative viscosity $\eta_{r,*}$ of a suspension of particles in a liquid with viscosity μ. If we suppose that the particles are instead suspended in a bubble suspension with viscosity η_b (i.e. we treat the bubble suspension as an 'effective medium') we obtain

$$\frac{\eta_*}{\eta_b} = \left(1 - \frac{\phi_p}{\phi_m}\right)^{-2}. \tag{3.1}$$

Treating the bubble suspension as the continuous phase carries the implicit assumption that the bubbles should be small compared with the particles. At low bubble capillarity, from equations (2.4) and (2.5), we have $\eta_b = \mu(1 - \phi_b)^{-1}$; hence

$$\eta_{r,*} = (1 - \phi_b)^{-1} \left(1 - \frac{\phi_p}{\phi_m}\right)^{-2}. \tag{3.2}$$

At high bubble capillarity, equation (2.6) would take the place of equation (2.5); while for intermediate capillarity, equation (2.4) would take its place, and polydispersity would have to be explicitly accounted for (see §2*a*).

This effective medium method has been used elsewhere in rheological models. Of most relevance, Phan-Thien & Pham [2] use the approach to derive an equation for the viscosity of three-phase suspensions of bubbles and particles that is similar to the model we derive above, but contains a different expression for the particle suspension contribution: $(1 - \phi_p)^{-5/2}$, which they derive using a differential method. Although they do consider a maximum packing fraction in some variants of their model, their implicit solutions reduce to exact equations only under restrictive conditions, e.g. $\phi_p \sim \phi_m$ or $\phi_m = 1$. Consequently, the treatment of the contribution of the particles to the suspension rheology in our formulation is a significant improvement over that of Phan-Thien & Pham [2].

(a) Defining volume fractions in three-phase suspensions

Particle volume fraction and gas volume fraction are unambiguously defined for two-phase suspensions; however, care must be taken to define them appropriately for three-phase suspensions. In our model formulation above, we treat the bubble suspension as the effective medium, hence, the appropriate definitions are

$$\phi_b = \frac{V_b}{V_l + V_b} \tag{3.3}$$

and

$$\phi_p = \frac{V_p}{V_l + V_b + V_p}, \tag{3.4}$$

where V_l, V_b and V_p are the respective volumes of the liquid, bubble and particle phases.

For many three-phase applications, we are interested in characterizing how the rheology of a suspension of particles changes as bubbles are added to it (or, equivalently, as bubbles grow within it). For example, a magma that contains solid crystals may be bubble-free at depth, but become increasingly bubble-rich during ascent. In this case, it is more intuitive to define a particle volume fraction and bubble volume fraction as follows:

$$\phi_b^* = \frac{V_b}{V_l + V_b + V_p} \tag{3.5}$$

and

$$\phi_p^* = \frac{V_p}{V_l + V_p}. \tag{3.6}$$

In this formulation, the particle volume fraction does not change from its initial value as bubbles grow, and the bubble volume fraction reflects the value that would be measured by applying Archimedes' principle on the bulk sample. The different formulations for volume fractions are simply related

$$\phi_b = \frac{\phi_b^*}{1 - \phi_p^*(1 - \phi_b^*)} \tag{3.7}$$

and

$$\phi_p = \phi_p^*(1 - \phi_b^*), \tag{3.8}$$

allowing the three-phase model (equation (3.2)) to be applied when it is ϕ_b^* and ϕ_p^* that are known.

In the following sections, we work with both of these definitions, since equations (3.3) and (3.4) underpin the model formulation, while equations (3.5) and (3.6) are more natural for some applications of the model, and aid physical insight. A further volume fraction of interest is the fraction of the total volume that is made up of suspended bubbles and/or particles—the total suspended fraction:

$$\phi_s = \frac{V_b + V_p}{V_l + V_b + V_p}. \tag{3.9}$$

4. Experiments

(a) Samples

Three-phase samples were prepared by adding spherical glass beads (Potters Ballotini; density 2448 kg m^{-3}, size fraction 63–125 µm) to a sugar syrup (Tate & Lyle Golden Syrup; density 1438 kg m^{-3} and surface tension 0.08 N m^{-1} [7]) and aerating with a domestic electric whisk. The rheology of the pure syrup was determined individually for each sample batch and found to be strictly Newtonian; measured viscosities were in the range $55.68 \leq \mu \leq 61.69$ Pa s at 20°C (presented later in data table 1). Particle volume fraction was controlled by adding a known mass of beads to a known mass of syrup (typically equating to 100–150 ml) to prepare sample suites of similar initial (bubble-free) particle volume fraction $\phi_p = 0.05$, 0.1, 0.2, 0.3, 0.4 and 0.5. Bubble volume fraction was varied by adjusting the duration and speed of whisking, and suspension temperature. Errors in particle volume fraction and bubble volume fraction are ±3% and ±5%, respectively.

Of the resulting three-phase suspension, about 60 ml was used for rheometric analysis, and a small amount was imaged with a Zeiss SteREO V.8 stereomicroscope. With the remaining sample material, the bubble volume fraction ϕ_b^* was determined by measuring its weight and its volume in a 100 ml measuring cylinder. The bubble size distribution of each sample was determined using the image analysis software JMicroVision. A photomicrograph of a typical sample is presented in figure 2, along with its bubble size distribution.

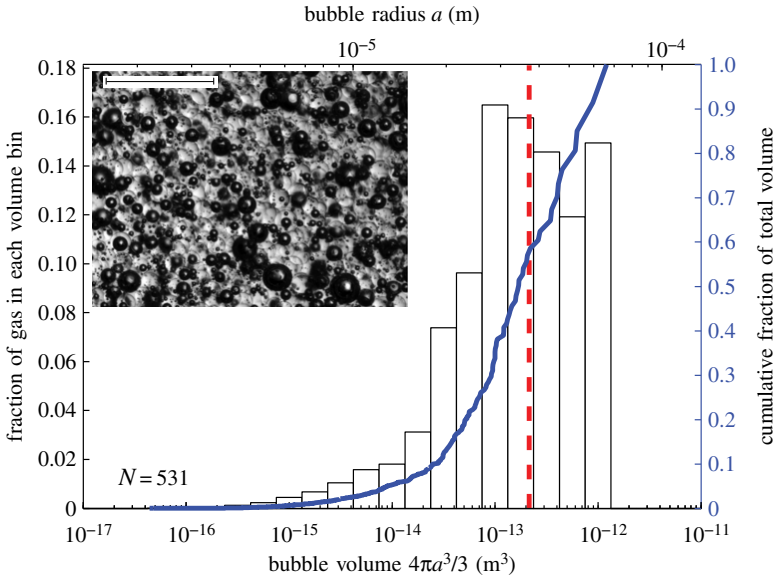

Figure 2. Bubble size distribution for sample 3P-42 ($\phi_p = 0.42$ and $\phi_b = 0.29$). Histogram shows the fraction of the total bubble volume in the sample represented in each volume bin. Solid line shows the cumulative fraction of the total bubble volume. Dashed line is the volume-mean-radius $\langle a \rangle \sim 37$ µm (see §4*c*). Inset shows photomicrograph of sample, in which dark-rimmed spheres are bubbles, and glass beads are light and translucent. Scale bar, 500 µm. (Online version in colour.)

(b) Rheometry

Rheometric data were collected using a ThermoScientific Haake MARS II rheometer with Z40DIN concentric cylinder sensor geometry (rotor diameter 40.0 mm, cup diameter 43.4 mm, gap width 1.7 mm). A standard flow-curve determination consisted of a 20-step 'up ramp' of incrementally increasing shear stress τ up to a maximum value of 500 Pa ('controlled-stress mode'), followed by a 20-step 'down ramp'. At each stress step, the rheometer recorded the corresponding strain-rate $\dot{\gamma}$ once it had reached equilibrium flow conditions. To ensure equilibrium starting conditions for each test, flow curve determinations were preceded by a 4 min, continuous 0–150–0 Pa stress ramp as pre-shear treatment (following [19]). All experiments were performed at 20°C; the precision of the stress and strain-rate measurements is estimated at ±2%.

The densities of the particles and the suspending liquid are not well-matched in our experiments so settling must be considered; similarly, the bubbles are prone to buoyant rise ('creaming'). The concentric cylinder sensor geometry was chosen because it is relatively insensitive to effects of settling and creaming compared with, say, a parallel plate geometry, because particles and bubbles move vertically past the sensor, rather than accumulating in a layer against it. From Stokes' law, we can compute that the time required for an isolated particle or bubble in a dilute suspension to fall or rise the full length of the sensor is more than 120 h for the largest particle and around 1.5 h for the largest bubble; for a concentrated suspension, it is much longer because settling and creaming are hindered. Since total runtimes for our rheometric experiments are much shorter for each sample (the mean experiment duration was 5 min, maximum 12 min), the development of spatial gradients in the particle and bubble volume fractions is considered negligible.

(c) Data analysis

Our rheometric experiments yield flow curves of applied shear stress τ against resultant shear strain-rate $\dot{\gamma}$; an example is shown in figure 3. For some samples, the highest experimental

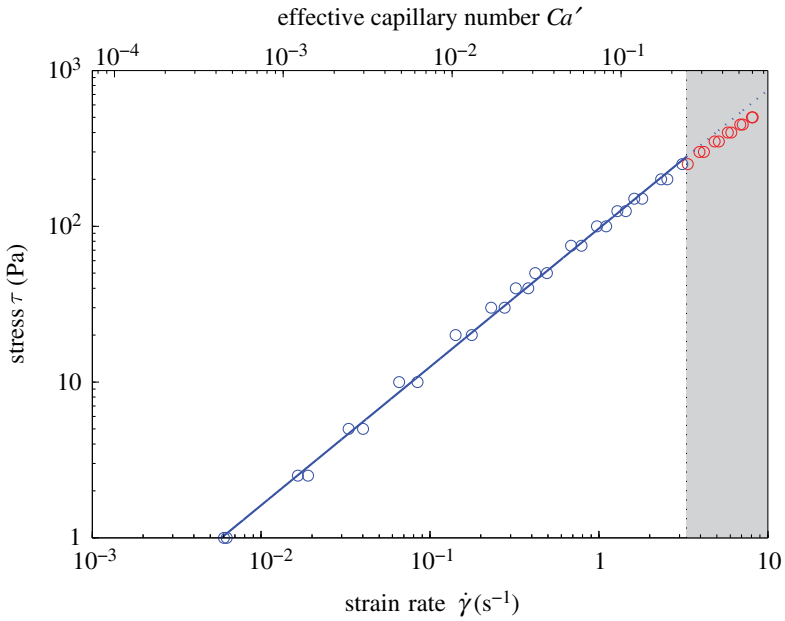

Figure 3. Flow curve of shear stress τ against shear strain-rate $\dot{\gamma}$ for sample 3P-30 with $\phi_b = 0.30$ and $\phi_p = 0.04$. Datapoints are collected during both the up-ramp and down-ramp (§4*b*). Datapoints are discarded (shaded region) for Ca' (defined in §4*c*) greater than the upper bound of the low-capillarity region, defined according to equation (4.2); for $\phi_b = 0.30$, this is $Ca' \geq 0.248$. Solid line is the best fit of equation (4.3) to the remaining datapoints, giving $\eta_{r,*} = 1.74$ and $n = 0.89$; dashed line is the fit extended into the discarded region. (Online version in colour.)

strain-rates are sufficient that the bubbles cannot be assumed to be in the low-capillarity regime. We filter data to remove these datapoints by calculating an upper bound on the low-capillarity region for each sample as follows. For three-phase suspensions, the effective strain-rate in the bubbly effective medium $\dot{\gamma}'$ is higher than the bulk strain-rate $\dot{\gamma}$, because the solid particles cannot accommodate strain through internal shearing. The effective strain-rate is approximately given by $\dot{\gamma}' = \dot{\gamma}/(1 - \phi_p/\phi_m)$; this is a conservative estimate because it does not account for the accommodation of shear strain through solid-body rotation of the particles. A typical bubble radius for each sample may be calculated as the volume-mean-radius $\langle a \rangle = \sum a^4 / \sum a^3$ where summation is over all measured bubbles in that sample (following [1]). We adopt the more conservative criterion of calculating the capillary number using the radius of the largest bubble measured a_{max}. Putting these values into equations (2.2) and (2.3), we obtain an equation for the effective capillary number: $Ca' = \mu a_{max} \dot{\gamma}'/\Gamma$. We define the low-capillarity region on the basis of the mismatch between the viscosity calculated from equation (2.5) (the low-capillarity asymptotic viscosity), and from equation (2.4) (which is valid for all capillary numbers). We set the upper bound of the low-capillarity region as the value of Ca' for which the mismatch reaches 5%; i.e. for low capillarity

$$\frac{\eta_{r,0} - \eta_{r_b}}{\eta_{r,0}} < 5\% \tag{4.1}$$

or equivalently, from equation (2.4)

$$Ca' < \sqrt{\frac{5}{144(0.95 - (1 - \phi_b)^{8/3})}}. \tag{4.2}$$

The 5% threshold is chosen to be in line with experimental error. After filtering, all flow curves comprise at least 15 datapoints. Based on this conservative criterion, the discrepancy (equation (4.1)) for a bubble with volume-mean-radius is never greater than 1%.

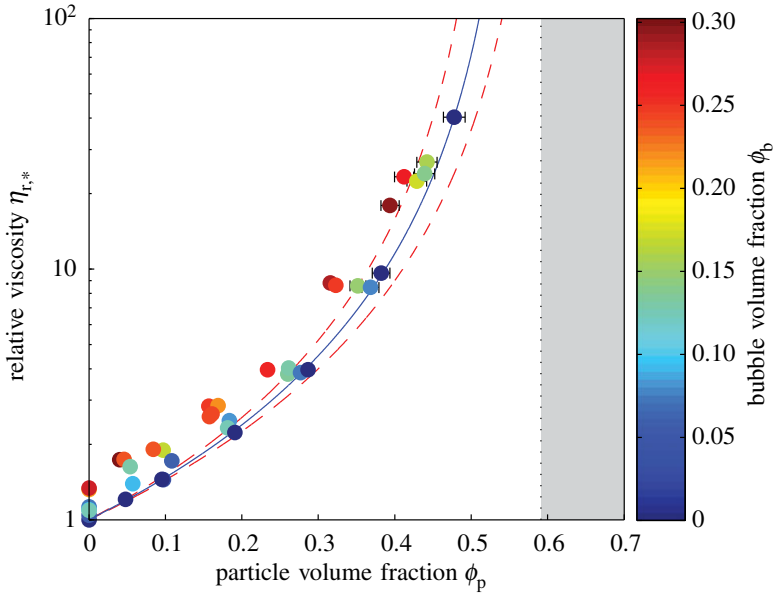

Figure 4. Relative viscosity $\eta_{r,*}$ against particle volume fraction ϕ_p for three-phase suspensions; circles are shaded according to bubble volume fraction ϕ_b. Solid curve is the best fit of the Maron–Pierce equation (2.11) to data from bubble-free suspensions ($\phi_b = 0$, dark circles), giving $\phi_m = 0.593 \pm 0.018$. Shaded area shows the region where $\phi > \phi_m$. Dashed curves show the 95% confidence limits for ϕ_m based on the potential error in the data fitting technique, as presented in the electronic supplementary material. Error bars (1σ) are shown when larger than the data points. (Online version in colour.)

We determine the yield stress τ_0, consistency K and flow index n for each sample by fitting the Herschel–Bulkley model (equation (2.7)) to each filtered flow curve (figure 3) and determine errors using the bootstrapping method presented in the electronic supplementary material. For all samples, the yield stress is found to be either small and negative (which is unphysical) or positive, but within 2σ error of zero; hence, yield stress can be neglected and equation (2.7) can be expressed as the simple power law relationship given in equation (2.9). This is consistent with the experimental results of Mueller *et al.* [19], who found that yield stress is negligible for $\phi_p/\phi_m \lesssim 0.8$. This allows us to fit for η_* and n in log-space using the relationship

$$\log \tau = \log \eta_* + n \log t_c \dot{\gamma}, \tag{4.3}$$

which avoids biasing the fit to large values of τ and $\dot{\gamma}$. As discussed in §2*b*, we assume $t_c = 1$ s, based on previous experimental work [19,20]. The reference viscosity η_* that we determine is normalized by the viscosity of the syrup μ to give the relative reference viscosity $\eta_{r,*}$ (equation (2.12)), hereafter referred to as the relative viscosity.

5. Results

Experimental data are presented in table 1. Results for relative viscosity are presented in figure 4, which plots $\eta_{r,*}(\phi_p)$, with datapoints coloured according to ϕ_b. Similarly, experimental results for the flow index are presented in figure 5, which plots $n(\phi_p)$, with datapoints coloured according to ϕ_b.

It is useful at this stage to confirm that the data for the two-phase end members (bubble-free particle suspension and particle-free bubble suspension) adhere to the relevant two-phase constitutive equations. The solid curve in figure 4 represents the best fit of equation (2.11) (in which the only free parameter is ϕ_m) to data for bubble-free particle suspensions ($\phi_b = 0$). We find an excellent fit for $\phi_m = 0.593$, with $R^2 = 1.00$; this value of the maximum packing fraction

Table 1. Experimental data for each sample, to three significant figures, and 1 s.d. errors where appropriate. Column a_{max} gives the largest bubble measured for each sample, where asterisk (*) indicates that no bubble size distribution was measured, and an average value was used instead. Column $\dot{\gamma}_{max}$ gives the maximum strain-rate that satisfies equation (4.2), and N_{data} are the number of stress–strain-rate data points that remain after filtering.

sample	$\phi_p \pm 3\%$	$\phi_p^* \pm 5.83\%$	$\phi_b \pm 5.83\%$	$\phi_b^* \pm 5\%$	μ (Pa s)	a_{max} (μm)	η_* (Pa s) $\pm$ (error)	$n\pm$ (error)	$\dot{\gamma}_{max}$ (s^{-1}) $\pm$ 2%	N_{data}
3P-3	0.102	0.120	0.168	0.151	61.7	455	117 (1)	0.944 (0.004)	0.646	18
3P-5	0.088	0.113	0.237	0.216	61.7	245	118 (1)	0.916 (0.005)	1.15	15
3P-6	0.113	0.120	0.058	0.051	61.7	177	106 (1)	0.979 (0.003)	3.43	32
3P-7	0.102	0.105	0.033	0.030	61.7	122	89.2 (0.4)	0.991 (0.003)	5.73	38
3P-8	0.192	0.207	0.085	0.068	61.7	129	153 (1)	0.965 (0.003)	3.14	36
3P-9	0.165	0.207	0.244	0.204	61.7	*160	159 (1)	0.914 (0.003)	1.44	26
3P-10	0.164	0.207	0.247	0.206	61.7	234	175 (2)	0.935 (0.003)	0.903	24
3P-11	0.177	0.216	0.220	0.181	61.7	144	176 (1)	0.938 (0.003)	1.57	28
3P-12	0.190	0.212	0.127	0.103	61.7	116	143 (1)	0.965 (0.003)	2.60	32
3P-13	0.169	0.212	0.245	0.204	61.7	*160	163 (2)	0.930 (0.003)	1.36	26
3P-14	0.272	0.302	0.135	0.098	61.7	103	235 (1)	0.959 (0.003)	2.28	38
3P-15	0.244	0.303	0.256	0.194	61.7	123	245 (2)	0.908 (0.003)	1.62	32
3P-17	0.274	0.302	0.130	0.094	58.1	*160	234 (2)	0.956 (0.003)	1.59	32
3P-18	0.289	0.306	0.075	0.053	58.1	*160	224 (2)	0.972 (0.003)	2.10	36
3P-19	0.331	0.409	0.287	0.192	58.1	*160	512 (4)	0.845 (0.002)	0.834	34
3P-20	0.338	0.405	0.249	0.165	58.1	150	500 (4)	0.838 (0.002)	0.963	36
3P-21	0.368	0.406	0.147	0.093	58.1	142	498 (3)	0.917 (0.002)	1.07	38
3P-22	0.385	0.405	0.078	0.048	58.1	120	491 (3)	0.937 (0.002)	1.06	38

(*Continued*.)

Table 1. (*Continued.*)

sample	$\phi_p \pm 3\%$	$\phi_p^* \pm 5.83\%$	$\phi_b \pm 5.83\%$	$\phi_b^* \pm 5\%$	μ (Pa s)	a_{max} (μm)	η_* (Pa s) ± (error)	$n \pm$ (error)	$\dot{\gamma}_{max}$ (s^{-1}) ± 2%	N_{data}
3P-23	0.000	0.000	0.213	0.213	58.1	229	76.6 (0.7)	0.926 (0.004)	1.72	21
3P-24	0.000	0.000	0.054	0.054	58.1	*160	60.5 (0.4)	0.974 (0.003)	5.30	30
3P-25	0.000	0.000	0.075	0.075	58.1	173	65.4 (0.4)	0.970 (0.004)	3.27	26
3P-26	0.000	0.000	0.095	0.095	58.1	129	63.6 (0.4)	0.959 (0.003)	4.29	28
3P-27	0.000	0.000	0.123	0.123	55.7	136	60.7 (0.4)	0.953 (0.003)	3.58	26
3P-28	0.000	0.000	0.275	0.275	55.7	239	74.4 (0.7)	0.920 (0.004)	1.49	20
3P-29	0.463	0.505	0.157	0.085	55.7	147	1490 (20)	0.771 (0.004)	0.124	38
3P-30	0.042	0.059	0.302	0.290	55.7	99.9	96.5 (0.6)	0.888 (0.003)	3.11	27
3P-31	0.048	0.062	0.240	0.228	55.7	110	97.0 (0.7)	0.919 (0.003)	3.09	28
3P-32	0.057	0.065	0.130	0.123	55.7	150	90.6 (0.6)	0.928 (0.009)	2.84	18
3P-33	0.060	0.065	0.090	0.085	55.7	*160	77.6 (0.6)	0.963 (0.010)	3.57	20
3P-35	0.050	0.050	0.000	0.000	55.9	—	67.4 (0.5)	0.994 (0.006)	7.53	38
3P-36	0.100	0.100	0.000	0.000	55.9	—	81.1 (0.6)	0.994 (0.006)	6.25	38
3P-37	0.200	0.200	0.000	0.000	55.9	—	125 (1)	0.993 (0.006)	4.05	38
3P-38	0.300	0.300	0.000	0.000	55.9	—	222 (1)	0.988 (0.006)	1.36	38
3P-39	0.400	0.400	0.000	0.000	55.9	—	540 (4)	0.955 (0.006)	0.924	38
3P-40	0.500	0.500	0.000	0.000	55.9	—	2260 (40)	0.818 (0.004)	0.083	38
3P-41	0.431	0.508	0.266	0.151	57.0	149	1330 (20)	0.676 (0.002)	0.111	27
3P-42	0.412	0.499	0.295	0.174	57.0	132	1020 (10)	0.689 (0.002)	0.164	27
3P-43	0.449	0.496	0.173	0.095	57.0	133	1280 (10)	0.809 (0.002)	0.177	30
3P-44	0.460	0.497	0.141	0.076	57.0	96.5	1370 (10)	0.803 (0.002)	0.302	38

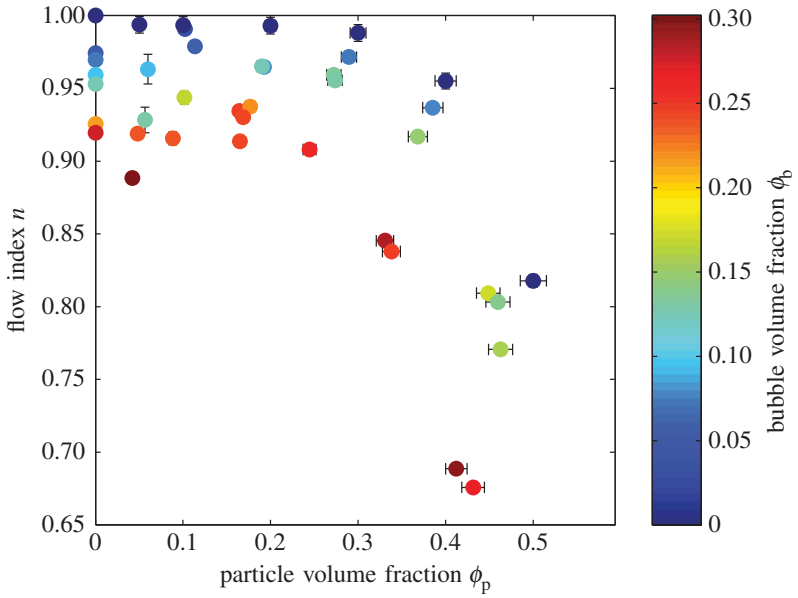

Figure 5. Flow index n against particle volume fraction ϕ_p for three-phase suspensions; circles are shaded according to bubble volume fraction ϕ_b. Error bars (1σ) are shown when larger than the data points. (Online version in colour.)

is slightly lower than the value of $\phi_m = 0.633$ quoted by Mueller *et al.* [19,20] for suspensions of monodisperse spheres, but we note that the 2σ errors of the two estimates overlap. Both of these values are lower than the value of $\phi_m = 0.66$ calculated from equation (2.13) with $r_p = 1$. We propose that equation (2.13) overestimates ϕ_m for nearly spherical particles because it is based on a fit to data that assumes a Gaussian relationship between ϕ_m and r_p. Studies of non-sheared particle packs have reported that the maximum packing fraction is actually highest for slightly non-spherical aspect ratios [22,23]; consequently, the $\phi_m(r_p)$ curve dips around $r_p = 1$ leading to the overestimate given by equation (2.13).

Figure 6 plots two-phase data for the relative viscosity of particle-free bubble suspensions, i.e. $\eta_{r,*}(\phi_b)$ with $\phi_p = 0$. The solid curve is equation (2.5), which gives a good fit to data, with $R^2 = 0.87$. Figures 4 and 6, therefore, demonstrate the validity of the two-phase constitutive models (equations (2.5) and (2.11)) on which we build our three-phase model.

6. Discussion

(a) Reference viscosity

In figure 4, all suspensions that contain bubbles have a higher reference viscosity than a two-phase particle suspension with the same particle volume fraction. Conceptually, this is equivalent to saying that, for a given particle suspension, the viscosity increases if some of the suspending liquid is replaced with bubbles. This is intuitive, because bubbles in the low-capillarity regime increase suspension viscosity.

Recasting our data in terms of ϕ_b^* and ϕ_p^* yields figure 7. It is evident from this plot that the effect of *adding* bubbles to a particle suspension (or growing bubbles in a particle suspension) depends upon the initial particle volume fraction ϕ_p^*. For dilute particle suspensions ($\phi_p^* \lesssim 0.25$), adding bubbles increases the suspension viscosity; whereas, for more concentrated particle suspensions ($\phi_p^* \gtrsim 0.25$), adding bubbles decreases suspension viscosity.

These relationships are more clearly demonstrated by figure 8. The plot shows that the rheology of a particle suspension becomes increasingly sensitive to the addition of a small volume

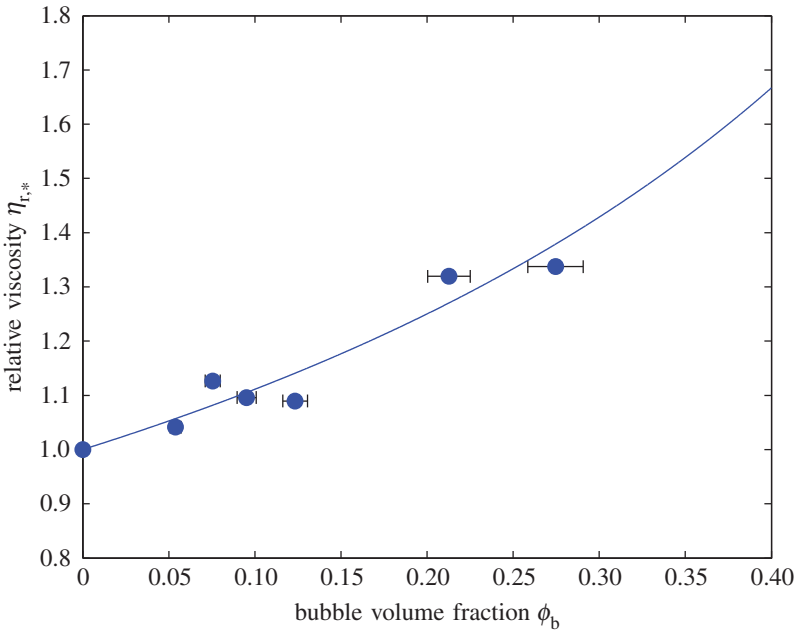

Figure 6. Relative viscosity $\eta_{r,*}$ against bubble volume fraction ϕ_b for particle-free (two-phase) bubble suspensions. The solid curve is equation (2.5). Error bars (1σ) are shown when larger than the data points. (Online version in colour.)

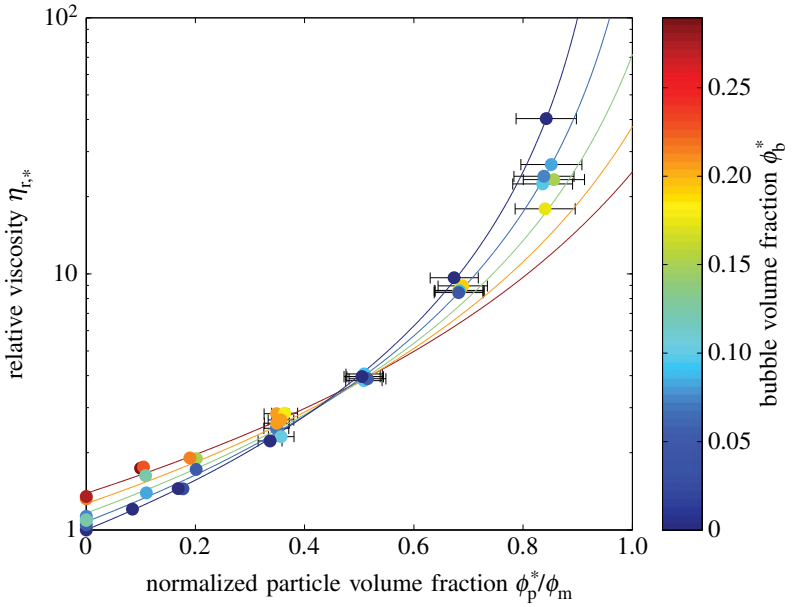

Figure 7. Three phase data from figure 4 recast in terms of ϕ_b^* and ϕ_p^*. Solid lines are the three-phase model (equation (3.2)) contoured in ϕ_b^*. Error bars (1σ) are shown when larger than the data points. (Online version in colour.)

fraction of bubbles as its particle volume fraction approaches the maximum packing fraction. The physical explanation for this behaviour is straightforward and relies on two competing processes. As discussed above, the addition of low-capillarity (i.e. spherical) bubbles to a fluid increases its viscosity. For dilute particle suspensions, this is the dominant trend, hence our data show an

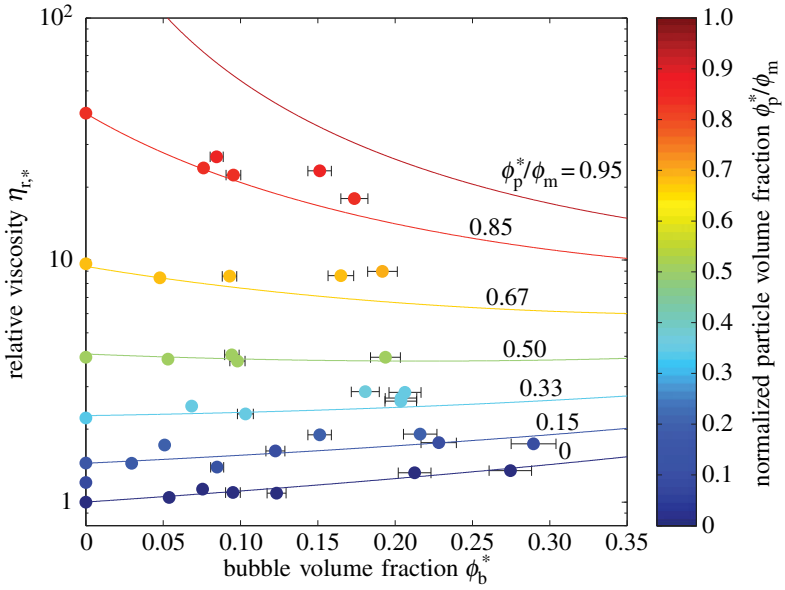

Figure 8. Relative viscosity $\eta_{r,*}$ against ϕ_b^*. Datapoints are shaded according to ϕ_p^*/ϕ_m. Solid curves are the three-phase model (equation (3.2)) for experimental values of ϕ_p^*/ϕ_m appropriate for each suite of samples, contoured according to the same scale. Error bars (1σ) are shown when larger than the data points. (Online version in colour.)

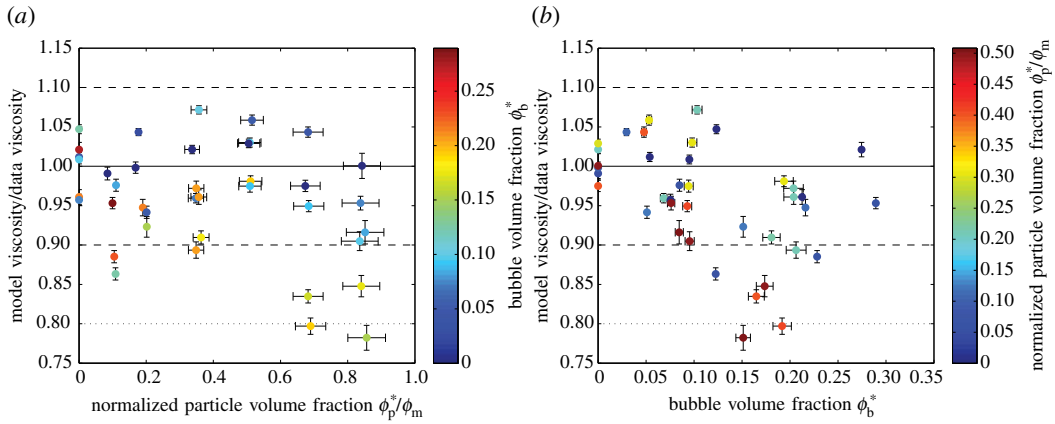

Figure 9. Comparison between $\eta_{r,*}$ predicted by the model (equation (3.2)) and $\eta_{r,*}$ calculated from experimental data, against (*a*) ϕ_p^*/ϕ_m, shaded for ϕ_b^*, and (*b*) ϕ_b^*, shaded for ϕ_p^*/ϕ_m. Error bars (1σ) are shown when larger than the data points. The solid line indicates a perfect match between model and data; the dashed and dotted lines, respectively, indicate $\pm 10\%$ and $\pm 20\%$ discrepancy. (Online version in colour.)

increase in reference viscosity with increasing bubble content for $\phi_p^* \lesssim 0.25$. Opposing this is a 'dilution' effect, in which the addition of bubbles to a suspension of particles moves the particles further apart; this decreases the particle volume fraction ϕ_p, reduces the impact that particle–particle interactions have on suspension rheology and reduces suspension viscosity. This process dominates for concentrated particle suspensions; indeed, because the Maron–Pierce relationship is a power law, the higher the initial particle volume fraction, the greater the impact the same dilution with bubbles will have.

It is also clear from these figures that the data agree well with the three-phase model that we propose (equation (3.2)). The model predicts the relative viscosity to within $\pm 20\%$ for all but two of the samples, and within $\pm 10\%$ for the majority (figure 9). Furthermore, there is no strong

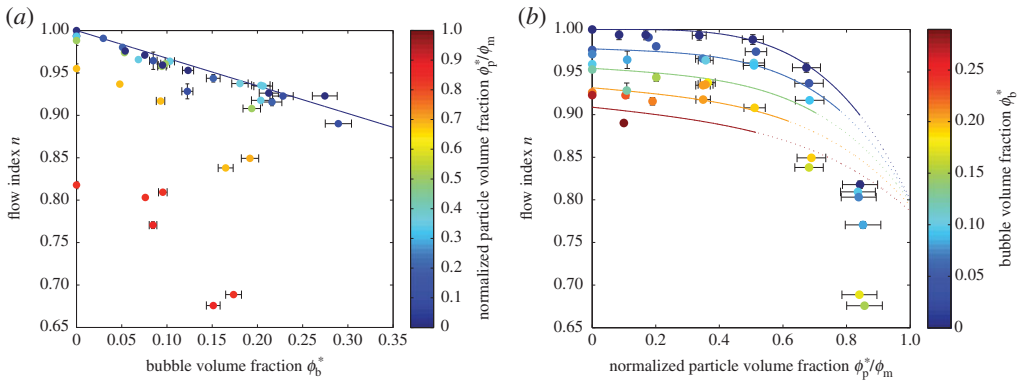

Figure 10. Flow index n against (*a*) ϕ_b^*, shaded according to ϕ_p^*/ϕ_m, and (*b*) ϕ_p^*/ϕ_m, shaded according to ϕ_b^*. Error bars (1σ) are shown when larger than the data points. (*a*) The solid line shows the linear relationship between n and ϕ_b^* for $\phi_p^* = 0$ (equation (6.1)). (*b*) The curves, contoured according to ϕ_b^*, plot equation (6.2); curves are solid over the range of particle volume fractions for which the total suspended fraction $\phi_s < 0.5$, and are dotted outside this range. (Online version in colour.)

systematic trend relating the discrepancy to either ϕ_b^* or ϕ_p^*. We note that the close agreement between model and data is found despite the fact that some samples violate the model assumption that bubbles are small compared with particles (§3). In all samples, the majority (by number) of the bubbles are smaller than the particles and so it makes sense to choose the bubble suspension as the effective medium. However, the average bubble radius is between 0.20 and 0.97 times the average particle radius and the bubble volume-mean-radius (§4*c*) is between 0.57 and 2.4 times the particle volume-mean-radius indicating that the 'typical' bubble in many samples is comparable in size to the particles.

The largest discrepancy between our model and data occurs when both ϕ_p^* and ϕ_b^* are large: our model tends to underpredict the reference viscosity in such samples. This discrepancy is probably caused by bubble–particle interactions, which are not captured in our simple approach of combining two-phase equations. Further work is needed to formulate a model that captures such interactions.

For a given bubble and particle volume fraction, it is useful to know whether the addition of further bubbles (or the growth of existing bubbles) will result in an increase or decrease in viscosity. An analysis of this scenario is presented in the electronic supplementary material.

(b) Flow index

Reference viscosity provides only a partial description of the rheology of a shear-thinning suspension; for a practical rheological model, the flow index n is also required (equation (2.9)). Figure 10 re-presents the flow index data shown in figure 5, plotting them against ϕ_b^* and ϕ_p^*/ϕ_m.

Figure 10*a* shows clearly that shear thinning is observed for all suspensions, even those containing only bubbles. Our data indicate a linear relationship between n and ϕ_b for particle-free suspensions, in the low-capillarity regime, such that shear thinning becomes more pronounced as bubble volume fraction increases:

$$n = 1 - 0.334\phi_b. \tag{6.1}$$

(Note that $\phi_b = \phi_b^*$ when $\phi_p = 0$.) Bubble suspensions are known to be strongly shear thinning in the range $0.1 \lesssim Ca \lesssim 10$ but, at lower and higher capillary number, current models predict that shear thinning is negligible (see figure 1 and §2*a*), which makes this result surprising. One potential explanation is that, despite our data filtering methodology (§4*c*), there are a small number of very large bubbles in the samples, larger than those measured in our sample images, which have a correspondingly long relaxation time and, as a consequence, have a capillary

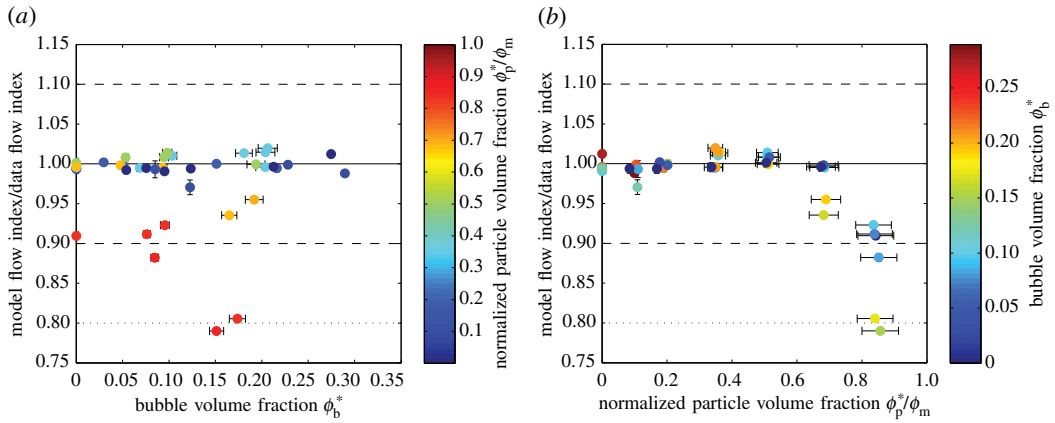

Figure 11. Comparison between n predicted by the model (equation (6.2)) and n calculated from experimental data, against (*a*) ϕ_b^*, shaded for ϕ_p^*/ϕ_m and (*b*) ϕ_p^*/ϕ_m, shaded for ϕ_b^*. Error bars (1σ) are shown when larger than the data points. The solid line indicates a perfect match between model and data; the dashed and dotted lines, respectively, indicate $\pm 10\%$ and $\pm 20\%$ discrepancy. (Online version in colour.)

number in the transitional regime. An alternative explanation is that the current model for bubble suspension rheology (equation (2.4)) is inadequate for non-dilute suspensions. That model can be derived from the theoretical treatment of Frankel & Acrivos [24] and Llewellin *et al.* [25], which is analytically exact in the limit of a dilute suspension (in which bubble–bubble interactions can be neglected) and in the limit of small bubble deformations. It is possible that bubble–bubble interactions in non-dilute samples act to introduce shear thinning—this would be consistent with our finding that shear thinning becomes more pronounced as bubble volume fraction increases. Further experimental work would be required to underpin a more detailed investigation of this phenomenon.

Superimposed on the decrease in flow index due to increasing bubble volume fraction is the effect of increasing particle volume fraction, shown most clearly in figure 10*b*. This relationship is nonlinear and appears to follow the empirical model proposed by Mueller *et al.* [19] (equation (2.14) with $r_p = 1$ for spherical particles). For bubble-free suspensions—comparable to those investigated by Mueller—there is excellent agreement between data and model for $\phi_p/\phi_m < 0.8$, which is consistent with the limits of applicability given by Mueller *et al.* [19].

The combined effect of bubbles and particles on the flow index appears to be a simple superposition of these two effects: the flow index of a pure fluid is 1 and is reduced by some amount dependent on bubble volume fraction, and again by some amount dependent on particle volume fraction. Consequently, we propose the following purely empirical model for flow index for suspensions of spherical particles:

$$n = 1 - 0.2\left(\frac{\phi_p}{\phi_m}\right)^4 - 0.334\phi_b. \tag{6.2}$$

Curves of this model for various bubble volume fractions are shown in figure 10*b* and indicate that the model is valid for all samples with a total suspended fraction $\phi_s \lesssim 0.5$ (figure 11). The model agrees with the data to within $\pm 5\%$ for all samples below this cut-off. Note that this cut-off is drawn empirically from our data and has no theoretical basis.

For suspensions of non-spherical particles, the aspect ratio may be included in equation (6.2) in a manner analogous to equation (2.14). However, further experiments would be required to validate this extension.

7. Conclusion

Our results demonstrate that the proposed three-phase rheological model (equation (3.2)) based on an effective medium approach is in close agreement with experimental data over the full range $0 \leq \phi_b^* \lesssim 0.3$ and $0 \leq \phi_p^*/\phi_m \lesssim 0.85$ investigated. Our preliminary experiments involve spherical particles and steady flow in the low capillarity regime; hence, the model's validity is only demonstrated subject to these restrictions. The model's applicability is, however, potentially much broader (though extensions to the model require further experimental validation).

Mueller *et al.* [20] demonstrate that the Maron–Pierce relationship (equation (2.11)) is valid for suspensions of non-spherical particles when ϕ_m is calculated as a function of particle shape (equation (2.13)). Adopting this methodology for equation (3.2) broadens its applicability to natural systems, in which particles are rarely spherical.

The low-capillarity assumption can also be relaxed. Substituting equation (2.6) for equation (2.5) in the formulation of equation (3.2) yields a three-phase model suitable for high-capillarity flows. This version of the model predicts that the addition of bubbles will always reduce the reference viscosity of a three-phase suspension, even when particle concentration is low. At high particle concentrations, the reduction in viscosity is much more dramatic than in the low capillarity case.

Relaxing the assumption of steady flow is more challenging because, while the rheology of bubble suspensions in unsteady flow is well known [7,9], there is no adequate model for particle suspensions in unsteady flow.

The model developed in this study assumes that bubbles are small compared with particles, although the experimental data demonstrate that the model remains valid when bubbles and particles are comparable in size. Further experiments are required, however, to determine the rheology of suspensions in which bubbles are large compared with particles.

The proposed model for the flow index of three-phase suspensions (equation (6.2)) also provides good agreement with experimental data for which $\phi_s \lesssim 0.5$. Since this model is purely empirical, the relationship between the coefficients found here and the physical properties of the material is not clear: without a physical explanation for the occurrence of shear thinning in bubble and particle suspensions, more work is still needed.

Data accessibility. The full rheological data can be found online at the Earth Science Academic Archive, doi:10.5285/e729d509-a616-4787-bb41-44c1169685b6.

Acknowledgements. We would like to thank two anonymous reviewers for their helpful comments.

Funding statement. J.M.T. acknowledges support from NERC Studentship NE/K500999/1; S.P.M. acknowledges support from NERC Research Fellowship NE/G014426/1; we would also like to acknowledge support from RCUK in making this article open access.

References

1. Mader HM, Llewellin EW, Mueller SP. 2013 The rheology of two-phase magmas: a review and analysis. *J. Volcanol. Geoth. Res.* **257**, 1–51. (doi:10.1016/j.jvolgeores.2013.02.014)
2. Phan-Thien N, Pham DC. 1997 Differential multiphase models for polydispersed suspensions and particulate solids. *J. Non-Newton Fluid* **72**, 305–318. (doi:10.1016/S0377-0257(97)90002-1)
3. Harris AJL, Allen JS. 2008 One-, two-, and three-phase viscosity treatments for basaltic lava flows. *J. Geophys. Res.* **113**, B09212. (doi:10.1029/2007JB005035)
4. Vona A, Romano C, Giordano D, Russell JK. 2013 The multiphase rheology of magmas from Monte Nuovo (Campi Flegrei, Italy). *Chem. Geol.* **346**, 213–227. (doi:10.1016/j.chemgeo.2012.10.005)
5. Pistone M, Caricchi L, Ulmer P, Burlini L, Ardia P, Reusser E, Marone F, Arbaret L. 2012 Deformation experiments of bubble- and crystal-bearing magmas: rheological and microstructural analysis. *J. Geophys. Res.* **117**, 1–39. (doi:10.1029/2011JB008986)
6. Taylor GI. 1934 The formation of emulsions in definable fields of flow. *Proc. R. Soc. Lond. A* **146**, 501–523. (doi:10.1098/rspa.1934.0169)
7. Llewellin EW, Mader HM, Wilson SDR. 2002 The rheology of a bubbly liquid. *Proc. R. Soc. Lond. A* **458**, 987–1016. (doi:10.1098/rspa.2001.0924)

8. Rust AC, Manga M. 2002 Effects of bubble deformation on the viscosity of dilute suspensions. *J. Non-Newton Fluid* **104**, 53–63. (doi:10.1016/S0377-0257(02)00013-7)
9. Llewellin EW, Manga M. 2005 Bubble suspension rheology and implications for conduit flow. *J. Volcanol. Geoth. Res.* **143**, 205–217. (doi:10.1016/j.jvolgeores.2004.09.018)
10. Taylor GI. 1932 The viscosity of a fluid containing small drops of another fluid. *Proc. R. Soc. Lond. A* **138**, 41–48. (doi:10.1098/rspa.1932.0169)
11. Mackenzie JK. 1950 Elastic constants of a solid containing spherical holes. *Proc. Phys. Soc. B* **63**, 2–11. (doi:10.1088/0370-1301/63/1/302)
12. Zarraga IE, Hill DA, Leighton DT. 2000 The characterization of the total stress of concentrated suspensions of noncolloidal spheres in Newtonian fluids. *J. Rheol.* **44**, 185. (doi:10.1122/1.551083)
13. Sierou A, Brady JF. 2002 Rheology and microstructure in concentrated noncolloidal suspensions. *J. Rheol.* **46**, 1031. (doi:10.1122/1.1501925)
14. Fernandez N *et al.* 2013 Microscopic mechanism for shear thickening of non-Brownian suspensions. *Phys. Rev. Lett.* **111**, 108301. (doi:10.1103/PhysRevLett.111.108301)
15. Singh A, Nott PR. 2000 Normal stresses and microstructure in bounded sheared suspensions via Stokesian Dynamics simulations. *J. Fluid Mech.* **412**, 279–301. (doi:10.1017/S0022112000008375)
16. Tanner RI, Qi F, Dai S. 2013 Scaling the normal stresses in concentrated non-colloidal suspensions of spheres. *Rheol. Acta* **52**, 291–295. (doi:10.1007/s00397-013-0676-8)
17. Herschel WH, Bulkley R, 1926 Konsistenzmessungen von Gummi-Benzollösungen. *Kolloid Zeitschrift* **39**, 291–300. (doi:10.1007/BF01432034)
18. Ostwald W. 1925 Concerning the function rate of the viscosity of dispersion systems. IV. *Kolloid Zeitschrift* **36**, 248–250. (doi:10.1007/BF01422893)
19. Mueller SP, Llewellin EW, Mader HM. 2010 The rheology of suspensions of solid particles. *Proc. R. Soc. A* **466**, 1201–1228. (doi:10.1098/rspa.2009.0445)
20. Mueller SP, Llewellin EW, Mader HM. 2011 The effect of particle shape on suspension viscosity and implications for magmatic flows. *Geophys. Res. Lett.* **38**, 1–5. (doi:10.1029/2011GL047167)
21. Maron SH, Pierce PE. 1956 Application of Ree-Eyring generalized flow theory to suspensions of spherical particles. *J. Coll. Sci.* **11**, 80–95. (doi:10.1016/0095-8522(56)90023-X)
22. Delaney GW, Cleary PW. 2010 The packing properties of superellipsoids. *Europhys. Lett.* **89**, 34002. (doi:10.1209/0295-5075/89/34002)
23. Donev A, Cisse I, Sachs D, Variano EA, Stillinger FH, Connelly R, Torquato S, Chaikin PM. 2004 Improving the density of jammed disordered packings using ellipsoids. *Science* **303**, 990–993. (doi:10.1126/science.1093010)
24. Frankel NA, Acrivos AA. 1970 The constitutive equation for dilute emulsions. *J. Fluid Mech.* **44**, 65–78. (doi:10.1017/S0022112070001696)
25. Llewellin EW, Mader HM, Wilson SDR. 2002 The constitutive equation and flow dynamics of bubbly magmas. *Geophys. Res. Lett.* **29**, 1–4. (doi:10.1029/2002GL015697)

Appendix B

Submitted work

Mobilizing magma mushes in the largest explosive volcanic eruptions

J. M. Truby, E. W. Llewellin
Department of Earth Sciences, Durham University
Durham DH1 3LE, UK

J. Taddeucci
Istituto Nazionale di Geofisica e Vulcanologia
Via di Vigna Murata, 605, 00143 Roma, Italia

Abstract

Magma crystallizes as it cools and degasses. Once its crystal content exceeds a critical value the crystals jam against one another, forming an immobile magma mush. Counterintuitively, many of the largest explosive volcanic eruptions involve magma that has a crystal content above the critical value. How is such a mush mobilized? We propose that the pervasive formation and growth of bubbles of magmatic gas pushes the crystals apart, unjamming the mush. We test our model using analogue suspensions, and demonstrate that the growth of bubbles alone is sufficient to mobilize an initially jammed particle suspension. Processes that have previously been proposed for mush mobilization include underplating by a recharge magma, decompression related to tectonic stresses, and seismic shaking, all of which may trigger bubble nucleation; consequently, our model provides a fundamental mechanism that reconciles previous models. We apply the model to the Fish Canyon Tuff (Colorado, USA) as a case study.

1 Background

Many of the largest known explosive volcanic eruptions involve magma that is extremely crystal-rich (table 1). In order to produce such large eruptions, significant volumes of magma must accumulate in the crust; however, seismic studies do not show evidence for large volumes of high melt-fraction magma beneath historically active volcanic systems[5], despite being extremely sensitive to variations in melt fraction[6]. This implies that such systems spend a large proportion of their lifetimes with a high crystal fraction, or with only isolated pockets of melt[7]. This interpretation is supported by geochemical studies e.g. [8;9;10;11], which show that, whilst it can take hundreds of thousands or millions of years to accumulate a large volume magma reservoir, the magma is melt-rich

Deposit [reference]	Volume	Crystallinity
Indian Peak Volcanic Field [1]	<2000km^3	40%^{a}
Fish Canyon Tuff, San Juan Volcanic Field [2]	>5000km^3	45%^{a}
Lund Tuff, Great Basin [3]	>3000km^3	>40%^{a}
Cerro Galan, NW Argentina [4]	>1200km^3	40-55%^{b}

Table 1: Volumes and crystallinities for a number of large explosive eruptions. ^{a} Crystallinity on a whole rock basis; ^{b} crystallinity on a vesicle-free basis.

for only a small fraction of that time. The implication is that mush-like magma chambers must be capable of producing voluminous eruptions. This is difficult to reconcile with rheological models for crystal-rich magmas, which indicate that such mushes should be rheologically jammed.

The viscosity of magma η increases with increasing crystal fraction ϕ_p, at first linearly [12], then non-linearly as crystal–crystal interactions become increasingly important [13;14]. As the maximum packing fraction ϕ_m is approached the crystals begin to jam against one another, giving rise to a yield stress [15]. If the yield stress is greater than the stress driving deformation, the magma is immobile; we term this state 'jammed', and term the critical crystal fraction for jamming $\phi_{\rm crit}$. When the maximum packing fraction ϕ_m is reached, viscous deformation can only be accommodated by crystal–melt segregation and crystal fracturing [16;17]; we term this state 'locked'. Crystal fractions above ϕ_m require some degree of crystal intergrowth, which may cause the magma to develop a substantial mechanical strength.

As a magma crystallizes, therefore, we expect to see an evolution in its rheology, from low viscosity and mobile, to an immobile crystal mush [18]. The conundrum posed by the deposits of the largest eruptions, such as the Fish Canyon Tuff, is that they often have phenocryst fractions close to, or above ϕ_m. Such magma reservoirs would be expected to remain immobile in the crust, eventually forming plutons. Indeed in many areas, both plutons and massive ignimbrites are present and, in some cases, a genetic link between pluton and ignimbrite has been proposed [19].

Explaining the mobilization of crystal-rich magma is therefore a significant and general problem in volcanology, and a number of models have been proposed. Some invoke external triggers, including tectonic controls [20;21;22] and seismic shaking [23]. Others focus on evidence for intrusion and mixing of a hot, mafic, volatile-rich magma into the pre-existing, more-evolved reservoir e.g. [24;25], and invoke 'unzipping' of the mush caused by intrusion of a vesiculating recharge magma [26], or 'sparging' of gas through the mush, carrying heat from a recharge magma [27;28]. None, however, directly addresses the fundamental issue that the crystal fraction must be below $\phi_{\rm crit}$ before the magma can mobilize.

2 A new model for mobilizing magma mush

We propose that a jammed or locked crystal mush may be effectively mobilized through the *in situ* growth of small bubbles. The fundamental mechanism is simple and intuitive: growth of bubbles pushes the crystals apart, reducing the bulk crystal fraction in the magma; when the crystal fraction falls below ϕ_{crit}, the magma can flow. Experiments by Pistone et al. [29] using natural magmas show that the presence of bubbles in a crystal-rich magma strongly reduces its viscosity, supporting this conceptual model.

We adopt the following definitions for crystal fraction $\phi_p = V_p/(V_l+V_b+V_p)$, and bubble fraction $\phi_b = V_b/(V_l+V_b)$, where V_p, V_l, and V_b are the volumes of the crystal (particle), liquid, and bubble phases respectively, in a control volume of magma[30]. In this formulation the crystal fraction decreases from its initial value $\phi_p^* = V_p/(V_l+V_p)$ as bubbles nucleate and grow. For volcanological applications it is common to employ the bulk bubble fraction $\phi_b^* = V_b/(V_l+V_b+V_p)$, which is the value that would be measured using Archimedes principle on the bulk sample; in this case the simple relationship $\phi_p = \phi_p^*(1-\phi_b^*)$ describes how the crystal fraction decreases as the bubble fraction increases.

A magma is jammed while $\phi_p \geq \phi_{\text{crit}}$. From the relationships given above, we can determine the minimum fraction of bubbles that must grow in order to mobilize a magma with a given initial crystal fraction and critical crystal fraction: $\phi_{b,\text{min}}^* = 1 - \phi_{\text{crit}}/\phi_p^*$ (figure 1). Note that a locked magma ($\phi_p \geq \phi_m$) may also be mobilized via this mechanism, as long as the crystals are not strongly intergrown.

The nucleation and growth of bubbles requires that the melt phase must become saturated in volatile species (typically H_2O and CO_2 are the most important). Nucleation and growth of bubbles is promoted by decompression, heating, or crystallization of anhydrous crystal phases in the magma reservoir. An additional consequence of bubble growth is that the bulk density of the magma decreases. The growth of bubbles, therefore, can both unjam the magma, and provide the buoyancy required to initiate its eruption.

3 Experimental proof of concept

We test our hypothesis — that a jammed suspension will become mobile when the fraction of bubbles grows to a value such that $\phi_p < \phi_{\text{crit}}$ — by performing rheometry on a three-phase, analogue suspension of air bubbles and spherical particles in a Newtonian liquid. The rheometry is performed under variable confining pressure, which allows us to vary the bubble fraction in a particle-rich suspension, mimicking bubble growth in a magma mush. We work with analogue materials so that the fundamental effect of changing bubble fraction can be isolated from inter-related processes — such as nucleation, exsolution, volatile-dependent melt viscosity, and crystallization — that operate in a magma mush.

The experiments were run in a rotational rheometer fitted with a six-vane

sensor system (figure 2). A three-phase suspension with $\phi_p^* = 0.6$ and $\phi_b^* = 0.1$ at ambient pressure was pressurized to 4 bars, shrinking the bubbles by a factor of four and decreasing ϕ_b^* commensurately. A constant shear stress was applied and the rate of deformation of the sample was recorded continually as the pressure was dropped, in steps, back to ambient. Details of experimental procedures are included in the online supplementary material: 'Materials and methods'.

3.1 Results and discussion

Figure 3a plots the relative viscosity of the sample ($\eta_r = \eta/\mu$, where η is the suspension viscosity and μ is the liquid viscosity) over time, for isobaric runs at pressures between 3.7 bars ($\phi_b^* = 0.029$) and 1 bar ($\phi_b^* = 0.100$). For the highest pressure shown, the viscosity of the sample increases dramatically over the course of the isobaric run (note logarithmic scale). Towards the end of this run, very small or negative rotation rates are observed, indicating that the sample viscosity is above the rheometer's range. The same pattern is seen for the next highest pressure (3.5 bars, $\phi_b^* = 0.031$). Runs at 4.0 bar ($\phi_b^* = 0.027$) and 3.8 bar ($\phi_b^* = 0.028$) yield even higher viscosities, but these are not shown because of very large scatter, indicating viscosities above the rheometer's range. By contrast, the viscosities for runs at 3.3 bars and lower tend towards finite values, indicating that the sample is flowing as a viscous liquid (although we note that the run at 3.3 bars may not have reached steady state). We conclude that the sample is jammed when the bubble fraction $\phi_b^* \leq 0.031$, and mobile when $\phi_b^* \geq 0.033$, giving $\phi_{b,\min}^* \approx 0.032$.

The maximum packing fraction for a monodisperse suspension of smooth spheres is $\phi_m = 0.633$ [15], which is higher than the highest particle fraction ($\phi_p = 0.584$) achieved in our experiments, at 4 bars pressure. The implication of our experimental observations is that $\phi_{\text{crit}} < \phi_m$, as expected; in this case, the sample becomes mobile at $\phi_{\text{crit}} \approx 0.92\phi_m$.

The viscosity drops considerably in response to the decompression at the end of each isobaric run. This is particularly noticeable for runs in which the sample was jammed at the end of the run — in these cases, the sample appears to mobilize briefly in response to the pressure drop, before jamming again. Figure 3b shows the cumulative strain γ in the sample over time, for four isobaric runs: 4.0 bars ($\phi_b^* = 0.027$); 3.7 bars ($\phi_b^* = 0.029$); 3.3 bars ($\phi_b^* = 0.033$); and 2.9 bars ($\phi_b^* = 0.037$). Each curve starts at $\gamma = 0$ at the time when the pressure reaches its new value following a pressure drop. The strain is approximated following Barnes and Carnali [31]. The plot for 4.0 bars demonstrates that the sample is essentially jammed throughout the run — the cumulative strain shows decaying oscillations around a small, fixed value of γ. When pressure is dropped to 3.7 bars, the sample deforms slightly over 40–50 seconds, then stops deforming once a small strain (around 0.1) is reached. Our interpretation is that bubble growth resulting from the pressure drop pushes the jammed particles apart allowing some flow; after a small strain the particles come back into contact, jamming the suspension once again. At pressures of 3.3 and 2.9 bars, the strain does not reach a constant value; rather it tends towards constant strain rate ($\dot{\gamma}$),

indicating viscous flow of a mobile suspension.

For runs in which the viscosity approaches a fixed, finite value, the final measurement of the run is taken as an approximation to that value. These values are plotted in figure 3c, which demonstrates the transition from jammed to mobile as bubbles grow, and the subsequent reduction in viscosity observed with increasing bubble fraction.

4 Mobilization of the Fish Canyon Tuff magma

The Fish Canyon Tuff (FCT) is a well-studied example of a monotonous intermediate — a high-volume, crystal-rich dacite, produced by a massive explosive eruption. The pre-eruptive phenocryst content of the magma is estimated to have been around 55 vol.%[27]; i.e. $\phi_p^* \approx 0.55$. The maximum packing fraction of crystals in the magma can be estimated using equation 49 in Mader et al.[32] if the crystal aspect ratio r_p is known. From photomicrographs of the FCT in Bachmann et al.[33] we estimate $r_p \approx 2$, giving $\phi_m = 0.53$; since $\phi_p^* > \phi_m$ we expect the FCT magma to have been jammed in the magma reservoir.

The pressure and temperature in the magma reservoir are estimated as 100 MPa and 760°C[27], and the dissolved water content of the melt is estimated at 5 wt.%[34]. We calculate the melt density in the reservoir using the Matlab function created by Pering[35], based on the work of Bottinga and Weill[36], with major oxide composition taken from Bachmann et al.[33]. The molar density of exsolved H_2O is calculated using the equations of state derived by Pitzer and Sterner[37].

This framework allows us to calculate the change in bubble fraction ϕ_b^* produced by the exsolution of a given wt.% of dissolved H_2O, and the resultant change in ϕ_p. For example, for an initially bubble-free magma, exsolution of 1 wt.% H_2O (changing from 5 to 4 wt.% dissolved in the melt) produces a bubble fraction of $\phi_b^* = 0.035$, which gives a crystal fraction of $\phi_p = 0.531$. Figure 4a shows how ϕ_b^*, and ϕ_p vary with exsolution.

The viscosity of the mobilized magma can be estimated using the constitutive law for three-phase rheology proposed by Truby et al.[30]:

$$\eta_* = \mu \left(1 - \phi_b\right)^{-1} \left(1 - \frac{\phi_p}{\phi_m}\right)^{-2}, \tag{1}$$

where η_* is the apparent viscosity of the suspension at a reference strain-rate of $\dot{\gamma} = 1\,\mathrm{s}^{-1}$. This model assumes that bubbles are small compared with the crystals, and are in the low capillary number regime — i.e. strain-rate is small — which is appropriate for the scenario that we outline. Note also that Truby et al.[30] demonstrate validity of equation 1 only up to $\phi_p/\phi_m \approx 0.85$; for more concentrated suspensions the equation tends to under-predict viscosity.

The viscosity of the melt phase μ is a strong function of dissolved water content. Using the model of Hess and Dingwell[38] we calculate the initial viscosity of the melt μ_0 (at 5 wt.% H_2O and 760°C) to be 1.5 x 10^5 Pa s. The variation in melt viscosity with exsolution is shown in figure 4b.

Combining equation 1 with the calculated melt viscosity, we can calculate the three-phase magma viscosity as a function of exsolved volatile content; we plot the relative viscosity of the three-phase magma, which we define as $\eta_{*,r} = \eta_*/\mu_0$, in figure 4b. The figure shows that magma remains jammed until 1.3 wt.% H_2O has been exsolved; further exsolution causes the viscosity to fall sharply as the growing bubbles push the crystals apart, reducing the effective crystal fraction ϕ_p. Continued exsolution reduces the viscosity further until around 2.5 wt.% H_2O has been exsolved; at this point, the increasing melt viscosity becomes the controlling factor, and the magma viscosity begins to rise again.

5 Mobilization or pluton formation?

Our analysis shows that the jammed FCT magma mush could have been mobilized by the exsolution of as little as 1.3 wt.% H_2O, depending on how close ϕ_{crit} is to ϕ_m. Exsolution depends on the development of a supersaturation in the melt, which could result from an increase in temperature or a decrease in pressure — both of which decrease water solubility in silicate melt — or by the growth of predominantly anhydrous crystal phases, which concentrates water in the residual melt. Whilst a magma mush may or may not experience a temperature increase or a pressure decrease during its lifetime, all cooling mushes experience crystallization. Nonetheless, the existence of plutons testifies that not all magma mushes are erupted, so what factors influence whether a mush is mobilized, or a pluton is formed?

Pluton formation will result if the fraction of exsolved bubbles never reaches a value that is sufficient to push ϕ_p below ϕ_{crit}. This situation would be favoured by multiple factors: low initial water content in the melt such that the quantity of exsolved gas is small; high-pressure in the magma reservoir such that the bubble fraction produced by exsolution of a given quantity of gas is small; crystallization of hydrous crystal phases; and highly anisometric crystals (i.e. $r_p \ll 1$ or $r_p \gg 1$) such that ϕ_m, and hence also ϕ_{crit}, are low. Another factor that could mitigate against mobilization is the intergrowth of crystals prior to vesiculation, which could cause the formation of a framework with sufficient strength to prevent relative motion of the crystals as bubbles grow[39].

6 Conclusions

In order for any highly crystalline mush to become mobile, its crystal fraction must first be reduced below a critical value, ϕ_{crit}. Using experiments with analogue materials, we have shown that the growth of bubbles is sufficient to mobilize an initially jammed suspension. In the context of a natural case study — the eruption of the Fish Canyon Tuff — we have shown that the exsolution of 1.3 wt.% H_2O is sufficient to make the magma eruptible.

Our model is consistent with existing models of eruption triggers and provides a unifying, underlying mechanism for magma mobilization. Previous mod-

els have suggested underplating by recharge magma, decompression related to changing tectonic stresses, and seismic shaking, as potential triggers for mobilization. Each of these mechanisms has the potential to induce vesiculation, either through heating (underplating), decompression (tectonic stress), or rarefaction (seismic shaking). Furthermore, vesiculation may occur in the absence of external triggers, through second boiling. Our model postulates that it is the vesiculation event that mobilizes the magma, regardless of the trigger: the growth of bubbles pushes the crystals apart, decreasing the effective crystal fraction below a critical value. The bubbles also provide the buoyancy to drive the eruption of the unlocked magma.

All magmas at depth contain dissolved volatiles and, at some point in their lifetime, the growth of bubbles — whether externally or internally triggered — may cause or assist mobilization. The model presented here provides the framework to determine whether, for a given magma composition and volatile content, a known pressure-temperature-time pathway would lead to bubble exsolution, growth, and subsequent magma mobilization, or to viscous death and pluton formation.

References

[1] MG Best, EH Christiansen, and RH Blank. Oligocene caldera complex and calc-alkaline tuffs and lavas of the Indian Peak volcanic field, Nevada and Utah. *Geol. Soc. Am. Bull.*, 101:1076–1090, 1989.

[2] O Bachmann and G Bergantz. Rejuvenation of the Fish Canyon magma body: A window into the evolution of large-volume silicic magma systems. *Geology*, 31:789–792, 2003.

[3] LL Maughan, EH Christiansen, MG Best, AL Deino, DG Tingey, and CS Gromme. The Oligocene Lund Tuff, Great Basin, USA: a very large volume monotonous intermediate. *J. Volc. Geoth. Res.*, 113:129–157, 2002.

[4] CB Folkes, SL de Silva, HM Wright, and RAF. Cas. Geochemical homogeneity of a long-lived large silicic system; evidence from the Cerro Galan caldera, NW Argentina. *Bull. Volc.*, 73:1455–1486, 2011.

[5] S Hansen, C Thurber, M Mandernach, F Haslinger, and C Doran. Seismic velocity and attentuation structure of the East Rift Zone and South Flank of Kilauea volcano, Hawai'i. *Bull. Seism. Soc. Am.*, 94:1430–1440, 2003.

[6] WC Hammond and ED Humphreys. Upper mantle seismic wave velocity: Effects of realistic partial melt geometries. *J. Geophys. Res.*, 105:10975–10986, 2000.

[7] KV Cashman and G Giordano. Calderas and magma reservoirs. *J. Volc. Geoth. Res.*, 288:28–45, 2014.

[8] J-F Wotzlaw, U Schaltegger, DA Frick, MA Dungan, A Gerdes, and D Gunther. Tracking the evolution of large-volume silicic magma reservoirs from assembly to supereruption. *Geology*, 41:867–870, 2013.

[9] KM Cooper and AJR Kent. Rapid remobilization of magmatic crystals kept in cold storage. *Nature*, 506:480–483, 2014.

[10] DS Coleman, W Gray, and AF Glazner. Rethinking the emplacement and evolution of zoned plutons: Geochronologic evidence for incremental assembly of the Tuolumne Intrusive Suite, California. *Geology*, 32:433–436, 2004.

[11] RE Frazer, DS Coleman, and RD Mills. Zircon U-Pb geochronology of the Mount Givens Granodiorite: Implications for the genesis of large volumes of eruptible magma. *J. Geophys. Res.*, 119:2907–2924, 2014.

[12] A Einstein. Eine neue Bestimmung der Molekuldimensionen. *Ann. Phys.*, 19:289–306, 1906.

[13] SH Maron and PE Pierce. Application of Ree-Eyring generalized flow theory to suspensions of spherical particles. *J. Colloid Sci.*, 11:80–95, 1956.

[14] R Champallier, M Bystricky, and L Arbaret. Experimental investigation of magma rheology at 300 MPa: From pure hydrous melt to 76vol.% of crystals. *Earth Planet. Sci. Lett.*, 267:571–583, 2008.

[15] SP Mueller, EW Llewellin, and HM Mader. The rheology of suspensions of solid particles. *Proc. R. Soc. A*, 466:1201–1228, 2010.

[16] L Caricchi, L Burlini, P Ulmer, T Gerya, M Vassalli, and P Papale. Non-Newtonian rheology of crystal-bearing magmas and implications for magma ascent dynamics. *Earth Plant. Sci. Lett.*, 264:402–419, 2007.

[17] M Pistone, L Caricchi, P Ulmer, L Burlini, P Ardia, E Reusser, F Marone, and L Arbaret. Deformation experiments of bubble- and crystal- bearing magmas: Rheological and microstructural analysis. *J. Geophys. Res.*, 117: B05208, 2013.

[18] BD Marsh. On the crystallinity, probability of occurrence, and rheology of lava and magma. *Contrib. Min. Petrol.*, 78:85–98, 1981.

[19] PW Lipman. Incremental assembly and prolonged consolidation of Cordilleran magma chambers: Evidence from the Southern Rocky Mountain volcanic field. *Geosph.*, 3:42–70, 2005.

[20] J Gottsmann, Y Lavallee, J Marti, and G Aguirre-Diaz. Magma-tectonic interaction and the eruption of silicic batholiths. *Earth Planet. Sci. Lett.*, 284:426–434, 2009.

[21] ASR Allan, DJ Morgan, CJN Wilson, and M-A Millet. From mush to eruption in centuries: assembly of the super-sized Oruanui magma body. *Contrib. Mineral. Petrol.*, 166:143–164, 2013.

[22] F Begue, CD Deering, DM Gravley, BM Kennedy, I Chambefort, GAR Gualda, and O Bachmann. Extraction, storage and eruption of multiple isolated magma batches in the paired Mamaku and Ohakuri eruption, Taupo Volcanic Zone, New Zealand. *J. Petrol.*, 55:1653–1684, 2014.

[23] AT Linde and IS Sacks. Triggering of volcanic eruptions. *Nature*, 395: 888–890, 1998.

[24] AJR Kent, C Darr, AM Koleszar, MJ Salisbury, and KM Cooper. Preferential eruption of andesitic magmas through recharge filtering. *Nature. Geosci.*, 3:631–636, 2010.

[25] M-A Longpre, A Klugel, A Diehl, and J Stix. Mixing in mantle magma reservoirs prior to and during the 2011-2012 eruption at El Hierro, Canary Islands. *Geology*, 42:315–318, 2014.

[26] A Burgisser and GW Bergantz. A rapid mechanism to remobilize and homogenize highly crystalline magma bodies. *Nature*, 471:212–215, 2011.

[27] O Bachmann and G Bergantz. Gas percolation in upper-crustal silicic mushes as a mechanism for upward heat advection and rejuvenation of near-solidus magma bodies. *J. Volc. Geoth. Res.*, 149:85–102, 2006.

[28] C Huber, O Bachmann, and M Manga. Two competing effects of volatiles on heat transfer in crystal-rich magmas: Thermal insulation vs defrosting. *J. Petrol.*, 51:847–867, 2010.

[29] M Pistone, L Caricchi, P Ulmer, E Reusser, and P Ardia. Rheology of volatile-bearing crystal-mushes: Mobilization vs. viscous death. *Chem. Geol.*, 345:16–39, 2013.

[30] JM Truby, SP Mueller, EW Llewellin, and HM Mader. The rheology of three-phase suspensions at low bubble capillary number. *Proc. R. Soc. A*, 2015.

[31] HA Barnes and JO Carnali. The vane-in-cup as a novel rheometer geometry or shear thinning and thixotropic materials. *J. Rheol.*, 34:841–866, 1990.

[32] HM Mader, EW Llewellin, and SP Mueller. The rheology of two-phase magmas: A review and analysis. *J. Volc. Geoth. Res.*, 257:1–51, 2013.

[33] O Bachmann, MA Dungan, and PW Lipman. The Fish Canyon magma body, San Juan volcanic field, Colorado: Rejuvenation and eruption of an upper-crustal batholith. *J. Petrol.*, 43:1469–1503, 2002.

[34] MC Johnson and MJ Rutherford. Experimentally determined conditions in the Fish Canyon Tuff, Colorado, magma chamber. *J. Petrol.*, 30:711–737, 1989.

[35] T Pering. Matlab codes for volcanology - magma density. *https://vhub.org/resources/2790*, 2013.

[36] Y Bottinga and DF Weill. Densities of liquid silicate systems calculated from partial molar volumes of oxide components. *Am. J. Sci.*, 269:169–182, 1970.

[37] KS Pitzer and SM Sterner. Equations of state valid continuously from zero to extreme pressures for H2O and CO2. *J. Chem. Phys.*, 101:3111–3116, 1994.

[38] K-U Hess and DB Dingwell. Viscosities of hydrous leucogranite melts: A non-Arrhenian model. *Am. Min.*, 81:1297–1300, 1996.

[39] A Costa, S Blake, and S Self. Segregation processes in vesiculating crystallizing magmas. *J. Volcanol. Geotherm. Res.*, 153:287–300, 2006.

Acknowledgements

J.M.T. acknowledges support from NERC Studentship NE/K500999/1.

Author information

Affiliations

Department of Earth Sciences, Durham University, Durham DH1 3LE, UK
J. M. Truby, E. W. Llewellin
Istituto Nazionale di Geofisica e Vulcanologia, Via di Vigna Murata, 605, 00143 Roma, Italia
J. Taddeucci

Contributions

All authors contributed to designing the experiments, which J.M.T. carried out in Rome with the support of J.T. J.M.T. and E.W.L. wrote the manuscript and J.T. participated in the drafting process.

Competing financial interests

The authors declare no competing financial interests.

Corresponding author

Correspondence to J. M. Truby.

Materials and methods

The sample was prepared by adding a known mass of particles (in this case ballotini — spherical glass beads — with diameters $75-150\,\mu$m) to a known mass of Newtonian silicone oil (with viscosity 59.84 Pa s at experimental temperature). The mixture was then aerated with an electric hand-whisk. The initial bubble-free particle fraction was calculated, using the ballotini and oil densities, to be $\phi_p^* = 0.6000 \pm 0.0006$. Similarly, the bubble fraction was calculated, from volume measurements pre- and post-aeration, to be $\phi_b^* = 0.10 \pm 0.03$.

The apparent viscosity η of the sample was measured using an Anton Paar MCR301 rheometer with pressure cell CC25/Pr150/ In/A1/SS. The sensor system was a purpose-made vane-spindle (six blades, 11.5 mm radius, 16 mm length) in a cylindrical cup (12.5 mm radius). Since the sensor system is of our own design, the conversion factors from torque to stress, and rotation rate to strain rate, cannot be calculated analytically (although approximations can be derived following Barnes and Carnali [31]). Instead, the ratio of torque to rotation rate was calibrated for viscosity by performing flow curves of incrementally increasing then decreasing torque on two silicone oils with strictly Newtonian viscosities $\mu = 60.3$ Pa s and $\mu = 816.7$ Pa s, respectively. The pressure-dependence of the viscosity of the silicone oil was found to be very small: viscosity increased by around 4% as pressure increased by a factor of four. Throughout the experiment, temperature — measured by a thermocouple built into the sensor system — was maintained at 20.000 ± 0.003°C and no shear heating was observed.

In parallel with the rheometer was a transparent imaging cell, with internal geometry designed to parallel the rheometer sensor system, containing more of the same sample. This allowed us to image the sample and qualitatively observe volume changes as pressure changed. Some coalescence was observed, but no bubbles were seen to nucleate during the course of the experiment. The material in the imaging cell was not subjected to rheometric shearing during the experiments. The bubble fraction under pressure P was calculated, assuming the isothermal ideal gas law, as: $\phi_b = P_0\phi_{b0}^*/(P(1-\phi_{b0}^*) + P_0\phi_{b0}^*)$, where ϕ_{b0}^* is the bubble fraction at reference pressure P_0. Experimental uncertainty in ϕ_b^* is $\pm 30\%$, but note that this is a systematic uncertainty — we expect random errors to be small.

Once the sample was placed in the rheometer and imaging cell, the system was pressurized to 4 bars, using argon, and controlled with a pressure regulator. A constant shear stress was then imposed on the sample by setting the torque on the vane spindle to a value of 5 mN m throughout, and the rotation rate of the vane spindle was recorded by the rheometer every second. Every hundred seconds, the pressure was reduced manually by roughly 0.2 bars as rapidly as possible (typically over less than 10 seconds). This step duration was chosen to

412 be short enough that particles did not sink more than one particle radius during
413 each step. This was repeated until ambient pressure was reached.

List of Figures

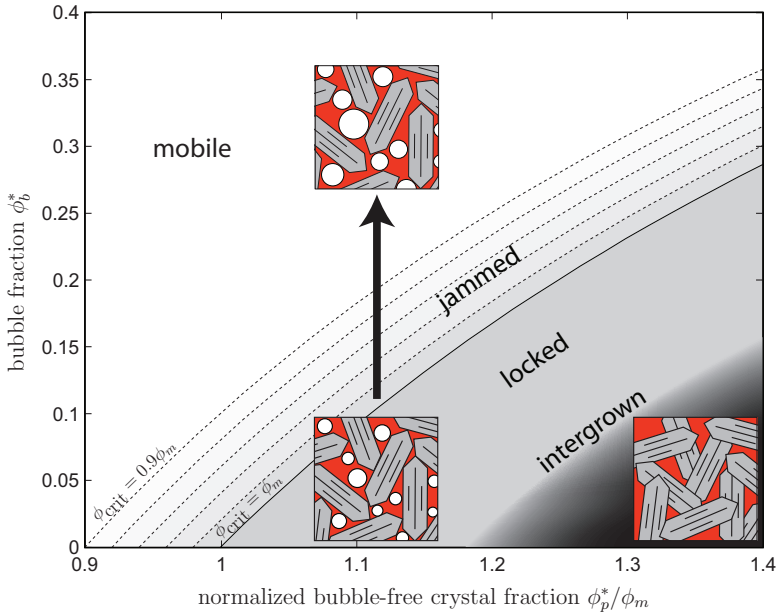

Figure 1: Mobility regimes, dependent on bubble fraction and initial crystal fraction. For $\phi_p < \phi_{\text{crit}}$ the magma is mobile; this is the case when $\phi_b^* > 1 - \phi_{\text{crit}}/\phi_p^*$. For $\phi_p \geq \phi_m$ the magma is locked; for $\phi_{\text{crit}} \geq \phi_p \geq \phi_m$ the magma is jammed. Bubble growth moves a magma in the direction of the arrow, and can mobilize a locked or jammed magma. If the crystals are strongly intergrown, then bubble nucleation or growth may be hindered and mobilization suppressed.

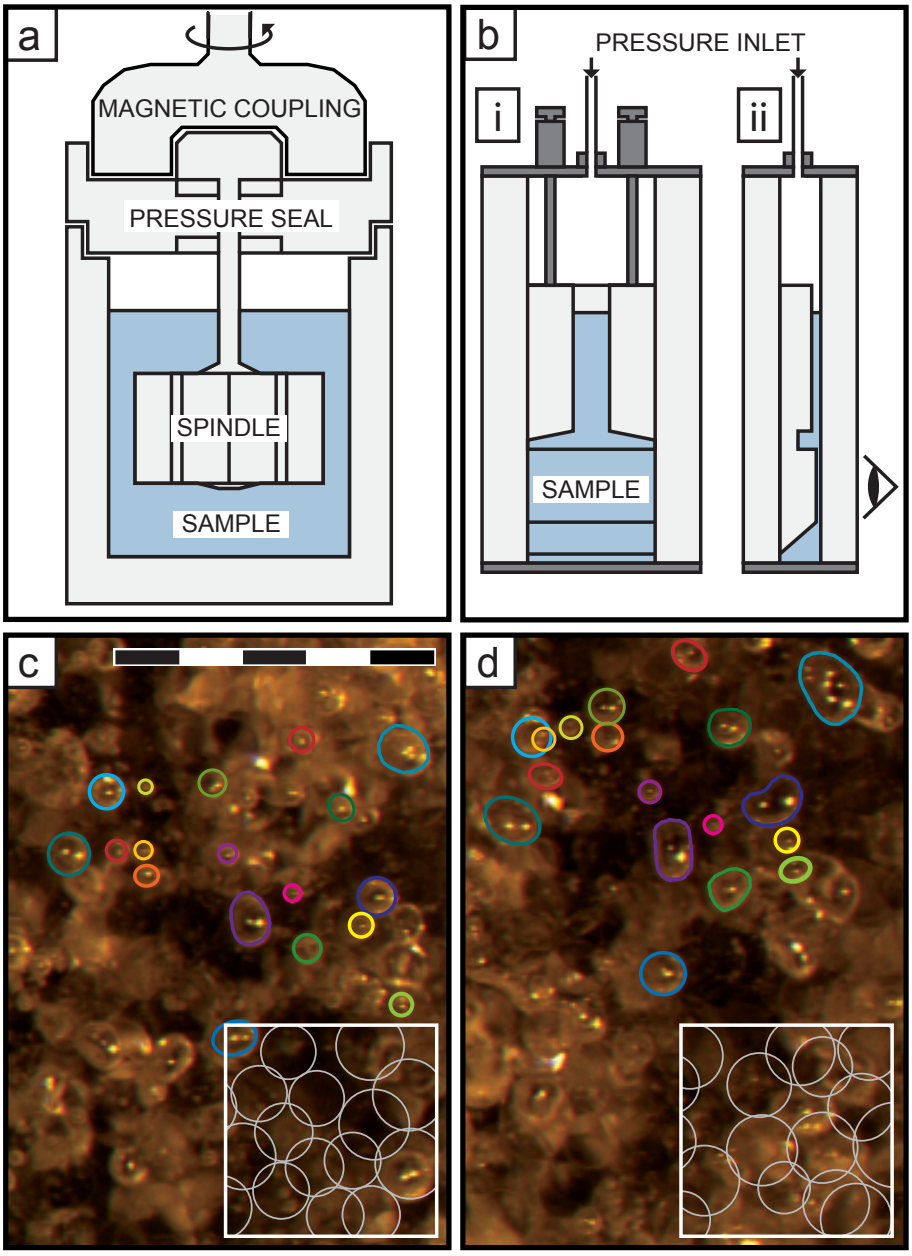

Figure 2: a) Sketch of rheometer internal geometry, showing cylindrical cup and vane spindle, inside pressurized cell. b) The 'imaging cell' used to photograph samples held under the same pressure conditions as those in the opaque rheometer. c) The analogue sample at 2 bars, and d) at 1 bar, in the imaging cell. The bubbles are clearly visible, and a number have been tracked between images: same bubble, same colour. The particles are very difficult to make out, tending to appear as faint arcs; those in a selected region in each figure are circled in grey. The scale bar is 500 μm.

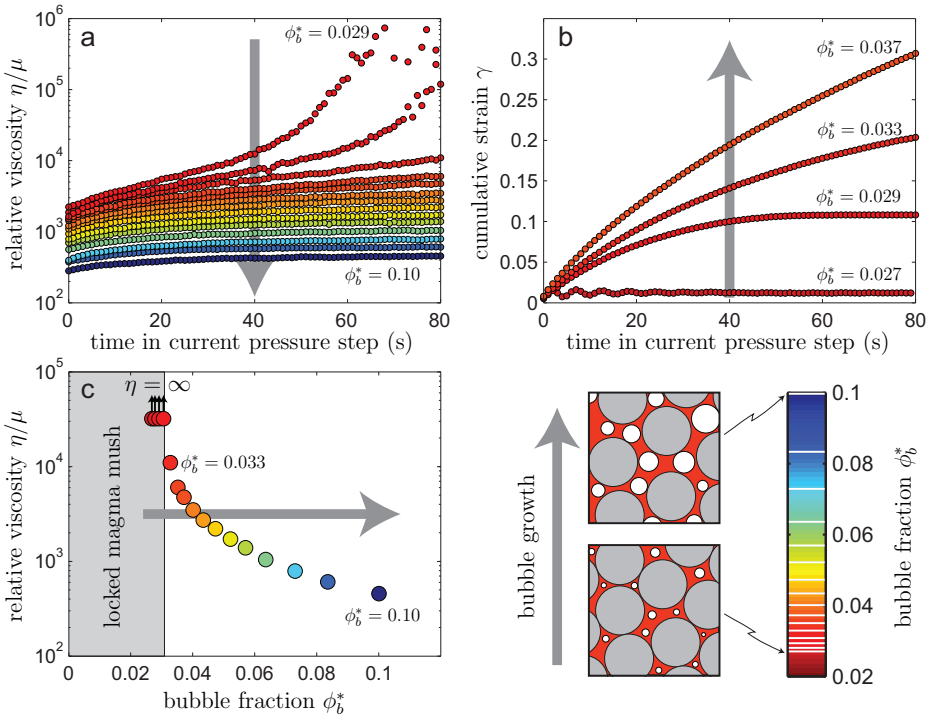

Figure 3: a) The relative apparent viscosity of the sample at a given pressure and bubble fraction, plotted against time in the relevant isobaric run. b) The cumulative strain in an isobaric run, plotted against time, for four selected pressures. c) The asymptotic (long time) relative viscosity for each bubble fraction (pressure). Bubble fractions at which the suspension is immobile are indicated by the grey area. In all parts, the grey arrow indicates the effect of increasing bubble fraction through bubble growth.

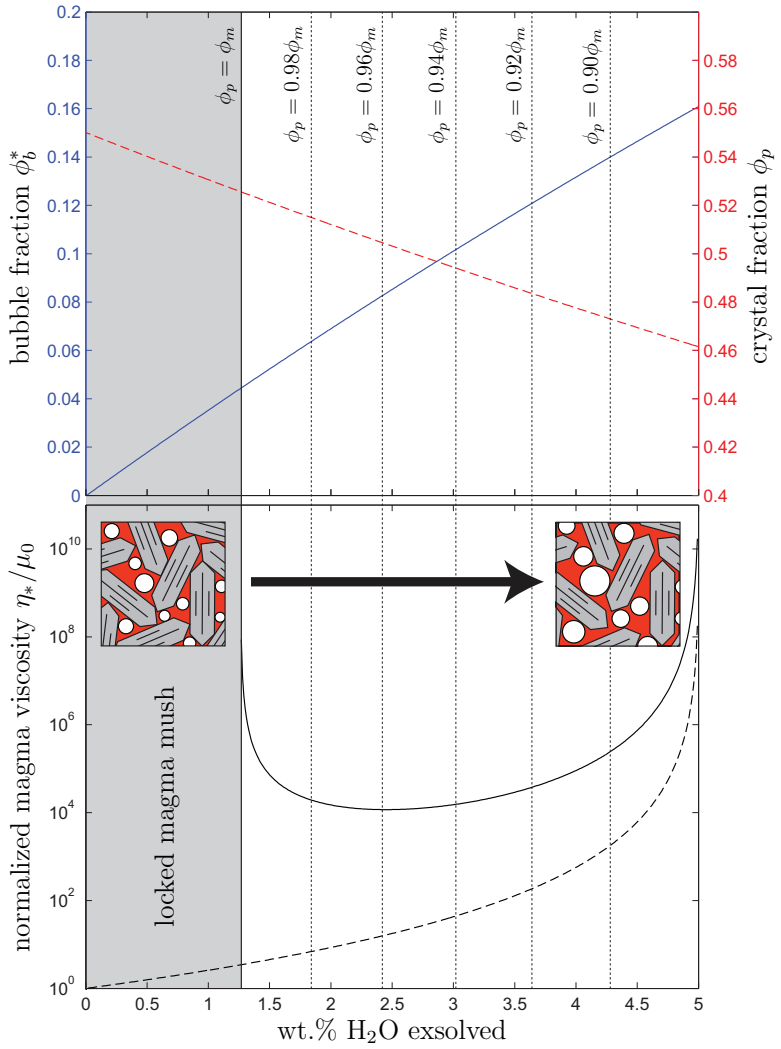

Figure 4: a) Bubble fraction (ϕ_b^*, blue solid) and normalised crystal fraction (ϕ_p/ϕ_m, red dashed) against exsolved H_2O wt%. b) Melt (dashed line) and magma (solid line) viscosity against exsolved H_2O content, normalized to the initial melt viscosity. Vertical solid line shows the exsolved H_2O wt% at which $\phi_p = \phi_m$; vertical dashed lines show the values at which $\phi_p = 0.9, 0.92, 0.96, 0.98\phi_m$.

Emplacement and morphology of rootless `a`ā mounds in a crystal-rich basaltic lava flow field

J. M. Truby[1], E. W. Llewellin*[1], M. A. Dungan[2], R.J. Brown[1]

[1]Department of Earth Sciences, Durham University, Durham DH1 3LE, UK

[2]Department of Geological Sciences, University of Oregon, Eugene, OR 97403, USA

*Corresponding Author: ed.llewellin@durham.ac.uk

Abstract

Basaltic lavas with phenocryst contents >45 vol.% are rare. Lava viscosity increases dramatically with increasing crystallinity, so crystal-rich magma should flow quite differently from its more common crystal-poor counterpart. We describe lava morphologies found in the crystal-rich (49–53 vol.%) 1780 flow field on Volcán Llaima, Chile. Within the 1780 flow field, we find: well-developed `a`ā, with broad, leveed channels; well-developed pāhoehoe; slabby pāhoehoe with transitions to and from `a`ā; and a cluster of features that we have termed "rootless `a`ā mounds", which we interpret to be higher viscosity analogues of rootless shields found on Kīlauea, Hawai'i, and comparable to megatumuli and terraces found on Mount Etna. While the lava flow features on Volcán Llaima are broadly comparable with more typical lava morphologies found, for example, on Hawai'i, there are significant differences, which we attribute to its higher viscosity. These features indicate that the erupted lava was very close to the pāhoehoe–`a`ā transition.

Keywords: lava morphology; lava rheology; pāhoehoe–`a`ā transition; crystal-rich lava; lava flow field; rootless shields

1 Introduction

Basaltic lava flows are conventionally divided into two categories according to their surface morphology. Pāhoehoe is characterized by smooth, often ropey surfaces, whereas `a`ā has a broken, clinkery surface (MacDonald, 1953). The lava flows produced by single eruptions – particularly long-lived events – may switch repeatedly between the two morphologies in both time and space, producing a flow-field with complex and heterogeneous morphology (e.g. Jurado-Chichay and Rowland, 1995; Hon *et al.*, 2003). Understanding the development of a flow-field is important because it influences the nature of lava transport from vent to flow front. Pāhoehoe flows typically develop insulated internal lava tubes that may deliver lava over long distances to a flow front that is usually broad and advances slowly; consequently such flows may persist for months or years (e.g. MacDonald, 1953; Swanson, 1973; Peterson *et al.*, 1994; Cashman *et al.*, 1999). By contrast, `a`ā flows tend to be fast-moving, spatially-focussed, and channelized, moving with a considerably higher volumetric flow rate (e.g. MacDonald, 1953; Pinkerton and Sparks, 1976; Rowland and Walker, 1990; Cashman *et al.*, 1999).

The morphology of the surface produced by a flow is controlled by the rheology of the lava and by the strain-rate that it experiences at the time the surface is formed (MacDonald, 1953; Peterson and Tilling, 1980). At low viscosities and low strain-rates, lava surface crust remains coherent, favouring the development of pāhoehoe. At higher viscosities and higher strain-rates, the surface crust breaks under shear, forming clinkery `a`ā morphology. The surface morphology of a flow is, therefore, not

uniquely linked to the physical properties of the magma that formed it, and it is possible for the still-fluid lava in the interior of a flow to go on to produce either surface type, regardless of its up-stream morphology (Jurado-Chichay and Rowland, 1995; Guest and Stofan, 2005). Pāhoehoe flows commonly transition to `a`ā if either strain rate or viscosity increases (MacDonald, 1953; Peterson and Tilling, 1980; Polacci and Papale, 1999; Sehlke *et al.*, 2014). Strain rate is controlled by volumetric flow rate and the angle of the surface on which the lava flows. For a constant volumetric flow rate and viscosity, the transition from pāhoehoe to `a`ā is often associated with a break to steeper slope angles. The reverse transition sometimes occurs when an `a`ā lava flow reaches a shallower slope (Hon *et al.*, 2003).

An increase in lava viscosity resulting from cooling or crystallization may promote the transition from pāhoehoe to `a`ā (Cashman *et al.*, 1999). More generally, the rheology of a lava dictates its propensity to form pāhoehoe or `a`ā for a given slope angle and flow rate (Peterson and Tilling, 1980). The viscosity of a silicate melt (i.e. the liquid component of a lava) depends on its composition, temperature, and dissolved volatile content (Giordano and Dingwell, 2003; Giordano *et al.*, 2008); in addition, most lavas contain both bubbles and crystals, which may dramatically affect the rheology depending on their volume fractions (Mader *et al.*, 2013). Crystal fractions of lavas are highly variable, although few have more than 45% crystals, and most lie in the ranges <10% and 25-45% (Ewart, 1976). The bubble fraction of lavas is even more variable, ranging from 0 – 80% (e.g. Cashman and Mangan, 2014). The fraction of each of these components may vary with both time and distance from the vent, in a single lava flow.

The presence of crystals always increases the viscosity of lava, whilst the presence of bubbles may increase or decrease viscosity depending on conditions of shear (Mader *et al.*, 2013; Llewellin and Manga, 2005). As crystal content approaches the maximum packing fraction (~55% for equant crystals, Mader *et al.*, 2013) the viscosity of the lava increases dramatically and it develops a yield strength. This favours the formation of `a`ā, and it has been observed that, for crystallinity ≥35%, lava flows occur almost exclusively as `a`ā (Hoover *et al.*, 2001; Cashman *et al.*, 1999). However, in some cases extremely crystal-rich lava is capable of producing pāhoehoe flows; examples include the "cicirara" lavas at Mount Etna (Lanzafame *et al.*, 2013).

In this study, we focus on crystal-rich lava from one voluminous historic eruption of Volcán Llaima (38.7°S), Andean Southern Volcanic Zone. This eruption occurred in 1780 CE on the south flank of the edifice and includes lavas with up to 64% crystals (Bouvet de Maisonneuve *et al.*, 2012) that produced both `a`ā and pāhoehoe morphologies. Comparably crystal-rich historic lavas on nearby Volcán Villarrica are dominantly pāhoehoe flows. The 1780S eruption (denoted 'S' to distinguish it from a contemporaneously emplaced flow on the northern flank) produced a compound flow field (Walker, 1971), comparable to those typically produced by Mount Etna, Italy, and sharing a number of features in common. Bouvet de Maisonneuve *et al.* (2012, 2013) attribute the high crystallinity of many mafic Volcán Llaima lavas to remobilization of crystal mush immediately before and during eruptions. Multiple lines of evidence suggest that accumulation of mush bodies in the Volcán Llaima conduit/reservoir system is related to persistent magma recharge (Bouvet de Maisonneuve *et al.*, 2012, 2013).

2 Volcán Llaima

Volcán Llaima (Figure 1) is located in Chile's Southern Volcanic Zone, and is one of the largest and most active volcanoes in Chile. Over 50 eruptions have occurred since 1640 CE (Bouvet de Maisonneuve *et al.*, 2012), although the historical record prior to ~1850 is most reliable for exceptionally large eruptions (Dzierma and Wehrmann, 2010). Historic activity at Volcán Llaima, including the 2008–09 eruption, has been dominated by basaltic to basaltic-andesitic Strombolian eruptions both near the summit and on the flanks. Volcán Llaima lies within a transtensional half-graben near the northern extent of the Liquiñe-Ofqui fault zone (Naranjo and Moreno, 2005). The

structurally controlled, main vent system parallels a large normal fault that bounds the east side of this depression. The 1640, 1751, and 1780S eruptions appear to have issued from N- or NNE-trending fissures that radiated down the south flank from the southern summit area vent (Pichi Llaima). The proximal portions of these lavas are obscured by snow, glaciers, and multiple types of fragmental deposits. The 1751 and 1780S vents appear to be coincident, as the bifurcated distributions of flows from both are down the SSW and ESE flanks, and below we discuss evidence that suggests that the initial phase of the 1780S eruption consists of residual 1751 magma. The 1751 lava was extensively eroded, apparently by lahars related to the 1780 eruption. The only known written record of the 1780S eruption comes from Jesuit missionaries, who noted that the eruption lasted 10 years (H. Moreno, pers. comm., 2014).

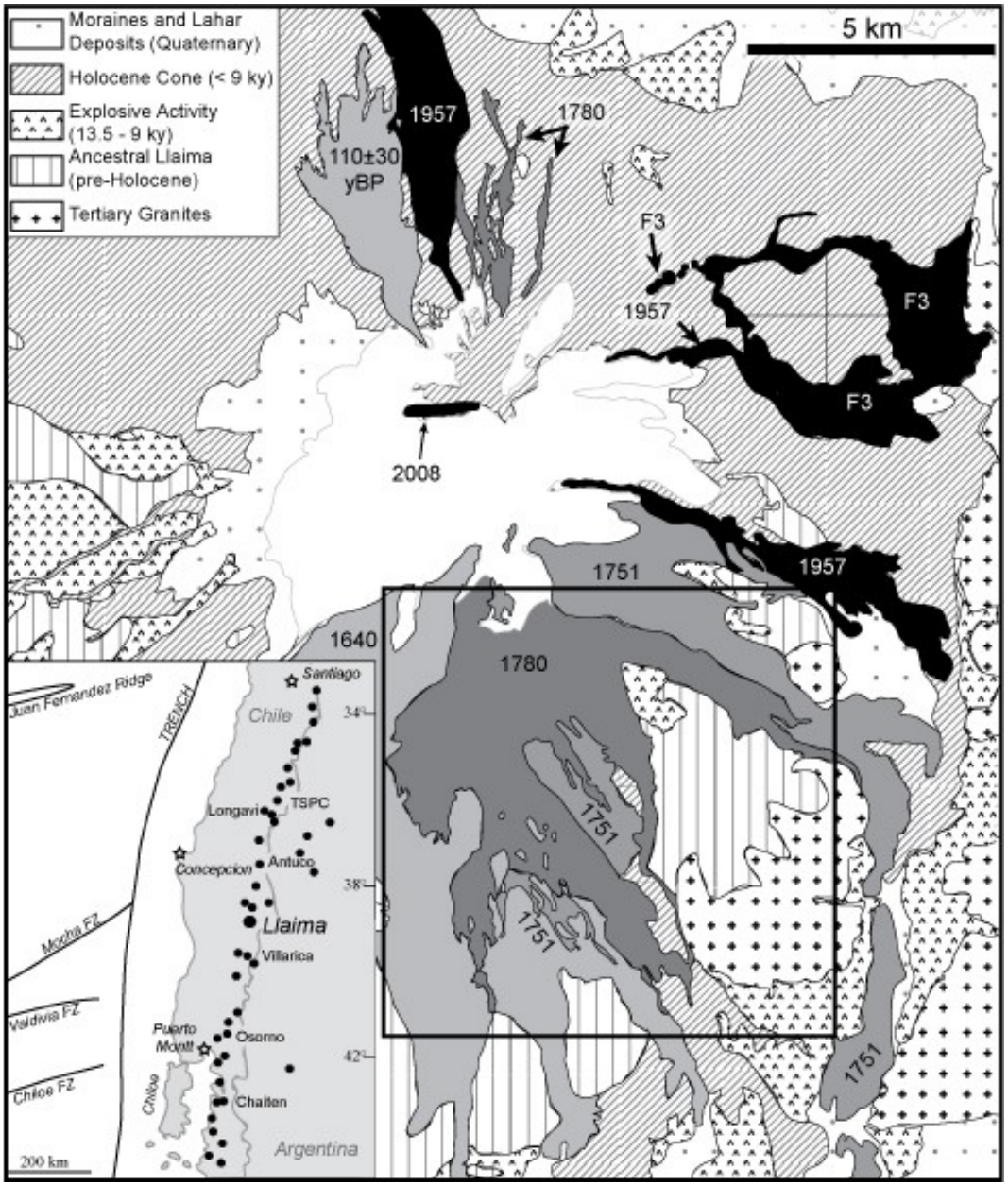

Figure 1. Geological map of Volcán Llaima, after Bouvet de Maisonneuve *et al.* (2012). The inset shows the location of Volcán Llaima within Chile's Southern Volcanic Zone, and the black box shows our field area, shown in more detail in Figure 2.

3 Features of the compound lava flow field

A range of volcanic landforms occur across the 1780S flow field (Figure 2). These were investigated in detail during fieldwork by three of the authors (JMT, EWL, MAD) in January 2014, building on earlier reconnaissance fieldwork by MAD.

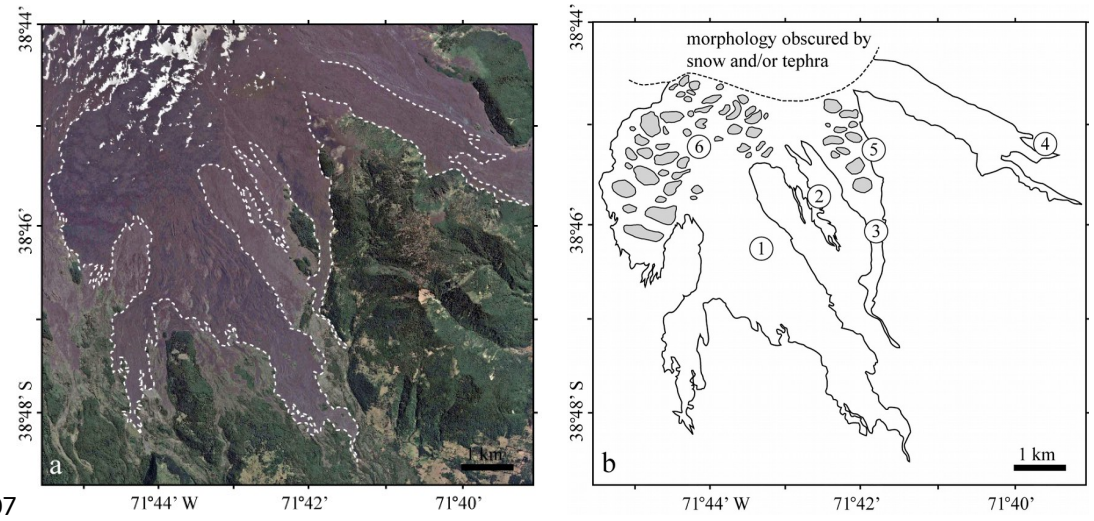

Figure 2. a) Aerial image of the 1780 lava flow field, with the outline marked by dashed white lines. b) Outline of the 1780 lava flow field, showing key features and locations discussed in this study. Grey outlines indicate the summits of `a`ā mounds. 1: Channelized `a`ā. 2: Slabby `a`ā and pāhoehoe. 3: Pāhoehoe. 4: Transitions between `a`ā and pāhoehoe. 5: `A`ā mounds observed in detail. 6: `A`ā mounds observed from a distance and interpreted from aerial imagery.

3.1 `A`ā channels

The region around location 1 (Figure 2) contains many overlapping `a`ā channels. The slope of the volcano flank in this area is ~8–10° (rarely up to 15–20°), and the most proximal exposed `a`ā flows are around 5km from the vent. Levees can exceed 5–10m high and the channels are 10–30m wide; some reach 80m wide. The wider flows tend to be longer, and may run for up to 3km, however the overlapping nature of the channels makes them difficult to trace. It is common to find stacked channels, and overspills from the levees locally feed subsidiary `a`ā flows up to 300m long.

In some channels, the lava has drained out of the channel and the internal structure of the levees is exposed. Although the outer carapace of the levees is formed from clinker breccia, the interior margins have a more complex structure. This consists of sub-vertical walls composed of alternating sheets of massive and brecciated lava, running parallel to the channel. The massive lava is almost avesicular; the few vesicles present show a weak foliation parallel to the channel. The material also appears fresh and is dark grey to black. The brecciated material is much less well consolidated, and is formed of oxidised fragments of clinker, ash, and agglutinated clinker (i.e. lava balls).

3.2 Pāhoehoe

Lava flows with exclusively pāhoehoe surface morphology are volumetrically minor in the 1780S flow field, but flow lobes of dominantly `a`ā morphology that include patches of pāhoehoe morphology are widespread, particularly in proximal locations (Figure 2). There appear to be two temporal and spatial categories of pāhoehoe. The first is present along the margins of the narrow lobe denoted by locations 3 and 5 in Figure 2, where relatively inflated proximal pāhoehoe lies directly on bedrock of the pre-Holocene Volcán Llaima edifice (Figure 2; north of location 5), and is not closely associated with subsequent `a`ā. Flow morphology along the axis of this lobe becomes increasingly mixed to the south in the sense that both `a`ā and pāhoehoe are closely associated over a range of spatial scales,

and much of the pāhoehoe occurs as broken and rotated blocks and sheets that are mingled with later `a`ā. These broken sheets are accompanied by subsequent, combined `a`ā–pāhoehoe breakouts related to features that we interpret as manifestations of rootless mounds, which are described in detail later, in section 3.4. However, the flow margin that lies directly on pre-Holocene rocks remains pāhoehoe as far south as location 3, where thin lobes of relatively dense pāhoehoe have been emplaced along the flow edge after 'climbing' short distances upslope. Contiguous with the proximal eastern margin of this lobe is the large flow that descended to the ESE. This lobe terminates in the area of transitional lava described later in section 3.3 (Figure 2; location 4).

In a number of other locations, which are dominated by `a`ā, some features of pāhoehoe morphology are still seen. For example, in location 2 in Figure 2, where the volcano flank slope is 6–8°, the `a`ā is slabby, and in some places includes scratched pāhoehoe surfaces up to 2m^2 in area. In many places, the slabs do not appear to have been rafted far by the `a`ā. These features are most common where the `a`ā flows are thinner, and have not developed channels. Occasionally, regions of the larger `a`ā channels are predominantly slabby.

3.3 Transitional lava

At the distal end of the eastern limb of the 1780S flow field (location 4 on Figure 2), the palaeotopography is consistently shallow, with a slope of 4–6°. In this region, the lava morphology switches downslope between `a`ā and pāhoehoe several times, over a distance of around 400m (Figure 3). We examined the breakout of pāhoehoe and the progressive transition to `a`ā in detail at one location, and observed the same sequence repeated at least three times as the flow progressed downslope.

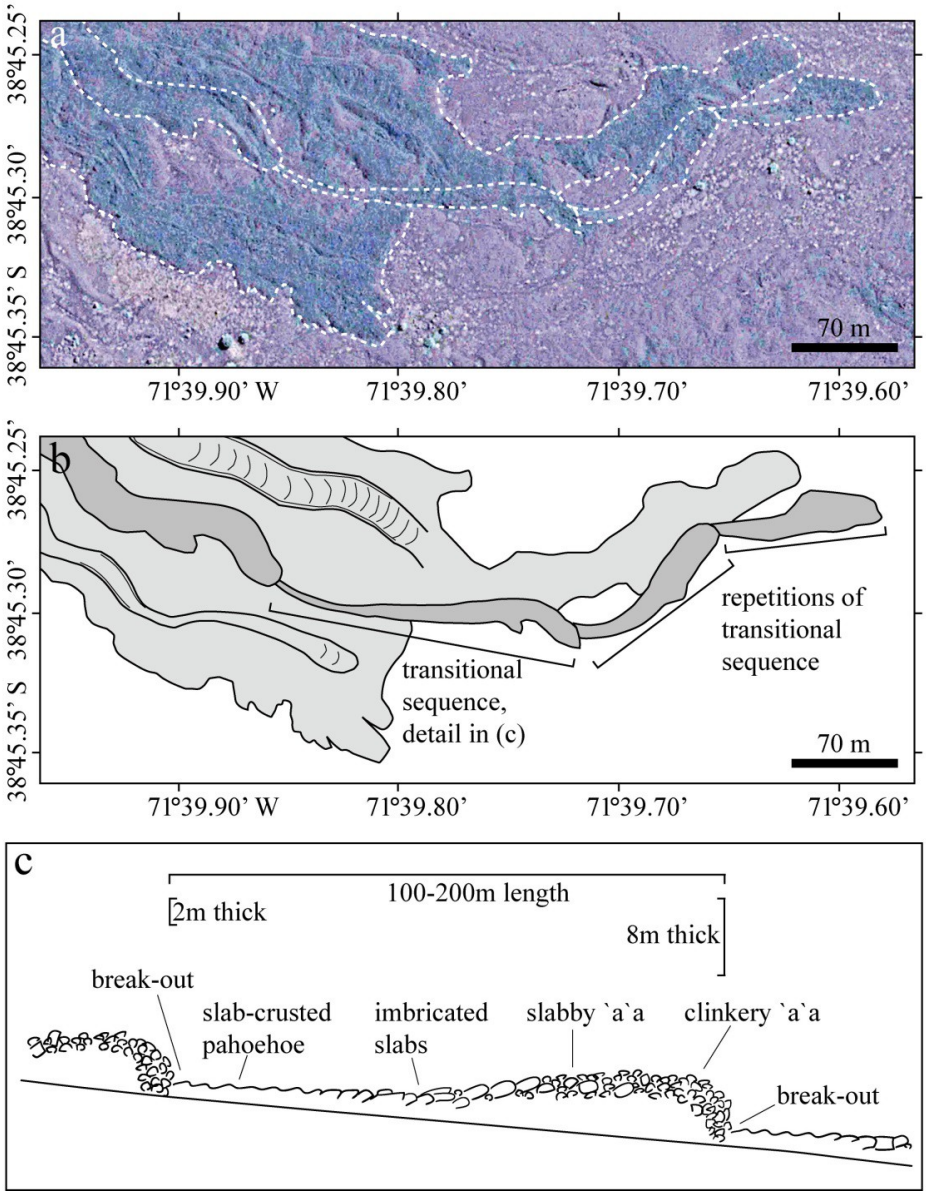

Figure 3. a) Aerial image of the region in which repeated slab-crusted pāhoehoe flows occur (location 4 on Figure 2), with the outline of the 1780 flow marked by dashed white lines. b) Map of the 1780 lava, based on the image in (a). Pale grey indicates 1780 `a`ā lava flows; dark grey indicates the transitional lavas, which appear to overlie all other 1780 flows in this region. c) Overview cross-section sketch, highlighting the key features in the transition from slab-crusted pāhoehoe break-out to clinkery `a`ā. This sequence repeats at least three times along the same flow.

The initial transition from `a`ā to pāhoehoe occurs at the front of an 8m high `a`ā lobe. A slab-crusted pāhoehoe flow (Guest and Stofan, 2005) emerges from near the base of the `a`ā lobe. This flow widens from 1m to 2m over the first 15m, and proceeds as a well-confined channel flow, with solid rubbly levees, for around 50m. The lava surface shows scratch marks within 1m of the breakout. The height of the preserved flat surface is approximately level with the top of the levees.

As the channel continues downslope, the surface begins to break into imbricated slabs. For a further 10m, the channel shape is still apparent, but becomes increasingly disrupted until it transitions into a thicker, wider, slabby `a`ā flow, and then a clinkery `a`ā flow for a further 50m, with thickness increasing from 2m to 8m over the length of the flow. From the front of this next `a`ā lobe, a second,

much thinner, flat-topped break-out occurs. The sequence of flow and breakup followed by break-out is repeated.

3.4 `A`ā mounds

We use the field term "`a`ā mounds" to refer to features that are found in two regions of the 1780S flow field marked 5 and 6 on Figure 1. We examined location 5 in detail and location 6 at reconnaissance level. Figure 4 highlights the key features of the mounds.

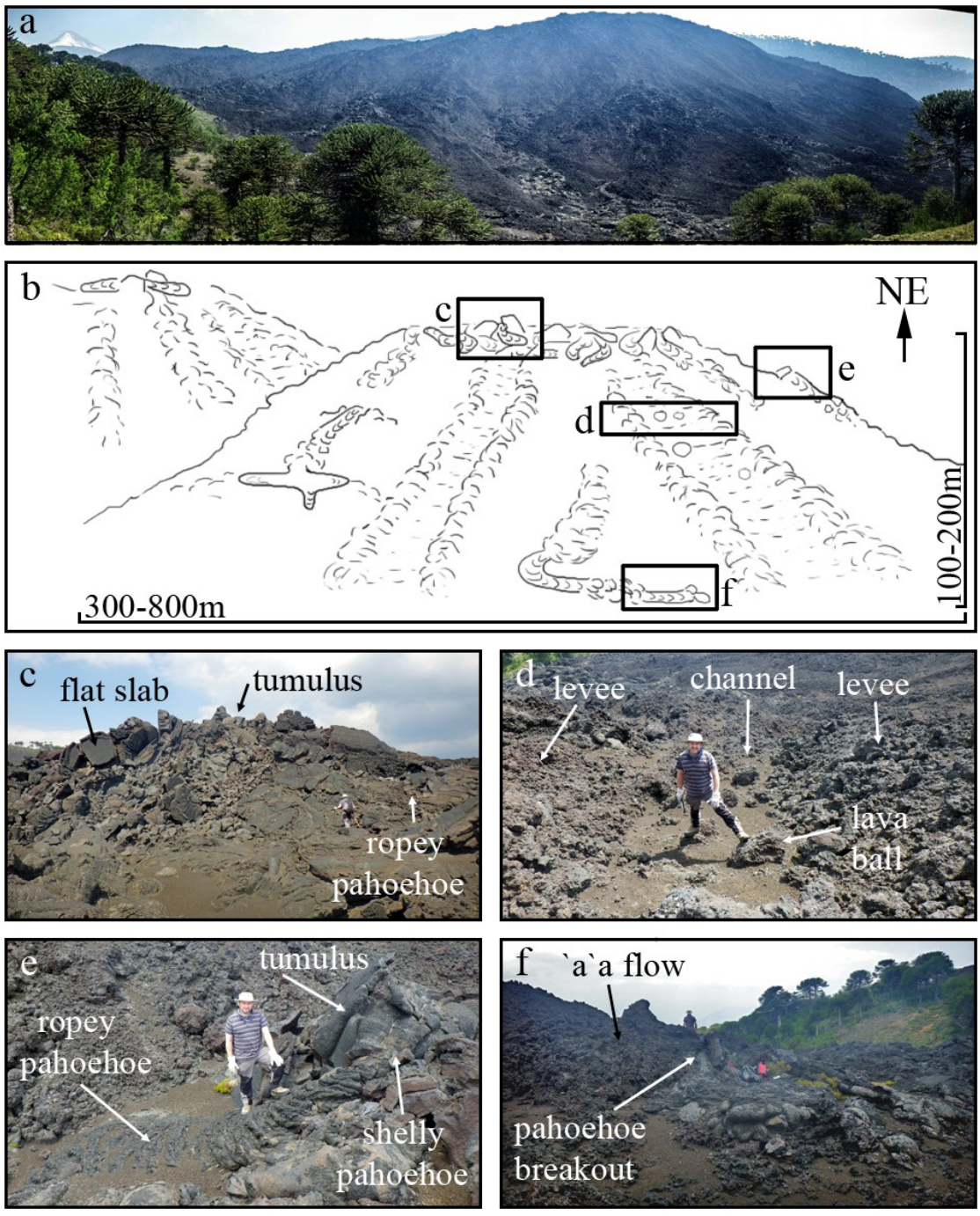

Figure 4. a) Panorama photo of a mound that we examined in detail. Further mounds can be seen in the distance, at the left of the image. b) Overview sketch highlighting the key features of a typical mound, based loosely on the image in (a).

c) Summit tumulus, with part of a rotated flat slab visible at the left. d) Looking downslope, down the centre of a leveed `a`ā flow. e) Pāhoehoe breakout from a flank tumulus. f) Pāhoehoe breakout from an `a`ā flow at the base.

3.4.1 Summit

The summit of each `a`ā mound is defined by a broadly flat region (average slope <5°), which forms a local topographic high, typically 100–200m above the base of the mound. The summits are roughly circular and range from 100m to 400m in diameter. In aerial imagery (Figure 2a), the summit regions are clearly visible, and appear more reflective than the surrounding flanks.

Each summit is covered with numerous randomly-oriented elongate tumuli (e.g. Figure 4c), up to 10 metres high, 10–30 metres long, and 5–20 metres wide. The tumuli are closely spaced such that little of the summit is left undisrupted. The tumuli are often associated with small squeeze-ups of ropey pāhoehoe, which rarely extend more than 5m from their sources. Some tumuli show multiple generations of squeeze-ups.

The predominant lava morphology on the summit is short (<15m) and narrow (<1m) pāhoehoe flows with well-developed surface ropes. These flows follow local downslope directions, which are highly variable due to the close spacing of the tumuli. There are regions of flat, smooth lava, up to 10m wide, often with deep ropes near the margins, which appear to be contiguous with the pāhoehoe flows. Flat slabs that are uplifted and rotated by tumuli reveal cross sections through vesicular upper crust up to 4m thick. Within the slabs are layers, 10–20cm thick, of variably shaped vesicles: small, spherical vesicles contrast with larger irregularly shaped vesicles, which are often elongated parallel to the flat surface of the slab. The interiors of the slabs show poorly-developed columnar jointing.

3.4.2 Flanks

Away from the flat summit region, the typical slope angle on the `a`ā mounds increases smoothly, but rapidly, towards the flanks, which have a maximum slope angle of 30–35°. Two intermediate, annular zones are identified. The first is immediately adjacent to the summit region, is up to 100m in width for most mounds, and has slope angles that are 5–10°. It is characterized by pāhoehoe flows that predominantly flowed towards the flanks, and by an absence of flat slabs. The second is immediately adjacent to the flanks, is 100–200m in width for most mounds, and has a slope angle of 10–30°. It is characterized by intermingled pāhoehoe and slabby, transitional `a`ā flows, that also flowed towards the flanks. Within this latter zone, the proportion of pāhoehoe lava decreases, while the proportion of `a`ā increases, towards the flanks.

The steepest portions of the rootless mound flanks are composed almost exclusively of `a`ā, the majority of which appears to be sourced from the summit region. As the `a`ā becomes well developed away from the summit, it forms channels up to 8m wide, with rubbly levees (Figure 4d). The lava surface in the channels is typically 1–2m lower than the levees and contains numerous lava balls, 0.2–1m in diameter.

Scattered across the flanks are tumuli (Figure 4e) up to 10m across, which have uplifted the `a`ā flows. In some instances the tumuli now represent local topographic highs, in others the tumuli form humps on the flanks – in both cases the tumuli locally deflect the flank upwards by around 5–10m, measured perpendicular to the main flank slope. Many tumuli have breakout flows that extend more than 30m downslope. The breakout flows are typically shelly pāhoehoe adjacent to the breakout point, but transition into ropey pāhoehoe within 10m; they then break up and transition into `a`ā at distances of 20–30m from their tumulus source.

3.4.3 Base

Near the bases of the mounds the slope of their flanks decreases to <5°. The proportion of pāhoehoe increases as the slope angle decreases until `a`ā and pāhoehoe are present in roughly equal proportions. `A`ā and pāhoehoe flows overlap considerably in this region, and it is generally difficult to trace any flow for more than 20m.

Where the source of the pāhoehoe flows can be traced, they are sourced from breakouts in `a`ā flows on the flanks that reach the base of the mound (Figure 4f). In some cases, these pāhoehoe flows then break up, and transition into slabby `a`ā and then `a`ā. Most do not extend more than 120m, and many form lobate flows with multiple toes. The sources of other pāhoehoe flows are not clear, as they are overridden by both `a`ā and pāhoehoe.

In some places, the pāhoehoe lavas form flat regions up to 10m wide, apparently as a result of ponding within pre-existing depressions. In some cases, this ponded pāhoehoe then overflows and feeds another flow.

4 Petrological insights

Samples of `a`ā, pāhoehoe and transitional lavas from the 1780S flow field were collected at locations 2–5. The lava contains phenocrysts of plagioclase feldspar and olivine in a variably crystalline matrix (Figure 5). Three-dimensional x-ray computed tomography (XRCT) scans of three of the samples were collected using an XRadia/Zeiss Versa XRM 410, and then reconstructed. The data were processed in Avizo Fire, using a non-local means filter to smooth the data, and watershed thresholding to separate the components. A filtered section through a 3D scan is shown in Figure 5c. Here, the vesicles appear black; plagioclase crystals are dark grey; olivines are palest grey; and the melt or groundmass is a mid-grey. The scans show clusters of rounded olivines, 500 microns to 1 mm diameter, surrounded by a network of large inter-grown sieve-textured plagioclase phenocrysts; these clusters were not encountered in thin section. The phenocrysts together comprise 49–53% of the solid volume, determined by XRCT. This is somewhat lower than the value presented in Bouvet de Maisonneuve et al (2012), who quote a crystallinity of 64% for their 1780 lava sample.

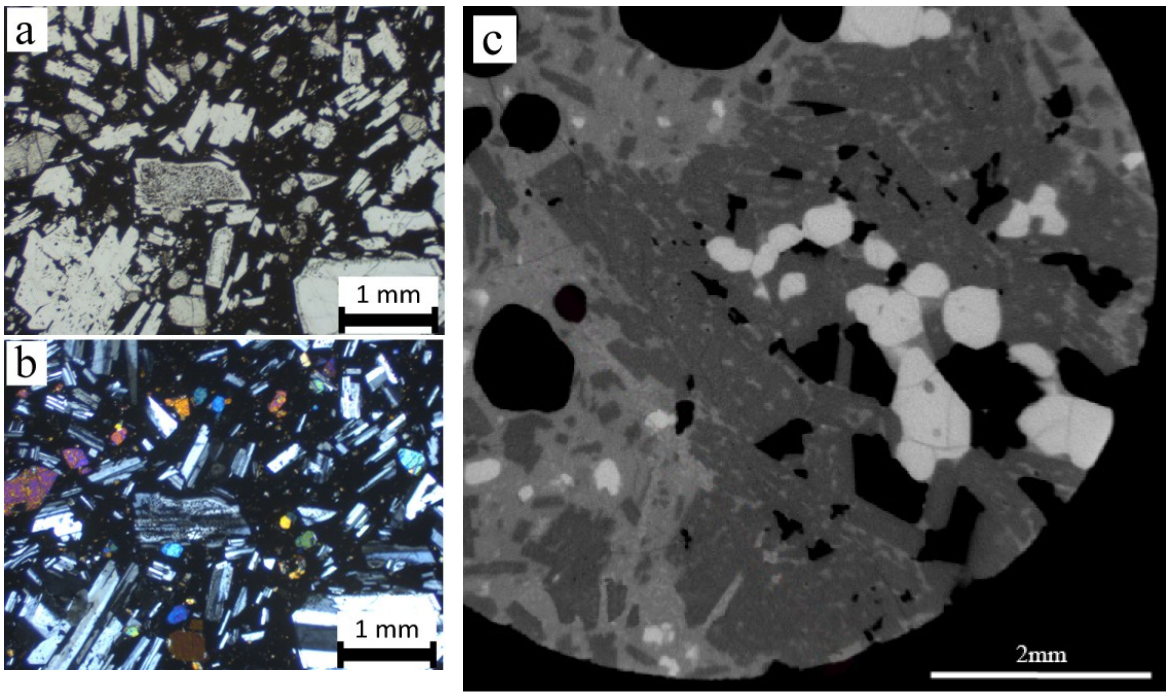

Figure 5. Textures and crystal assemblages in 1780S lava samples. Photomicrograph in (a) plane-polarized light, and (b) cross-polarized light. c) XRCT scan, showing cluster of rounded olivine phenocrysts (off-white crystals) surrounded by inter-grown and inclusion-rich plagioclase phenocrysts (darker grey crystals).

Plagioclase phenocrysts make up 42–46% of the solid volume (determined by XRCT), and are up to 4mm in length. The smaller plagioclase crystals (up to 1mm in length) are lath-shaped and un-zoned (see Figure 5). Larger plagioclase phenocrysts, however, commonly show zoning, which may be complex, and are more likely to have a less simple shape (larger crystals in Figure 5, and Figure 6).

Some of these larger crystals appear to be inter-grown. Bands of inclusions associated with the zoning are common in these larger crystals (Figure 6a), and in some the cores have a sieve texture, which contrasts with inclusion-free rims (Figure 6c).

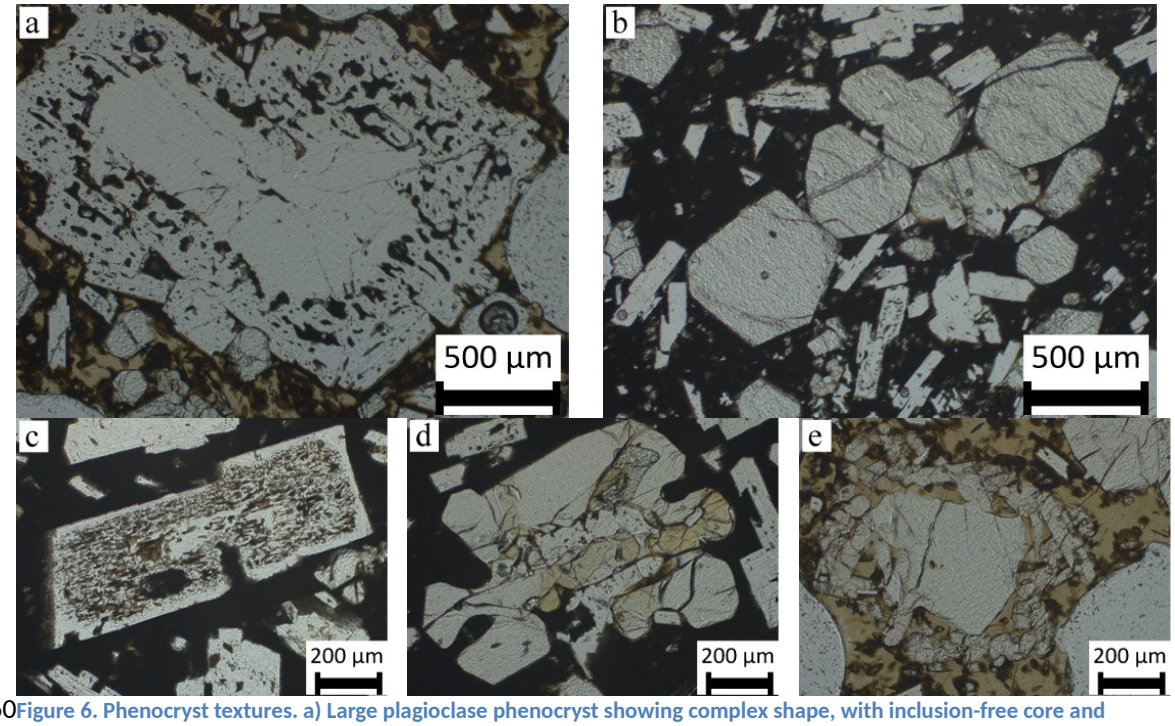

Figure 6. Phenocryst textures. a) Large plagioclase phenocryst showing complex shape, with inclusion-free core and inclusion-rich rim. b) Cluster of euhedral and rounded olivine phenocrysts. c) Large plagioclase phenocryst with inclusion-rich core and narrow inclusion-free rim. d) Olivine phenocryst with resorbed margin. e) Olivine phenocryst surrounded by a reaction rim.

Olivine phenocrysts make up 6–7% of the solid volume, determined by XRCT. These are rarely euhedral, commonly occurring as rounded crystals less than 200 microns in diameter, and in clusters of 200–700 micron crystals (Figure 6b). Some rare isolated crystals, around 1mm across, show signs of resorption (Figure 6d) or reaction rims (Figure 6e).

The microlite fraction in these rocks is variable. Some samples have a glassy matrix, and in others the matrix is wholly microcrystalline. However, it is difficult to tell how representative this is of the true microlite content during lava flow, as very little glass is preserved on the 1780S flow as a whole, due to weathering and erosion.

The bubble fraction is considerably more variable than the crystallinity, ranging from 12% to 23% in the samples we analysed. Bubble sizes range from less than 50 microns to 2 mm. The bubble populations within a single sample may also be quite complex – some bubbles are rounded, while others have crenulated margins, which may be representative of tearing of the melt in response to stress as the lava cooled, or of dissolution by a corrosive vapour phase.

4.1 Evidence for interaction of 1751 and 1780 magma

Many historic Volcán Llaima magmas contain crystal populations of olivine and plagioclase (with minor augite), in which the crystals are complexly zoned, different crystals from the same thin section have different core compositions and contrasting zoning profiles, and the populations in different thin sections from the same eruption are distinct from one another. These complexities, along with reversely zoned shoulders near the rims of some olivine crystals, contribute to the hypothesis that these magmas are carrying crystal cargoes derived from multiple, sub-volcanic crystal

284mush bodies that were mobilized and assembled by relatively vigorous mafic magma recharge events
285(Bouvet de Maisonneuve *et al.*, 2013). Detailed presentations of whole-rock, mineral chemistry, and
286U-series data for the historic Volcán Llaima system and further discussion of its operation are in
287progress, but olivine compositions determined by electron microprobe are used here to address the
288unusual bi-modal population in the 1780S lavas. Nine samples were analysed: three from the 1751
289eruption, and six from the 1780S flow field (three pāhoehoe, three `a`ā).

290The 1780S and 1751 eruptions contain plagioclase populations that are typical of all historic eruptive
291products, but the olivine populations in both are unusual with respect to other eruptions. Both suites
292of magmas contain volumetrically minor fragments of plutonic-textured olivine and plagioclase
293intergrowths in which the olivine core compositions are ~$Fo_{84.5-81}$ (plus normally zoned rims). These
294are not discussed further. The 1751 lavas are unique in that the olivine grains that texturally
295resemble phenocrysts are characterized by core compositions that are exceptionally Fo-poor ($Fo_{73.5-71.5}$), and which are uniquely limited to a narrow range (Figure 7a). Normally-zoned rims extend the
297compositional range down to Fo_{60}. The feature of olivine chemistry that is critical for this study is that
298three samples of early 1780S pāhoehoe contain olivines that are identical in terms of core
299compositions to those erupted 29 years previously in 1751 (Figure 7b). A significant fraction of the
300olivine crystals in one of the three pāhoehoe samples that were investigated has low-amplitude,
301reversely-zoned, near-rim shoulders that extend the 1751 core range from a maximum of $Fo_{74.5}$ to
302$Fo_{75.5}$ (Figure 7b). Three samples of 1780S `a`ā have olivines that are comparatively diverse, including
303a wide range of compositional zoning profiles, and these are distinctively more Fo-rich ($Fo_{79-74.5}$). A
304substantial fraction of the limited overlap between the 1780S pāhoehoe and `a`ā olivines is due to
305normally-zoned rims on the `a`ā population (Fo_{75-65}). These nine rocks from two eruptions are all very
306close in whole-rock composition (~5.7-5.9 wt.% MgO).

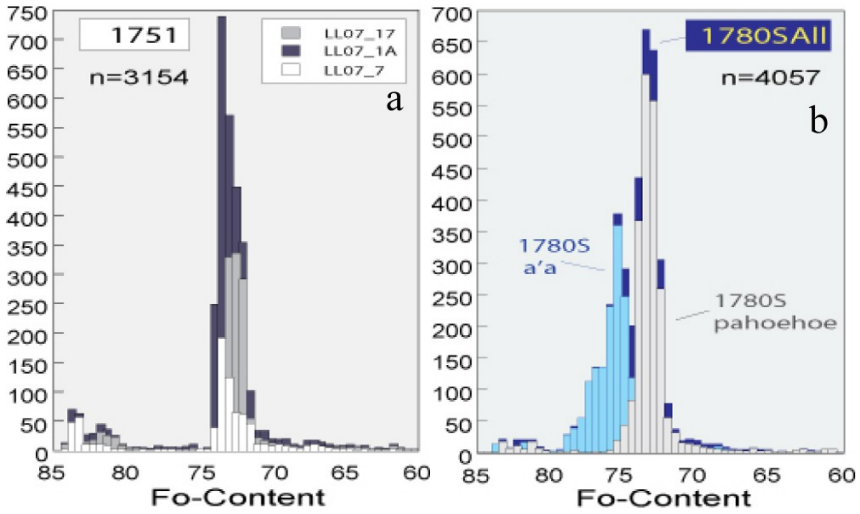

307

308**Figure 7. Olivine core compositions determined by microprobe for the a) 1751, and b) 1780S lavas. The 1751 olivines**
309**contain a narrow range of core compositions, which is mirrored by olivines found only in the early pāhoehoe flows of the**
310**1780 eruption. Later `a`ā lavas from the 1780 eruption contain a different population of olivine cores.**

311The simplest first-order interpretation of the origin of the bi-modal 1780S olivine populations is that:
312(1) the early pāhoehoe magmas are mobilized 1751 magma, and (2) the more Fo-rich olivines in the
313`a`ā lavas reflect a larger contribution from recharge magma. More complicated alternatives, which
314would not be easy to test, can be imagined. However, the remarkable similarity of the 1751 olivines
315to their counterparts in 1780S pāhoehoe is difficult to interpret as anything other than a close
316genetic connection between these two eruptions. The reversely zoned shoulders in 1780S pāhoehoe
317fit the inference of a recharge-related eruption in 1780, and the near lack of such shoulders in the
3181751 olivines is consistent with the fact that there was a large subduction-channel earthquake near

Concepción in 1751; i.e. the 1751 eruption trigger is more likely to have been seismic energy than magma recharge.

5 Discussion

Much of the most influential literature on lava flow morphology is based on the study of flows at Kīlauea (e.g. MacDonald, 1953; Rowland and Walker, 1990) and Mount Etna (Sparks *et al.*, 1976; Pinkerton and Sparks, 1976); we seek to place our observations within that context. One of the key controls on lava flow morphology is its rheology (e.g. Peterson and Tilling, 1980; Gauthier, 1973). We therefore begin the discussion by comparing the likely rheology of the lavas at Volcán Llaima with those at Kīlauea and Mount Etna.

5.1 Rheology of crystal-rich lava

The rheology of a lava depends on its suspended crystal and bubble content (e.g. Mader *et al.*, 2013; Pistone *et al.*, 2013), as well as the viscosity of the interstitial melt phase. By examining each parameter that influences viscosity, we can estimate the apparent viscosity of the crystal-rich lava at Llaima, and compare it to values of viscosity from the literature for Kīlauean and Etnean lava.

In a two-phase magma composed of bubbles suspended in a melt phase, the bubbles may act to increase or decrease the suspension viscosity relative to the melt viscosity μ, depending on capillary number, $Ca = \mu a \dot{\gamma} / \Gamma$, where a is the bubble radius, $\dot{\gamma}$ is the strain rate in the magma, and Γ is the melt–bubble interfacial tension (Llewellin and Manga, 2005). The relative viscosity $\eta_{r,b}$ of a bubbly magma (i.e. suspension viscosity normalized by the melt viscosity) is given by

$\eta_{r,b} = \left(1 - \phi_b\right)^{-1}$, for bubbles in the low capillarity regime (Ca << 1), or Eq. 1

$\eta_{r,b} = \left(1 - \phi_b\right)^{5/3}$, for bubbles in the high capillarity regime (Ca >> 1), Eq. 2

where ϕ_b is the bubble volume fraction, defined as $\phi_b = V_b / \left(V_b + V_l\right)$, where V_b and V_l are the volumes of the bubble phase and liquid phase respectively.

For a two-phase magma containing crystals suspended in a melt phase, the crystals always act to increase the suspension viscosity relative to the melt viscosity (Mader et al., 2013). Many formulations have been proposed for the relationship between relative viscosity $\eta_{r,p}$ and crystallinity, but Mueller et al. (2010, 2011) found a good fit to experimental data for that given by Maron and Pierce (1956):

$$\eta_{r,p} = \left(1 - \frac{\phi_p}{\phi_m}\right)^{-2}, \quad \text{Eq. 3}$$

where ϕ_p is the crystal volume fraction, defined as $\phi_p = V_p / \left(V_p + V_b + V_l\right)$, where V_p is the volume of the particle phase, and ϕ_m is the maximum packing fraction, which depends on the aspect ratio,

roughness, and size distribution of the suspended fraction. Note that the formulation for ϕ_b and ϕ_p adopted here implies that the equations are valid when the bubbles are small compared to the crystals, such that the bubbly magma can be viewed as an effective medium in which the crystals are suspended.

Based on a qualitative inspection of photomicrographs of our samples (Figures 5–6), we estimate that the aspect ratio of the majority of the phenocrysts in the 1780 lava is around 2. Using Eq. 49 of Mader *et al.* (2013), the maximum packing fraction of these crystals is approximately 0.53. The crystal content of the lava at Volcán Llaima (49–53 vol.%) is therefore at the maximum packing fraction, or very near it and subject to a large yield stress. Based purely on this crystal content, the lava would be expected to be jammed and unable to flow.

Truby et al. (2015) performed experiments on three-phase fluids (i.e. fluids containing both crystals and bubbles), and demonstrated that the addition of bubbles in the low capillarity regime to a high crystal-content fluid leads to a decrease in suspension viscosity. We use the theoretical framework of Truby *et al.* (2015) to postulate the expected relative viscosity of the crystal-rich, bubble-bearing lavas at Llaima:

$$\eta_r = \eta_{r,p}\,\eta_{r,b} \qquad \text{Eq. 4}$$

where $\eta_{r,p}$ is given by Eq. 3, and $\eta_{r,b}$ is given by Eqs. 1 or 2 for low or high capillarity respectively, and η_r is the three-phase maga viscosity normalized by the melt viscosity. Truby *et al.* (2015) validated this approach for low capillarity using analogue experiments, however the high capillarity version has not yet been experimentally validated. We note that, notwithstanding the implicit assumption that the bubbles should be small compared to the crystals, Truby *et al.* (2015) found that the equations remained valid even for samples in which the bubble size was comparable with the size of the crystals.

Using this model, we plot the dependence of viscosity on bubble content for the highest and lowest crystal fractions measured in our samples, and for both low and high capillarity (Figure). The definitions of crystal and bubble fraction used in Eqs. 1–3 differs from that typically used by volcanologists. It is common, instead, to express the bubble volume fraction as $\phi_b^* = V_b / \left(V_p + V_b + V_l\right)$, which is the value that would be measured using Archimedes principle, and the crystal volume fraction as $\phi_p^* = V_p / \left(V_p + V_l\right)$, which is the crystal fraction on a bubble-free basis. Values for measured bubble and crystal volume fraction that we quote in earlier sections of this article are expressed as ϕ_b^* and ϕ_p^*, and this is the convention that we adopt in Figure 8. One can convert between conventions using: $\phi_b = \phi_b^* / \left(1 - \phi_p^* \left(1 - \phi_b^*\right)\right)$; and $\phi_p = \phi_p^* \left(1 - \phi_b^*\right)$ (Truby *et al.*, 2015).

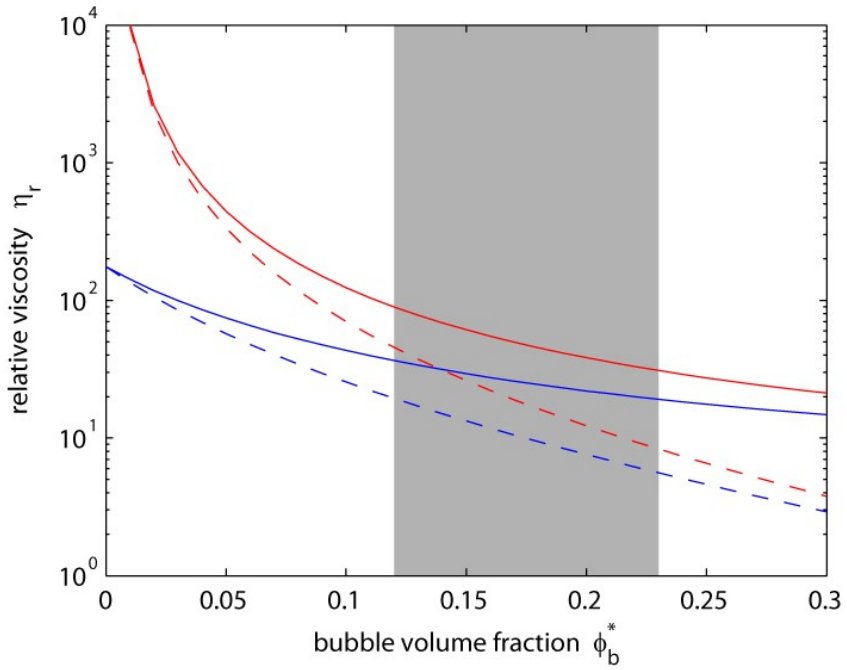

382

383**Figure 8. Calculated relative viscosity plotted against bubble fraction. Red curves are for the highest measured**
384**crystallinity, 53% ($\phi_p^* = 0.53$); blue curves are for the lowest measured crystallinity, 49% ($\phi_p^* = 0.49$). Solid lines are**
385**for the low capillarity regime; dashed lines are for the high capillarity regime. The shaded region indicates the range of**
386**bubble fractions measured in the 1780S lava ($0.12 \le \phi_b^* \le 0.23$).**

387Clearly, in both capillarity regimes, we would expect that the addition of bubbles will lead to a
388reduction in viscosity. The range of bubble fractions measured in the lava and a lack of knowledge of
389the strain rates experienced by the lava make it difficult to place a single value on the viscosity.
390Instead, we suggest that it would have been a factor of between 5 (for the lowest crystal content,
391highest bubble fraction, and high capillarity) and 90 (for the highest crystal content, lowest bubble
392content, and low capillarity) times higher than the viscosity of the melt alone. In any case, the
393expected viscosity is much lower for the three phase lava than it would have been for bubble-free
394lava.

395In order to calculate apparent viscosity, rather than relative viscosity, we need to know the viscosity
396of the suspending melt. This is controlled by a number of factors, including melt composition, water
397content, and temperature. Using the model of Giordano et al. (2008), and the highest and lowest
398silica content glass compositions given in table 1 of Bouvet de Maisonneuve et al. (2012), we
399estimate that the erupted melt at Llaima could have a viscosity in the range 100–4000 Pa s.

400Combining this pure melt viscosity with the relative viscosities calculated for the observed bubble
401and crystal fractions in the 1780S lava, we estimate that the lava had a viscosity in the range 500–
402400,000 Pa s. We can compare this range of absolute viscosity values to measured lava viscosities at
403Etna and Kīlauea in order to understand their variable propensities for producing pāhoehoe or `a`ā
404flows. Interpolation between measurements at higher and lower temperatures by Robert *et al.*
405(2014) provides a Newtonian viscosity value of ≈100 Pa s for Kīlauean basalt at 1150°C (which is
406commonly the temperature of near-vent lavas on Kīlauea; Helz et al., 2003); for cooler or more
407crystalline lavas, the yield stress becomes appreciable, and Bingham viscosity up to 3700 Pa s is
408found (Moore, 1987). For Mount Etna basalt, Pinkerton and Norton (1995) also found that the lava

was Newtonian above 1120°C, with viscosity around 150 Pa s. Cooler and more crystalline lavas were found to have rheology matching a power law fluid, with viscosities at unit strain rate up to 8625 Pa s (Gauthier, 1973; Pinkerton and Sparks, 1978; Pinkerton and Norton, 1995).

These ranges of viscosity are plotted in Figure 9, alongside the regions in which pāhoehoe and `a`ā flow morphology will form, adapted from Hon *et al.* (2003). Lavas from all three volcanoes span a wide range of possible viscosities, and depending on viscosity and strain rate, it is possible to produce both pāhoehoe and `a`ā at each. However, the `a`ā field is much larger for lavas from Volcán Llaima than those from Kīlauea and Mount Etna, indicating that, under similar conditions of emplacement, lavas from Volcán Llaima are more likely to form `a`ā.

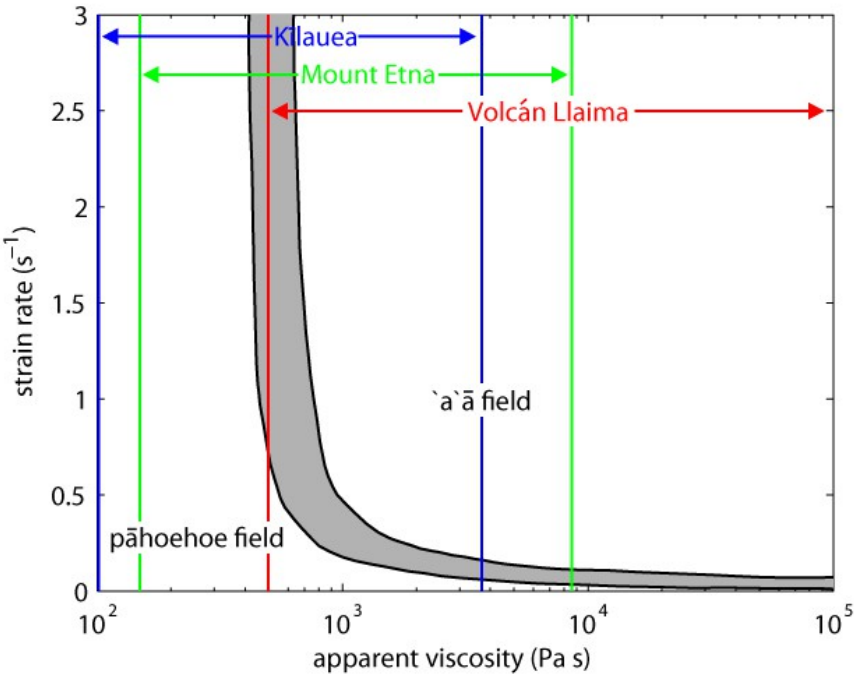

Figure 9. Diagram showing the relationship between strain rate, lava viscosity, and lava flow morphology, after Hon et al. (2003). The shaded region indicates the transition zone between pāhoehoe and `a`ā; the pāhoehoe field is found at low viscosities and strain rates; the `a`ā field is found at high viscosities and strain rates. The vertical lines indicate the observed lava viscosity ranges at Kīlauea (blue), Mount Etna (green), and Volcán Llaima (red).

5.2 Formation of `a`ā mounds

5.2.1 Formation of the summit features

The flat slabs observed at the summit of the `a`ā mounds indicate that lava ponded. Disruption of the surface by tumuli, and resurfacing by later squeeze-up pāhoehoe flows sourced from them, mean that it is not possible to determine whether there was a single pond that was continuous across the whole summit area, or several discrete ponds that formed within local depressions.

The numerous tumuli indicate that the summits of the mounds underwent a period, or periods, of inflation following ponding (Walker, 1991). The inflation was sufficient to rotate many large (5m wide, 4m thick) slabs to a near vertical orientation. Based on the crust thickness–time relationship of Hon *et al.* (1994), we calculate that there must have been at least 3–4 months of cooling during the formation of the summit tumuli. The squeeze-ups and short lava flows sourced from the tumuli support the interpretation that the tumuli were produced by pressurization of a core of molten lava beneath them (Anderson *et al.*, 2012). Our observations of the morphology of the summits of the

mounds allow us to build a clear interpretation only of the final stages of the processes that formed them – presumably evidence of earlier processes is buried beneath the preserved surface.

5.2.2 Formation of flank and base features

We consider two possible interpretations of the tumuli found on the flanks of the mounds. The first is that they are summit tumuli, preserved from a time when the mound was lower. In this scenario they would have formed at the summit margin, and escaped being overridden by later `a`ā as the mound grew. However, the flank tumuli distort the flanks much more than we see from any of the summit tumuli. On the summit, tumuli tend to create a vertically oriented bulge, whereas on the flanks, the bulge has a radial component as well. In addition, there are no other features preserved from when the mound was lower – the resurfacing by `a`ā has been complete everywhere else.

The second interpretation, which we prefer, is that the interior of the mound became pressurized, and the extent of pressurization was enough to force lava out through the flanks, overcoming the strength of that material, and producing the tumuli. This mechanism would also explain the pāhoehoe at the base that cannot be traced back to a parent `a`ā flow. These breakouts are interpreted as cognate with the "seeps" identified at the base of rootless shields at Kīlauea (Hawai'i) by Patrick and Orr (2012), and are distinct from breakouts formed from an active lava surface, such as those at the summit or from a lava flow.

5.2.3 Controls on the distribution of `a`ā and pāhoehoe

In all places where a flow's origin can be confidently identified, the most proximal part of the flow has pāhoehoe morphology. This includes breakouts from tumuli on the summit and the flank, breakouts from `a`ā flows, and breakouts from the ponded lava. Not one `a`ā flow can be traced back to a breakout, but many can be traced back to a pāhoehoe flow source. This suggests that the lava breaks out from the mounds exclusively or almost exclusively as pāhoehoe (as per Wolfe *et al.*, 1988; Jurado-Chichay and Rowland, 1995).

In the flat summit regions, the lavas are entirely pāhoehoe; on the steepest slopes they are predominantly `a`ā; around the flat base they are mostly pāhoehoe again. Rapid transitions from pāhoehoe to `a`ā on the flanks of the mound are associated with breaks in slope, at which lava from the summit or from a flank tumulus meets a steeper slope. Transitions from `a`ā to pāhoehoe occur where the lava reaches the base of the mound, encountering a much shallower slope. Thus, the morphology that develops appears to be correlated with – and controlled by – the angle of the slope on which it flows (Peterson and Tilling, 1980). Previous studies (e.g. Rowland and Walker, 1990; Pinkerton and Sparks, 1976) have found that both viscosity and volumetric flow rate together control lava morphology: we conclude that the lava building the mounds at Volcán Llaima has viscosity such that a small increase in volumetric flow rate, caused by an increase in slope, is enough to trigger the transition to `a`ā.

5.2.4 Construction of the `a`ā mounds

The majority of the visible lava on each `a`ā mound appears to have been sourced from its summit region, and flowed as `a`ā down the flanks. Each mound forms a local topographic high, and all the mounds are several kilometres from the main 1780S vent. In order to flow out of the summit of each mound, lava must have travelled downslope from the main vent, and then flowed up into and out of each mound – the summit regions effectively form secondary, superficial vents.

Features that have some of the same characteristics as the `a`ā mounds have been observed on long-lived flow fields on Kīlauea, Hawai'i, where they are called "rootless shields" (Kauahikaua *et al.*, 2003; Patrick and Orr, 2012). They normally form over a well-established lava tube, and are built by repeated overflows of lava from a pond, so that the shield becomes higher and larger over time (Kauahikaua *et al.*, 2003). The Kīlauea rootless shields also form local topographic high points, 20-30m higher than the surrounding lava surface, and up to 700m wide (Patrick and Orr, 2012). Throughout their lifetimes they commonly have an ephemeral lava pond in the summit region, but

484this often appears to have been disrupted towards the end of the eruption. Features characteristic of
485overpressure, such as tumuli and hornitos, are common at rootless shields (T. Orr, pers. comm.,
4862015). Observations made while the rootless shields were active show that the entire system – from
487the main vent, through all the mounds, to the distal end of the flow field – can be active
488simultaneously, for several months (Kauahikaua *et al.*, 2003).

489We choose to use the term “rootless mounds” to describe the features we observe at Volcán Llaima,
490by analogy to the rootless shields on Kīlauea. We base this identification on the following common
491features: (1) both types of edifice form a local topographic high, which is built by repeated overflows
492from a lava pond; and (2) they do not directly overlie the primary volcanic vent: the lava may flow for
493several kilometres before reaching the rootless mound.

494There are some notable morphological differences between rootless mounds and rootless shields.
495Rootless shields are low aspect-ratio shield edifices composed entirely of pāhoehoe lava. Rootless
496mounds at Volcán Llaima are steep sided and are mantled by `a`ā lavas. We propose that this is
497primarily due to the differences in the viscosity of the lavas that constructed the two edifice types
498(Figure 9).

499Similar features are found on Mount Etna. Guest *et al.*, (1984, 2012) describe flat topped “terraces”
500of lava up to 300m wide and 150m high that step down the flank of the volcano. They have flanks
501mantled with `a`ā and pāhoehoe, and summits covered by tumuli, squeeze-ups, and short pāhoehoe
502flows. This description matches closely those at Volcán Llaima and we tentatively suggest that our
503rootless mounds are cognate with these terraces. Another group of features called megatumuli, or
504tumulus complexes, are similar, but with a more domed shape, and are indicative of significant
505inflation Guest *et al.* (1984). Guest *et al.* (1984) interpret the megatumuli to have developed from
506terraces. The terraces and megatumuli on Mount Etna have one feature that is not observable at
507Volcán Llaima – a well-mapped feeder tube system. The lava tubes explored by Guest *et al.* (1984)
508clearly fed lava flowing from the terraces and megatumuli, and it is likely that a similar system of
509tubes existed at Volcán Llaima. The system at Volcán Llaima is either deep enough to have not
510collapsed, or perhaps never drained of lava.

511Combining our observations at Volcán Llaima, the observations of Guest *et al.* (1984) and Guest *et al.*
512(2012) at Mount Etna, and our understanding of the processes that build rootless shields on Kīlauea
513(Kauahikaua *et al.*, 2003; Patrick and Orr, 2012) allows us to postulate the sequence of formation of
514an individual rootless mound (Figure 10). Stage 1: lava that had erupted from a vent higher up on a
515volcano’s flanks stalls and ponds, possibly in a local depression, or attempts to spread out on
516reaching a shallower slope (Figure 10a) (Wilson and Parfitt, 1993; Guest *et al.*, 2012). Stage 2: the
517pond continues to be fed by the flow and, once the capacity of the region containing the pond is
518reached, lava breaks out, and overflows (Figure 10Error: Reference source not foundb). This
519overflowing lava initially forms pāhoehoe, but transitions to `a`ā as it reaches the steeper slope at
520the edge of the pond. Stage 3: if the effusion rate is not high enough to sustain a flow, the breakout
521simply builds up the edifice, rather than allowing lava to continue to flow out of the pond. Further
522breakouts build the edifice incrementally, and the pond becomes raised above the surrounding lava
523field, armoured and flanked by lava that had previously overspilled (Figure 10 c). As the mound
524grows, the flanks steepen, and the summit widens. Although the summit may have initially started as
525a single pond of lava, it may have evolved into a more complex system, in which overflows from the
526pond are preceded by inflation and tumuli formation. Stage 4: thermal erosion within the mound
527may result in the formation of an interior “kettle” shape, based on observations of rootless shields at
528Kīlauea (Figure 10d). Stage 5: eventually, the height of the mound is such that the magmastatic
529pressure of lava contained within it is enough to overcome the strength of the flanks, leading to
530seeps on the flanks and at the base; the final phase of inflation at the summit fails to produce
531overflows (Figure 10e).

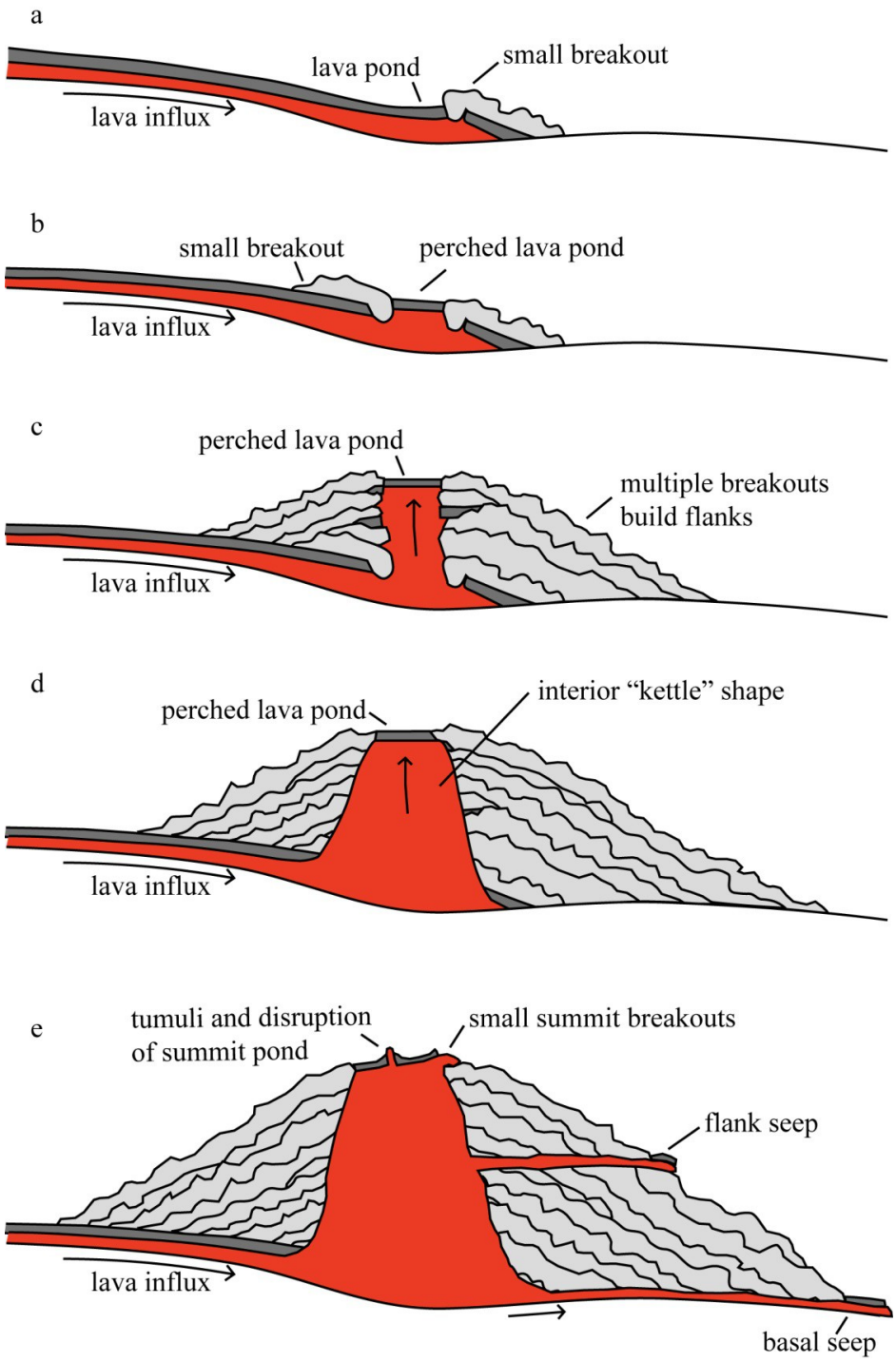

Figure 10. Hypothesised sequence of formation of a rootless mound. See main text in Section 5.2.4 for detailed commentary.

At Volcán Llaima, the rootless mounds are spread over an area of at least 6km^2, and there is a difference in elevation of around 550m from the top to the bottom of the rootless mound field. However, the order of formation of the mounds within the field is unclear. It is possible that, once a mound is breached at the base, the lava is then able to flow through that seep, so that more distal mounds formed after the proximal mounds. This was the case in the 2007–2008 phase of shield building on Kīlauea (Patrick and Orr, 2012). Rootless shields have also been observed to form at lava tube breakouts on Kīlauea, both after a pause in the eruption, in 1999, and over continuously active

lava tubes, in 2001-2002 (Kauahikaua et al., 2003). It is also possible that all the mounds were active at the same time, similar to each of the rootless shield fields already mentioned (Kauahikaua et al., 2003; Patrick and Orr, 2012). Another potential sequence of formation is that the most distal mound formed first, and as it built up, the lava became 'backed up' in the system, until it was able to break out closer to the main vent, so that the sequence of mounds propagated back towards the vent. It might be possible to distinguish the order of mound formation if the saddles between the mounds were sufficiently well exposed; however, at Volcán Llaima, the saddles that were investigated were mantled with complex, interacting pāhoehoe and `a`ā flows that defied simple interpretation.

5.3 Comparison of `a`ā mounds with other rootless lava structures

5.3.1 Kīlauea

The key differences between the rootless shields on Kīlauea and the rootless mounds on Volcán Llaima are the shape of the edifice that they build, and the morphology of lava as it overflows. At Kīlauea, the shields are wide and flat, with average slopes no more than 7° (based on heights and widths given by Kauahikaua *et al.*, 2003), and are composed exclusively of fluidal pāhoehoe lava. At Volcán Llaima, the mounds are taller, with average slopes of 20–25°, and the flanks are composed predominantly of `a`ā. It seems that the lava rheology may hold the key to these differences.

Kīlauean lava tends to be erupted as low viscosity (100 Pa s at 1150°C, Robert *et al.*, 2014) basalt (45–53 wt. % SiO_2, Jackson *et al.*, 2012) with a very low phenocryst fraction (Cashman *et al.*, 1999). It typically flows as pāhoehoe for many kilometres before cooling and microlite crystallization cause it to transition to `a`ā (Cashman *et al.*, 1999). In some locations, a sharp steepening in slope can also cause a transition to `a`ā (Peterson and Tilling, 1980). However, this normally only occurs after many kilometres of flow, when the lava has been primed for transition by the crystallization of microlites. The Kīlauean rootless shields are proximal, and fed by a long-lived lava tube system, and so they produce pāhoehoe that remains pāhoehoe as it flows away from the shield (Patrick and Orr, 2012; Kauahikaua *et al.*, 2003). The potential morphological evolution of the lava is evident fromFigure Figure 9: on eruption, the lava has viscosity close to the left-most blue line, and significant increases in viscosity and/or strain rate are necessary before the lava crosses into the transition zone.

At Volcán Llaima, the lava is basalt to basaltic andesite (51–56wt. % SiO_2, Bouvet de Maisonneuve *et al.*, 2013), and the 1780S lava has a very high crystal fraction – both the melt viscosity (100–4000 Pa s) and the bulk magma viscosity (500–400,000) are higher than on Kīlauea. As discussed above, the presence of bubbles in the lava appears to have been a key factor in allowing it to erupt as pāhoehoe. However, we infer that on eruption the lava was much closer to the pāhoehoe–`a`ā transition than Kīlauean lava, as indicated in Figure 9, and was more susceptible to changing morphology when slope angle, and therefore strain rate, changed. Thus the lava at Volcán Llaima formed pāhoehoe as it initially over-spilt from its pond, but as the slope steepened, it transitioned to `a`ā. This allowed it to build up steeper-sided edifices through repeated overflows.

5.3.2 Mount Etna

Many Etnean lavas (49–53wt.% SiO_2, Lanzafame *et al.*, 2013) are crystal rich, and at least one of the flow fields known to have produced terraces contained 29% phenocrysts (Guest *et al.*, 2012). It is possible that the crystallinity is one factor that increases the likelihood that this type of feature – rootless mounds and terraces or megatumuli – will form.

Another common factor between the specific eruptions at Volcán Llaima and Mount Etna that produced rootless mounds or lava terraces, is their longevity. The flow that produced these features on Mount Etna in 1614–1624 lasted 10 years, which is considerably longer than most Etnean eruptions (Guest *et al.*, 1984). The 1780S flow on Volcán Llaima also lasted 10 years, although it is difficult to compare with other eruptions at Volcán Llaima, due to poor historical records. It is

possible that these features are limited to long-lived lava flow fields with a correspondingly well-established lava tube network.

5.3.3 Vesuvius

Rittmann (1962) described lava morphologies at Vesuvius that are reminiscent of rootless mounds:

> "In the level ground of the Valle dell'Inferno, the dammed-up Vesuvius lava built dome-shaped hillocks 50–70m in height, best designated *rootless flow-domes*. The lava flowing down the outer slopes of Vesuvius in its thick-walled, tube-like tunnels was under high hydrostatic pressure, causing it to break through the solidified crust which had formed over the more level parts of the flow in the valley below. The now viscous lava welled out from the rents in contorted masses; these in turn acquired a congealed crust which was further ruptured to emit fresh masses of contorted plastic lava. In this manner the hillocks grew steadily higher, so long as the hydrostatic pressure behind the lava and the strength of the walls of the feeding tunnels allowed the process to continue."

Although there is no mention of a perched lava pond, and it is unclear how high the rootless flow domes grew, their mechanism of formation seems similar to features at Volcán Llaima and elsewhere.

5.3.4 Volcán Villarrica

Observations made by MAD indicate that, at nearby Volcán Villarrica, similarly crystal-rich lava forms almost exclusively pāhoehoe, with no evidence of the rootless `a`ā mounds seen at Volcán Llaima. One potential explanation for this is the comparatively short duration of eruptions at Volcán Villarrica. The 1780S rootless mounds are thought to have formed during a decade-long eruption, whereas historic eruptions at Volcán Villarrica have typically lasted for months only.

5.4 Synthesis of lava morphology features on Volcán Llaima

Lava from the 1780S flow field of Volcán Llaima may form a variety of morphological features: `a`ā; pāhoehoe; transitional features; and rootless mounds. However, one property is consistent everywhere: fresh breakouts produce pāhoehoe lavas. The lava then rarely flows as pāhoehoe for more than 50m before breaking up and transitioning into `a`ā.

We infer that the lava flows in a well-insulated tube prior to emerging at a downslope vent, such that it does not cool significantly (Helz *et al.*, 2003). When the lava breaks out – either close to the main vent, or from a rootless source – it carries a high volume fraction of phenocrysts, and is able to flow as fluidal pāhoehoe only because of the presence of bubbles. The rapid transition to `a`ā may result from an increase in viscosity, or from an increase in strain rate.

In the case of the transitional features seen at location 4, it appears that a change in viscosity is responsible for the transition. As the lava moves away from the vent, it cools, degases, loses bubbles through outgassing, and crystallizes microlites. All of these processes lead to an increase in viscosity. The lava continues flowing on the same slope, but reaches the transition between pāhoehoe and `a`ā as a result of this viscosity increase. Once the flow forms a substantial carapace – whether pāhoehoe, slabby pāhoehoe, or `a`ā clinker – the interior becomes insulated again, allowing lava to flow through it without significant cooling. Thus the flow is able to break out again, downslope, as pāhoehoe, repeating the cycle.

In the case of the rootless mounds seen at locations 5 and 6, it appears that a change in strain rate is predominantly responsible for the transition. The lava reaches a break in slope when it moves off the summit of a rootless mound and onto the steeper flanks. The resulting increase in strain rate causes it to transition to `a`ā. Lava in the interior of a flow that reaches the edge of a mound, and transitions

to `a`ā to flow down the flank, may then remain insulated and hot enough to break out as pāhoehoe again, once the flow reaches the shallower slope at the base.

Lava flowing down the slopes of Vesuvius broke out when the tubes reached flatter ground (Rittmann, 1962). At Mount Etna, the breakouts were interpreted to occur in part as a result of the steep slope, maintaining a high hydrostatic pressure on lava in the tubes (Guest *et al.*, 1984), and often formed on reaching a break in slope (Guest *et al.*, 2012). The slopes of Volcán Llaima are similarly steep, and sharp breaks in slope occur on the current ground surface in many locations, often because of the presence of erosional gullies cut by lahars. It is probable that the combination of steep slopes and breaks in slope are factors that favour the breakouts and ponding that must occur to trigger the building of rootless mounds.

5.5 Hazards associated with rootless edifices

One further aspect of rootless edifice growth that we have not touched on previously is the hazard implications of such features. During the 2007–2008 eruption of Kīlauea, in which multiple rootless shields formed, the edifices collapsed on a number of occasions (Patrick and Orr, 2012). These collapses released large volumes of lava and produced fast-moving `a`ā lava flows, a significant contrast to the slowly advancing pāhoehoe flows typically produced during this eruption. Similarly, Guest *et al.* (1984) suggest that `a`ā flows associated with the 1614–1624 eruption of Mount Etna may have burst out from the front of a terrace. Storage and sudden release of large volumes of mobile lava from potentially unstable edifices is therefore an aspect of these features that would need to be considered should they form during a contemporary eruption.

6 Conclusions

The 1780S lava flow field on Volcán Llaima displays a wide range of lava morphologies. The erupted lava was consistently close to the pāhoehoe-`a`ā transition: a small change in either strain rate or viscosity was enough to cause a transition in flow morphology in a number of settings. This flow field also produced newly described features – rootless mounds – that are comparable to rootless shields on Kīlauea, terraces and megatumuli on Mount Etna, and rootless flow domes on Vesuvius. This family of rootless edifices shares many features in common, while their differences depend on lava viscosity. Rootless edifices never form the dominant landform at any of these volcanoes, and occur only in a minority of eruptions at a single volcano.

Controls on the formation of rootless mounds, and similar edifices at Kīlauea, Mount Etna, and Vesuvius, include the crystallinity of the lava, the eruption duration, and the presence of steep slopes and breaks in slope. Rootless edifices are not common enough to determine which of these characteristics are necessary to trigger their formation.

Acknowledgements

We would like to thank Tim Orr for discussions regarding the comparison to Hawaiian volcanism, and Hugo Moreno for discussion during our fieldwork in Chile. JMT acknowledges support from NERC Studentship NE/K500999/1.

References

Anderson SW, Smrekar SE, Stofan ER. 2012. Tumulus development on lava flows: Insights from observations of active tumuli and analysis of formation models. *Bull. Volcanol.* **74**(4), 931-946.

Bottinga Y, Weill DF. 1972. The viscosity of magmatic silicate liquids: A model for calculation. *Am. J. Sci.* **272**, 438-475.

674Bouvet de Maisonneuve C, Dungan MA, Bachmann O, Burgisser A. 2012. Insights into shallow magma
675storage and crystallization at Volcán Llaima (Andean Southern Volcanic Zone, Chile). *J. Volcanol.*
676*Geotherm. Res.* **211-212**, 76-91.

677Bouvet de Maisonneuve C, Dungan MA, Bachmann O, Burgisser A. 2013. Petrological insights into
678shifts in eruptive styles at Volcán Llaima (Chile). *J. Petrol.* **54**(2), 393-420.

679Caricchi L, Burlini L, Ulmer P, Gerya T, Vassalli M, Papale P. 2007. Non-Newtonian rheology of crystal-
680bearing magmas and implications for magma ascent dynamics. *Earth Planet. Sci. Lett.* **264**, 402-419.

681Cashman KV, Mangan MT. 2014. A century of studying effusive eruptions in Hawai`i. In Poland MP,
682Takahashi TJ, Landowski CM (eds) Characteristics of Hawaiian volcanoes. *U.S. Geol. Surv. Prof. Pap.*
683**1801**, 357-394.

684Cashman KV, Thornber J, Kauahikaua JP. 1999. Cooling and crystallization of lava in open channels
685and the transition of pāhoehoe lava to `a`ā. *Bull. Volcanol.* **61**, 306-323.

686Dzierma Y, Wehrmann H. 2010. Eruption time series statistically examined: Probabilities of future
687eruptions at Villarrica and Llaima Volcanoes, Southern Volcanic Zone, Chile. *J. Volcanol. Geotherm.*
688*Res.* **193**, 82-92.

689Ewart A. 1976. Mineralogy and chemistry of modern orogenic lavas – some statistics and
690implications. *Earth Planet. Sci. Lett.* **31**, 417-432.

691Gauthier F. 1973. Field and laboratory studies of the rheology of Mount Etna lava. *Phil. Trans. R. Soc.*
692*Lond. A.* **274**, 83-98.

693Giordano D, Dingwell DB. 2003. Non-Arrhenian multicomponent melt viscosity: a model. *Earth*
694*Planet. Sci. Lett.* **208**, 337-349.

695Giordano D, Russell JK, Dingwell DB. 2008. Viscosity of magmatic liquids: A model. *Earth Planet. Sci.*
696*Lett.* **271**, 123-134.

697Guest JE, Wood C, Greeley R. 1984. Lava tubes, terraces and megatumuli on the 1614-1624
698pāhoehoe lava flow field, Mount Etna, Sicily. *Bull. Volcanol.* **47**, 635-648.

699Guest JE, Stofan ER. 2005. The significance of slab-crusted lava flows for understanding controls on
700flow emplacement at Mount Etna, Sicily. *J. Volcanol. Geotherm. Res.* **142**, 193-205.

701Guest JE, Duncan AM, Stofan ER, Anderson SW. 2012. Effect of slope on development of pāhoehoe
702flow fields: Evidence from Mount Etna. *J. Volcanol. Geotherm. Res.* **219-220**, 52-62.

703Helz RT, Heliker C, Hon K, Mangan M. 2003. Thermal efficiency of lava tubes in the Pu`u `Ō`ō-
704Kūpaianaha eruption. In Heliker C, Swanson DA, Takahashi TJ (eds) The Pu`u `Ō`ō-Kūpaianaha
705eruption of Kilauea Volcano, Hawai`i: the first 20 years. *U.S. Geol. Surv. Prof. Pap.* **1676**, 105-120.

706Hon K, Kauahikaua JP, Denlinger R, Mackay, K. 1994. Emplacement and inflation of pāhoehoe sheet
707flows: Observations and measurements of active lava flows on Kilauea Volcano, Hawai`i. *Geol. Soc.*
708*Am. Bull.* **106**, 351-370.

709Hon K, Gansecki C, Kauahikaua J. 2003. The transition from `a`ā to pāhoehoe crust on flows emplaced
710during the Pu`u `Ō`ō-Kūpaianaha eruption. In Heliker C, Swanson DA, Takahashi TJ (eds) The Pu`u
711`Ō`ō-Kūpaianaha eruption of Kilauea Volcano, Hawai`i: the first 20 years. *U.S. Geol. Surv. Prof. Pap.*
712**1676**, 89-103.

713Hoover SR, Cashman KV, Manga M. 2001. The yield strength of subliquidus basalts – experimental
714results. *J. Volcanol. Geotherm. Res.* **107**, 1-18.

715Jackson MG, Weis D, Huang S. 2012. Major element variations in Hawaiian shield lavas: Source
716features and perspectives from global ocean island basalt (OIB) systematics. *Geochem. Geophys.*
717*Geosys.* **13**(9), 1-24.

718Jurado-Chichay Z, Rowland SK. 1995. Channel overflows of the Pohue Bay flow, Mauna Loa, Hawai`i:
719Examples of the contrast between surface and interior lava. *Bull. Volcanol.* **57**, 117-126.

720Kauahikaua J, Sherrod DR, Cashman KV, Heliker C, Hon K, Mattox TN, Johnson JA. 2003. Hawaiian
721lava-flow dynamics during the Pu`u `Ō`ō-Kūpaianaha eruption: A tale of two decades. In Heliker C,
722Swanson DA, Takahashi TJ (eds) The Pu`u `Ō`ō-Kūpaianaha eruption of Kilauea Volcano, Hawai`i: the
723first 20 years. *U.S. Geol. Surv. Prof. Pap.* **1676**, 63-87.

724Lanzafame G, Mollo S, Iezzi G, Ferlito C, Ventura G. 2013. Unraveling the solidification path of a
725pāhoehoe ``cicirara'' lava from Mount Etna volcano. *Bull. Volcanol.* **75**, 703.

726Llewellin EW, Manga M. 2005. Bubble suspension rheology and implications for conduit flow. *J.*
727*Volcanol. Geotherm. Res.* **143**, 205-217.

728MacDonald GA. 1953. Pāhoehoe, aa, and block lava. *Am. J. Sci.* **251**, 169-191.

729Mader HM, Llewellin EW, Mueller, S. 2013. The rheology of two-phase magmas: A review and
730analysis. *J. Volcanol. Geotherm. Res.* **257**, 1-51.

731Maron SH, Pierce PE. 1956. Application of Ree-Eyring generalized flow theory to suspensions of
732spherical particles. *J. Coll. Sci.* **11**, 80-95.

733Marsh BD. 1981. On the crystallinity, probability of occurrence, and rheology of lava and magma.
734*Contrib. Mineral. Petrol.* **78**, 85-98.

735Moore HJ. 1987. Preliminary estimates of the rheological properties of 1984 Mauna Loa lava. In
736Decker RW, Wright TL, Stauffer PH (eds) Volcanism in Hawaii. *U.S. Geol. Surv. Prof. Pap.* **1350**, 1569-
7371588.

738Mueller S, Llewellin EW, Mader HM. 2010. The rheology of suspensions of solid particles. *Proc. R.*
739*Soc. A* **466**, 1201-1228.

740Mueller S, Llewellin EW, Mader HM. 2011. The effect of particle shape on suspension viscosity and
741implications for magmatic flows. *Geophys. Res. Lett.* **38**(13), L13316.

742Patrick MR, Orr TR. 2012. Rootless shield and perched lava pond collapses at Kilauea Volcano,
743Hawai`i. *Bull. Volcanol.* **74**(1), 67-78.

744Peterson DW, Tilling RI. 1980. Transition of basaltic lava from pāhoehoe to aa, Kilauea volcano,
745Hawaii: Field observations and key factors. *J. Volcanol. Geotherm. Res.***7**, 271-293.

746Peterson DW, Holcomb RT, Tilling RI, Christiansen RL. Development of lava tubes in the light of
747observations at Mauna Ulu, Kilauea Volcano, Hawaii. *Bull. Volcanol.* **56**, 343-360.

748Pinkerton H, Norton G. 1995. Rheological properties of basaltic lavas at sub-liquidus temperatures:
749laboratory and field measurements on lavas from Mount Etna. *J. Volcanol. Geotherm. Res.* **68**, 307-
750323.

751Pinkerton H, Sparks RSJ. 1976. The 1975 sub-terminal lavas, Mount Etna: A case history of the
752formation of a compound lava flow field. *J. Volcanol. Geotherm. Res.* **1**, 167-182.

753Pinkerton H, Sparks RSJ. 1978. Field measurements of the rheology of lava. *Nature* **276**, 383-385.

754Pistone M, Caricchi L, Ulmer P, Burlini L, Ardia P, Reusser E, Marone F, Arbaret L. 2013. Deformation
755experiments of bubble- and crystal-bearing magmas: Rheological and microstructural analysis. *J.*
756*Geophys. Res.* **117**, B05208.

757Pistone M, Caricchi L, Ulmer P, Reusser E, Ardia P. 2013. Rheology of volatile-bearing crystal mushes:
758Mobilization vs. viscous death. *Chem. Geol.* **345**, 16-39.

759Polacci M, Papale P. 1999. The development of compound lava fields at Mount Etna. *Phys. Chem.*
760*Earth* **24**, 949-952.

761Rittmann A. 1962. Volcanoes and their activity (Trans. Vincent EA), *Wiley (New York, London)*, 305 pp.

762Robert B, Harris A, Gurioli L, Medard E, Sehlke A, Whittington A. 2014. Textural and rheological
763evolution of basalt flowing down a lava channel. *Bull. Volcanol.* **76**, 824.

764Rowland SK, Walker GPL. 1990. Pāhoehoe and aa in Hawaii: volumetric flow rate controls the lava
765structure. *Bull. Volcanol.* **52**, 615-628.

766Sehlke A, Whittington A, Robert B, Harris A, Gurioli L, Medard E. 2014. Pāhoehoe to `a`ā transition of
767Hawaiian lavas: an experimental study. *Bull. Volcanol.* **76**, 876.

768Sparks RSJ, Pinkerton H, Hulme G. 1976. Classification and formation of lava levees on Mount Etna,
769Sicily. *Geology* **4**(5), 269-271.

770Swanson DA. 1973. Pahoehoe flows from the 1969-1971 Mauna Ulu eruption, Kilauea Volcano,
771Hawaii. *Bull. Geol. Soc. Am.* **84**, 615-626.

772Truby JM, Mueller SP, Llewellin EW, Mader HM. 2015. The rheology of three-phase suspensions at
773low bubble capillary number. *Proc. Roy. Soc. A.* **471**, 20140557.

774Walker GPL. 1971. Compound and simple flows and flood basalts. *Bull. Volcanol.* **35**, 579-590.

775Walker GPL. 1991. Structure, and origin by injection of lava under surface crust, of tumuli, “lava
776rises”, “lava-rise pits”, and “lava inflation clefts” in Hawaii. *Bull. Volcanol.* **53**(4), 612-634.

777Wilson L, Parfitt EA. 1993. The formation of perched lava ponds on basaltic volcanoes: the influence
778of flow geometry on cooling-limited lava flow lengths. *J. Volcanol. Geotherm. Res.* **56**, 113-123.

779Wolfe EW, Neal CA, Banks NG, Duggan TJ. 1988. Geological observations and chronology of eruptive
780events. *U.S. Geol. Surv. Prof. Pap.* **1463**, 1-98.